Transient Monotonic and Cyclic Load Effects on Mono Bucket Foundations

Nielsen, Søren Dam

DOI (link to publication from Publisher):
10.5278/VBN.PHD.ENGSCI.00100

Publication date:
2016

Document Version
Publisher's PDF, also known as Version of record

TRANSIENT MONOTONIC AND CYCLIC LOAD EFFECTS ON MONO BUCKET FOUNDATIONS

BY
SØREN DAM NIELSEN

DISSERTATION SUBMITTED 2016

AALBORG UNIVERSITY
DENMARK

Transient Monotonic and Cyclic Load Effects on Mono Bucket Foundations

Ph.D. Dissertation
Søren Dam Nielsen

Dissertation submitted April 14, 2016

Dissertation submitted:	April 14, 2016
PhD supervisor:	Prof. Lars Bo Ibsen Aalborg University
Assistant PhD supervisor:	Assoc. Prof. Benjaminn Nordahl Nielsen Aalborg University
PhD committee:	Professor Lars Damkilde (chairman) Aalborg University, Denmark
	Professor Martin Achmus Leibniz University Hannover, Germany
	Dr. Paul Doherty Gavin & Doherty Geosolutions, Ireland
PhD Series:	Faculty of Engineering and Science, Aalborg University

ISSN (online): 2246-1248
ISBN (online): 978-87-7112-552-8

Published by:
Aalborg University Press
Skjernvej 4A, 2nd floor
DK – 9220 Aalborg Ø
Phone: +45 99407140
aauf@forlag.aau.dk
forlag.aau.dk

Printed in Denmark by Rosendahls, 2016

Preface

This thesis "Transient Monotonic and Cyclic Load Effects on Mono Bucket Foundations" has been prepared in connection with a Ph.D. study carried out at the Department of Civil Engineering, Aalborg University, Denmark. The realization of this PhD project has only been possible with the financial support by The Danish National Advanced Technology Foundation project, entitled “Cost-effective deep water foundations for offshore wind turbines”.

I would like to thank my supervisor Professor Lars Bo Ibsen, for the opportunity to realise this PhD project and for his guidance during my studies. I would also like to thank my co-supervisor Associate Professor Benjaminn Nordahl Nielsen for his guidance and input to my work.

During my study I have had the opportunity of corporation with Universal Foundation A/S. I would like to thank the staff at Universal Foundation for their kindness and helpfulness, and for making me realise that there are many other factors than geotechnical issues that influence a good and cost-effective foundation design.

Most of the presented research is based on laboratory tests. I could not have conducted these tests without the assistance of my colleges at the geotechnical laboratory at Aalborg University. I appreciate their help and willingness to assists me when unexpected problems arose. I would also like to thank my colleagues at the Division of Structures, Materials and Geotechnics for their support and fruitful discussions.

Finally, I would like to thank my wife Ditte for her belief in me, her patience and love, and for granting me with the greatest gift of all, our daughter Emma.

Søren Dam Nielsen
Aalborg University, April 14, 2016

Abstract

The mono bucket foundation is a cost-effective foundation concept for offshore wind turbines and is a competitor the monopile, which currently supports almost 80 % of all installed European offshore wind turbines. Since the 1990s the bucket foundation concept has been widely used in the oil and gas industry. Arround the turn of the millennium, the industry started considering the mono bucket foundation for offshore wind turbines. The transition from supporting oil and gas structures to supporting offshore wind turbines, also meant a change in the loading conditions, and the use of existing design methods was not a possibility.

The dominating load for an offshore wind turbine is the overturning moment, mainly coming from wind and waves. Especially wave loads affects the foundation with repeated loads where a wave load is succeeded by the load from the next coming wave. This is denoted as cyclic loading, which is transferred via the foundation to the soil. The soil response to cyclic loading is complex, and there is still no generalised design methods that account for cyclic loading of the soil. Beside cyclic loading, large waves may also lead to impact loads with a short duration. This can lead to the generation of excess pore pressure in the soil, of which the effect is ambiguous.

Small-scale tests have shown that a short load duration creates suction in the pore water inside the bucket. This suction acts as a stabilising force and enhances the bearing capacity of the foundation. The shorter load duration the more enhancement, and thereby a higher bearing capacity.

The behaviour of the mono bucket foundation exposed to cyclic loading is also investigated by small-scale testing. Compared to previous similar investigations, the used load frequency is 1.0 Hz, which is 10 times faster compared to previous tests. In contradiction to previous findings, the experiments showed that two-way loading leads to the highest accumulation of permanent rotation. The tests have been used to calibrate a model, which can predict the accumulated rotation of a mono bucket foundation exposed to cyclic loading.

Abstract

Resumé

Bøttefundamentet er en omkostningseffektiv fundamentstype for havvindmøller og er en direkte konkurrent til monopælen, som i øjeblikket bruges ved næsten 80 % af alle installerede europæiske havvindmøller. Bøttefundamentskoncepter har været brugt i olie- og gasindustrien siden 1990'erne, hvor den har være den foretrukne funderingsløsning. Omkring årtusindeskiftet begyndte man at overveje brugen af bøttefundamentet til havvindmøller. Overgangen fra at bære olie- og gasstrukturer til at bære en havvindmølle, ændrer belastnigen betydeligt, hvorfor tidligere design metoder ikke kan anvendes direkte.

Den dominerende last for et havvindmøllefundament er det væltende moment, som primært skabes af belastninger fra vind og bølger. Især bølgelaster påvirker fundamentet med gentagende belastninger, hvor en bølgelast afløses af lasten fra den efterfølgende bølge. Dette benævnes som cyklisk belastning, som via fundamentet skal overføres til jorden. Jordens respons over for cyklisk belastning er kompleks, og der er endnu ikke udviklet nogle generelle metoder til at tage højde for den cykliske belastning af jorden. Udover cyklisk belastning, kan store bølger også påvirke konstruktionen med store laster af kort varighed. Dette medfører dannelsen af poretryk i jorden, hvoraf effekten heller ikke er klar.

Små-skala forsøg har vist at en kort lastvarighed medfører at der dannes et sug i porevandet inde i bøtten. Dette sug virker som en stabiliserende kraft og er med til at forstærke jordens bæreevne. Jo kortere lastvarigheden er, desto større bliver forstærkningseffekten, og dermed også bæreevnen.

Bøttefundamentets egenskaber ved cyklisk belastning er ligeledes undersøgt ved små-skala forsøg. I forhold til tidligere lignende forsøg er lastfrekvensen i de præsenterede forsøg 1.0 Hz, hvilket er 10 gange så højt som tidligere anvendt. Forsøgene viste, i modsætningen til tidligere forsøg, at tovejsbelastning medførte den største akkumulering af permanent rotation af fundamentet. Forsøgene er anvendt til at kalibrere en model, som kan beskrive den akkumulerede rotation af et bøttefundament udsat for cyklisk belastning.

Resumé

Contents

Preface iii

Abstract v

Resumé vii

1 Introduction 1
- 1.1 Motivation . . . 1
- 1.2 Introduction to Shear Strength of Sand . . . 3
- 1.3 Foundations for Offshore Wind Turbines . . . 5
- 1.4 The Suction Bucket . . . 8
  - 1.4.1 Suction Buckets for Oil & Gas Structures . . . 9
  - 1.4.2 Suction Bucket for Offshore Wind Turbines . . . 11
- 1.5 Mono Bucket Foundations . . . 12
  - 1.5.1 Installation and Decommissioning . . . 14
  - 1.5.2 Loading . . . 15
  - 1.5.3 Design of Mono Bucket Foundations . . . 17
  - 1.5.4 Current use of Mono Bucket Foundations . . . 19
- 1.6 Overview of the Thesis . . . 22

2 State-of-the-Art 25
- 2.1 Bearing Capacity Models . . . 25
- 2.2 Small-Scale Testing . . . 27
  - 2.2.1 Monotonic Loading . . . 27
  - 2.2.2 Cyclic Loading . . . 29
- 2.3 Numerical Modelling . . . 33
- 2.4 Structural Monitoring . . . 35

3 Scope of the Thesis 37
- 3.1 Main Findings of State-of-the-Art . . . 37
- 3.2 Aim and Objectives . . . 38

4 Summary of Research **39**
4.1 Laboratory Test Facility 39
4.2 Transient Monotonic Load Effects 42
4.3 Cyclic Load Effects 46
4.3.1 Cyclic Load Response Diagram 48
4.4 Monitoring of a mono bucket foundation at Dogger Bank . . . 50
4.4.1 Comparison with Laboratory Results 52

5 Conclusions **55**
5.1 Recommendation for future research 57

References **59**

A Undrained Cyclic Behaviour of Dense Frederikshavn Sand **67**
References 81

B Advanced Laboratory Setup for Testing Offshore Foundations **83**
References 106

C Dynamic behaviour of mono bucket foundations subjected to combined transient loading **109**
References 124

D Transient Loaded Bucket Foundations in Saturated Dense Sand - a Demonstration of The Boot Effect **125**
References 145

E Response of Cyclic Loaded Bucket Foundations in Saturated Dense Sand **147**
References 168

F Performance of a Mono Bucket Foundation - a Case Study at Dogger Bank **171**
References 184

G Manual for Pressure Tank **187**
G.1 Safety Instructions 187
G.2 Test Set-Up 188
G.3 Special Equipment 189
G.4 Preparation of laboratory tests 194

H Laboratory Results **199**

Chapter 1

Introduction

1.1 Motivation

The majority of European offshore wind turbines are installed on monopiles. A more cost-effective foundation is the mono bucket foundation, shown in Figure 1.1. The bucket foundation concept is well known in the oil and gas industry where it has been widely used since the 1980s. In the years surrounding the turn of the millennium, the bucket foundation was considered for offshore wind turbines and the idea of a new cost-effective foundation concept for offshore wind turbines was developed - the Mono Bucket Foundation (see Figure 1.1), (Byrne and Houlsby, 1999), (Byrne, 2000), (Feld, 2001), (Houlsby et al., 2005), (Ibsen, 2008). So far one wind turbine has been installed on a mono bucket foundation. It was a demonstration project in Frederikshavn where a prototype was installed in 2002, see Figure 1.19. Today, the mono bucket foundation has not yet been used for an offshore wind farm, and design codes does not provide design methods for the geotechnical design of the mono bucket foundation. However, the foundation must be designed to be able to resist the loads from possible load scenarios. If the foundation behaviour to a load scenario is unknown, a more conservative design must be chosen to account for the uncertainties related to the unknown behaviour. A more conservative foundation design will lead to a higher cost of the foundation. Therefore, it is likely that the cost of a foundation is reduced when the designer is able to make a more precise design. To do so, it is important that the foundation behaviours to possible load scenarios are investigated and documented.

The most common load scenario for an offshore wind turbine is a combination of wind and wave loading. The major part of the wind load act on the blades and the wave loads act on the foundation at sea level. During a storm, high wind speeds and large waves arise and, to protect the wind turbine, the

Fig. 1.1: Mono bucket foundations at the installation vessel Brave Tern, prior to installation at Dogger Bank in 2013. Photo by Universal Foundation A/S.

rotor is stooped, to minimise the wind load. However, in a storm scenario the foundation could be exposed to the impact from a breaking wave. Other load scenarios could be a collision of a vessel or an emergency stop of the wind turbine. These loads will typically be huge and have a short duration. Another possible load scenario is the impact from a large number of waves. With an average wave period of 10 s the foundation will be exposed to more than 60 million waves during a life-time of 20 years. This thesis investigates the bucket foundation behaviour in the mentioned scenarios, i.e. simulating the impact of a huge load with a short duration (transient load effect) and cyclic load effects, coming from the high number of waves hitting the foundation. All these forces leads to an overturning moment, which is the dominant load for an offshore wind turbine structure.

With the topic of the thesis now presented, the remaining part of this chapter will introduce the reader to the following subjects. As the foundation is installed in soil (in this thesis mostly dense sand), the bearing capacity is dependent on the soil conditions. Therefore, an introduction to shear strength of sands is given, followed by a description of the current foundation methods for offshore wind turbines. The chapter will also give an overview of how the bucket has been used in the oil and gas industry and why this is different compared to an offshore wind turbine foundation. Finally, the installation, the loading conditions and the design of the mono bucket foundation is described along with the current use of mono bucket foundations.

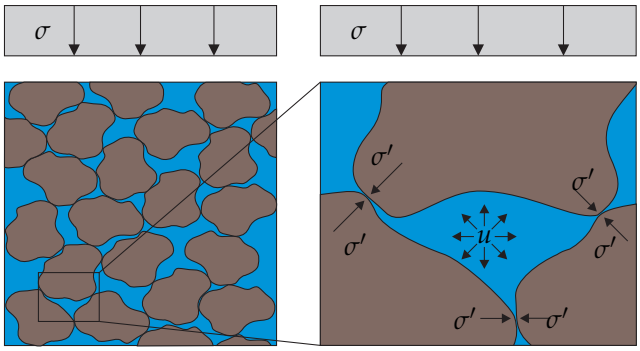

Fig. 1.2: Illustration of the effective stresses and the pore pressure in the soil. The effective stresses are transferred in the soil skeleton and the excess pore pressure is transferred in the pore water.

1.2 Introduction to Shear Strength of Sand

This section has the purpose of introducing the reader to the shear strength of sand. First a general description of soil properties is given, followed by a description of the shear strength of sand.

Mineral soils are divided into fractions depending on grain size. Soils with a grain size less than 0.002 mm is classified as clay, silt is the range from 0.06-0.002 mm, sand is 2-0.06 mm and gravel is the range from 60-2 mm. Beside the grains (solid), soils also consists of the spaces between them (voids). Offshore, the voids are filled with water and the soil is therefore saturated, as illustrated in Figure 1.2. The void ratio (e) is a relative measure of the volume of the voids (V_v) compared to the volume of solids (V_s). A soil which is well compacted therefore have a low void ratio and vice versa.

When a foundation is exposed to a load, it transfer the load to the surrounding soil. The stress that is transferred to the soil is called the total stress (σ). The soil reaction has two contributions 1) the effective stresses (σ') transferred to the soil skeleton and 2) the pore pressure (u) transferred to the pore water. Hence, $\sigma = \sigma' + u$.

When a soil is loaded the total stresses changes ($\Delta\sigma$) and is transferred to the soil as a change in effective stresses ($\Delta\sigma'$) and an excess the pore pressure (Δu). How the total stress is distributed between the effective stresses and the excess pore pressure depends on how fast the excess pore pressure can dissipate compared to the load duration. The dissipation rate depends on the hydraulic conductivity of the soil and the seepage. The hydraulic conductivity is a measure of how fast water can move through a soil. The finer soil the lower hydraulic conductivity. Hence, clay have a much lover hydraulic conductivity compared to sand. The seepage is the distance the water has

to travel. Therefore, the lower hydraulic conductivity and the longer seepage, the more of the total stress is transferred as excess pore pressure. If n excess pore pressure is generated during loading, all of the load change is transferred as effective stresses (σ'). This is called drained soil behaviour. On the other hand, if the excess pore pressure is unable to dissipate during loading the load change is transferred as excess pore pressure. This is called undrained behaviour. Partly drained soil response is then when only some of the excess pore pressure is able to dissipate. This means, that beside hydraulic conductivity and seepage, also the load duration influences if the soil response is drained, partly drained or undrained. Offshore foundations are huge structures and especially wave loads have a short duration. This means that even though sand have a high hydraulic conductivity, a long seepage and a short load duration can lead to undrained conditions. Drained conditions are defined as no excess pore pressure ($\Delta u = 0$) and undrained conditions are defined as no change in volume ($\epsilon_V = 0$).

The shear strength of the soil is governed by the effective stresses (σ') and, therefore, a positive excess pore pressure will lead to a reduction in soil strength and a negative excess pore pressure will increase the soil strength. A soil producing positive excess pore pressure when sheared is a contractive soil and a soil producing negative excess pore pressure when sheared is a dilative soil. The Critical State Soil Mechanics (CSSM) is a good tool to predict if a soil have a contractive or dilative behaviour. The framework is among others described by Holtz (2001) and Randolph and Gourvenec (2011). The basis of the critical state soil mechanics is that both the initial void ratio and the mean effective stress influence if a soil is contractive or dilative.

Figure 1.3 illustrates the stress path in a $q - p'$ diagram for sand sheared to failure. Figure 1.3(a) show the stress path for drained behaviour. In this case no excess pore pressure is generated, and during shearing the effective stresses increases until the stress path intersects the failure envelope. Figure 1.3(b) show a stress path for a contractive sand sheared undrained. Dur-

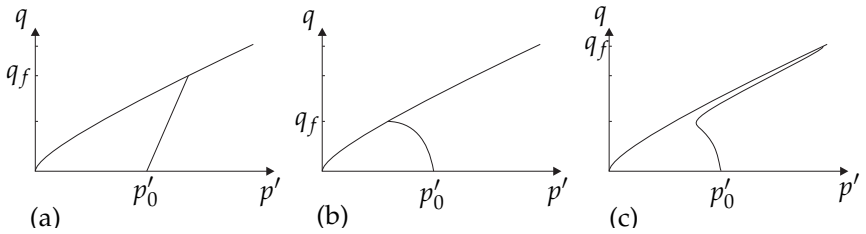

Fig. 1.3: Illustration of the effective stresses paths for (a) drained soil behaviour, (b) undrained contractive soil behaviour and (c) undrained dilative soil behaviour. q_f is the deviatoric stress at failure.

ing shearing positive excess pore pressure is generated, lowering the mean effective stresses until the stress path reaches the failure envelope. Figure 1.3(c) show the stress path for a dilative sand sheared undrained. The soil generates negative excess pore pressure, which increases the mean effective stresses. At failure the pore pressure has reached the cavitation pressure of the pore water. At this stage, the stress path intersects the failure envelope.

As mentioned, soils up to the grain size of sand may behave undrained for large offshore foundations, when exposed to impact loads. If positive pore pressure is generated (contractive behaviour) the undrained strength will be lower than the drained strength. But, if negative excess pore pressure is generated (dilative behaviour) the undrained shear strength will be higher than the drained strength. In this case, failure is reached when the cavitation pressure of the pore water is reached. Investigations hereof is also presented in Paper A, showing that the shear strength of dilative sand in undrained conditions is dependent on the initial total stress level.

1.3 Foundations for Offshore Wind Turbines

Installing wind turbines offshore was first demonstrated in Denmark with the wind farm Vindeby in 1991 (The guardian, 2015). Ever since, offshore wind energy is thought to be one of the substitutions for energy from fossil fuels. In 2014, Vestas installed an 8 MW wind turbine at a Danish test site at Østerild, which, at the time of writing, is the maximum capacity of a single turbine. According to Byrne and Houlsby (2003), up to 35 % of the installed cost of an offshore wind turbine is related to the foundations whereas RAB (2010) reports that the foundation cost accounts for 16 % of the life-time cost of wind energy where materials alone are 9.3 %. There is no doubt that foundations for offshore wind turbines are expensive, and the relative cost will only increase with water depth. Therefore, optimisation of these foundations will lead to cost savings and contribute to bringing down the cost of offshore wind energy.

Different foundation solutions to support an offshore wind turbine have been developed, each of them designed to be the most cost-effective for specific site conditions. Figure 1.4 show illustrations of the foundation concepts. Often, the usability of the foundations is related to the water depth which is directly comparable to the overturning moment, which is the dominating load. However, soil conditions also influence the choice of foundation. The following section will give a brief description of the foundation concepts shown in Figure 1.4.

Gravity based foundations (GBFs) are usually used in lower water depths. The overturning moment is counteracted by the self weight of the foundation, and the load is transferred at the base line of the foundation. The structures

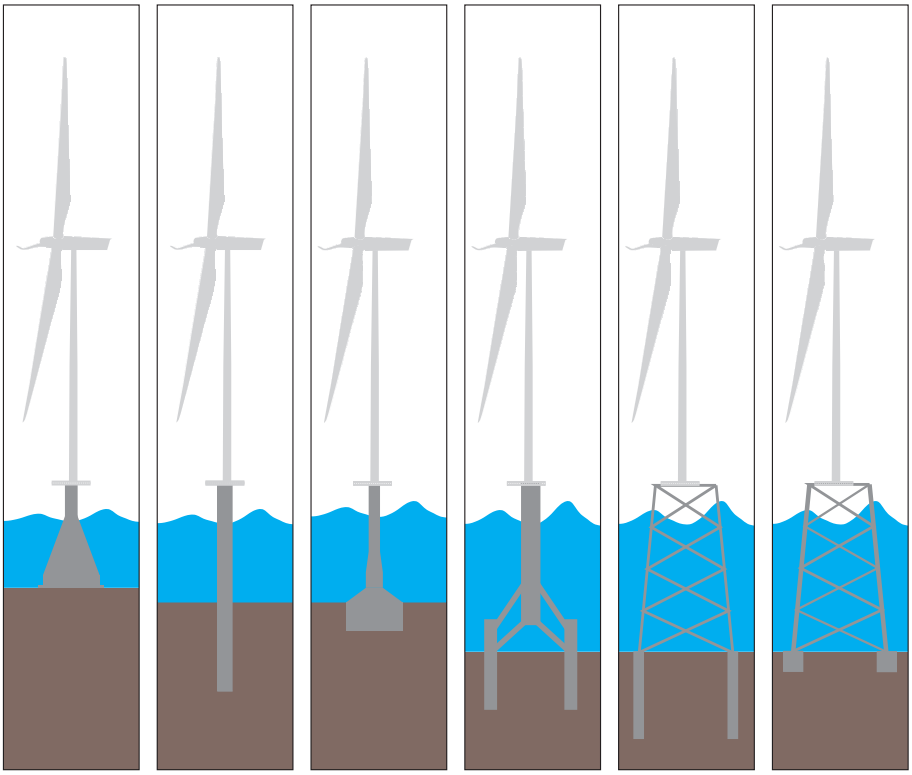

Fig. 1.4: Foundation concepts for offshore wind turbines. From left: Gravity Based Foundation (GBF), Monopile, Mono Bucket, Tripod on piles, Jacket structure on piles, jacket structures on buckets.

are well-suited for water depths in the range 0-25 m in positions with firm soil conditions, and preparation of the sea bed is necessary (DNV-OS-J101, 2013). MT Højgård (2014) reports that concrete GBFs will be used at a French site where the water depth is 35 m.

A monopile is a single pile, typically made of steel with a circular cross section. Usually they are used at deeper waters than GBFs. The overturning moment is counteracted by the horisontal earth pressure on the pile. The structure is well suited for water depths in the range 0-25 m (DNV-OS-J101, 2013). In 2015, DONG Energy installed a monopile with a diameter of 7.5 m (XL-monopile, which is a monopile with a large diameter) in 33 meters water depth (DONG Energy, 2015). The structure is less dependent on the soil conditions and is usable when the top soil layers are weak. However, if an impenetrable layer is reached before sufficient moment capacity is reached, other solutions must be considered.

A mono bucket foundation is a steel structure with a large diameter com-

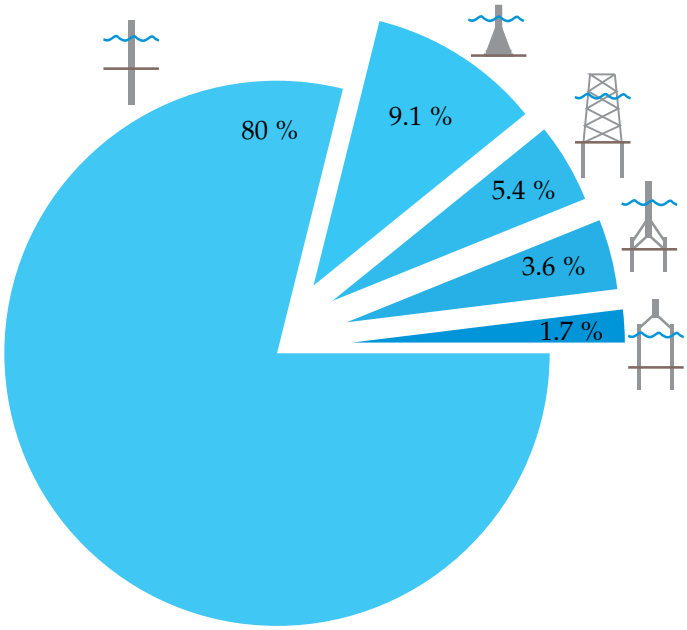

Fig. 1.5: Distribution of used foundation concepts for European offshore wind turbines up to 2014. 80 % monopiles, 9.1 % GBF, 5.4 % jackets, 3.6 % tripods, and 1.7 % tripiles, (EWEA, 2016)

pared to the penetration depth. It looks like a short, large diameter monopile where the length is typically smaller than the diameter. Hence the geotechnical behaviour is a mix of a GBF and a monopile. It is suitable for water depths from 0 to 25 m (DNV-OS-J101, 2013). For sites where soil layers with sufficient strength are located deep in the ground, alternatives have to be considered.

Common for the above mentioned foundations is that they consist of a single foundation structure. For wind turbines at deeper waters, the aforementioned foundations become uneconomical compared to foundation systems consisting of more than one foundation - multi foundations. These types of structures are usually jacket structures or tripods. A jacket is a lattice structure typically with three or four corners at seabed. Each corner is supported by a foundation which is typically a pile. However, a variant where bucket foundations are used instead of piles has been installed in 2014 (DONG Energy, 2014). A tripod is a three-legged structure where each leg consists of cylindrical steel tubes connected to a central steel column. For these types of structures, the overturning moment is counteracted as a pair of forces in the foundations, creating tension on the impact side and compression on the other. These structures are suitable for water depths in the range 20-50 m. (DNV-OS-J101, 2013). One variation of the tripod is called tripile founda-

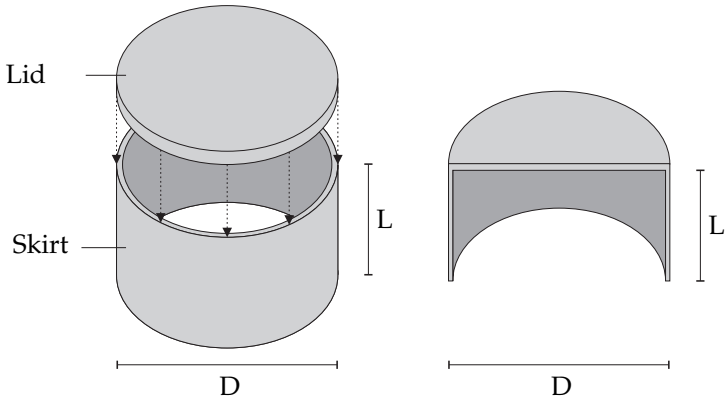

Fig. 1.6: Bucket foundation with circular cross section.

tion, where the foundation piles reach above the water level and are here connected to a short centre column.

According to EWEA (2016), 80 % of the European offshore wind turbines are supported by monopiles. 9.1% are supported by gravity based foundations, 5.4% by jackets, 3.6% by tripods and 1.7% is supported by tripiles, as illustrated in Figure 1.5. For wind farms completed in 2014, the average water depth was 27 m with an average distance to shore of 43 kM (EWEA, 2016). Looking only at the foundations installed in 2015, 97 % (385 foundations) of the installed foundations were monopiles and 3 % (12 foundations) was jacket structures (EWEA, 2016).

The mono bucket foundation is a more cost-effective alternative to the monopile (Carbon Trust, 2014). In order to optimize the design of the mono bucket, the foundation response to various load scenarios must be considered. Typically, research on mono bucket foundations has been investigating the drained response to monotonic and cyclic behaviours. However, design loads for offshore wind turbine foundations are typically from wind and waves where especially large waves may result in partly drained or undrained response.

1.4 The Suction Bucket

The bucket foundation, suction caisson, suction bucket, suction pile or suction anchor all refer to the same foundation concept of which the principle is a cylindrical steel shell structure (the skirt), closed in one end (the lid). The name "bucket" is due to the design of the foundation, see Figure 1.6. It resembles a bucket which is turned upside down. The driving force during installation is suction, created by pumping out trapped water from the in-

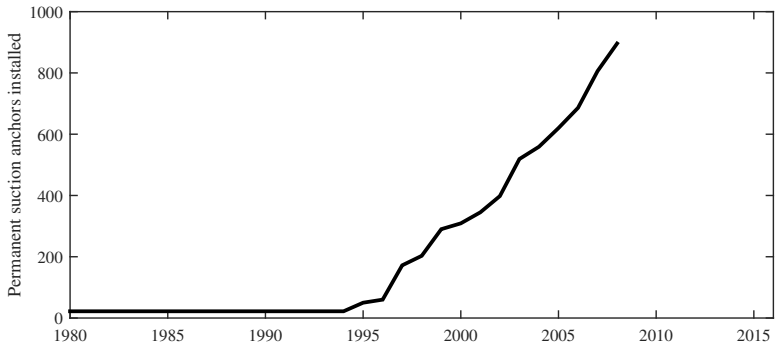

Fig. 1.7: Numbers of installed suction anchors. The graph is an approximated reproduction of the one presented in Tjelta (2015).

side of the bucket. Hence, the name "suction". After installation, the pumps are disconnected and the suction vanishes. The foundation then basically behaves like a buried GBF.

1.4.1 Suction Buckets for Oil & Gas Structures

The suction bucket technology was originally developed for the oil and gas industry. Tjelta (2015) reported that the number of installed suction anchors in the years 1980-1990 was only a few. By 2008 this number had increased to almost a 1000 installations, see Figure 1.7. The following years the numbers of installed suction anchors increased so much that it was impossible to keeping track of the numbers.

Tjelta (2015) reports that despite mooring structures, the suction installation technique was used for the first time on the Gullfaks C concrete oil platform in the North Sea in 1989. The platform had a weight of 55000 tons and was installed at a water depth of 218 m (Tjelta, 1992), see Figures 1.8. The installation of the concrete foundation, consisting of 16 large concrete piles, was assisted by two suction piles attached to the concrete foundation. After full installation, the piles penetrated 22 m into the seabed. The foundation is of the category gravity based structure (GBS).

From 1990 to 1992, the suction foundation concept was used for supporting the tension leg platform (TLP) Snorre A, see Figure 1.8. Despite a weight of the platform of 33000 tons, the Snorre A platform was floating and positioned at a water depth of 335 m (Offshore technology, 2015). Tjelta (2015) reports that the suction foundation concept, at this time, was the preferred foundation type.

In 1994, the Drauptner E platform was installed in dense sand at a water depth of 70 m, (Hansteen et al., 2003). Instead of a concrete structure, the

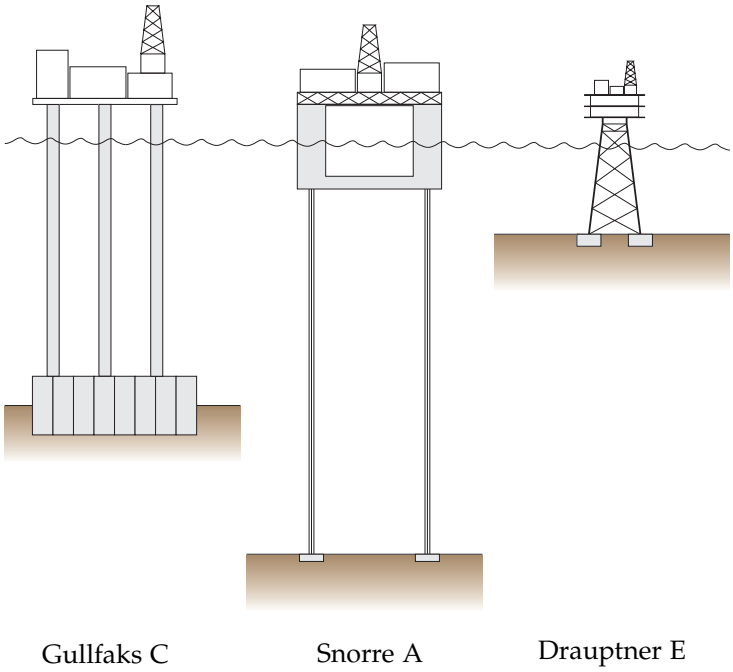

Fig. 1.8: Illustrations of the platforms: Gullfaks C (218 m of water), Snorre A (335 m of water) and Drauptner E (70 of water). Only the water depths are comparable; sizes of the platforms are not.

Drauptner E (Figure 1.8), consisted of a steel jacket foundation. The jacket structure was supported by a skirted foundation, in each of the four corners, where suction was used to reach full penetration (Tjelta, 2015). The self weight of the structure resulted in a load of 57 MN on each of the four legs (Randolph and Gourvenec, 2011).

At the Drauptner E platform, the excess pore pressure inside the bucket foundations and accelerations of the foundation and platform were monitored. Within the first half year, the platform was exposed to a severe storm including one extremely large wave. This type of wave is also called a "monster wave" or a "freak wave" (Hansteen et al., 2003). The video recording of the wave incident is shown online by NGI (2015). According to Hansteen et al. (2003), the freak wave height was 26 m and exposed the platform to a major impact load. Horisontal platform accelerations were measured to approximately $0.5g$ (Tjelta, 2015). However, the accelerations of the foundation were insignificant. The explanation of the response should be found in the pore pressure response. The overturning moment from the wave was distributed as a tension force on the toe legs (wave impact side) and a compression force on the heel legs. Tjelta (2015) reports that excess pore pressures of -80 kPa

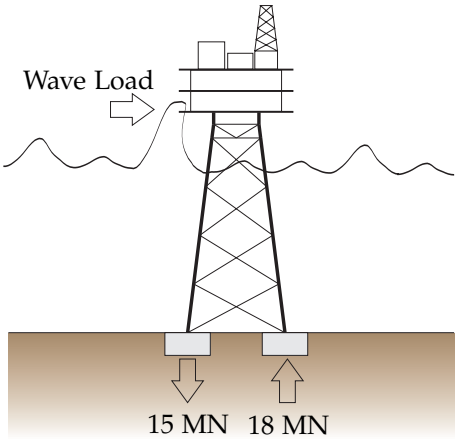

Fig. 1.9: The impact of a monster wave on the Drauptner E platform, induced excess pore pressures in the bucket foundations of which the resultant forces were 15 MN and 18 MN

and 100 kPa were measured in the toe and heel legs, respectively, and induced forces of 15 MN (downward) and 18 MN (upward), illustrated in Figure 1.9. The induced excess pore pressure dissipated quickly after the wave impact. Beside monitoring the wave impact, measurements also showed that there was no accumulation of excess pore pressure with time. Tjelta (2015) writes:

> *It is actually the best of two worlds:*
>
> - *undrained behaviour and capacity of the maximum load; and*
> - *drained behaviour to eliminate significant strength degradation from pore pressure accumulation.*

With the success as a foundation concept for oil and gas structures, the wind industry is now considering it as a cost-effective solution for offshore wind energy.

1.4.2 Suction Bucket for Offshore Wind Turbines

Two usages of the bucket foundation are considered for the offshore wind industry: buckets as foundations for a jacket structure and the use of a bucket as a mono structure, see Figure 1.10.

DNV-OS-J101 (2013) reports that jackets with buckets are suitable for water depths in the range 20 m to 50 m, Carbon Trust (2015b) reports suitable water depths to be in the range 30-60 m and SPT Offshore (2015) reports up to 120 m. For the mono buckets (suction buckets), DNV-OS-J101 (2013) reports it to be well suited for 0 to 25 m of water depth. However, Universal

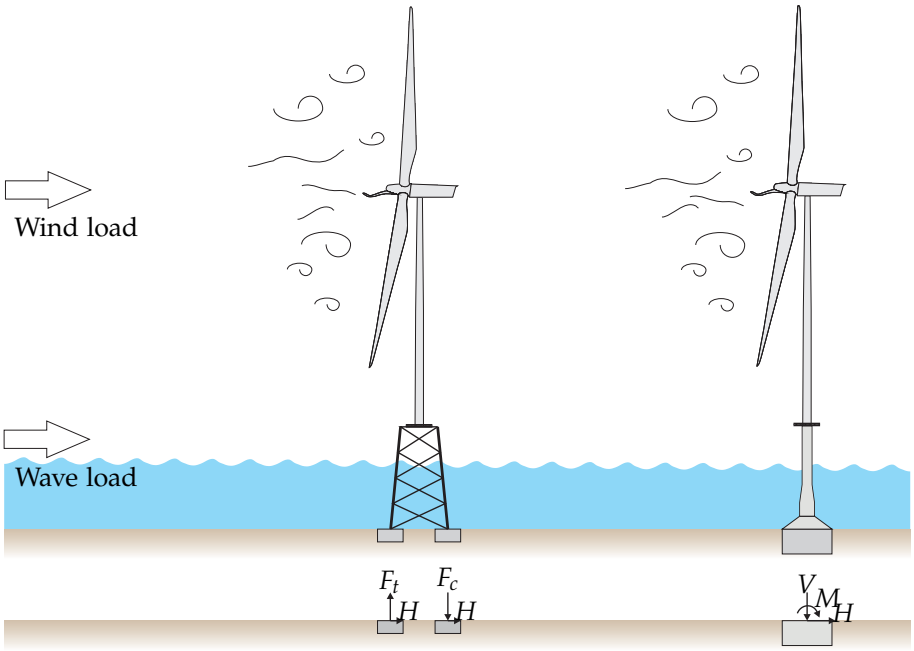

Fig. 1.10: Wind and wave loading on a bucket supported jacket structure (left) and a mono bucket foundation (right). The loads on the foundations are illustrated at the bottom part. V and H are vertical and horisontal loads and M is a moment. F_t and F_c are tension and compression forces. Only large overturning moments will trigger tension forces. For small overturning moments, the self-weight of the structure may be dominant creating only compression forces.

Foundation (2015d) reports that the concept has been verified up to 55 m of water depth supporting an 8 MW wind turbine.

Despite the estimated suitable water depths, the forces acting on the two foundations differ significantly, even though they both are exposed to the same types of loading. On the jacket structure, the overturning moment is taken as tension and compression forces in the foundations as illustrated left in Figure 1.10, and for the mono bucket foundation the foundation is exposed to an overturning moment as shown right in Figure 1.10.

As the research topic of this thesis is mono bucket foundations, the remaining part will only focus on the mono bucket foundation.

1.5 Mono Bucket Foundations

The mono bucket foundation is a cost-effective foundation concept developed for light-weight offshore structures, aiming at supporting offshore wind turbines, but does also have a huge potential as foundations for meteorological

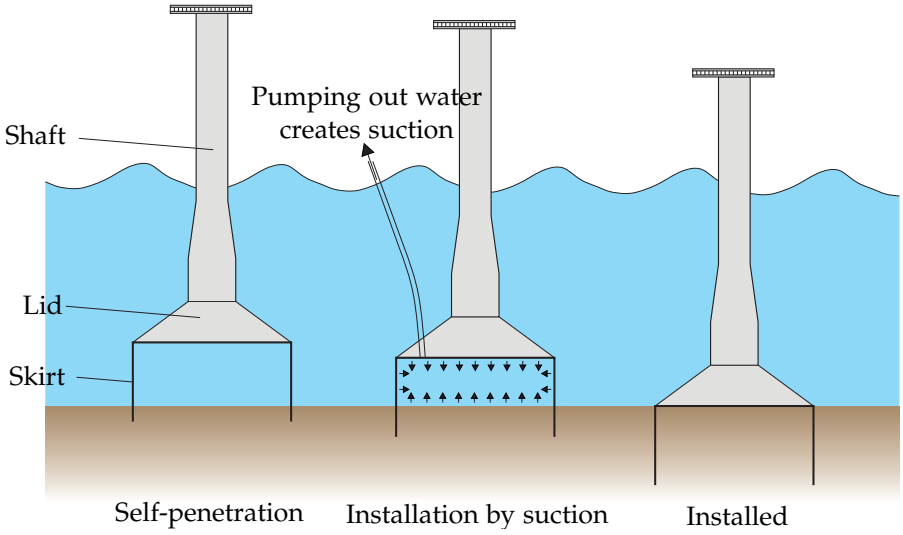

Fig. 1.11: Installation of a mono bucket foundation.

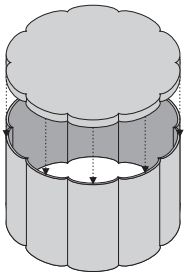

Fig. 1.12: Bucket foundation with multi-shell cross section.

masts (met masts). The mono bucket foundation is one structure that has the lowest parts penetrating into the sea bed and the upper part above sea level.

The Mono Bucket Foundation consists of three pieces: the skirt, the lid and the shaft, illustrated in Figure 1.11. The skirt is a relatively short cylindrical structure that penetrates into the soil. In the first designs, the bucket foundation had a circular cross section. Later the cross section changed shape into what is called the multi shell in order to enhance the buckling capacity, see Figure 1.12. Madsen et al. (2013) and Madsen et al. (2014) have investigated buckling of the new shape. It showed an enhanced buckling capacity which is important for the installation procedure where a larger driving force then can be applied. The lid is the middle part, sealing the top end of the skirts and connecting the skirts with the shaft, which is a conical structure with a circular cross section reaching from the sea bed to above sea level.

Fig. 1.13: Floating mono bucket foundation prior installation at Horns Reef II in 2009. Photo by Universal Foundation A/S.

1.5.1 Installation and Decommissioning

Before installation, the foundation is transported as one piece either floating (Figure 1.13) or on a vessel (Figure 1.1) to the location, for installation. At the location the bucket is lowered to the seabed where a part of the skirt is penetrating the soil due to the self-weight of the structure, the so-called self-penetration. The remaining part of the foundation (skirt) is installed by a suction technique where the pressure inside the bucket foundation is lowered, creating a downward force and thereby forcing the foundation to penetrate the seabed.

Previously, the mono bucket foundation has been considered for clayey or sandy soils only (layers were thought to be problematic), but a trial installation campaign by Universal Foundation (2015b) showed successful installation in a wide range of soil profiles: Soft clay, Moraine clay, Boulder bank clay with sand spikes and layers, Clay crust, Sand and Silt. However, the concept will though still have limited use for sites with weak top soils and is not applicable in gravel and rocks.

After many years of supporting a structure, like an offshore wind turbine, the turbine has exceeded its design life-time and has to be decommissioned. The same goes for the foundation. The suction technique for installation is reversed, and by increasing the pressure inside the bucket, an upward force is created, forcing the foundation out of the seabed. This makes it possible to remove the foundation completely contrary to monopiles where the steel beneath the soil surface is left after use. This has been proven at Horns Rev II, where a bucket foundation was removed in 2015 after six years of service, (Universal Foundation, 2015c).

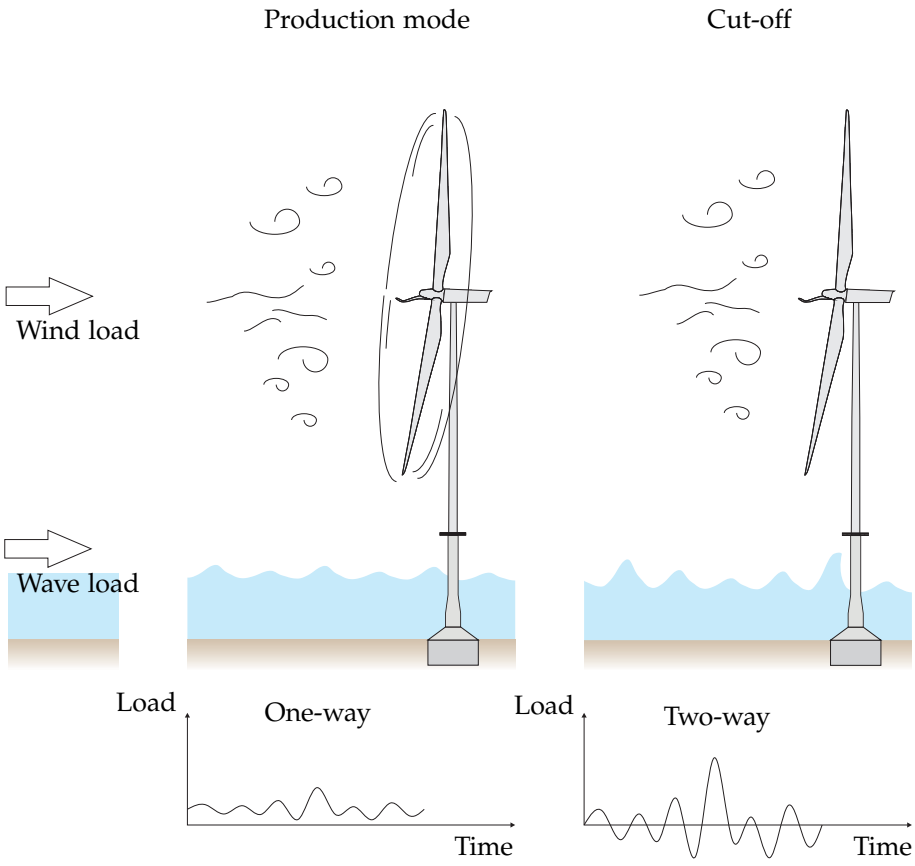

Fig. 1.14: Loads on a mono bucket during production mode and a storm event (cut-off).

1.5.2 Loading

As the foundation is developed for offshore structures, it will be exposed to severe environmental loads coming from wind and waves and, in some areas, ice, current and seismic loads may also be present. Figure 1.10 presents an illustration of a wind turbine exposed to wind and wave loading. The wind loads on the blades create a horisontal force at hub height and waves create horisontal loads near the sea water level.

When designing foundations, all loads are translated to the centre point of the foundation at mud line, creating the loads depicted in Figure 1.10. Hence, the loads from wind and wave will create a horisontal and a moment load on the foundation. This type of loading is often referred to as combined loading. The moment arms on the wind and wave loads are different. Hence, creating different ratios between the moment (M) and horisontal loading (H).

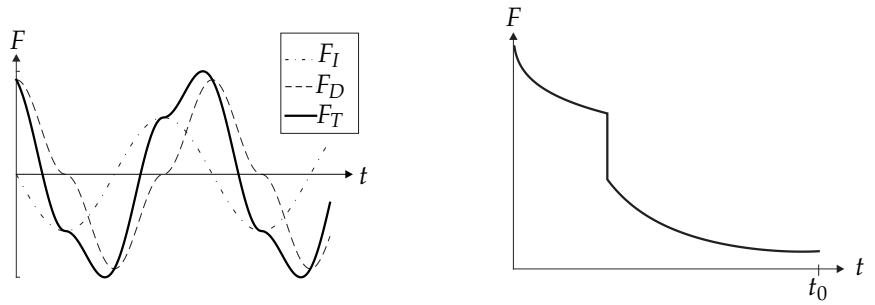

(a) Wave load from regular wave.

(b) Slamming load from a breaking wave.

Fig. 1.15: (a) shows an example of wave loads with time from a regular wave and (b) shows an example of the load from a slamming load with time. Wienke et al. (2004) calculate t_0 to 80 ms for an example of a breaking wave hitting a monopile.

When the velocity of the wind is lower than the cut-out speed of a wind turbine, the rotor is spinning and the turbine is producing electricity. Here, the wind load at hub height is high, and the cyclic loads from the waves will introduce one-way cyclic loading, see Figure 1.14. When the wind speed exceeds the cut-out wind speed, the blades pitch out of the wind and stop rotating to minimise the wind loads. Even though the wind load is minimised, it is still not negligible. However, wave loading may often be the dominant load for a design of an offshore wind turbine in the ultimate limit state. This situation will lead to two-way loading on the foundation, see Figure 1.14.

Wave periods are typically in the range 4 s to 25 s, (DNV-OS-J101, 2013). For sites in the southern North Sea, the significant peak period with a 50 years return period is 10 s to 15 s and 10 s to 14 s for a return period of 1 year (Lesney, 2010). Assuming an average wave period of 10 s and a life-time of 20 years the structure will be exposed to $6 \cdot 10^7$ waves. Figure 1.15a gives an example of a time series of wave loading from a regular wave load on a cylindrical structure. The wave load (F_T) calculated by morison's equation is the sum of inertia (F_I) and drag (F_D) forces on the structure and is only valid for non-breaking waves. For breaking waves, Wienke et al. (2004) present an expression calculating the slamming load from a breaking wave. Figure 1.15b illustrates the wave load with time. Wienke et al. (2004) present an example of an impact from a breaking wave on a mono pile where the duration (t_0 in Figure 1.15b) is 80 ms.

Waves, therefore, lead to significant cyclic loading and severe impact loads. An impact load could also be a result of an emergency stop where the rotor is brought to a halt in a few seconds leading to high accelerations. Therefore, the foundation response of impact and cyclic loads are highly relevant for the design of an offshore wind turbine foundation. Byrne and

Houlsby (2004) give an example of loads on a 3.6 MW wind turbine in a water depth of 10 m. The self-weight of the structure was estimated to 6 MN and the combined horisontal force from wind and wave was estimated to 4 MN acting at an average height of 30 m above seabed and, thereby, creating an overturning moment of 120 MNm. The overturning moment of the foundation is the dominant load, which is also indicated in the example.

1.5.3 Design of Mono Bucket Foundations

An offshore wind turbine foundation basically has to meet two requirements: the overall stability must be ensured and the permanent rotation should not exceed a specified criterion, based on the wind turbine performance (typical 0.5°). (There is also a requirement to the allowed natural frequency, but this will not be described in this thesis).

A stability analysis calculates the bearing capacity of the foundation. The stability must be ensured for different limit states: Ultimate limit state (ULS), accidental limit state (ALS) and the effect of cyclic loading should also be included. In the ULS, the loads are multiplied a safety factor larger than one, and the strength parameters for the soil are divided by a safety factor larger than one in order to introduce safety. Examples of ULS loads could be environmental loads with a return period of 50 or 100 years. The critical load combinations must not exceed the bearing capacity. The stability must also be ensured for ALS where partial safety factors of 1.0 are used. The ALS represents a scenario of e.g. a ship impact. Lastly, the stability should also be ensured for cyclic loading, which may influence the strength of the soil.

The defined criteria for maximum rotation should be ensured in a characteristic consideration in the serviceability limit state (SLS) where the rotation for any critical load combination should be calculated. Furthermore, cyclic loading may also lead to a degradation of the secant stiffness which will lead to accumulation of permanent rotation.

Guidelines for designing bucket foundations for offshore wind turbines are given in DNV-OS-J101 (2013), and a mono bucket foundation is recommended to be designed as a gravity based foundation where the loads are transferred from the foundation base line to the adjacent soil as illustrated in Figure 1.16. For homogeneous soils, the general bearing capacity formula can be used where the loads are transferred to the load centre (LC) on the foundation base which is assumed at skirt tip as illustrated in Figure 1.16. At the load centre only vertical and horisontal forces acts. Moments will move the load centre and, thereby, force the foundation to be eccentric loaded with the eccentricity $e = M/V$, as shown in Figure 1.16.

Figure 1.17a illustrates the failure mechanism for an eccentric loaded foundation. If the eccentricity exceeds $e > 0.3b$, the foundation is extremely eccentric loaded. In this situation, another failure mechanism may occur

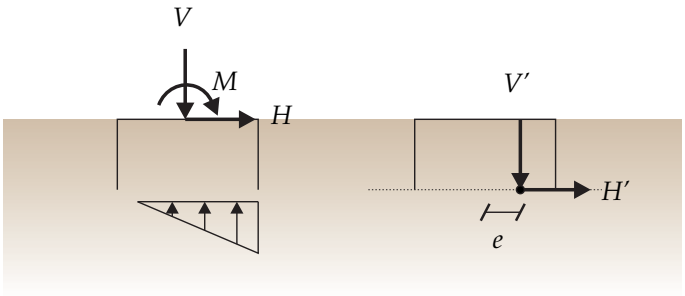

Fig. 1.16: Loads on bucket foundations

(a) Adjacent soil contribute to the bearing capacity.

(b) Failure mechanism is formed below the foundation.

Fig. 1.17: Failure mechanism for eccentric loaded gravity based foundations.

which is formed below the foundation as illustrated in Figure 1.17b. Hence, an extremely eccentric loaded foundation must be designed for both situations.

In the load example given by Byrne and Houlsby (2004), the eccentricity is $e = M/V = 20$m. If the turbine was supported by a mono bucket foundation, the minimum diameter of the foundation must be $D \approx 75$ m in order to not be extremely eccentric loaded. A mono bucket foundation of this size is unrealistic. In Frederikshavn, a 3 MW turbine only exposed to wind loads is supported by a bucket foundation with $D = 12$ m. Hence, it is believed that mono bucket foundations supporting offshore wind turbines will be extremely eccentric loaded. By only accounting for the failure mode in Figure 1.17b, the earth pressure on the skirts is not considered. Excluding this will lead to a very conservative design.

According to DNV-OS-J101 (2013), it is acceptable to use the conventional bearing capacity formula for mono bucket foundations in uniform soil conditions. Hence, both of the failure modes illustrated in Figure 1.17 must be considered. In addition, the sliding resistance must also be larger than the horisontal load. Typically, sand is considered as a drained material and clay as an undrained material. However, DNV-OS-J101 (2013) states that the most accurate conditions must be applied, whether it is drained, partly drained or undrained conditions. For large structures exposed to loads with a short

Fig. 1.18: Bathemetry of the North Sea, showing the locations of Frederikshavn and Dogger Bank. (edited, EEA (2015))

duration, even sandy soils may have a partly drained or almost undrained behaviour.

As mentioned, the effect of cyclic loading must be considered in the foundation design. However, there is no standardised way of including these effects in the foundation design. Analysis of cyclic loading should include the stiffness and strength degradation and it should evaluate if there will be any excess pore pressure build up. However, it is up to the designer to use appropriate design methods.

1.5.4 Current use of Mono Bucket Foundations

The major goal of using mono bucket foundations as support structures for offshore wind turbines has not yet been reached. Nevertheless, a situation in which an offshore wind farm will be installed on mono bucket foundations has come closer. During the last decades, large steps have been made to approach the goal. These major steps are listed below:

Fig. 1.19: Installation of the mono bucket in Frederikshavn in 2002.

- The first prototype of the Mono Bucket Foundation was installed in Frederikshavn in 2002, see Figures 1.18 and 1.19, supporting a Vestas V90 3MW turbine, (Ibsen, 2008). The bucket has a diameter of 12 meters and a skirt length of 6 meters. It was installed in shallow water in a bassin close to the port of Frederikshavn. The foundation has been exposed to the self weight of the foundation of 135 ton and the weight of the turbine of 264 ton. Furthermore, the wind turbines have been exposed to wind loads, and a high number of emergency stops. The emergency stops have been utilised to investigate the dynamic response by Damgaard et al. (2013). As it has been installed in a basin, the turbine has not been exposed to wave loading. The wind turbine is still in use and producing electricity.

- In 2005, Enercon attempted to install a bucket foundation in Wilhelmshaven. However, the installation was unsuccessful as a component buckled (Renewables International, 2015).

- In 2008, The Carbon Trust[1] launched their Offshore Wind Accelerator Programme, a joint industry project between the Carbon Trust and nine offshore wind developers: DONG Energy, E.ON, Mainstream Renewable Power, RWE Innogy, Scottish Power Renewables, SSE Renewables, Statkraf, Statoil and Vattenfall (Carbon Trust, 2015c). The project had one major goal: reduce the cost of offshore wind. One of the topics was foundations. Here, the mono bucket foundation was selected as one out of four winners among 104 participating concepts. The four winners were chosen as the most promising innovative foundation concepts

[1] *Citet from Carbon Trust (2015a): "The Carbon Trust is an independent, expert partner of leading organisations around the world, helping them contribute to and benefit from a more sustainable future through carbon reduction, resource efficiency strategies and commercialising low carbon technologies."*

Fig. 1.20: Installed mono bucket foundation at Horns Rev II in 2009. Photo by Universal Foundation A/S.

Fig. 1.21: Removal of the mono bucket foundation (Figure 1.20) at Horns Rev II in 2015. Photo by DDB Jack-up Services.

for offshore wind energy.

- In March 2009, a meteorological mast (metmast) was installed on a bucket foundation at Horns Reef 2, see Figures 1.18 and 1.20. On the 7th of July 2015, the metmast was decommissioned (see Figure 1.21), and the bucket was successfully removed by inverting the suction technique used for installation (Universal Foundation, 2015c).

- In 2013, two meteorological masts were installed on mono bucket foundations at Dogger bank, see Figures 1.18, 1.22 and 1.23, named Dogger Bank East and Dogger Bank West after their relative locations (Universal Foundation, 2015a). This thesis presents some of the measurements from Dogger Bank West metmast.

- In September 2014, a trial installation campaign was completed with the goal of proving that the bucket can be installed in a broad variation of soil conditions. 28 installations were achieved in 24 days and all with less than 0.1° of inclination. (Carbon Trust, 2014).

- In June 2015, a non-profit organisation, Lake Erie Energy Development Corporation (LEEDCo), aiming at developing offshore wind energy in Ohio, USA, announced that they had chosen the mono bucket foun-

Fig. 1.22: Mono bucket foundation installed at Dogger Bank. Photo by Universal Foundation A/S.

Fig. 1.23: Met mast at Dogger Bank supported by a mono bucket foundation. Photo by Universal Foundation A/S..

dation to support the offshore wind turbines that must be installed in Lake Erie, Ohio. A final foundation design is planned for completion in early 2016. Furthermore, their goal is to generate 1000 MW of wind energy in 2020 (LEEDCo, 2015).

1.6 Overview of the Thesis

It has now been outlined that offshore wind turbine foundations are exposed to severe impact loads and a high number of cyclic loads. These effects should be included in the design of a foundation. However, there is no standardised procedure to take the transient and cyclic load effects into account. Therefore, these topics are of interest, and the thesis will present research on these topics.

To utilise existing knowledge and aviod unnecessary investigations, the research already performed on the topics are examined. The remaining part of this thesis will first present state-of-the-art within research on the mono bucket foundation followed by a chapter explaining the overall scope of the thesis, which has been investigated through the research presented here. The research is disseminated in six papers: two conference proceedings and four journal papers. A summary of this research is given after scope of the thesis, followed by a conclusion.

The individual papers are given in the appendices named Paper A, B, C, D, E and F. Furthermore, in the making of this thesis a manual describing the used test set-up has been made, which is given in Appendix G. Appendix H contains the presented test results.

The structure of the remaining chapters of the thesis is given as bullets below:

- **Chapter 2** State-of-the-Art
- **Chapter 3** Scope of the Thesis
- **Chapter 4** Summary of Research
- **Chapter 5** Conclusions
- **Paper A** Undrained Cyclic Behaviour of Dense Frederikshavn Sand
- **Paper B** Advanced Laboratory Setup for Testing Offshore Foundations
- **Paper C** Dynamic behaviour of mono bucket foundations subjected to combined transient loading
- **Paper D** Transient Loaded Bucket Foundations in Saturated Dense Sand - a Demonstration of The Boot Effect
- **Paper E** Response of Cyclic Loaded Bucket Foundations in Saturated Dense Sand
- **Paper F** Performance of a Mono Bucket Foundation - a Case Study at Dogger Bank
- **Appendix G** Manual for Pressure Tank
- **Appendix H** Laboratory Results

Chapter 2

State-of-the-Art

Research on the load response of mono bucket foundations involves multiple disciplines. These are analytical/semi imperical formulations, small scale testing, numerical modeling and structural monitoring. This section summaries the existing research on the behaviour of the mono bucket foundation on the mentioned topics. Special attention is given to the bearing capacity to monotonic loading and the accumulated deformations due to cyclic loading.

2.1 Bearing Capacity Models

Analytical formulations follow the classic upper and lower bound theorems. Karl Terzaghi was the first to establish an upper bound formulation to describe the bearing capacity of a vertical loaded strip foundation laying on top of a horisontal homogenous soil layer, (Terzaghi, 1943). The formulation defined the vertical bearing capacity as the sum of the contribution from soil mass (R_γ), cohesion (R_c) and overburden pressure (R_q). Thereof, $R = R_\gamma + R_c + R_q$. Since then, the bearing capacity has been extended to account for load eccentricity that the foundation is buried, and that the foundation has a finite length by Hansen (1970). He described the vertical bearing capacity (Q) as

$$\frac{Q}{A} = \frac{1}{2}\gamma' B N_\gamma s_\gamma d_\gamma i_\gamma b_\gamma g_\gamma + \bar{q} N_q s_q d_q i_q b_q g_q + c N_c s_c d_c i_c b_c g_c \qquad (2.1)$$

where

γ'	effective unit weight
B	width of foundation
N_γ, N_q, N_c	bearing capacity factors
s_γ, s_q, s_c	shape factor
d_γ, d_q, d_c	depth factor
i_γ, i_q, i_c	inclination factor
b_γ, b_q, b_c	base inclination factor
g_γ, g_q, g_c	ground inclination factor

Later, the factors have been adjusted by many authors such as Michalowski (1997) and Ibsen et al. (2012). Gottardi and Butterfield (1993) mention that by describing the load conditions by the vertical load (Q), the inclination (i) and eccentricity (e), the designer has very little overview of the consequences of changes in loading conditions. Furthermore, sliding has to be investigated separately. However, the formulations are widely accepted and still used to calculate the bearing capacity of surface foundations.

Gottardi and Butterfield (1993) report the problem with the bearing capacity formula where superposition is used for a non-linear problem. In order to establish a complete formulation of bearing capacity of a foundation with the breadth (B) in $V, M/B, H$ space. Gottardi and Butterfield (1993) have established interaction diagrams. In total three diagrams describing the foundation behaviour in $V-H$, $V-M/B$ and $H-M/B$ planes. The diagrams were calibrated to laboratory tests on small-scale foundations exposed to a broad variety of load combinations and normalised with the maximum vertical load for each test (V_{max}) (Gottardi and Butterfield, 1993). Combining the three interaction planes can establish, a 3D interaction surface. This interaction surface has later been described as a cigar shaped yield surfaces, for example by Gottardi and Butterfield (1995).

Initially, the yield surfaces were developed for strip foundations (Roscoe and Schofield, 1957). The yield surfaces were based on work-hardening plasticity. They were not only able to predict failure loads, but also the elastic foundation response.

Butterfield et al. (1997) made standardised sign conventions (Figure 2.1a) to reduce the numbers of different coordinate systems to a single one. Gottardi et al. (1999) and Houlsby and Cassidy (2002) developed yield surfaces for circular footings. Byrne and Houlsby (1999) presented a yield surface for suction caissons and observed that the yield surface changed shape as the skirt length increased, cf. Figure 2.2. Villalobos et al. (2009) and Ibsen et al. (2013) has since reproduced this finding. Additional work on monotonic loading described by yield surfaces are given in Mangal and Houlsby (1999), Salciarini and Tamagnini (2009), Ibsen et al. (2012), Larsen et al. (2013), (Ibsen et al., 2013), (Ibsen et al., 2014) and (Ibsen et al., 2015). Byrne and Houlsby (2004) and Foglia et al. (2015) investigated cyclic loading of bucket foundations.

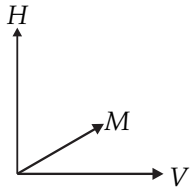

(a) (V, M, H) sign convention using right-handed coordinate system.

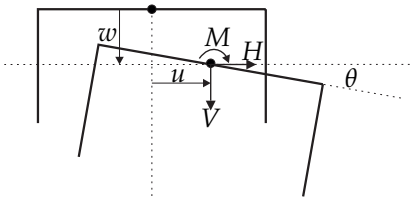

(b) Standardised sign convention of the mono bucket foundation.

Fig. 2.1: Signconvention used for the mono bucket foundation. w and u are the vertical and horisontal translations, and θ is the rotation. V and H are the vertical and horisontal forces, and M is the moment, all applied at the centre of the bucket. x and y refer to the local coordinate system with reference point at the centre of the bucket lid.

Common for the yield surfaces is that they all need to be calibrated against laboratory tests. Since full-scale tests are expensive and very demanding, small-scale tests are often used.

2.2 Small-Scale Testing

Small-scale tests are laboratory tests conducted on miniature models of a full size foundation. They can either be conducted at $1g$, meaning that they are exposed to the gravity on earth or at multiple g where the gravity in the tests is increased. Multiple g is obtained by conducting the tests in a centrifuge, where the centrifugal force acts as gravity on the model. The artificial gravity on the model is then increased by increasing the angular velocity of the centrifuge.

2.2.1 Monotonic Loading

Byrne and Houlsby (1999) conducted 1g small-scale tests on four mono bucket foundations with diameters of 100 mm and embedment ratios (skirt length/ diameter) of 0, 0.16, 0.33 and 0.66. The tests were performed in a loading rig developed to calibrate macro models for foundations. The mono bucket foundations were installed in dry sand with a relative density of 95 % and loading rates of 0.01 mm/s or 0.01 °/s to ensure drained conditions and ensure that no rate effects were present. The paper concluded that the yield surface of a mono bucket foundation can be described by parabolic ellipsoids and that different embedment ratios will have different shapes of the yield surfaces.

Byrne and Houlsby (2004), Houlsby et al. (2005), Kelly et al. (2006), Villalobos et al. (2009) also performed tests with the loading rig used in Byrne

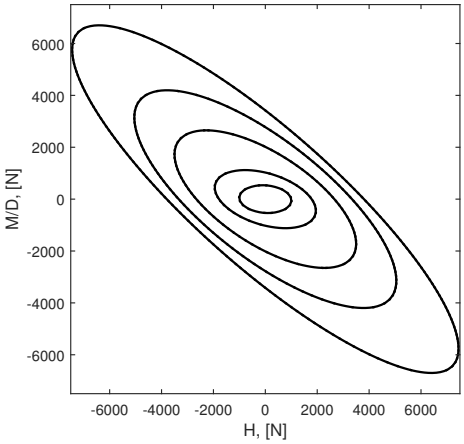

Fig. 2.2: Shape and relative size of yield surfaces for mono bucket foundations in $H - M/D$ space. Yield surfaces for embedment ratios (L/D) is 0.00, 0.25, 0.50, 0.75 and 1.00. Parameters to describe the yield surface is given by Ibsen et al. (2014).

and Houlsby (1999) with a tank size of 1.1 m $\times$ 0.4 m. The relative density of the sand was 23 %, and the arguments for using a loose sand were to a) account for loose to medium dense sand at locations for renewable energy structures and b) to counter the effects of low stress levels in small-scale laboratory tests. The main results were with respect to the numerical work on hardening plasticity. However, one of the results showed that the foundation is able to resist a horisontal and moment load when the foundation is exposed to a tensile vertical load. Other testing rigs as the ones used by Ibsen et al. (2012), Larsen et al. (2013), Ibsen et al. (2013), Ibsen et al. (2014), Ibsen et al. (2015) with buckets with a diameter of 300 mm in dense sand were investigated.

Li et al. (2015) presented a modified mono bucket foundation with an embedment ratio (L/D) of 2 where an additional outer skirt was added. Tests were conducted in a sand box with the dimensions 1 m $\times$ 1 m $\times$ 0.8 m. The foundations were tested in dense sand with a relative density of 99.7 %. Tests showed that the additional skirt increased the bearing capacity in the range from 30 % to 80 %, depending on the length of the extra skirt.

Wang et al. (2006) and Wang et al. (2010) presented results on transient loaded bucket foundations in sand. It was found that liquefaction did occur for large load amplitudes. Foglia et al. (2013) presented results of mono bucket foundations loaded with varying loading rates, resulting in drained and partly drained foundation behaviours. The tests showed a clear trend of increasing capacity with increasing loading rates.

Choo et al. (2015) presented centrifuge tests on mono bucket foundations in sand (Relative density of 70 %) with a model diameter $D = 221.4$ mm. The foundation was installed in a cylindrical container with a diameter of 900 mm and a depth of 700 mm. The model test was exposed to $70g$ during testing and the drained and undrained bearing capacity were investigated. They found that undrained behaviour generated negative excess pore pressure which increased the bearing capacity. Brennan et al. (2006) and Brennan et al. (2011) presented results from centrifuge tests of laterally loaded piles in clay. Zhang et al. (2007), Lu et al. (2007) and Li et al. (2010) presented results from centrifuge tests conducted at $50g$ on model buckets with a diameter of 60-62 mm, installed in silt and sand. Here topics as liquefaction were investigated.

2.2.2 Cyclic Loading

Byrne and Houlsby (2004) used a loading rig with Baskarp cyclone sand saturated with silicon oil. The sand was prepared to relative densities of 76 % and 92 %. Silicon oil was chosen as fluid to account for some of the issues related to the low effective stress levels in laboratory model tests. Byrne and Houlsby (2004) reported that using oil compared to water lowered the friction angle with 3° and peak dilation was reduced by half. Furthermore, they also reported that the oil reduced the soil stiffness. The combination of these effects is claimed to make oil-saturated sand at low stress levels to behave like water saturated sand at higher stress levels. Byrne and Houlsby (2004) tested irregular cyclic loading with different periods of: 3 s, 6 s, 10 s and 12 s and found no significant rate dependency. A yield surface being able to capture the main features of the cyclic loading was formulated where the cyclic behaviour was described by three parameters (Byrne and Houlsby, 2004).

Houlsby et al. (2006) presented field trial tests of mono bucket foundations (moment loading) with a diameter of 3 m and a skirt length of 1.5 m. Tests on a smaller vertical loaded foundation were also presented, but will not be described here. The tests were conducted at a site where a sand bed, of the size 40 m $\times$ 15 m $\times$ 3.5 m was prepared, and estimated values of the relative density was 80-85 %. The sand was water-saturated and during testing, the water depth was 150 mm above the sand surface. The sand had a significant content of gravel (15 %) and also minor stones were found. Two tests were conducted with the bucket: one where the load was applied via a loading frame and one where the load was applied by a mass hanging in a wire. The tests showed that the secant stiffness decreased with a larger rotation. The behaviour observed is described as *typical of 'gapping' response*, and gaps were also observed during testing. In one test, the foundation was applied a series of cyclic loads, each of 10 cycles and with amplitudes of: 42 kNm, 85 kNm,

169 kNm, and 254 kNm. Again the amplitude of the displacement increases with increasing load amplitude. A slight shakedown is also reported for low rotation amplitudes. The shape of the plotted $\log(\Delta\theta) - G$ curve has a pattern similar to what is seen on a $\log(\Delta\gamma) - G$ curve for soil. The paper also presents an expression of how to up-scale the results to full-scale tests. The expression is given in Equation (2.2) and is valid for a mono bucket foundation at low vertical loads.

$$\frac{M}{2R} = \left(f_1 + \frac{2RH}{M} f_2\right)^{-1} (V + f_3\, W) \tag{2.2}$$

M is the moment, R is the radius of the foundation, H and V are the horisontal and vertical loads, respectively, and W is the weight of the sand inside the caisson. f_1, f_2 and f_3 are factors obtained from laboratory tests. The values have been reported to: 3.26, 1.07 and 0.71, respectively.

Kelly et al. (2006) reported comparison of field and laboratory work. Comparisons are made both for vertically and moment loaded foundations. Here, only the comparison of the moment loaded foundation in sand will be summarised. The compared results are small-scale laboratory tests (diameter of 0.2 m and 0.3 m) and large-scale tests (diameter of 3.0 m) presented in Houlsby et al. (2006). The paper presents dimensionless equations to compare laboratory and field tests. The paper presents the elastic stiffness matrix as

$$\begin{bmatrix} V \\ M/2R \\ H \end{bmatrix} = 2RG \begin{bmatrix} k_1 & 0 & 0 \\ 0 & k_3 & k_4 \\ 0 & k_4 & k_2 \end{bmatrix} \begin{bmatrix} w \\ 2R\theta \\ u \end{bmatrix} \tag{2.3}$$

where G is the soil shear modulus. V, M and H are the loads as depicted in Figure 2.1, where also w, θ and u are shown as the translations and rotation. Taking into account the stress dependency of the shear modulus, the paper suggests that both stiffness and strength can be compared satisfactory by plotting $M/\gamma'(2R)^4$ against $\theta(p_a/2R\gamma')^{0.5}$.

Zhu et al. (2013) conducted small-scale tests on bucket foundations with diameter (D), skirt length (L) and skirt thickness (t) of 0.2 m, 0.2 m and 1 mm, respectively. The scaling of the dimensions were chosen to be 1:100. The foundation was installed in dry, fine, silty sand, with a relative density of 20 %, in a soil container with the dimensions: 0.55 m $\times$ 0.6 m $\times$ 0.6 m. The test programme describes tests with two different normalised vertical loads, $\tilde{V} = V/(\gamma' D^3)$, equal to 0.19 and 0.57. This normalisation is described in Kelly et al. (2006). The bucket foundations were exposed to cyclic moment and horisontal loading with a period of 9.3 s ($\approx$ 0.11 Hz). A relation between the normalised accumulated rotation as a function of applied number of cycles and the cyclic load was presented. The expression was originally developed

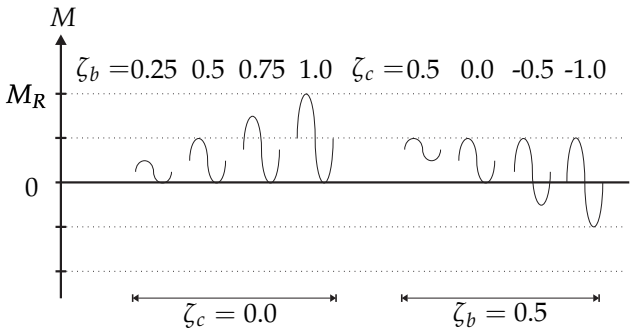

Fig. 2.3: Different combinations of ζ_b and ζ_c. M_R represents the failure moment for a monotonic test.

for monopiles by LeBlanc et al. (2010) and is given as

$$\frac{\Delta\theta(N)}{\theta_s} = T_b(\zeta_b)\ T_c(\zeta_c)\ N^{\alpha} \tag{2.4}$$

where $\Delta\theta(N) = (\theta_N - \theta_0)$ is the accumulated rotation after N cycles, and θ_s is the rotation for a monotonic test at the maximum load during a load cycle, see Figure 2.4. α is for mono piles 0.31 by LeBlanc et al. (2010) and for mono bucket foundations with $L/D = 0.5$ equal to 0.39, (Zhu et al., 2013). T_b and T_c are dimensionless functions dependent on ζ_b and ζ_c, respectively. ζ_b and ζ_c, are given in equations (2.5) and (2.6).

$$\zeta_b = \frac{M_{max}}{M_R} \tag{2.5}$$

$$\zeta_c = \frac{M_{min}}{M_{max}} \tag{2.6}$$

M_{max} and M_{min} are the maximum and minimum moment experienced during a load cycle, respectively, see Figure 2.4. M_R is the ultimate moment resistance measured in a monotonic test. ζ_b is dependent on the relative size of the cyclic load and is only defined for the interval]0;1[. ζ_c describes whether the cyclic load is one- or two-way loading, where $\zeta_c = 1$ corresponds to a monotonic test, $\zeta_c > 0$ corresponds to one-way loading, $\zeta_c < 0$ corresponds to two-way loading and $\zeta_c = -1$ corresponds to symmetric two-way loading. ζ_c is defined for the interval [-1;1]. An illustration of ζ_b and ζ_c is given in Figures E.6.

LeBlanc et al. (2010) and Zhu et al. (2013) describe that $T_c(\zeta_c = 0) = 1$. T_b is found to be dependent on the relative density, whereas T_c was found to be independent. $T_c(\zeta_c = 1) = 0$ as no rotation will accumulate in a monotonic test. $T_c(\zeta_c = -1) = 0$ is also reported with the argument that such a load will be equal in both loading direction and, therefore, result in no accumulated

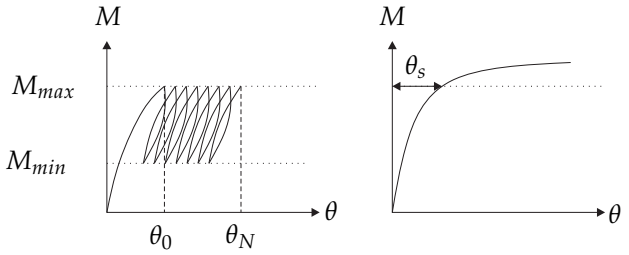

Fig. 2.4: Maximum and minimum moments (M_{max} and M_{min}), and initial rotation, equivalent static rotation and rotation after N cycles (θ_0, θ_s and θ_N).

rotation. Zhu et al. (2013) present expressions for T_b and T_c, which are given in equations (2.7) and (2.8), respectively.

$$T_b = \begin{cases} 0 & \text{for } \zeta_b < 0.23 \\ 0.67\zeta_b - 0.16 & \text{for } \zeta_b \geq 0.23 \end{cases} \tag{2.7}$$

$$T_c = \begin{cases} 5.7 + 5.7\zeta_c & \text{for } \zeta_c < -0.7 \\ 1 - \zeta_c & \text{for } \zeta_c \geq -0.7 \end{cases} \tag{2.8}$$

The expression in equation (2.7) result in no rotation for $\zeta_b < 0.23$. Hence, a quadratic function given in equation (2.9) which will result in accumulating rotation for $\zeta_b \in [0;1]$.

$$T_b = 0.7\zeta_b^2 \tag{2.9}$$

Foglia (2015) performed similar tests on small-scale bucket foundations with a diameter of 0.3 m and L/D ratios of 1.0, 0.75 and 0.25 and a skirt thickness of 1.5 mm. The tests were performed in a sand box with the dimensions 1.6 m $\times$ 1.6 m $\times$ 1.1 m. The sand was prepared to an average relative density of 89 %. Loads were applied with frequencies of mainly 0.1 Hz, but also 0.2 Hz, 0.03 Hz and 0.05 Hz were used. Foglia (2015) reported that beside the relative density, T_c is also independent on the imbedment ratio (L/D). The value α given in Equation (E.14), was found to 0.19. Another expression for T_b was given in Equation (2.10), (Foglia, 2015).

$$T_b = 2.41\zeta_b^{1.64} \tag{2.10}$$

Figure 2.5 depicts the functions for T_b and T_c. Agreement on the expression for T_c in Equation (2.8) were found between LeBlanc et al. (2010), Zhu et al. (2013) and Foglia (2015).

The models described here are simple and only takes into account uniform soil conditions. In order to account for layered soil conditions, more advanced methods must be used.

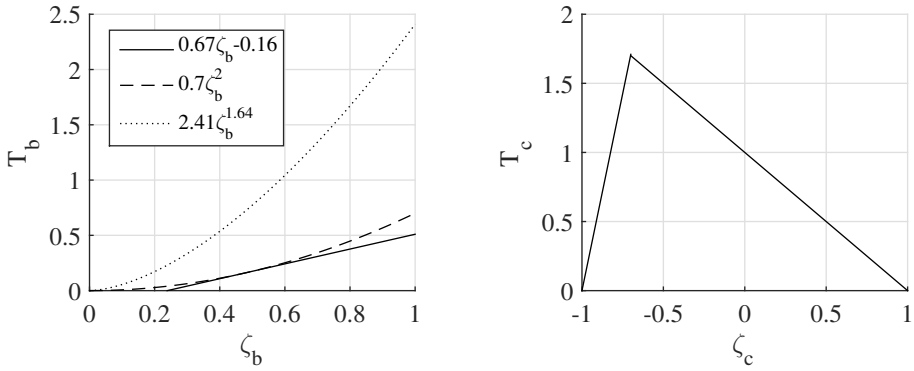

(a) $T_b(\zeta_b)$. (b) $T_c(\zeta_c)$.

Fig. 2.5: Dimensionless expressions. (a) $T_b(\zeta_b)$ (b) $T_c(\zeta_c)$.

2.3 Numerical Modelling

One of the more famous concepts, based on element testing, is the cyclic contour diagrams developed by NGI and especially Knut Andersen. Through various of papers as Andersen and Berre (1999), Andersen (2009) and Andersen (2015), the description and use of the contour diagrams have been refined. Andersen and Berre (1999) developed the contour diagrams for undrained behaviour of sands, and Andersen (2009) and Andersen (2015) presented contour diagrams based on triaxial and direct simple shear tests om Drammen clay. The method defines the average and cyclic shear stress as shown in Figure 2.6a. These parameters are for clay normalised with the undained shear strength and for sand with the effective vertical consolidation stress. Normalised, the parameters are called the cyclic (CLR) and average (ALR) load ratios.

In the contour diagram, the abscissa is the average load ratio and the ordinate is the cyclic load ratio. For each test, the number of cycles to failure is plotted for each combination of ALR and CLR. When sufficient tests are available, contour lines can be drawn to get the full picture of the cyclic soil behaviour where each contour represents the same number of cycles to reach failure. Figure 2.6b shows an example of a contour diagram. Natural cyclic loads are irregular in contradiction to laboratory tests where regular load series in most cases are investigated. Therefore, an irregular load scenario is converted to an equivalent shear stress and an equivalent number of cycles, that leads to the same damage, which could be shear strain or pore pressure build-up. By plotting the normalised maximum shear stress during a load cycle (sum of mean and amplitude) against the number of cycles to failure,

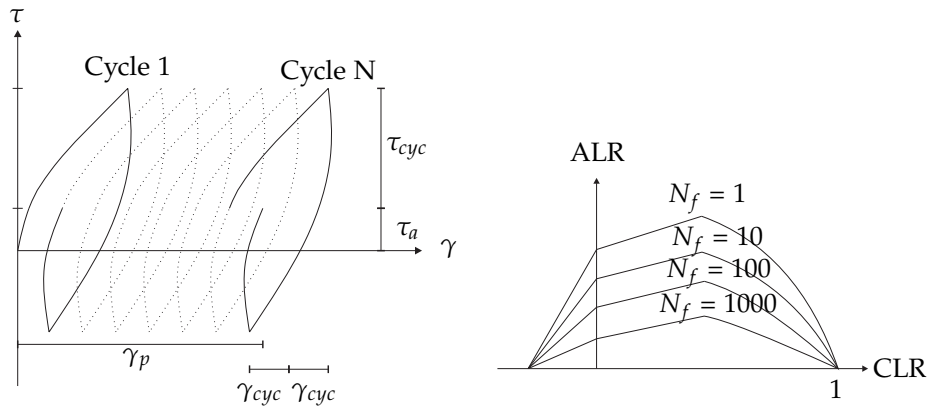

(a) $\gamma - \tau$ (b) Cyclic contour diagram.

Fig. 2.6: (a) Definitions of average shear stress (τ_a), cyclic shear stress (τ_{cyc}), permanent shear strain (γ_p) and cyclic shear strain (γ_{cyc}). (b) Cyclic Contour Diagram

an equivalent regular cyclic load and equivalent number of cycles can be estimated. Performing laboratory tests on a soil sample with the equivalent characteristics could then be used to determine soil properties. Andersen (2015) also presents various diagrams of empirical relations based on cyclic loaded DSS and triaxial tests. The soil parameters can then be used for numerical modelling. Jostad et al. (2015) presents a numerical model, which accounts for cyclic loading by using the contour diagrams.

One of the major issues due to cyclic loading is the accumulated deformation with the number of cycles. One way to model this behaviour is by reducing the stiffness. A stiffness degradation model describes how the secant stiffness of the soil degrade with the number of cycles (Abdel-Rahman and Achmus, 2005; Achmus et al., 2013, 2009; Achmus and Thieken, 2010; Kuo et al., 2012). The model describes how the soil parameters change for each load cycle and need calibration against triaxial tests.

Gourvenec (2007) has investigatied the failure mechanism for shallow foundations to different combinations of V, M, H loading. Gourvenec (2007) made a comparison between analytical and numerical investigations. Gourvenec (2008) investigated numerically the effect of the skirt length on the bearing capacity where a yield surface was fitted.

Zhang et al. (2010) present numerical analysis investigating the three dimensional failure mechanisms of the bucket foundation.

Thieken et al. (2014) presents numerical simulations of tension loaded bucket foundations and investigates the effect of excess pore pressure. The paper concludes that a rapid load increases the tensile strength, but also that a heave of the bucket is necessary to mobilise the extra strength.

The above-mentioned models are used to predict the foundation response

to various load combinations. However, they are only able to account for the phenomena that the designer choose, and the accuracy is dependent on models and calibration hereof.

2.4 Structural Monitoring

The only way to find the real response of a structure is by measuring it. Therefore, monitoring the structural response can help verifying design methods and maybe address behaviours which were not accounted for in the design. Unfortunately, very little data has been published in the public.

Tjelta (1995a) reports the major findings for a large amount of tests prior the design of bucket foundations for the Europipe Jacket. The main findings were that buckets have major benefit compared to piles, that the tension capacity for loads with short durations were huge and that it did not lead to any design problems. Furthermore, the installation of bucket foundations by suction in dense sand was achieved. By structural monitoring, of the platform the findings by model testing was verified (Tjelta, 1995b). Hansteen et al. (2003) reported the incident of a monster wave hitting the Drauptner E platform installed on bucket foundations. The main findings were the additional holding capacity created by suction that occurred for short load durations. A review of the usage and experiences by using bucket foundations in the oil and gas industry is given by Tjelta (2015).

For mono piles, structural monitoring shows momentary drops in natural frequency which is thought to be related to effects of the excess pore pressure for short duration loads (Kallehave et al., 2015).

In Fredesikshavn, Denmark, a wind turbine has been installed on a prototype bucket foundation. Monitorings were used by Liingaard (2006) to estimate the natural eigenfrequency. Monitorings of planned emergency stops were used to estimate the damping and to identify the contribution from the soil on the total damping (Damgaard et al., 2013).

Chapter 3

Scope of the Thesis

3.1 Main Findings of State-of-the-Art

The previous chapters have presented insight into the development of the mono bucket foundation. Published research has mostly been focusing on the drained monotonic and drained cyclic behaviours. Instead of the bearing capacity formula, the drained monotonic behaviour is best described by a yield surface calibrated against $1g$ small-scale laboratory tests. Different aspect ratios (L/D) were tested, and the movement behaviour changes with the rotation of the yield surface. The longer the skirts, the more the relative rotation compared to horisontal translation. However, as described in the introduction, it is likely that the foundation response, especially to wave loads, is partly drained or undrained. Few numerical models have been made to capture the effect of transient loading (Thieken et al., 2014). Also few experiments on transient loading have been performed. They show a negative pore pressure response. However, a full investigation of the transient response has not yet been presented.

Cyclic contour diagrams has been developed for undrained behaviour both for sand and for clay. Other investigations on cyclic loaded bucket foundations mainly focus on the drained response where the accumulated rotation over the lifetime is in focus. Drained response has in previous research been insured by conducting experiments in dry sand and/or with a low frequency (often 0.1 Hz). Different methods have been suggested. The cyclic contour diagram and the stiffness degradation models are calibrated against cyclic triaxial testing whereas the accumulated rotation model is calibrated against small-scale laboratory tests.

Common for published experimental work on small scale bucket foundations is, that they have investigated the drained monotonic and cyclic load effects of the mono bucket. However, offshore wind turbines are exposed

to environmental loads where especially wave loads are of a short duration. Therefore, the soil response will not always be drained for large offshore structures as an offshore wind turbine foundation, but more likely partly drained or even undrained.

3.2 Aim and Objectives

This study aims at investigating the transient monotonic and cyclic load effects. Hence, partly drained response is investigated. The scenario for the thesis is a storm event. During a storm event the dominating force may often be wave loading. This will induce two-way cyclic loads on the foundation with relatively large loads. Furthermore, a storm may lead to the impact of huge single waves, which in some cases may be breaking.

The aim of the PhD is then to extend the existing knowledge of the foundation response to monotonic and cyclic loads with a short load duration. This will be done by $1g$ small-scale testing and by analysis of measurements of a full-scale foundation. The specific objectives of the thesis are as follows:

- **Improving laboratory test facility for transient loading**, making it able to obtain both drained, partly drained and undrained foundation response.

- **Transient monotonic load effect** with focus on how the bearing capacity is affected.

- **Cyclic load effect** with focus on the accumulated rotation and how it depends on the load conditions.

- **Monitoring of a full-scale bucket** supporting a metmast at Dogger Bank.

Chapter 4

Summary of Research

4.1 Laboratory Test Facility

This section is based on the work presented in of Paper B:
Nielsen, S. D, Ibsen, L. B. and Nielsen, B. N. (2016) "Advanced Laboratory Setup for Testing Offshore Foundations" *Geotechnical Testing Journal* Vol. 39, No. 4, July 2016

A laboratory test facility for testing offshore foundation has been developed at Aalborg University by professor Lars Bo Ibsen. In the work of upgrading the test set-up for offshore foundations, a manual describing the hydraulic and electrical equipment is given in Appendix G.

The test set-up consists of a pressure tank as shown in Figure 4.1, and tests are performed at $1g$. Inside the steel tank is a layer of gravel (1) and on top of that a layer of sand (2). In between the two layers is a geotex canvas to prevent the sand from filling out the voids in the gravel and, at the same time, ensure free flow of water between the layers. The water is saturated through the bottom of the tank, and the water table (3) is adjusted to 5 to 10 cm above the sand layer. A small-scale bucket with a tower on top (4) is installed inside the pressure tank. In order to measure the pore water pressure during testing, pressure transducers are mounted on the bucket foundation (5). The movement of the bucket is measured by two vertical displacement transducers (6) and one horisontal displacement transducer (9). On the side of the pressure tank is mounted a new hydraulic actuator (8) with a load cell in the one end (7). All pore pressure transducers are connected to a MOOG PTC (12) via a distribution box (11). All other transducers are connected directly to the MOOG PTC. The purpose of the distribution box is solely for practical reasons as it makes assembling and disassembling easier.

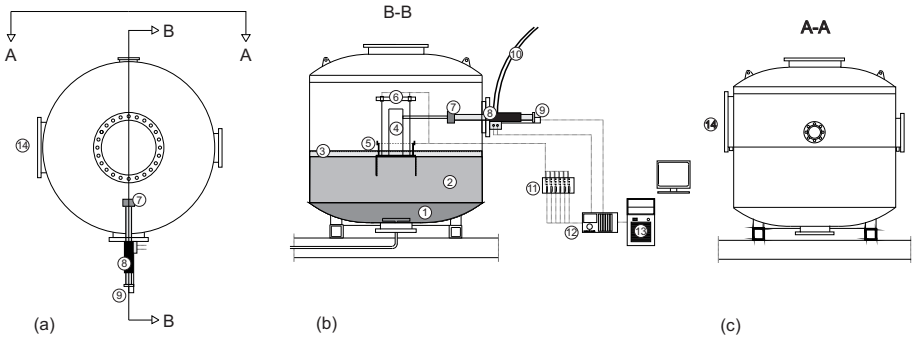

Fig. 4.1: The pressure tank test facility. (a) Top view. (b) is the B-B cut and (c) is the A-A cut.

During this study, the test facility has been upgraded to be able to apply impact loads. The upgrade is the implementation of the new hydraulic actuator (8), the connector box (11), MOOG PTC (12) and the computer (13). Furthermore, the tests demanded high loads and, therefore, a new design on the tower (4) was made additionally.

The sand inside the pressure tank is first loosened by an upward gradient and next prepared to a dense to very dense state by vibration. The vibration is performed in a specific pattern with a poker vibrator. Afterward, a laboratory CPT probe is used to ensure a homogenous sand layer and to determine the relative density of the sand. The model buckets are installed by pushing the skirts into the sand until the lid reaches the sand layer. Next, all transducers are connected, and the actuator is connected to the foundation. Then, the pressure tank is sealed, and the internal pressure is increased by 200 kPa. This corresponds to the pressure at the sea bed at 20 meters of water and acts as a back pressure (like in triaxial testing), ensuring a better water saturation and thereby better measurements.

After the upgrade, the test facility is now able to apply loads ranging from static to loads with a very short duration (500 mm in one second for small loads). This has been proved by a number of trial tests on scaled mono bucket foundations. Two buckets were made with a diameter (D) of 0.5 m, and skirt lengths (L) of 0.25 (Figure 4.2(b)) m and 0.5 m (Figure 4.2(c)). The ratio between the skirt length and diameter is called the aspect ratio (L/D).

The bucket with an aspect ratio of 0.5 was used for trial testing of the transient monotonic behaviour. Three different loading rates were tested displacement controlled and with increasing loading rate. The ultimate resistance increased with an increasing loading rate, see Figure 4.3. Figure 4.3 shows the moment rotation curve for three tests. One with a loading rate (of the actuator) of 0.1 mm/s resulted in drained response, as shown in Figure 4.3(a). The drained response was assessed due to no generation of excess pore pressure, as seen in Figure 4.4(a). Figures 4.3(b) and 4.3(b) show the mo-

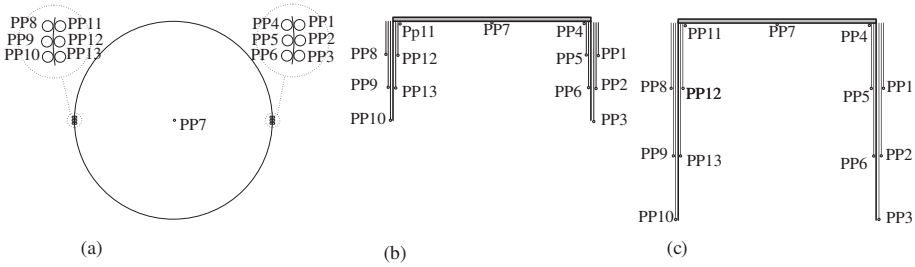

Fig. 4.2: Buckets used for model testing with positions of pore pressure measurements.

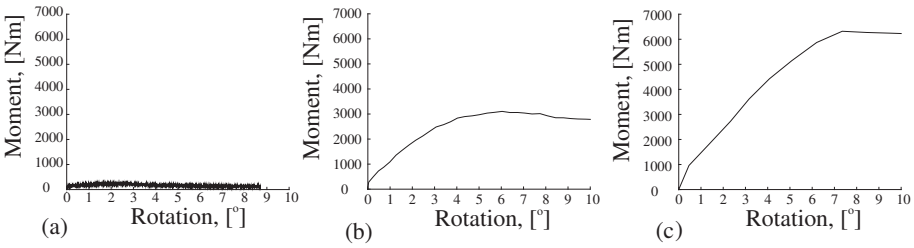

Fig. 4.3: Moment rotation curves for the three model tests on transient behaviour. a) 0.1 mm/s, b) 50 mm/s and c) 100 mm/s.

ment rotation curve for an actuator loading rate of 50 mm/s and 100 mm/s, respectively. The moment rotation curves show a significant increase in maximum moment capacity. Figures 4.4(b) and 4.4(c) shows the corresponding response in excess pore pressure. The measured excess pore pressure illustrated in Figure 4.4 are measured in the positions shown in Figure 4.2, and only show zero or negative excess pore pressure.

Another important load type for offshore foundations is cyclic loading. The ability to test foundations to cyclic loading is, therefore, tested with a cyclic trial test which was performed on the bucket with an aspect ratio of 1.0. After the cyclic loads have been applied, the bearing capacity was tested by a displacement controlled loading beyond failure of the foundation. The applied cyclic loads were applied load controlled with a frequency of 0.1

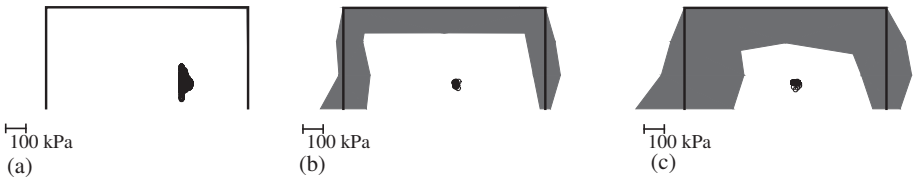

Fig. 4.4: Maximum generation of excess pore pressure along the bucket skirts.

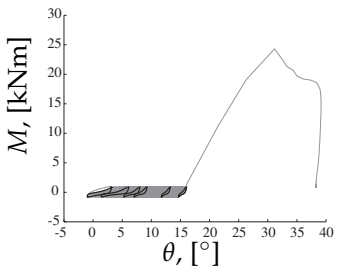

Fig. 4.5: Moment rotation curve for cyclic trial test.

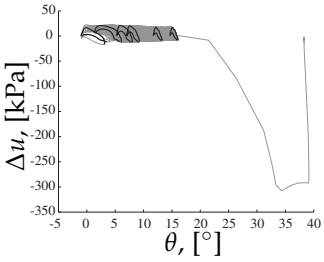

Fig. 4.6: Excess pore pressure vs. rotation for the cyclic trial test.

Hz and the moment rotation curve is shown in Figure 4.5. 4.6 shows the measured pore pressure response. Figures 4.5 and 4.6 depicts cycles no. 1, 10, 50, 100, 500 and 1000 in black.

The trial tests showed that the test set-up is capable of applying large loads with a short duration and, at the same time, of measuring the response in terms of movement and excess pore pressure response. Furthermore, the set-up also showed its ability to test foundations for cyclic load response.

This pressure tank has been used to test small-scale bucket foundations at 1g, from which results are presented in this thesis. The sign convention is defined in Figure 2.1a.

4.2 Transient Monotonic Load Effects

This section is based on the work presented in Paper C and D:
Nielsen, S. D, Ibsen, L. B. and Nielsen, B. N. (2015) "Dynamic behaviour of mono bucket foundations subjected to combined transient loading" *Frontiers in Offshore Geotechnics III, pp. 313-318*

Nielsen, S. D, Ibsen, L. B. and Nielsen, B. N. (2016) "Transient Loaded Bucket Foundations in Saturated Dense Sand - a Demonstration of The Boot Effect" *Submitted for Geotechnical and Geoenvironmental Engineering*

After successful trial tests, showing the capability of the test set-up to perform tests with high loading rates, a test series of transient monotonic loading tests were made. The purpose of the test series was to investigate the influence of loading rate on the behaviour of the bucket foundation. Both bucket foundations shown in Figure 4.2 have been tested. For each test the buckets were loaded until soil failure with a constant loading rate. Each test had different loading rates where the slowest loading rates resulted in

drained failure and the fastest tests in undrained failure. During testing, the excess pore pressure was measured, showing that undrained failure occurred when the pore water pressure reached the cavitation pressure, as explained in section 1.2 and Paper A.

The 1g test series on the two scaled bucket foundations showed a significant increase in bearing capacity with increasing loading rate. Thereby, the smallest bearing capacity was reached under drained conditions for both buckets. For each test, the measured bearing capacity was normalised with the drained bearing capacity. Figures 4.7 and 4.8 show how much the bearing capacities increase with increasing loading rate for the two buckets. For the bucket with an aspect ratio of 0.5, the undrained bearing capacity was measured 25 times higher than the drained one. For the bucket with an aspect ratio of 1.0, the undrained bearing capacity was measured 16 times higher than the drained bearing capacity.

This increase was explained by two factors: *The Boot Effect* and dilative soil behaviour. The dilative soil behaviour is explained in section 1.2 and Paper A. The boot effect is the generation of suction and, thereby, increase in bearing capacity when an uplift movement of the bucket foundation is attempted. In the included paper, "Transient Loaded Bucket Foundations in Saturated Dense Sand - a Demonstration of The Boot Effect", the boot effect is described as:

> *The name is metaphorical and draws the picture of a boot stuck in mud. Pulling out the boot slowly, will release the boot from the mud. Trying to pull the boot out with a rapid movement, the boot will barely move and will still be stocked in the mud.*

Figure 4.9 illustrates a more scientific explanation of the boot effect. The figure illustrates a drained bucket response. In this situation, water can flow

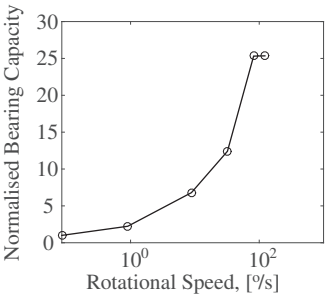

Fig. 4.7: Normalised bearing capacity as a function of rotational speeds for the bucket with aspect ratio (L/D) of 0.5.

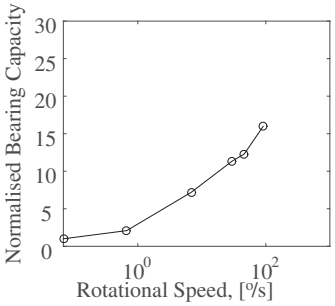

Fig. 4.8: Normalised bearing capacity as a function of rotational speeds for the bucket with aspect ratio (L/D) of 1.0.

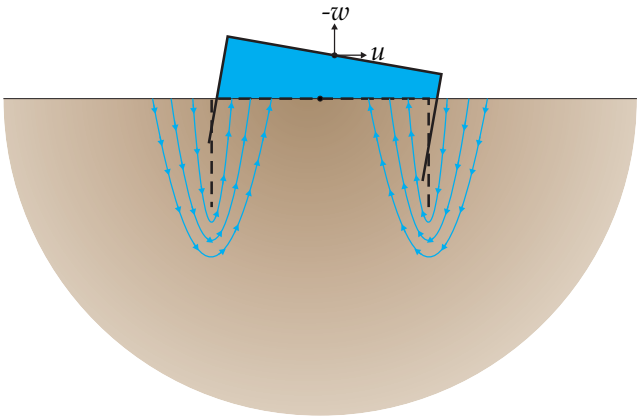

Fig. 4.9: When drained response is present, the water can flow into the bucket. In undrained conditions, a suction is created inside the bucket as the water are not able to flow. This suction is called the boot effect.

from outside to the inside of the bucket foundation, filling up the space between the lid and the soil surface. This is possible when the loading rate is sufficiently long compared to the seepage and the hydraulic conductivity of the soil. When the loading duration becomes short compared to the seepage and hydraulic conductivity, an undrained response is obtained. In this situation the load duration is so short that the water can-not flow to the inside of the bucket. Hence, suction is created inside the bucket foundation, which acts as a downward stabilising force. The created suction due to a limited dissipation of excess pore pressure is referred to as the boot effect. As the boot effect requires undrained behaviour, it can only occur in saturated soils. Furthermore, the boot effect is limited by the cavitation pressure of the water. Therefore, the ultimate boot effect increases with increasing water depth.

The movement pattern of the mono bucket at failure is dependent on the loading rate and the aspect ratio of the foundation. Figure 4.10 depicts the incremental rotation ($\dot{\theta}$) as a function of the incremental horisontal displacement ($\dot{u}$) at failure. The figure shows that a longer skirt length reduces the relative horisontal displacement compared to rotation. However, there is no indication of the loading rate having a significant effect. Figure 4.11 depicts the incremental vertical displacement ($-w$ is uplift) as a function of incremental horisontal displacement. The plot shows no significant change in this movement pattern due to changes in the aspect ratio. However, the figure indicates that the relative vertical movement compared to horisontal movement is lowered with increasing loading rate. The explanation for this is the boot effect, which enhances the capacity and reduces the relative upward movement.

At drained failure, the distribution of excess pore pressure is measured

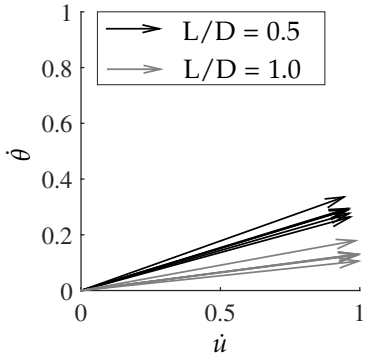

Fig. 4.10: Incremental rotation as a function of incremental horisontal displacement.

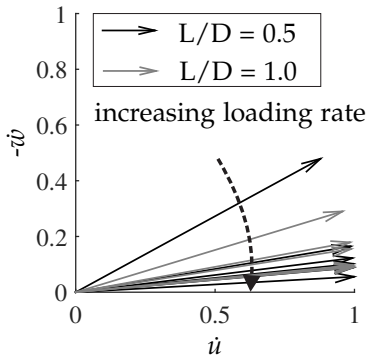

Fig. 4.11: Incremental vertical displacement as a function of incremental vertical displacement.

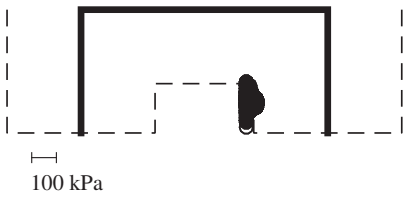

Fig. 4.12: Distribution of excess pore pressure in drained conditions for the bucket with an aspect ratio of 0.5.

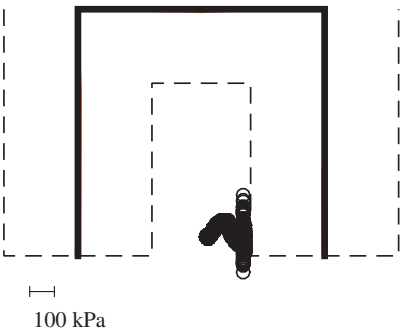

Fig. 4.13: Distribution of excess pore pressure in drained conditions for the bucket with an aspect ratio of 1.0.

as shown in Figures 4.12 and 4.13. As drained failure is presented, no excess pore pressure is measured. The black circles indicate calculated rotation points during loading. They are located on the right side of the vertical centre axis. For undrained failure, the distribution of excess pore pressure is measured as shown in Figures 4.14 and 4.15 for the bucket with an aspect ratio of 0.5 and 1.0, respectively. For undrained conditions, the rotation points are located very close the vertical centre axis. This indicates that the boot effect (downwards stabilising force created by suction) leads to a less eccentric loaded foundation.

Not only does the strength of the foundation increase with the loading rate the stiffness also increases. This is in good agreement with the idea that the stiffness increases with an increase in effective stress level. As too few

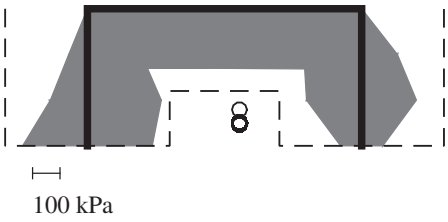

Fig. 4.14: Distribution of excess pore pressure in undrained conditions for the bucket with an aspect ratio of 0.5.

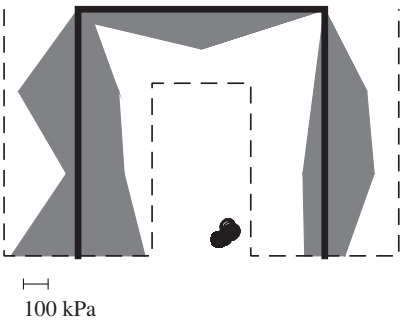

Fig. 4.15: Distribution of excess pore pressure in undrained conditions for the bucket with an aspect ratio of 1.0.

data points were measured during undrained loading, it was not possible to calculate an accurate stiffness. However, for the partly drained tests the stiffness was found to increase with a factor of 4 and 7 for the bucket with aspect ratios of 0.5 and 1.0, respectively.

4.3 Cyclic Load Effects

This section is based on the work presented in Paper E:
Nielsen, S. D, Ibsen, L. B. and Nielsen, B. N. (2016) "Response of Cyclic Loaded Bucket Foundations in Saturated Dense Sand" *Submitted for Geotechnical and Geoenvironmental Engineering*

The cyclic load effects are investigated by small-scale testing on the mono bucket foundation with an aspect ratio of 0.5 inside the pressure tank, illustrated in Figure 4.1. The purpose of the cyclic load program was to investigate the behaviour of the foundation when exposed to different cyclic loads. However, in order to compare the behaviour from different cyclic loads, the load frequency needs to be the same. An estimation of a scaled load frequency was based on the degree of consolidation and was calculated to 1.28 Hz. However, 1 Hz was used as it was not possible to tune the actuator, satisfactory, for high loads with frequencies above 1 Hz.

As offshore foundations are installed within a weather window with calm water, the risk of a severe storm just after installation is unlikely. Therefore, when performing cyclic triaxial tests to design offshore geotechnical structures, the samples are precycled. The precycling is a number of small cyclic loads presenting the small wave loads to which the structure is exposed, after

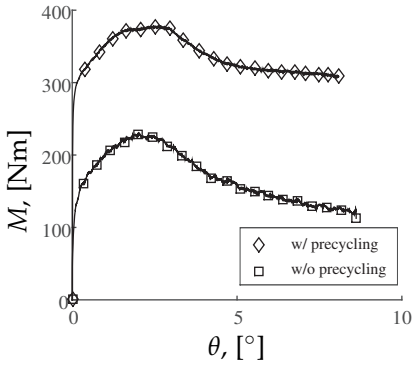

Fig. 4.16: Moment as a function of rotation for a bucket tested with and without precycling. By precycling, the ultimate bearing capacity increased from 225 Nm to 370 Nm.

installation but before any severe storm event. This procedure is also used in the cyclic test programme presented in this thesis. The precycling has been chosen to 1000 symmetric two-way loaded cycles with an amplitude of 5 % of the measured bearing capacity. During precycling, no accumulated rotation of the foundation was observed. However, the bearing capacity increased significantly. This is seen in Figure 4.16 where the moment as a function of rotation is shown for two monotonic tests: one where the bucket was precycled and one without. The effect of precycling was an increase in drained bearing capacity from 225 Nm to 370 Nm.

A formulation for calculating the accumulated rotation was calibrated to the performed tests. It expresses the accumulated rotation for a given number of cycles ($\Delta\theta$(N)) normalised with the rotation measured in a monotonic test at the maximum cyclic load level (θ_s) (see Figure 2.4) and is given as:

$$\frac{\Delta\theta(N)}{\theta_s} = T_b(\zeta_b)\ T_c(\zeta_c)\ N^{\alpha} \tag{4.1}$$

where α was found to 0.39. T_b and T_c are functions depending on ζ_b and ζ_c, which is defined as

$$\zeta_b = \frac{M_{max}}{M_R} \tag{4.2}$$

$$\zeta_c = \frac{M_{min}}{M_{max}} \tag{4.3}$$

M_{max} and M_{min} are the maximum and minimum moments applied during a load cycle. M_R is the monotonic drained bearing capacity. These are illustrated in Figure 2.4. The functions of T_b and T_c are calibrated against the

performed laboratory tests and are found as

$$T_b = 1.59\zeta_b^2 \tag{4.4}$$

and

$$T_c = \begin{cases} 1 - 6\zeta_b, & \text{for } -1 < \zeta_c < 0.17 \\ 0, & \text{for } 0.17 < \zeta_c < 0.0 \end{cases} \tag{4.5}$$

Compared to calibrations by other authors (Foglia, 2015; Zhu et al., 2013) who conducted small-scale tests with a loading frequency of 0.1 Hz, the presented 1.0 Hz tests lead to a higher accumulated rotation. This is caused by the observations that two-way loading did lead to the largest deformations, which is contrary to what has been reported for tests conducted at 0.1 Hz. However, in undrained triaxial testing, it is also usually found that two-way loading leads to the highest generation of excess pore pressure and largest deformations. Therefore, it is believed that the large rotation is a consequence of the higher frequency and, thereby, a significant excess pore pressure response.

4.3.1 Cyclic Load Response Diagram

To get a visual overview of the cyclic load response, two parameters are defined: The average load ratio (ALR) and the cyclic load ratio (CLR). These are defined as

$$ALR = \frac{M_a}{M_R} \tag{4.6}$$

$$CLR = \frac{M_{cyc}}{M_R} \tag{4.7}$$

By plotting the number of cycles to reach 0.1° against the ALR and CLR, a 3D diagram is formed. This is depicted in Figure 4.17. The figure shows that for small values of both ALR and CLR, the foundation did not reach 0.1° after 1000 cycles. It is also seen that a sudden drop in resistance for some combinations of ALR and CLR.

Instead of a 3D plot, the diagram is plotted in 2D, see Figure 4.18. The two axes are composed of the average (ALR) and the cyclic load ratio (CLR), which is defined as the average and the amplitude of the load, respectively. The diagram is composed into three areas: "No cyclic load effects", "Cyclic load effects", and "Severe cyclic load effects". The area with "no cyclic load effects" is in this example defined as a rotation of the model bucket less than 0.1°. "Severe cyclic load effects" are defined as the area with more than 0.25° of rotation. An area with "cyclic load effects" is defined, and have relatively small effects in the lower parts and as becomming more severe in

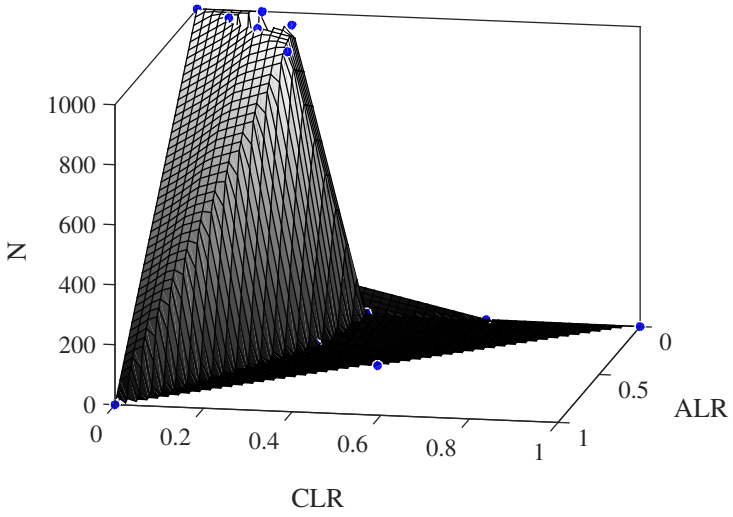

Fig. 4.17: 3D cyclic load response diagram.

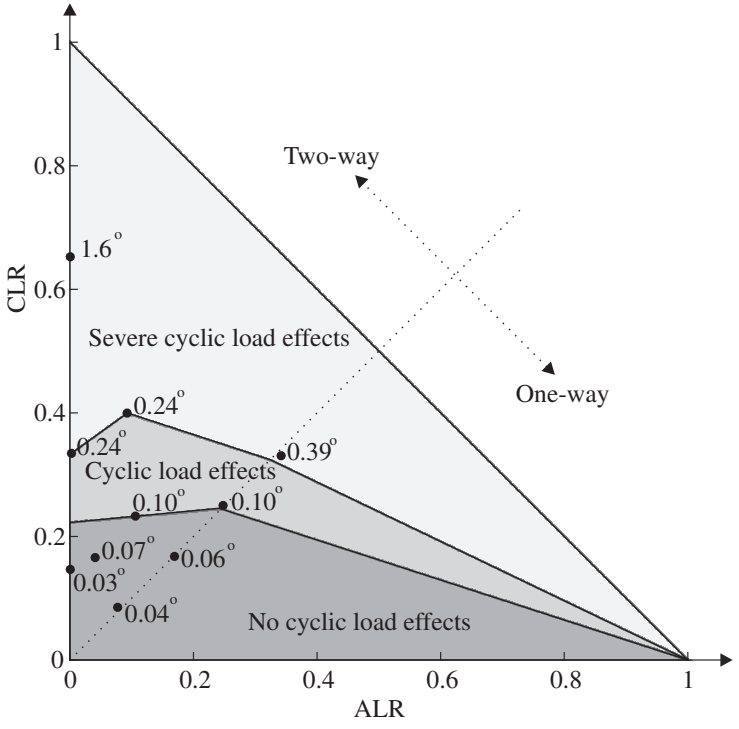

Fig. 4.18: Cyclic load response diagram.

the upper area. This is also the area between the two plateaus in Figure 4.17. As the criteria for maximum rotation are not fixed, the exact locations of the areas will change from case to case. However, the diagram provides good guidelines to the designer in an early design phase. By using the diagram, the foundation sizes leading to "severe cyclic load effect" can easily be avoided early in the design process.

4.4 Monitoring of a mono bucket foundation at Dogger Bank

This section is based on the work presented in Paper F:
Nielsen, S. D, Ibsen, L. B. and Nielsen, B. N. (2016) "Performance of a Mono Bucket Foundation - a Case Study at Dogger Bank" *Submitted for Journal of Ocean and Wind Energy*

Figure 1.1 shows the bucket foundation installed in September 2013 at Dogger Bank, which is a location between Denmark and Great Britain, see Figure 1.18. After installation, monitoring of surface elevation, inclination, excess pore pressure and acceleration started on the 23^{rd} of September 2013. The surface elevation was measured by a wave radar located at the platform where accelerometers also were placed. Figure 1.22 shows the platform. At the lid, inclination and acceleration were measured. Below the lid, a pressure transducer measured the excess pore pressure.

The bucket foundation was installed in layers of dense sand and stiff clay, with the skirt tip penetrating into a stiff clay layer, cf. Figure 4.19. The data from monitoring the bucket foundation at Dogger Bank has been analysed. The analysis had two major subjects: long- and short-term behaviour. The analysis was performed on the first half year of measurements. Figure 4.20

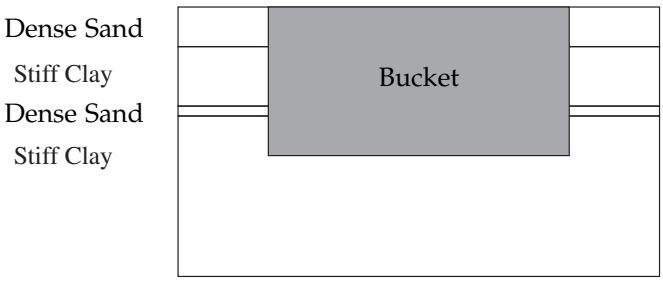

Fig. 4.19: Soil conditions at Dogger Bank where the mono bucket foundation has been installed.

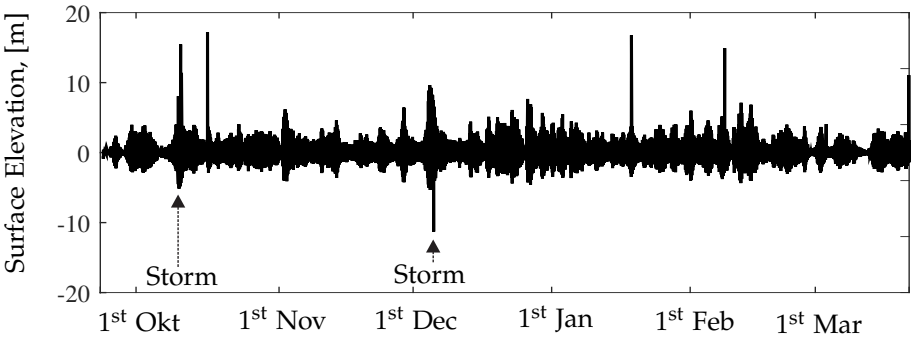

Fig. 4.20: Measured surface elevation at Dogger Bank, where tidal effects are removed. The measurements started in 2013.

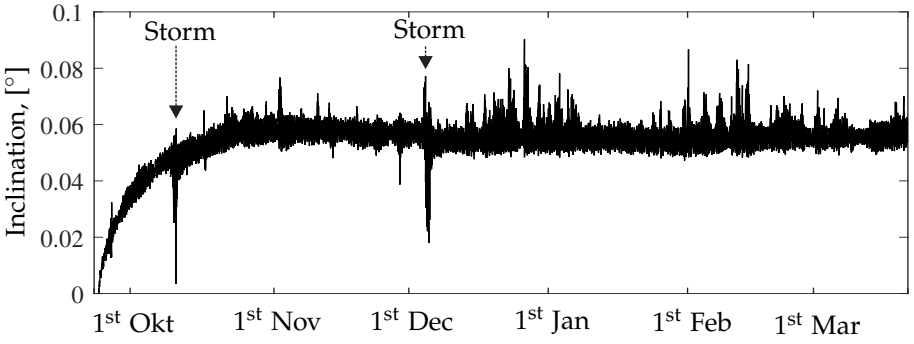

Fig. 4.21: Measured inclination in East-West direction of the lid at Dogger Bank.

depicts the measured surface elevation where tidal effect has been removed. As seen in the figure, there were two major storm events where large waves were measured. One storm is observed in October and another in December 2013.

The long-term behaviour showed that the accumulated permanent rotation stagnated after approximately one and a half months where after no additional permanent rotation accumulated. This can be observed in Figure 4.21 where the inclination of the foundation lid is shown. This happened even though storm events were observed after the stabilisation of the rotation. Looking at the excess pore pressure in Figure 4.22, there were no indications of a permanent pore pressure build-up.

Looking at the short-term behaviour, focus was aimed at the foundation response during the largest storm, which occurred within the first half year. Measurements of the water surface elevation showed one extra large wave, with a wave height of almost 20 m. This incident was used for the analysis.

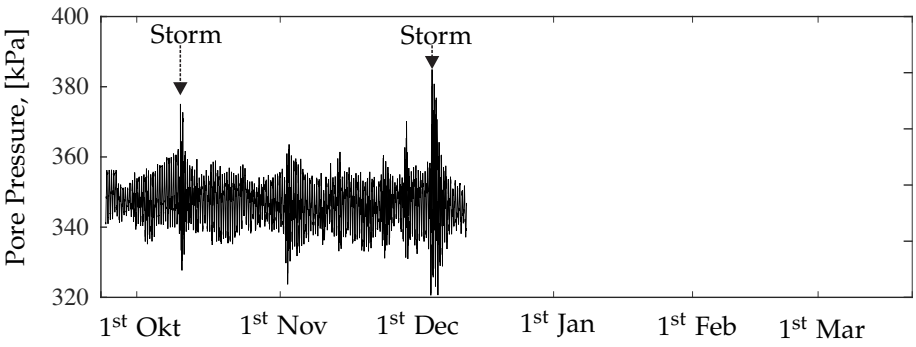

Fig. 4.22: Measured pore pressure below the lid at Dogger Bank.

The measured inclination of the foundation showed a clear indication of the wave incident by a clear fluctuation on the signal. However, after the wave impact the rotation reversed, and no accumulated rotation was observed, from that single wave. Since no accumulated rotation was observed from the impact of the large wave, elastic response must have been present. The explanation for the elastic response is likely that it is caused by the excess pore pressure response. At the wave impact, significant response in the excess pore pressure was observed, which corresponds to a downward force of 3 MN. Measurements of the acceleration were performed at the foundation and at the platform (see Figures 1.22 and 1.23). The measurements showed a significant acceleration level of 0.85 m/s^2 at the platform, whereas the acceleration of the foundation was measured to 0.03 m/s^2. This is another indication of that the movement of the foundation during the impact of the large wave being were very small.

4.4.1 Comparison with Laboratory Results

When comparing the findings from the laboratory tests with the measurements from Dogger Bank, there are similarities. Three of the major similarities are a) the presence of the boot effect to impact loads, b) a stagnation in the accumulated rotation and c) no build-up in excess pore pressure.

a) The boot effect

The boot effect is clearly seen when the foundation is exposed to impact loads both in the laboratory tests but also in the measurements from Dogger bank. At Dogger Bank, the foundation response to large loads looks like an elastic response. This could indicate that the load duration is so short that the dissipation of excess pore pressure during the impact is insignificant. This corresponds very well with the impact time for breaking waves investigated

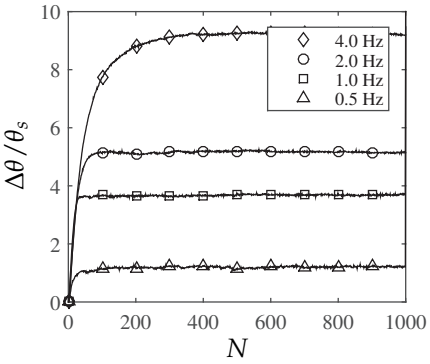

Fig. 4.23: Rotation as a function of applied number of cycles. All tests are performed with a symmetric two-way loaded cyclic load with an amplitude equal the drained bearing capacity.

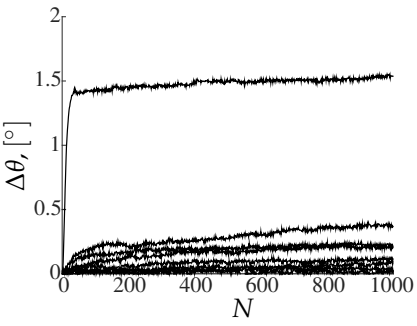

Fig. 4.24: Rotation as a function of applied number of cycles. The presented tests are used for analysis of the cyclic behaviour of the bucket tested in the laboratory.

by Wienke et al. (2004), see Figure 1.15b. However, it is not known whether or not the large waves were breaking.

b) Stagnation in accumulated permanent rotation

Looking at the accumulated rotation measured at Dogger Bank (see Figure 4.21), it is clear, that the accumulation of permanent rotation stops after approximately one and a half months (beginning of November 2013). This tendency is also seen in the laboratory results. Figures 4.23 and 4.24 present results from cyclic laboratory tests. Figure 4.23 presents results from cyclic tests where the mean and amplitude are identical in all tests. The only difference is the load frequency. All tests show that the rotation reaches a level from which no further rotation accumulates. This is also seen in Figure 4.24 where different cyclic loads are applied with 1.0 Hz. However, not all tests shown in Figure 4.24 have reached total stagnation after 1000 cycles.

c) No pore pressure build-up

The measured pore pressure below the lid of the mono bucket foundation at Dogger Bank is depicted in Figure 4.22. Measurements are only presented until December 2013 as the signal hereafter became corrupted. However, the data shows no sign of a permanent pore pressure build-up with cyclic loading, but that storm events lead to fluctuations in the excess pore pressure. This fluctuation is previously described as the boot effect.

Figure 4.25 presents the measured excess pore pressure (measurement PP11 in Figure 4.2) for the cyclic tests presented in Figure 4.24. Tests with

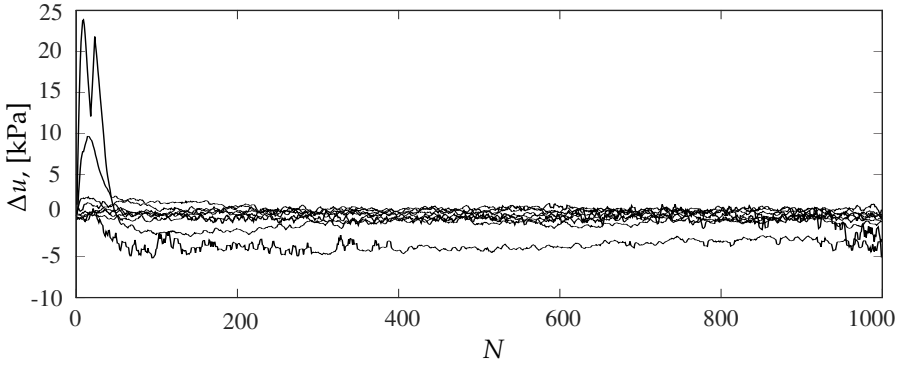

Fig. 4.25: Measured excess pore pressure on during model testing of the mono bucket foundation in the laboratory.

large amplitudes tend to produce positive excess pore pressure during the first cycles (where the most deformation accumulates), where after the excess pore pressure response drops to around zero, meaning no accumulation of excess pore pressure.

To this comparison, it should be mentioned that the model tests were performed on a bucket foundation installed in dense sand, and the bucket at Dogger Bank was installed in layers of dense sand and stiff clay, with skirt tip in clay. In the laboratory tests, the dissipation of excess pore pressure can occur relatively quickly, opposite to what will be expected at Dogger Bank where the clay layer is assumed to act as a membrane preventing a quick dissipation of excess pore pressure.

Chapter 5

Conclusions

During the presented study, an existing laboratory test facility has been upgraded, now capable of testing scaled offshore foundations exposed to impact loads and cyclic loads. The usability has been shown in a trial test campaign on mono bucket foundations followed by test series investigating the transient monotonic and cyclic load effects. However, the laboratory test facility can be used for testing any type of offshore foundation.

The transient monotonic behaviour of the mono bucket foundation has been investigated by a series of small-scale tests on two mono bucket foundations. Both foundations have a diameter of 0.5 meters where one has an aspect ratio of 0.5 and the other an aspect ratio of 1.0. Firstly, the foundation was brought to failure under drained soil response. This was ensured by a slow loading rate. At the same time, the excess pore pressure was measured, and the measurements showed no pore pressure response. Hence, drained behaviour. By increasing the loading rate, negative excess pore pressure was generated, and thereby a partly drained response was reached. The generation of negative excess pore pressure leads to an increase in the bearing capacity. By increasing the loading rate further, more suction was generated and a higher bearing capacity was measured. By increasing the loading rate sufficiently, the created suction reached the cavitation pressure of the pore water, and complete undrained behaviour was observed. Thereby, the maximum bearing capacity was measured, and further increase in loading rate had no effect. Only negative excess pore pressure was measured along the inner and outer sides of the skirts. The created suction was ascribed to two factors: the boot effect and the dilative soil behaviour. The boot effect has been described as the suction created due to uplift of the foundation whereas the dilative soil behaviour under undrained conditions creates negative excess pore pressure when sheared. The research was carried out with a constant vertical load and a constant ratio between the horisontal load and the

moment. Future research projects could investigate whether or not the same effect is present during other load conditions.

The cyclic load effect of the bucket foundation has, like the transient monotonic behaviour, been investigated by small-scale testing. Firstly, a scaled load frequency was calculated based on consolidation theory to 1.28 Hz. However, the tuning of the actuator was not satisfactory for high loads for frequencies above 1 Hz. Therefore, a load frequency of 1 Hz was used. Next, the effect of precycling was investigated and even though the precycling did not lead to any measurable deformation of the foundation, the strength and stiffness of the foundation increased significantly. The precycling was chosen to 1000 cycles with an amplitude of 5 % of the drained bearing capacity. After deciding a load frequency of 1 Hz and that the foundation should be precycled, investigations on the cyclic foundation response were performed. The tests were used to calibrate a model describing the accumulated rotation of the bucket foundation as a function of the cyclic loads. Contrary to tests under drained conditions, the presented investigations showed that two-way loading resulted in the largest accumulation of permanent rotation. This is believed mainly to be a result of a higher loading frequency and, thereby, partly drained soil response. Therefore, it is important to have equivalent drainage conditions between the full-scale foundation and the laboratory model.

During the cyclic loading, the pore pressure response was measured, and the measurements showed a response in the excess pore pressure during the first hundreds of cycles where-after the excess pore pressure dropped to approximately zero, meaning no pore pressure response for the remaining load cycles. The cycles where pore pressure was generated were also the cycles leading to the major part of the accumulated rotation of the foundation. The laboratory results showed a general trend of a stagnation on the accumulated rotation after the first hundreds of load cycles.

The study also presents measurements from the first half-year of service for a full-scale foundation installed at Dogger Bank supporting a met mast. The measurements showed that the rotation of the foundation only accumulated within the first one and a half months. Hereafter, no accumulation of deformation was measured. Measurements of the excess pore pressure showed no sign of pore pressure build-up, even though the skirt tip was installed in stiff clay and, thereby, preventing dissipation of excess pore pressure.

During the first months, the foundation was exposed to a severe storm event. Measurements showed a wave height of up to 20 meters, and a clear response was seen in the measurements of the inclination, acceleration and excess pore pressure. The acceleration was measured at the foundation lid and at the platform where the met mast was mounted. The maximum horisontal acceleration at deck was measured to 0.85 m/s^2 where the accelera-

tion during the same impact of the foundation was measured to 0.03 m/s^2. The measurements of the inclination showed a clear fluctuation during impact. However, the inclination was recovered after-wards and no additional permanent deformation was measured due to the wave impact. Looking at the measured pore pressure during the impact, a clear fluctuation is seen in the signal. Therefore, this behaviour is ascribed to the boot effect.

5.1 Recommendation for future research

This section will give thoughts and ideas for future research projects within the presented area of the thesis.

- The thesis has shown the presence of the boot effect. However, it is still unclear how much of the boot effect that can be included in foundation design. Therefore, an idea for future research projects could be to investigate how to account for the boot effect in the design of a mono bucket foundation and how it should be accounted for in different soil conditions.
- The cyclic tests have shown that the loading frequency have a relatively large effect on the accumulated rotation. Along with the seepage and hydraulic conductivity, the load frequency influences the drainage conditions. This has not been full covered and needs more investigation.
- The cyclic load effect has been investigated for one regular cyclic load at a time. However, investigations on how the order of different cyclic loads affects the foundation behaviour still need to be conducted.
- The only way to get the real foundation behaviour is by monitoring. Therefore, it is highly recommend that future foundations are monitored, as it will give invaluable information on the foundation behaviour.

References

Abdel-Rahman, K. and Achmus, M. (2005). Finite element modelling of horizontally loaded monopile foundations for offshore wind energy converters in germany. *Frontiers in Offshore Geotechnics*, pages 391–396.

Achmus, M., Akdag, C. T., and Thieken, K. (2013). Load-bearing behavior of suction bucket foundations in sand. *Applied Ocean Research*, 43:157–165.

Achmus, M., Kuo, Y.-S., and Abdel-Rahman, K. (2009). Behavior of monopile foundations under cyclic lateral load. *Computers and Geotechnics*, 36(5):725–735.

Achmus, M. and Thieken, K. (2010). On the behavior of piles in non-cohesive soil under combined horizontal and vertical loading. *Acta Geotechnica*, 5(3):199–210.

Andersen, K. H. (2009). Bearing capacity under cyclic loading - offshore, along the coast, and on land. the 21st bjerrum lecture presented in oslo, 23 november 2007. *Canadian Geotechnical Journal*, 46(5):513–535.

Andersen, K. H. (2015). Cyclic soil parameters for offshore foundation design. *Frontiers in Offshore Geotechnics III*, pages 5–82.

Andersen, K. H. and Berre, T. (1999). Behaviour of a dense sand under monotonic and cyclic loading. *ECSMGE XII Geotechnical Engineering for Transportation Infrastructure. Proc.*, 2:pages 667–676.

Brennan, A. J., Madabhushi, S. P. G., and Cooper, P. (2006). Dynamic centrifuge testing of suction caissons in soft clay. *Proceedings of the Sixth International Conference on Physical Modelling in Geotechnics, 6th ICPMG '06, Hong Kong*, pages 625–630.

Brennan, A. J., Madabhushi, S. P. G., and Cooper, P. (2011). Seismically-induced displacements of a suction caisson in soft clay. *Frontiers in Offshore Geotechnics II- Proceedings of the 2nd International Symposium on Frontiers in Offshore Geotechnics*, pages 711 –716.

Butterfield, R., Houlsby, G. T., and Gottardi, G. (1997). Standardized sign conventions and notation for generally loaded foundations. *Géotechnique*, 47(5):1051–1054.

Byrne, B. and Houlsby, G. (1999). Drained behaviour of suction caisson foundations on very dense sand. *Offshore Technology Conference*.

Byrne, B. and Houlsby, G. (2003). Foundations for offshore wind turbines. *Phil. Trans. R. Soc. Lond. A*, 361(1813):2909–2930.

Byrne, B. and Houlsby, G. (2004). Experimental investigations of the response of suction caissons to transient combined loading. *Journal of Geotechnical and Geoenvironmental Engineering ©ASCE*, 130(3):240–253.

Byrne, B. W. (2000). *Investigations of Suction Caissons in Dense Sand*. PhD thesis, University of Oxford, University of Oxford, England.

Carbon Trust (2014). Universal foundation put through its paces across major uk round 3 project sites as part of owa project. `https://www.carbontrust.com/about-us/press/2014/11/universal-foundation-put-through-paces-uk-round-3-project-sites\-owa-project/`. Accessed: 2016-03-02.

Carbon Trust (2015a). About us. `http://www.carbontrust.com/about-us/`. Accessed: 2015-11-15.

Carbon Trust (2015b). Dong energy and carbon trust team up to cut the costs of offshore wind. `https://www.carbontrust.com/about-us/press/2014/01/dong-energy-and-carbon-trust-team-up-to-cut-the-costs-of-\offshore-wind/`. Accessed: 2015-12-07.

Carbon Trust (2015c). Offshore wind accelerator. `http://www.carbontrust.com/our-clients/o/offshore-wind-accelerator/`. Accessed: 2015-11-15.

Choo, Y. W., Kang, T.-W., Seo, J.-H., Youn, J.-U., Kim, D.-J., Jee, S.-H., Lee, K.-Y., and Hossain, M. S. (2015). Centrifuge study on undrained and drained behaviors of a laterally loaded bucket foundation in a silty sand. *The Proceedings of the Twenty-fifth (2015) International Offshore and Polar Engineering Conference*, pages 963–968.

Damgaard, M., Ibsen, L., Andersen, L., Andersen, P., and K. F. Andersen, J. (2013). *Damping Estimation of a Prototype Bucket Foundation for Offshore Wind Turbines Identified by Full Scale Testing*. Escola de Engenharia da Universidade do Minho.

DNV-OS-J101 (January 2013). *DNV-OS-J101, Design of Offshore Wind Turbine Structures*. DNV.

DONG Energy (2014). Innovative suction bucket jacket foundation hits ground bed. `http://www.`

dongenergy.com/en/media/newsroom/news/articles/innovative-suction-bucket-jacket-foundation-hits-ground-bed. Accessed: 2016-14-01.

DONG Energy (2015). First foundation successfully installed. http://www.dongenergy.com/en/media/newsroom/news/articles/first-foundation-successfully-installed1. Accessed: 2016-26-02.

EEA (2015). European environmental agency. http://www.eea.europa.eu/data-and-maps/figures/north-sea-physiography-depth-distribution-and-main-currents. Accessed: 2015-06-30.

EWEA (2016). The european offshore wind industry - key trends and statistics 2015. http://www.ewea.org/statistics/offshore/. Accessed: 2016-26-02.

Feld, T. (2001). *Suction Buckets: a new innovation foundation concept, applied to offshore wind turbines*. PhD thesis, Aalborg University, Denmark. ATV Project EF675.

Foglia, A. (2015). *Bucket foundations under lateral cyclic loading: Submitted for the degree of doctor of philosophy*. PhD thesis, Aalborg University, Department of Civil Engineering, Aalborg University.

Foglia, A., Gottardi, G., Govoni, L., and Ibsen, L. B. (2015). Modelling the drained response of bucket foundations for offshore wind turbines under general monotonic and cyclic loading. *Applied Ocean Research*, 52:80–91.

Foglia, A., Ibsen, L. B., Nielsen, S. K., and Mikalauskas, L. (2013). A preliminary study on bucket foundations under transient lateral loading. *The Proceedings of the Twenty-third (2013) International Offshore and Polar Engineering Conference*, pages 465–471.

Gottardi, G. and Butterfield, R. (1993). On the bearing capacity of surface footings on sand under general planar loads. *Soils and Foundaions*, 33(3):68–79.

Gottardi, G. and Butterfield, R. (1995). The displacement of a model rigid surface footing on dense sand under general planar loading. *Soils and Foundaions*, 35(3):71–82.

Gottardi, G., Houlsby, G. T., and Butterfield, R. (1999). The plastic response of circular footings on sand under general planar loading. *Géotechnique*, 49(4):453–470.

Gourvenec, S. (2007). Failure envelopes for offshore shallow foundations under general loading. *Géotechnique*, 57(9):715–728.

Gourvenec, S. (2008). Effect of embedment on the undrained capacity of shallow foundations under general loading. *Géotechnique*, 58(3):177–185.

Hansen, J. B. (1970). A revised and extended formula for bearing capacity. In The Danish Geotechnical Institute, C., editor, *Bulletin No. 28*, pages 5–11.

Hansteen, O. E., Jostad, H. P., and Tjelta, T. I. (2003). Observed platform response to a monster wave. In Myrvoll, F., editor, *Field Measurements in Geomechanics*, pages 73–86. A.A. Balkema Publishers.

Holtz, R.D., K. W. S. T. (2001). *An Introduction to Geotechnical Engineering*. PEARSON, 2nd edition. ISBN-13 978-0-13-701132-2,.

Houlsby, G. and Cassidy, M. J. (2002). A plasticity model for the behaviour of footings on sand under combined loading. *Geotechniqué*, 52(1):117–129.

Houlsby, G., Kelly, R., Huxtable, J., and Byrne, B. (2006). Field trials of suction caissons in sand for offshore wind turbine foundations. *Géotechnique*, 56(1):3–10.

Houlsby, G. T., Ibsen, L. B., and Byrne, B. W. (2005). Suction caissons for wind turbines. *Frontiers in Offshore Geotechnics: ISFOG, Perth, WA, Australia*, 130:75–93.

Ibsen, L. (2008). *Implementation of a new Foundations Concept for Offshore Wind Farms*, pages 19–33. Norsk Geoteknisk Forening. Keynote: NGM 2008.

Ibsen, L. B., Barari, A., and Larsen, K. A. (2012). Modified vertical bearing capacity for circular foundations in sand using reduced friction angle. *Ocean Engineering*, 47:1–6.

Ibsen, L. B., Barari, A., and Larsen, K. A. (2013). Adaptive plasticity model for bucket foundations. *Journal of Engineering Mechanics ©ASCE*, 140(2):361–373.

Ibsen, L. B., Barari, A., and Larsen, K. A. (2014). Calibration of failure criteria for bucket foundations on drained sand under general loading. *Journal of Geotechnical and Geoenvironmental Engineering ©ASCE*, 140(7):1–16.

Ibsen, L. B., Barari, A., and Larsen, K. A. (2015). Effect of embedment on the plastic behaviour of bucket foundations. *Journal of Waterway, Port, Coastal, Ocean Engineering*, 141(6):1–9.

Jostad, H. P., Grimstad, G., Andersen, K. H., and Sivasithamparam, N. (2015). A FE procedure for calculation of cyclic behaviour of offshore foundations under partly drained conditions. *Frontiers in Offshore Geotechnics III*, pages 153–172.

Kallehave, D., Thilsted, C. L., and Troya, A. (2015). Bbserved variations of monopile foundation stiffness. In Meyer, editor, *Frontiers in Offshore Geotechnics III*, pages 717–722. ©2015 Taylor & Francis Gruoup.

Kelly, R., Houlsby, G., and Byrne, B. (2006). A comparison of field and laboratory tests of caisson foundations in sand and clay. *Géotechnique*, 56(9):617–626.

Kuo, Y.-S., Achmus, M., and Abdel-Rahman, K. (2012). Minimum embedded length of cyclic horizontally loaded monopiles. *Journal Geotechnical and Geoenvironmental Engineering ©ASCE*, 138(3):357–363.

Larsen, K., Ibsen, L., and Barari, A. (2013). Modified expression for the failure criterion of bucket foundations subjected to combined loading. *Can. Geotech. J.*, 50:1250–1259.

LeBlanc, C., Houlsby, G., and Byrne, B. (2010). Response of stiff piles in sand to long-term cyclic lateral loading. *Géotechnique*, 60(2):79–90.

LEEDCo (2015). Lake erie energy development corporation. `http://www.leedco.org/press-releases/icebreaker-offshore-wind-project-to-incorporate-new-foundation-design`. Accessed: 2015-30-09.

Lesney, K. (2010). *Foundations for Offshore Wind Turbines*. VGE Verlag GmbH. ISBN 978-3-86797-042-6.

Li, C., Lu, X., and Wang, S. (2010). Study on the capacity degradation of bucket foundation in liquefied sand layer under cyclic loads. *The Open Ocean Engineering Journal*, 3:86–92.

Li, D., Zhang, Y., Feng, L., and Gao, Y. (2015). Capacity of modified suction caissons in marine sand under static horisontal loading. *Ocean Engineering*, 102:1–16.

Liingaard, M. (2006). *Dynamic Behaviour of Suction Caissons*. PhD thesis, Aalborg University, Denmark.

Lu, X., Wu, Y., Jiao, B., and Wang, S. (2007). Centrifugal experimental study of suction bucket foundations under dynamic loading. *Acta Mechanica Sinica*, 23:689–698.

Madsen, S., Andersen, L., and Ibsen, L. (2013). Alternative shape of suction caisson to reduce risk of buckling under high pressure. *Research and Applications in Structural Engineering, Mechanics and Computation*, pages 2515–2520.

Madsen, S., Andersen, L., and Ibsen, L. (2014). Numerical buckling analysis of shape enhanced bucket foundations. *Numerical Methods in Geotechnical Engineering*, 2:1273–1278.

Mangal, J. and Houlsby, G. (1999). Partially-drained loading of shallow foundations on sand. *Offshore Technology Conference*.

Michalowski, R. L. (1997). An estimate of the influence of the soil weight on bearing capacity using limit analysis. *Soils and Foundations*, 37(4):57–64.

MT Højgård (2014). New techniques for foundation installation reduce the cost of future offshore wind. http://mth.com/About_Us/News/Press/PressReleases/PressReleases-2014/New-techniques-for-foundation-installation-reduce-the-cost-of\-future-offshore-wind.aspx. Accessed: 2015-15-12.

NGI (2015). Monster wave becomes world famous. http://www.ngi.no/en/News-archive/News/73844/. Accessed: 2015-06-11.

Offshore technology (2015). Snorre, norway. http://www.offshore-technology.com/projects/snorre/. Accessed: 2015-12-11.

RAB (2010). Value breakdown for the offshore wind sector. A report commissioned by the, Renewables Advisory Board.

Randolph, M. and Gourvenec, S. (2011). *Offshore Geotechnical Engineering*. Sangeet Patra, 1st edition. ISBN: 978-0-415-47744-4.

Renewables International (2015). The return of the bucket. http://www.renewablesinternational.net/the-return-of-the-bucket/150/435/77002/. Accessed: 2016-26-02.

Roscoe, K. H. and Schofield, A. N. (1957). The stability of short pier foundations in sand. *British Welding Journal*, pages 12–18.

Salciarini, D. and Tamagnini, C. (2009). The displacement of a model rigid surface footing on dense sand under general planar loading. *Acta Geotechnica*, 4:163–176.

SPT Offshore (2015). Jackets with suction pile foundations. http://www.sptoffshore.com/en/solutions/fixed-platforms/jackets-with-suction-pile-foundations/jackets-with-suction-pile-foundations. Accessed: 2015-12-07.

Terzaghi, K. (1943). Theoretical soil mechanics. *British Welding Journal*.

The guardian (2015). Timeline: The history of wind power. http://www.theguardian.com/environment/2008/oct/17/wind-power-renewable-energy. Accessed: 2015-15-12.

Thieken, K., Achmus, M., and Schröder, C. (2014). On the behavior of suction buckets in sand under tensile loads. *Computers and Geotechnics*, 60:88–100.

Tjelta, T. I. (1992). Foundation behaviour of gullfaks c. In *Offshore Site Investigation and Foundation Behaviour*, volume 28, pages 451–467. Society for Underwater Technology.

Tjelta, T. I. (1995a). Geotechnical aspects of bucket foundations replacing piles for the europipe 16/11 jacket. In *Offshore Technology Conference*, pages 897–908.

Tjelta, T. I. (1995b). Geotechnical experience from the installation of the europipe jacket with bucket foundations. In *Offshore Technology Conference*, pages 897–908.

Tjelta, T. I. (2015). The suction foundation technology. In Meyer, editor, *Frontiers in Offshore Geotechnics III*, pages 85–93. ©2015 Taylor & Francis Gruoup.

Universal Foundation (2015a). Case study: Dogger bank. `http://universal-foundation.com/case-studies/dogger-bank/`. Accessed: 2015-29-09.

Universal Foundation (2015b). Case study: Trial installation – uk north sea. `http://universal-foundation.com/case-studies/trial-installation-campaign/`. Accessed: 2015-29-09.

Universal Foundation (2015c). First mono bucket is decommissioned after 6 years of service. `http://universal-foundation.com/media/news/#100319`. Accessed: 2015-29-09.

Universal Foundation (2015d). Key features. `http://universal-foundation.com/technology/#key-features`. Accessed: 2015-07-12.

Villalobos, F. A., Byrne, B. W., and Houlsby, G. T. (2009). An experimental study of the drained capacity of suction caisson foundations under monotonic loading for offshore applications. *Soils and Foundaions*, 49(3):477–488.

Wang, L., Lu, X., and Shi, Z. (2010). Study on the capacity degradation of bucket foundation in liquefied sand layer under cyclic loads. *The Open Ocean Engineering Journal*, 3:20–30.

Wang, Y., Lu, X., Wang, S., and Shi, Z. (2006). The response of bucket foundation under horizontal dynamic loading. *Ocean Engineering*, 33:964–973.

Wienke, J., Sparboom, U., and Oumeraci, H. (2004). Theoretical formulae for wave slamming loads on slender circular cylinders and application for support structures of wind turbines. *29th International Conference Coastal Engineering, ASCE*, pages 4018–4026.

Zhang, J., Zhang, L., and Lu, X. (2007). Centrifuge modeling of suction bucket foundations for platforms under ice-sheet-induced cyclic lateral loadings. *Ocean Engineering*, 34(8-9):1069–1079.

Zhang, J. H., Chen, Z. Y., and Li, F. (2010). Three dimensional limit analysis of suction bucket foundations. *Ocean Engineering*, 37:790–799.

Zhu, B., Byrne, B., and Houlsby, G. (2013). Long-term lateral cyclic response of suction caisson foundations in sand. *Journal of Geotechnical and Geoenvironmental Engineering ©ASCE*, 139(1):73–83.

Paper A

Undrained Cyclic Behaviour of Dense Frederikshavn Sand

Søren Kjær Nielsen[1]
Lars Bo Ibsen
Kris Wessel Sørensen
Amir Shajarati

[1]Birth name: Søren Kjær Nielsen, Married name: Søren Dam Nielsen

The paper has been published in
The Proceedings of the Twenty-third (2013) International Offshore and Polar Engineering Conference. vol. 2, pp. 518-525.

The layout has been revised

Abstract

A modified contour diagram is created for the Frederikshavn Sand in the undrained case for a relative density of I_D = 80 %. It can be used to estimate the number of cycles to failure for a given combination of pore pressure, average and cyclic load ratio. The diagram is based on a series of undrained cyclic triaxial tests, which have been performed at the Geotechnical Laboratory at Aalborg University. In order to ensure offshore conditions, the tests were fully saturated and performed with a relative density of 80 %. During cyclic loading, special attention was given to the development of pore pressure and deformation.

KEY WORDS: Cyclic loading, contour diagram, undrained dense sand, triaxial testing.

Introduction

Offshore wind turbine foundations are exposed to severe environmental loads, which lead to significant cyclic loading. There is no standardised design method for offshore wind turbine foundation, which takes cyclic loading into account. Among the design tools for cyclic loading used in the offshore oil and gas industry, contour diagrams proposed by Andersen (2009) is one of them. Offshore, only a few number of subsequent load cycles lead to a complete, or partly, undrained response of the soil surrounding an offshore wind turbine foundation. The larger the forces acting on an offshore wind turbine foundation, the more subsequent cycles will trigger an undrained soil response. This article investigates the short-term effects of dense offshore sand taken from a test field in Frederikshavn, Denmark. It contains a new contour diagram for designing offshore wind turbine foundations, and it describes a new normalization parameter that accounts for undrained soil response. The proposed contour diagram not only takes into account the cyclic and average shear stress level and the mean effective stress, it also accounts for the initial pore pressure, which is governing for the shear strength at undrained failure for dilative soils (Ibsen, 1995).

The diagram in this article is based on a series of undrained cyclic triaxial tests, which have been performed in the Geotechnical Laboratory at Aalborg University. In order to ensure offshore conditions, the tests were fully saturated and performed with a relative density of 80 %. Finally, a K_0 procedure was used to obtain anisotropic consolidated test specimens.

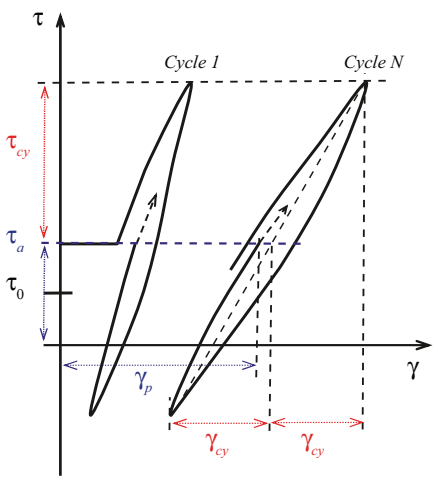

Fig. A.1: Stress-strain behaviour under cyclic loading. (Andersen, 2009)

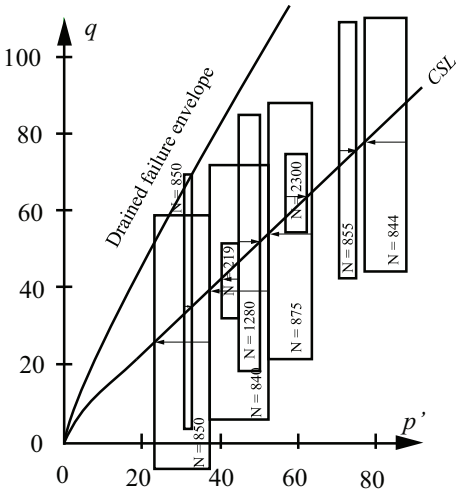

Fig. A.2: Test results from cyclic triaxial tests. (Ibsen, 1994)

Characteristics of Cyclic Loading

Cyclic environmental loads are irregular in their nature and changes both in amplitude and frequency over time. Like other offshore structures, offshore wind turbine foundations are exposed to such loads. In order to separate the responses from the individual load sequences, laboratory work is performed with regular cyclic load sequences. The cyclic load is defined by the cyclic shear stress, τ_{cy}, and the average shear stress, τ_a, with corresponding shear strain, γ_{cy} and γ_p, as illustrated in Figure A.1. τ_a consists of two parts: a drained part, τ_0, which is the shear stress obtained from the in-situ condition, and an undrained part, $\Delta\tau_a = \tau_a$-τ_0, which is the average shear stress from further loading, i.e. the mean shear stress created by cyclic loading.

During undrained cyclic loading of dense sand, a change in pore pressure is generated during each cycle. The sign of the accumulated pore pressure depends on the position of the average shear stress compared to the *Cyclic Stable Line*, CSL, described by Ibsen and Lade (1998a). This is shown in Figure A.2, where the CSL and examples of cyclic triaxial tests are depicted. When the average stress is below the CSL, the change in pore pressure is positive, and negative pore pressure is generated when the average shear stress is above the CSL. When the average shear stress intersects the CSL, the response becomes stable, as an equal amount of negative and positive pore pressure is generated during one cycle, and thereby neutralize each other, Ibsen and Lade (1998a). The CSL is similar to the *phase transformation line* for undrained conditions, and the *characteristic line* for drained conditions.

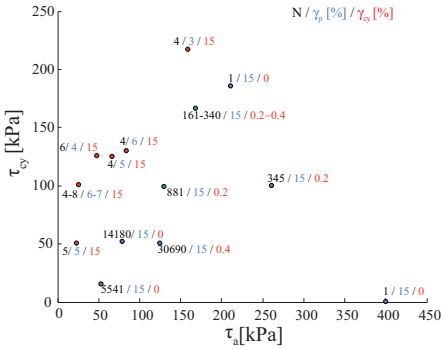

Fig. A.3: Test results of the 17 different cyclic triaxial tests and 1 monotonic test.

Beside pore pressure, distortional strain is also accumulated.

Soil and Test Specifications

The Frederikshavn Sand has a minimum and maximum void ratio of e_{min} = 0.64 and e_{max} = 1.05. The samples were prepared using the undercompaction method with five layers, where the samples were dry tamped to a relative density of I_D = 80 %, which is in good agreement to what is normally found at locations for offshore wind turbines. When the specimens were saturated, the stiffness of the soil skeleton, i.e. the bulk modulus, K, and the pore pressure level were taken into account, and it was ensured that the samples were at least 99.9 % saturated. Drained pre-shearing of 400 cycles with an amplitude of $0.04\sigma'_{vc}$ were applied, at an effective mean stress level of 30 kPa, in order to remove any stress concentration from the tamping process and thereby ensure a homogeneous sample. The effective mean stress was raised to 60 kPa afterwards.

In an earlier study made on Frederikshavn Sand by Ibsen et al. (2009) an expression for the friction angle as a function of relative density, I_D, and confining pressure, σ'_3, was calibrated to

$$\phi = 0.146 I_D + 41 {\sigma'_3}^{-0.0714} - 1.78^\circ \tag{A.1}$$

The expression has been validated by conducting three drained isotropic, consolidated monotonic triaxial tests with an effective confining pressure of 30, 60 and 120 kPa. The deviation between the measurements and the expression is in the interval 1-5 %. From the monotonic tests, the triaxial friction angle was found to be ϕ = 39.5° for an effective isotropic consolidation stress of 60 kPa, which gave a K_0 value of 0.36. This produces an anisotropic con-

Table A.1: Average and cyclic shear stress used in the test programme. Test No. 1 is a monotonic test, and test No. 2-17 is cyclic triaxial tests. Also the number of cycles to failure is given, which is used in Figure A.16.

Test No.	τ_a, [kPa]	τ_{cy}, [kPa]	u_0, [kPa]	N_f
1	400	0	111	1
2	210	185	106	1
3	260	101	109	345
4	167	167	110	340
5	130	100	100	881
6	125	50	110	30,690
7	78	50	121	14,181
8	53	17	100	5,541
9	167	167	302	161
10	50	123	100	6
11	24	51	140	5
12	25	100	100	6
13	25	100	161	4
14	25	100	300	8
15	66	126	300	4
16	84	129	100	4
17	159	217	100	4

solidation with an effective vertical consolidation stress, σ'_{vc}, of 167 kPa and an effective horizontal consolidation stress, σ'_{hc}, of 60 kPa.

The test samples were cylindrical with an initial height, H_0, of 71 mm, and an initial diameter, D_0, of 70 mm, hence $H/D \approx 1$. Two rubber membranes with high vacuum grease in between were placed at the cap and base to prevent friction. This was done to ensure homogeneous stress distribution throughout the sample, (Ibsen and Lade, 1998a).

During sample preparation the maximum decrease in height was approximately 1 %.

Cyclic Triaxial Testing

A total of 17 undrained triaxial tests were conducted; 1 monotonic and 16 cyclic tests. The results from these tests were used to design the contour diagram, where τ_{uf} is used as a normalisation parameter, which is explained later in this article. A complete list of the conducted tests is shown in Table A.1. Analysis of the cyclic test results showed that the failure modes can be separated into two main groups: One where cyclic shear strain, γ_{cy}, dominates, and another where permanent shear strain,γ_p, dominates. All spec-

imens subjected to one-way loading were dominated by permanent shear strain, γ_p, and the opposite effect is observed during two-way loading where γ_{cy} dominates. It is observed that all one-way loaded tests failed by incremental collapse, while all two-way loaded tests fail by liquefaction. This will be outlined in the following sections. Failure is defined as either γ_p = 15 % or γ_{cy} = 15 %. A plot of the different tests with number of cycles to failure can be seen in Figure A.3.

Liquefaction

The stress path in the $p' - q$ space for a two-way loaded cyclic test with τ_a = 25 kPa and τ_{cy} = 100 kPa is depicted in Figure A.4. The sample is subjected to cyclic loading with an amplitude so large that after a few cycles, the excess pore pressure, Δu, exceeds the initial effective horizontal stresses, σ'_h, which results in zero effective horizontal stress, coursing liquefaction and large deformations. When the sample liquefies, it will start to dilate, which generates negative pore pressure. Effective stresses are again mobilized, and cyclic loading continues. According to Andersen and Berre (1999) the required strain to mobilize dilatancy increases for every cycle.

Figure A.5 shows that the initial pore pressure is equal to 300 kPa indicated by point (a). This means that the confining pressure is 360 kPa, and the effective horizontal stress is 60 kPa. As the sample is exposed to more cycles the pore pressure will eventually increase to a value of 360 kPa, indicated by point (b), which is the point where liquefaction occurs. When liquefaction occurs, the soil has lost its bearing capacity, which produces large shear deformations as seen in Figure A.6. During all cyclic tests where liquefac-

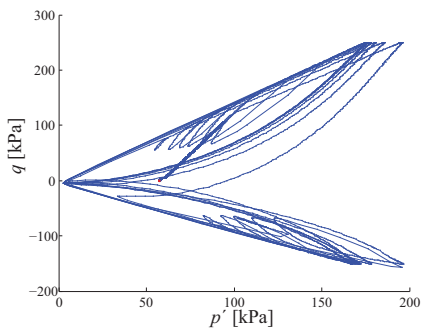

Fig. A.4: Data from test no. 14. $p' - q$ diagram for a cyclic triaxial test, where liquefaction is observed. The test failed at N = 8 with τ_a = 25 kPa and τ_{cy} = 100 kPa.

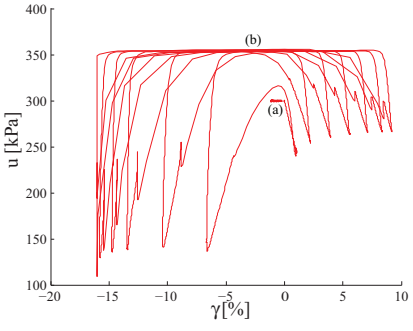

Fig. A.5: Data from test no. 14. Excess pore pressure development as a function of cyclic shear strain during cyclic triaxial test. The test failed at N = 8, with τ_a = 25 kPa and τ_{cy} = 100 kPa.

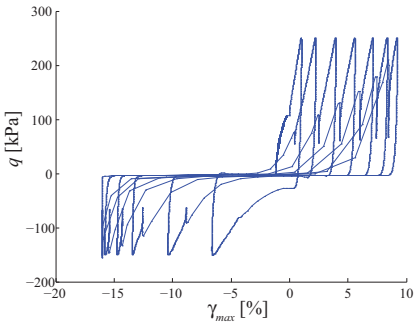

Fig. A.6: Data from test no. 14. $\gamma - q$ diagram for cyclic triaxial test, where liquefaction is observed. Large shear strains develop when q becomes zero. N = 8, τ_a = 25 kPa and τ_{cy} = 100 kPa.

tion occurs, liquefaction is observed twice in each cycle; once in compression and once in extension. For each time liquefaction occurs, the shear strain increases as cyclic loading continues, as seen in Figure A.5 and Figure A.6.

Incremental Collapse

Figure A.7 shows a one-way loaded test with τ_a = 167 kPa and τ_{cy} = 167 kPa. The response shows that as cyclic loading is being applied, p' decreases, which is due to pore pressure build up. The pore pressure development is illustrated in Figure A.8, and it is observed that initially the pore pressure decreases because the sample tries to dilate, resulting in an increase in ef-

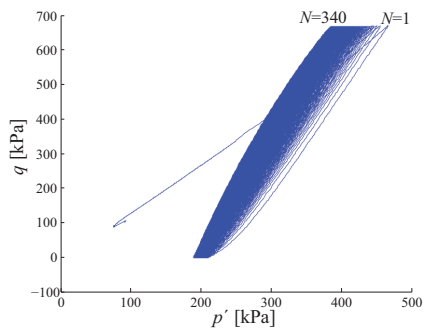

Fig. A.7: Data from test no. 14. Stress path in $p' - q$ space. The test was conducted with τ_a = 167 kPa and τ_{cy} = 167 kPa and failed at N = 340 cycles.

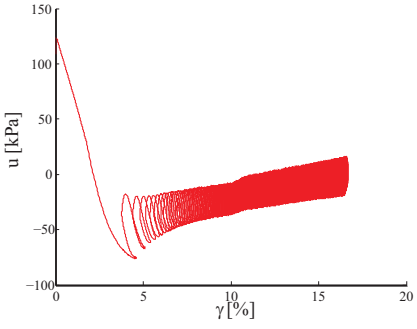

Fig. A.8: Data from test no. 14. Pore pressure development as a function of shear strains. The test is conducted with τ_a = 167 kPa and τ_{cy} = 167 kPa and failed at N = 340 cycles.

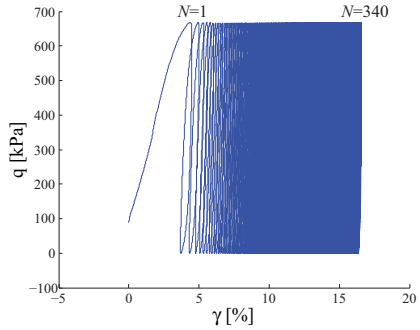

Fig. A.9: Data from test no. 9. $\gamma - q$ diagram for a test, which failed under incremental collapse. N = 340 cycles, τ_a = 167 kPa and τ_{cy} = 167 kPa.

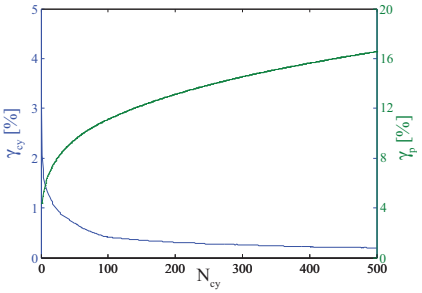

Fig. A.10: Data from test no. 9. Number of cycles – γ diagram. τ_a = 167 kPa and τ_{cy} = 167 kPa. At N = 340 cycles, the average shear strain has reached 15 %.

fective mean stresses. As cyclic loading continues the pore pressure starts to increase, which reduce the effective mean stresses. Moreover, Figure A.7 shows that the inclination of the cycles becomes steeper as more cycles are applied, which is due to an increase in soil stiffness. Consequently, γ_{cy} becomes smaller as N increases.

Figure A.9 shows that the incremental shear strain decreases, but the total shear strain increases with the number of cycles. This type of failure is also defined as incremental collapse by Peralta (2010). Figure A.10 also confirms that the incremental shear strain decreases with increasing number of cycles, while the permanent shear strain increases and eventually results in failure at γ_p = 15 % for N = 340 cycles.

Contour Diagrams

When constructing diagrams for practical design situations, the average and cyclic shear stresses are often normalized with respect to a certain stress value. When this normalisation is performed the average and cyclic shear stresses are defined as the *Average Load Ratio*, ALR, and the *Cyclic Load Ratio*, CLR.

Different authors have proposed various types of contour diagrams for cyclic loading. These all take the cyclic shear stress into account via the cyclic load ratio. Randolph and Gourvenec (2011) have made the strain contour diagram shown in Figure A.11. The diagram is based on one undrained monotonic and four undrained cyclic simple shear tests on sand performed by Mao (2000). The diagram shows the strain contours as a function of the cyclic load ratio and number of cycles. It can thereby predict the shear strain

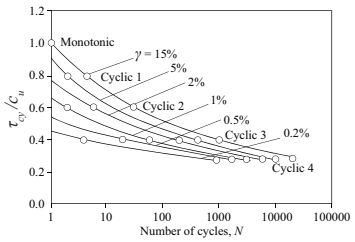

Fig. A.11: Data from test no. 9. Strain contour diagram for sand from simple shear tests with, τ_a = 0 kPa. (Randolph and Gourvenec, 2011)

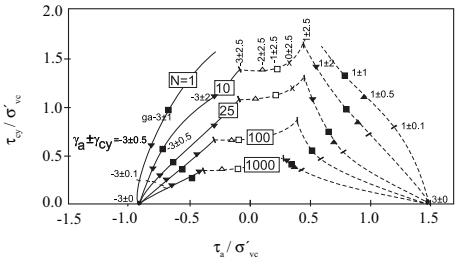

Fig. A.12: Data from test no. 9. Strain contour diagram for dense Baskarp Sand in the undrained state. (Andersen and Berre, 1999)

from cyclic loading, but it assumes symmetric cyclic loading (τ_a = 0). According to Andersen and Berre (1999), the response to cyclic loading not only depends on the cyclic shear stress but also on the average shear stress.

This means that it is the combination of τ_{cy} and τ_a that is decisive for the response. This is also indicated by the results from the conducted cyclic triaxial tests. Therefore, strain contour diagrams, which only take the cyclic load ratio into account, are insufficient for predicting the effects of cyclic loading where the average shear stress is different from zero.

Andersen and Berre (1999) have made a study on the effects of cyclic loading, where both the cyclic load ratio and the average load ratio were taken into account. This produced the contour diagram in Figure A.12, which was made for Baskarp sand with a relative density of 95 %. The diagram is normalized with the effective vertical consolidation stress, σ'_{vc}, and it can be observed that failure is dependent on the combination of average and cyclic shear stresses. It should be noted that, in this graph, cyclic failure is defined as either 3 % cyclic or permanent shear strain, and the tests were conducted with H/D = 2.

Normalisation parameters

When cyclic soil testing is conducted on sand, the cyclic and average shear stress are often normalized with respect to σ'_{vc}, as shown in Figure A.12. This is sufficient under drained conditions since the drained failure envelope is only dependent on the friction angle and effective mean stress. Therefore, σ'_{vc}can be used as a normalisation parameter for contour diagrams describing drained behaviour.

However, in the undrained case, the shear strength at undrained failure, τ_{uf}, for a dilative sand is not only dependent on the friction angle and mean effective stresses, but also the amount of initial pore pressure (Ibsen and Lade,

1998b). This is due to the fact that the shear strength at undrained failure is influenced by cavitation. Before a dense sand reaches failure (both in tension and extension) it tries to dilate, which generates negative excess pore pressure and thereby an increase in effective stresses. At first this will equalize the initial pore pressure and afterwards cavitation will occur at around u_{cav} = -95 kPa, which will lead to failure.

Even though this is a well-known problem, the normalisation parameter used in contour diagrams for dense sand in the undrained state is still often σ'_{vc} as seen in Figure A.12, which does not account for cavitation and the initial pore pressure.

Shear Strength at Undrained Failure

As mentioned, σ'_{vc} can in the drained case be related to the drained shear strength, τ_f. The drained shear strength accounts for the friction angle, the effective mean stress and cohesion, and is given as

$$\tau_f = \frac{1}{2}\frac{6\sin\phi'}{3-\sin\phi'}(p' + c'\cot\phi') \tag{A.2}$$

where $c' = 0$ for cohesionless soils. Instead of using σ'_{vc} as a normalisation parameter in the undrained case for sand, the shear strength at undrained failure, τ_{uf}, is used. Therefore, the use of the above expression is extended to the undrained case by using total stresses and adding the pore pressure at which cavitation occurs, u_{cav} = -95 kPa, which results in equation (A.3). This means that the shear stress at failure becomes a function of total stresses, rather than effective stresses. The expression is then given as

$$\tau_{uf} = \frac{1}{2}\frac{6\sin\phi'}{3-\sin\phi'}(p_{tot} - u_{cav}) \tag{A.3}$$

$$p_{tot} = \frac{-3+\sin\phi'}{3(\sin\phi'-1)}(p'_0 + u_0) \tag{A.4}$$

where p'_0 is the isotropic stress state. The argument for using the above expression is that the undrained bearing capacity for dense sand is governed by cavitation, as negative pore pressure develops during loading, (Ibsen and Lade, 1998b). This also entails that the bearing capacity depends on the total stresses, rather than the effective stresses. Therefore, it is important to include the pore pressure when calculating τ_{uf} in the undrained case for sand. The effect of adding the initial pore pressure, u_0, and the pore pressure at cavitation, u_{cav}, is illustrated in Figure A.13. The figure illustrates the effective stress paths for two examples with the same initial effective mean stress, p'_0. The two examples end up having different shear strengths at undrained

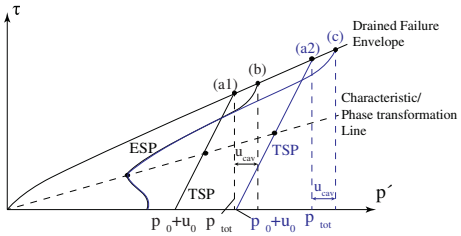

Fig. A.13: Illustration of the theoretically effect of including the initial pore pressure and the pore pressure at cavitation to the drained failure criterion.

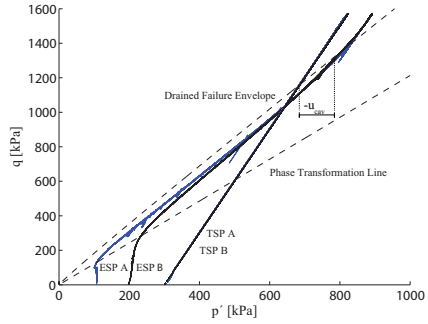

Fig. A.14: Undrained monotonic isotropic consolidated triaxial test results. ESP is the Effective Stress Path and TSP is the Total Stress Path. A and B refers to the two tests.

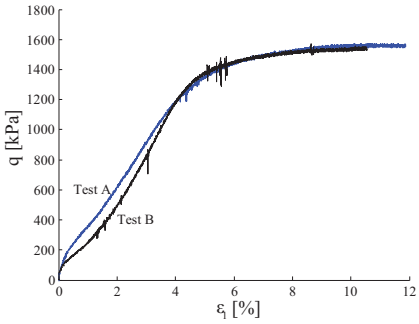

Fig. A.15: Stress-strain curve for the test depicted in Figure A.14. It is seen that the deviator stress at failure is identical.

failure, because of differences in initial pore pressure. Following the total stress paths will lead to drained failure in points (a1) and (a2), which are the points where p_{tot} is measured. From these points the pore pressure at cavitation is added to p_{tot}. This means that a higher amount of initial pore pressure will lead to a higher value of the undrained shear strength before failure is reached, which is illustrated by point (b) and (c) in Figure A.13.

The use of equation (A.3) requires that the shear strength at undrained failure only depends on the sum of p'_0 and u_0, and is independent of the combination of these. Hence, two undrained monotonic isotropic consolidated triaxial tests were conducted in the Danish triaxial cell on Baskarp Sand, named Test A and Test B. They were prepared by undercompaction with 5 layers to a relative density I_D = 90 %, and presheared with open drainage by 400 cycles with $\tau_{cy} \approx 0{,}04\sigma'_{vc}$. One test with an initial effective consolidation stress, p'_0 = 200 kPa and an initial pore pressure, u_0 = 100 kPa (Test B), and another with p'_0 = 100 kPa and u_0 = 200 kPa (Test A). Hence, p'_0 + u_0 = 300 kPa in both tests. The results are shown in Figure A.14 and Figure A.15. The figures show that the requirements for equation (A.3) is fulfilled,

Table A.2: Comparison of using σ'_{vc} and τ_{uf} as normalisation parameter. The comparison is made with two different combinations of τ_a and τ_{cy}, but with three different amounts of initial pore pressure, u_0.

	Contour Diagram		Modified Contour Diagram	
u_0	τ_a / σ'_{vc}	τ_{cy} / σ'_{vc}	τ_a / τ_{uf}	τ_{cy} / τ_{uf}
100 kPa	0.15	0.6	0.07	0.29
100 kPa	0.15	0.6	0.06	0.26
100 kPa	0.15	0.6	0.05	0.20
110 kPa	1.0	1.0	0.48	0.48
302 kPa	1.0	1.0	0.33	0.33

as the deviator stress at failure, q_f = 1575 kPa, coincide for the two tests. Moreover, it is seen that the theory illustrated in Figure A.13, concerning the intersection of the effective stress paths with the drained failure envelope, is as predicted.

Modified Contour Diagram

Based on the expression for shear strength at undrained failure in equation (A.3), a modified contour diagram is constructed for the Frederikshavn Sand in the undrained case with I_D = 80 %. The modified contour diagram is based on the 17 conducted tests and normalized with respect to τ_{uf} as shown in Figure A.16. It is seen that the graph shares the same tendency as the contour diagram by Andersen and Berre (1999) in Figure A.12. However, an important feature of the modified contour diagram is that it accounts for the initial pore pressure, which is important when dealing with the undrained bearing capacity.

Comparison of τ_{uf} and σ'_{vc}

To illustrate the limitations of the contour diagram when normalising with σ'_{vc} as proposed by Andersen and Berre (1999), a comparison between the two contour diagrams can be seen in Figure A.17 and Figure A.18. To make the comparison, two different combinations of τ_a and τ_{cy} were conducted with two and three different amounts of initial pore pressures, respectively. One combination was made with three different levels of initial pore pressure, u_0, namely 100, 160 and 300 kPa (Test No. 12, 13 and 14), and another combination with 110 and 302 kPa (Test No. 4 and 9). The calculated cyclic and average load ratios for the two contour diagrams can be seen in Table A.2.

In Figure A.17, the three tests are plotted in the same point since they have the same ALR and CLR when normalising with σ'_{vc}. However, Figure A.18, which is normalized with τ_{uf}, plots the three tests in different positions,

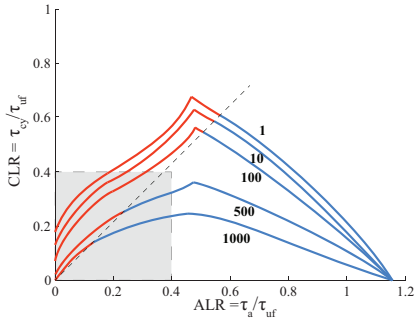

Fig. A.16: Modified contour diagram for Frederikshavn Sand in the undrained case with I_D = 80 %, where the circles marks test results. Red corresponds to two-way loading, while blue is oneway loading. The highlighted area is depicted in Figure A.18.

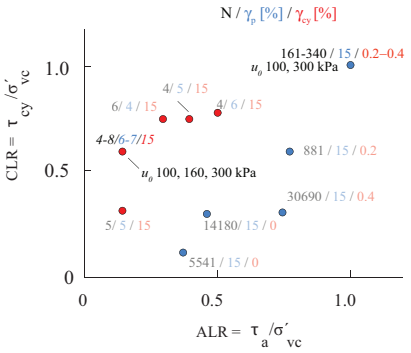

Fig. A.17: Data points where σ'_{vc} is used for normalisation.

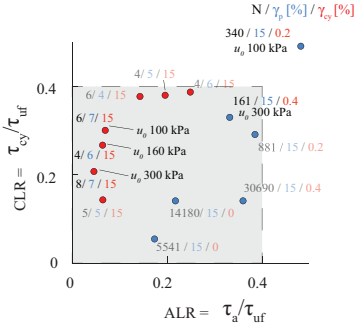

Fig. A.18: Data points where τ_{uf} is used for normalisation.

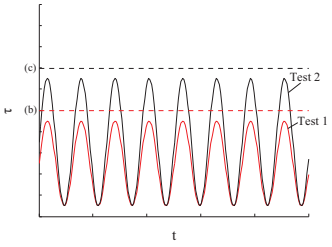

Fig. A.19: effect of amount of applied back-pressure, where (b) and (c) correspond to the two different shear strengths from Figure A.13.

because ALR and CLR depends on the initial pore pressure. The example given above illustrates that it is very important to construct a contour diagram in a manner which represents the in situ conditions as good as possible. Therefore, if the drained state is the design case it is sufficient to apply σ'_{vc} as a normalisation parameter. On the other hand if the undrained state is the design case, the initial pore pressure should be taken into consideration, and therefore τ_{uf} should be used when normalising τ_{cy} and τ_a.

When comparing Figure A.12 and Figure A.16 a considerable difference is observed at ALR = 0, which is $\tau_a/\sigma'_{vc} = 0$ and $\tau_a/\tau_{uf} = 0$, respectively. The difference can be explained by a large difference in applied back pressure. In the tests performed by Andersen and Berre (1999) a backpressure in the range from 500 - 1800 kPa was applied. Compared to the tests conducted to make

Figure A.16 with a backpressure at around 100 kPa, the limit in τ_{cy} without reaching cavitation is raised significantly. This makes it possible to perform tests with a load ratio combination of τ_a/σ'_{vc}= 0 and τ_{cy}/σ'_{vc} = 1.5. If the same test is performed with a low back pressure, cavitation will occur, and the test will correspond to a monotonic test. This can be explained with Figure A.19, where the dashed lines at (b) and (c) correspond to the two different shear strength from Figure A.13; (b) with a low initial pore pressure and (c) with a high amount of initial pore pressure. In this example, Test A can be conducted with a back pressure corresponding to points (b) and (c). Test B can only be conducted with a high amount of back pressure, corresponding to (c), as it will fail before the maximum load is reached, when a low amount of back pressure, (b), is applied. Hence, it will correspond to a monotonic loaded test.

This illustrates the importance of taking the initial pore pressure into account, or using a pore pressure corresponding to the design situation. This observation strengthens the argument for choosing τ_{uf} as the normalisation parameter for undrained situations.

Conclusion

A modified contour diagram is created for the Frederikshavn Sand in the undrained case for a relative density of I_D = 80 %. It can be used to estimate the number of cycles to failure for a given combination of pore pressure, average and cyclic load ratio.

When normalising cyclic and average shear stresses for use in contour diagrams, σ'_{vc} is found insufficient to use as a normalisation parameter in the undrained case, as it does not take pore pressure into account. This is important, since the shear strength at undrained failure for dense sand is governed by cavitation. Therefore the undrained shear strength, τ_{uf}, is used as a normalisation parameter for the modified contour diagram and should be used for other contour diagrams in the undrained case. The undrained shear strength, τ_{uf}, is dependent on total stresses, and thereby takes the pore pressure into account.

References

Andersen, K. H. (2009). Bearing capacity under cyclic loading - offshore, along the coast, and on land. the 21st bjerrum lecture presented in oslo, 23 november 2007. *Canadian Geotechnical Journal*, 46(5):513–535.

Andersen, K. H. and Berre, T. (1999). Behaviour of a dense sand under

monotonic and cyclic loading. *ECSMGE XII Geotechnical Engineering for Transportation Infrastructure. Proc.,*, 2:pages 667–676.

Ibsen, L., Hanson, M., Hjort, T., and Thaarup, M. (2009). Mc-parameter calibration of baskarp sand no. 15. *DCE Technical Report*, (62).

Ibsen, L. B. (1994). The stable state in cyclic triaxial testing on sand. *Soil Dynamics and Earthquake Engineering*, 13(1):pp. 63–72.

Ibsen, L. B. (1995). The static and dynamic strength of sand. *XI ECSMFE'95 - European Conference on Soil Mechanics and Foundation Engineering*, pages pp. 69–76.

Ibsen, L. B. and Lade, P. (1998a). The role of the characteristic line in static soil behavior. *Localization and Bifurcation Theory for Soils and Rocks*, pages 221–230.

Ibsen, L. B. and Lade, P. V. (1998b). *The Strength and Deformation Characteristics of Sand Beneath Vertical Breakwaters Subjected to Wave Loading*. Number ISSN: 1398-6465 in Soil Mechanics Paper No. 23. Aalborg University.

Mao, X. (2000). The behaviour of three calcareous soils in monotonic and cyclic loading. *Ph.D. Thesis, University of Western Australia*.

Peralta, P. K. (2010). Investigations on the behavior of large diameter piles under long-term lateral cyclic loading in cohesionless soil. Master's thesis, Leibniz University Hannover.

Randolph, M. and Gourvenec, S. (2011). *Offshore Geotechnical Engineering*. Sangeet Patra, 1st edition. ISBN: 978-0-415-47744-4.

Paper B

Advanced Laboratory Setup for Testing Offshore Foundations

Søren Dam Nielsen
Lars Bo Ibsen
Benjaminn Nordahl Nielsen

The paper has been published in
Geotechnical Testing Journal
Vol. 39, No. 4, July 2016.

The layout has been revised

Abstract

This paper describes a test set-up for testing small-scale offshore foundations under realistic conditions: of high pore-water pressure and high impact loads. The actuator, used for loading has enough capacity to apply sufficient force and displacement to achieve both drained and undrained failure modes for small scale-offshore foundations. Results from trial tests on two small-scale bucket foundations, subjected to transient or cyclic loading, are presented. Tests showed that cavitation limits the undrained bearing capacity. Hence, a high pore-water pressure is important for simulating offshore conditions.

Key Words: 1g Physical Modeling, Pressure Tank, Offshore Foundation, Small Scale Test Facility, Transient Loading, Cyclic Loading.

Introduction

Similarly to onshore structures, offshore structures require a foundation. However, the expenses and environmental loads of offshore foundations are much larger than those of onshore foundations. In extreme situations, waves might break and induce very large forces in a very short time interval. Even in sand, an undrained response might be possible, triggered by ship impact or emergency stopping of the wind turbine.

Locations in the North Sea suitable for offshore wind farms often have dense to very dense types of sand. When dense sand is loaded undrained, negative excess pore pressure is generated. Failure is reached when the excess pore pressure equals the cavitation pressure of the pore water, as described in Nielsen et al. (2013). For foundations in dilative soils, which have elevated cavitation pressure, an increased water depth will lead to an elevated undrained bearing capacity. This effect should be considered when performing small-scale testing of offshore foundations and investigating, the undrained response.

Optimizing the design of offshore foundations offers major potential for cost savings. Methods for design optimization include analytical, numerical, and experimental (i.e., small-scale testing) approaches. The analytical solution for the bucket foundation is often presented as a cigar-shaped yield surface in a space composed of horizontal, vertical, and moment loads. Ibsen et al. (2014) described and calibrated this yield surface against laboratory tests. Finite-element modeling estimates of the bearing capacity of bucket foundations, have been described by Gourvenec (2008) and Bransby and Yun (2009), among others.

Physical modeling has been used to determine the behavior of foundations under different load combinations. Physical models can be small-, large-, or even full-scale models of the real foundation. Researchers have used various setups to investigate different behaviors at $1g$. For example, Zhu et al. (2013) analyzed the long-term behavior of a small-scale bucket foundation in loose dry sand. Byrne and Houlsby (2004) investigated the drained behavior of a small-scale bucket foundation in dry dense sand. Bransby and Yun (2009) studied the response of a bucket foundation exposed to combined loading in dense oil-saturated sand, whereas Larsen (2008) and Ibsen et al. (2014) investigated the behavior in dense water-saturated sand. Kelly et al. (2006a) made large-scale field tests of bucket foundations installed in saturated clay and sand. Ibsen (2008) described a full-size bucket foundation installed in a test field in Frederikshavn, Denmark, where the soil consists of fine sand with rounded grains. The foundation, installed in a few meters of water, supported a Vestas V90 3.0 MW wind turbine.

However, none of the aforementioned tests accounted for the effects of water pressure, either because no or very low hydrostatic water levels were used or because no measurements of the excess pore pressure were made.

Kelly et al. (2006b) tested bucket foundations inside a pressure chamber with transient vertical loads, to which a total overburden pressure between 0 and 200 kPa was added. Soil response is governed by effective stresses. When sheared under undrained conditions, saturated dilative soils generate negative excess pore pressure, which increases the effective stress level. The cavitation pressure limits how much negative excess pore pressure can be generated in the pore water. Therefore, the initial total stress level controls the undrained strength of a dense soil. Investigations of the undrained bearing capacity of a foundation for offshore structures should account for the hydrostatic pressure of the pore water.

This paper describes a facility developed for the small-scale testing of offshore foundations under realistic conditions, of high pore-water pressure and high impact loads. Load is applied by an actuator, which has enough capacity to apply sufficient force and displacement to reach failure for small-scale offshore foundations. This paper describes the-set up and results from trial tests on two small-scale bucket foundations, subjected to transient or cyclic loading.

$1g$ Small-Scale Testing vs. Full Size

When conducting small-scale tests, the dimensions of the actual foundation are downscaled to a model size. However, applying to the pore-water pressure an overburden pressure equal to the hydrostatic pressure of an offshore location, will alter the shape of the stress profile. Consider the example of

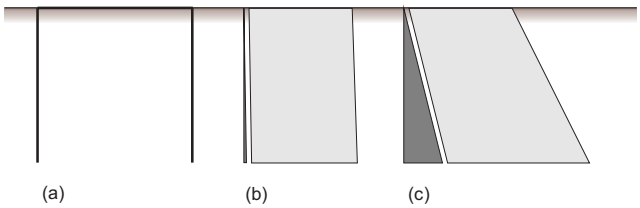

Fig. B.1: (a) Mono bucket foundation with diameter equal to the skirt length. (b) Shape of stress distribution in the laboratory setup. (c) Shape of stress distribution on an offshore location. Horizontal line represents the sea bed. Light and dark areas represents pore pressure and effective stresses, respectively.

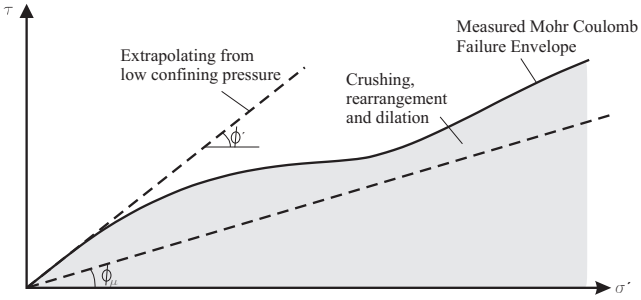

Fig. B.2: Stress dependent shear strength after Holtz (2001).

a mono bucket foundation with equal dimensions for the skirt length and diameter Figure B.1(a). Figure B.1(b) illustrates the shape of the stress distribution in the laboratory set-up when an overburden pressure of 200 kPa is applied to the pore water. The total stress is the sum of the effective stress (dark areas) and the pore pressure (light areas). Figure B.1(c) illustrates the shape of the stress distribution at an offshore location with a water depth of 20 m and a mono-bucket foundation with a diameter and a skirt length of 15 m and an effective soil unit weight of 10 kN/m3. Dark and light areas represent the same stress distributions as in Figure B.1(b). The shape of the cavitation pressure with depth follows the shape of the pore-water pressure. Hence, the cavitation pressure for the laboratory tests are almost constant, and for the real scenario increases with depth.

The effective stress level in the soil differs substantially between full-size structures and small-scale tests. As shown in Figure B.2, the effective friction angle (ϕ') consists of a basic mineral friction angle (ϕ_μ) and a dilation angle (ψ) that described the dilation, rearrangement, and crushing of soil. The mineral friction angle is the only contribution that is independent of the effective stress level. A soil tends to dilate more (and, thus, the effective friction angle tends to be higher) at low compared to higher effective stress levels.

Figure B.2 illustrates how the effective stress level affects the soil strength.

Fig. B.3: Pressure tank..

Extrapolation of the Mohr Coulomb failure envelope from measurements at a low effective stress levels will lead to an overestimation of the strength. Dilation is less dominant under the effective stress levels of real size structures, but these structures have a higher level of rearrangement. Therefore, linear scaling of results from laboratory tests will lead to overestimation of the bearing capacity of real structures. As dilation is more pronounced at low effective stress levels, small-scale tests (where the effective stress is low) tend to overestimate the pore pressure build-up. In laboratory tests, failure is defined as the peak strength, or the rotation at which the resistance tends towards a horizontal asymptote.

Test Set-up

This section, describes the laboratory test facility. Detailed descriptions of the individual parts of the test setup are given in the following subsections. The test setup comprises a steel tank, Figure B.3, where the internal pressure can be increased. This so-called pressure tank determines the physical boundaries for the tests. The test setup is specially developed for testing offshore foundations. The pressure tank is assumed to contain a water-saturated soil medium being either medium dense, dense or very dense, depending on the soil vibration during preparation. A foundation of any type is installed

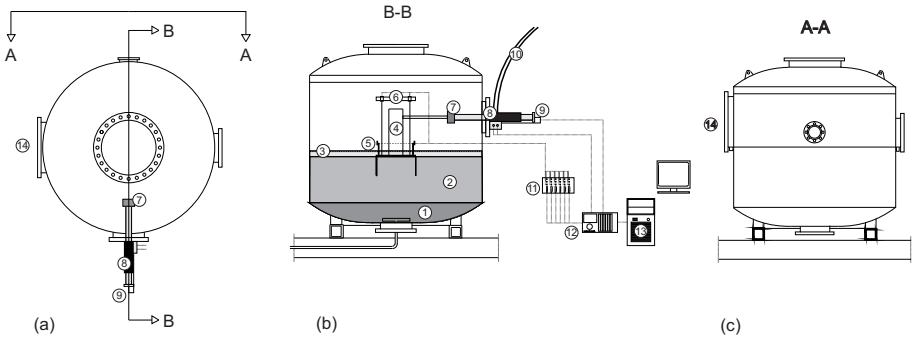

Fig. B.4: Setup of the pressure tank test setup. (a) Top view, (b) sectional view B-B, and (c) sectional view A-A. Elements of the setup are as follows: (1) gravel, (2) Aalborg University Sand No. 1, (3) water level, (4) loading tower installed on top of the bucket foundation, (5) pore pressure transducers, (6) vertical displacement transducers, (7) force transducer, (8) hydraulic actuator, (9) horizontal displacement transducer, (10) hydraulic cables, (11) distribution box, (12) MOOG PTC unit, and (13) PC. Dashed lines represent electrical wire connections.

in the sand and connected to an actuator that exposes the foundation to a prescribed displacement or force. Before testing, various transducers can be mounted to measure a given parameter. Data are measured during testing, collected, and stored on a computer.

Pressure Tank

The pressure tank (Figure B.4) is a large cylindrical steel tank with an internal diameter of 2.1 m and an internal maximum height of 2.1 m. The bottom of the tank contains a layer of gravel (1), that is topped by a permeable Geotextile canvas, followed by 0.6 m of Aalborg University Sand No. 1 (2). The sand is water-saturated through the bottom of the tank, where a valve is connected to a tap. The purpose of the gravel, is to ensure a free flow of water from the sand to the in- and outlet valve. The Geotextile canvas ensures that the soil does not erode and fills the voids in the gravel. The water level is 5 to 10 cm (3) above the sand level in the tank. A tower is mounted on top of the foundation (4). Pore pressure transducers are mounted on the bucket (5). Vertical displacement transducers (6) are attached to the bucket lid. The hydraulic actuator (8) is mounted on the side of the pressure tank. A force transducer (7) is attached to one end of the piston inside the tank with a horizontal displacement transducer (9) mounted on the other end. All transducers are connected to the MOOG PTC (12), which is connected to a PC (13).

Table B.1: Characteristics of Aalborg University Sand No. 1, determined according to the Danish standards described in DGF's Laboratoriekomité (2001)

Parameter	Symbol	Value
Grain size, 50 % fraction	d_{50}	0.14 mm
Uniformity coefficient, d10/d60	U	1.78
Specific gravity	G_s	2.64
Maximum void ratio	e_{max}	0.854
Minimum void ratio	e_{min}	0.549

Soil Specifications

The pressure tank contains an artificial sand, Aalborg University Sand No. 1, Which has been tested at Aalborg University by Borup and Hedegaard (1995) according to the Danish standards of DGF's Laboratoriekomité (2001). Characteristics of the sand are given in Table B.1. The sand is more angular than offshore sand, which typically have rounded grains.

Soil Preparation

Sand and water levels inside the pressure tank are left unchanged after a previous test. To obtain identical soil conditions in each test, a special preparation technique is used. First, the water-saturated sand is loosened by an upward gradient (i) of 0.9. Consequently, the hydraulic pressure ($h_0 - h_s$) should be 0.54 m above the water level in the tank because, the soil depth is 0.6 m. An expression for the gradient is given in Equation (B.1) and the parameters are illustrated in Figure B.5.

$$i = \frac{h_0 - h_s}{d} \tag{B.1}$$

The gradient is removed after a few minutes, once the soil is loosened.

Next, the sand inside the tank is vibrated by poker vibrators, see Figure B.6, until the desired relative density is reached. The vibration pattern depends on the size and type of foundation, loading conditions, and the desired relative density. After vibration, the relative density is approximated from the cone resistance measured by mini cone penetration testing (CPT). Figure B.7 provides an example of five tests performed after vibration.. If the results of CPT indicate that the soil is too inhomogeneous, then further vibration is performed, followed by new CPT. Once acceptable soil conditions are reached, the soil preparation phase has ended.

After the preparation phase is completed the pore pressure measuring system on the foundation is saturated. The measuring system comprises pressure transducers connected to thin metal tubes, placed at positions on

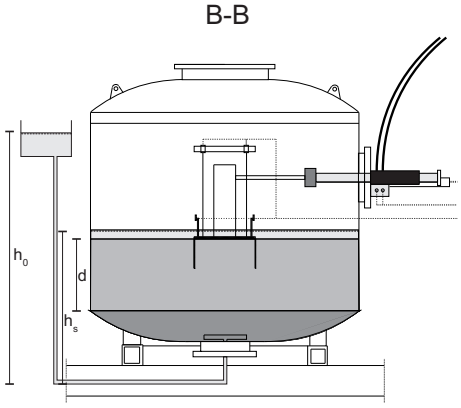

Fig. B.5: Application of a gradient to the sand in the pressure tank. h_0 external water table; hs internal pressure head; d depth of the soil layer. Seen from sectional view B-B in Figure B.4(a).

the foundation where pore pressure should be measured. Figure B.8, shows the pore pressure measurement system for the bucket foundation used in the trial tests. The tubes should be saturated with water before the foundation is installed. If the tubes are not saturated beforehand, they will tend to plug easier, which will disturb the pore pressure measurements. Finally, the foundation is installed.

Mini CPT

The relative density of the soil is tested with a mini CPT prototype unit manufactured at Aalborg University by Larsen (2008). Ibsen et al. (2009) determined an expression for the relative density (D_r, in Danish I_D), as a function of cone resistance

$$D_r = 5.24 \left(\frac{\sigma'_{v0}}{q_c^{0.75}} \right)^{-0.42} \tag{B.2}$$

where the initial effective vertical stress (σ'_{v0}) and the cone resistance (q_c) are given in MPa. Ibsen et al. (2009) calibrated the asymptotic friction angle for a curved Mohr Coulomb failure envelope as given in Equation (B.3).

$$\phi_s = 0.152\, D_r + 27.4(\sigma'_3)^{-0.28} + 23.2 \tag{B.3}$$

CPT is performed at five positions: in the center of the pressure tank and at four positions approximately 0.5 m from the center (corresponding to 3, 6, 9 and 12 o'clock, see Figure B.9.

Fig. B.6: Poker vibrator used for vibration of the soil.

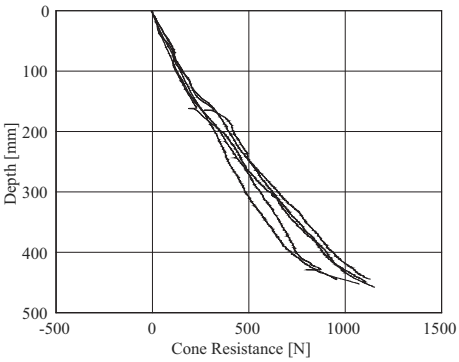

Fig. B.7: Example of measured cone resistance from mini CPT. The y-axis is the depth (in mm), where 0 mm corresponds to the soil surface.

Equipment and Transducers

Three types of transducers are used: displacement transducers, pressure transducers, and a force transducer. Displacement transducers, measuring the vertical displacement, are mounted on a metal frame that is placed in inside the pressure tank, see Figure B.4 and attached to the foundation. The rotation and the vertical and horizontal displacements can be calculated from displacement transducer measurements. Vertical displacement transducers are set up as potentiometers with a resolution of 1/40 mm. The horizontal displacement transducer is a magnetic position transducer with a resolution of at least 10 μm. Pore pressure transducers are mounted on the foundation to measure the development of pore pressure along the structure. Seven 500 kPa pore pressure transducers and five 1000 kPa pressure transducers are available. All pore pressure and force transducers are set up as full bridges. The force, which has a range of 100 kN is mounted on one end of the hydraulic actuator inside the pressure tank, Figure B.4.

Actuator

A hydraulic actuator with a stroke length of 0.5 m is mounted on the side of the pressure tank. The actuator can deliver a static force up to 35 kN under a hydraulic oil pressure of 60 bar (6 MPa). Increasing the hydraulic oil pressure from 60 to 250 bar (25 MPA) increases the capacity to 150 kN. The piston can perform any combination of force- and/or displacement-controlled loading, (e.g. monotonic and/or cyclic loading). These capabilities enable tests to be performed with advanced loading. A 100 kN force transducer is mounted on the end of the horizontal hydraulic actuator, see Figure B.4. The

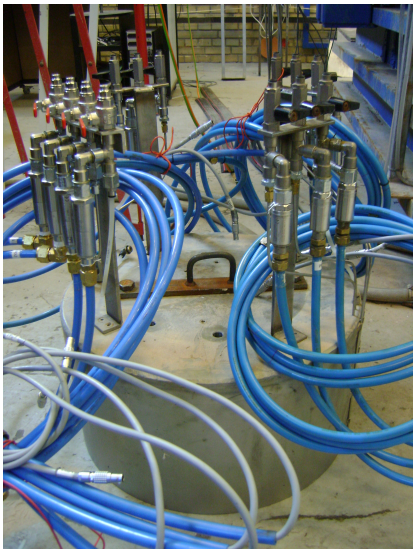

Fig. B.8: Bucket foundation with a diameter of 500 mm and a skirt length of 250 mm. Pore pressure transducers are mounted on top of the foundation. Electrical wires are hidden inside pressure- and water-proof tubes.

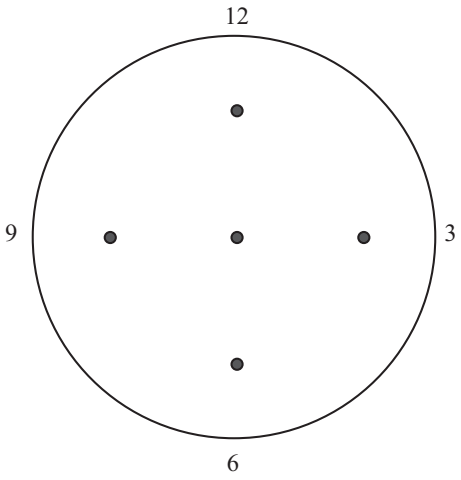

Fig. B.9: Top view of the pressure tank. Black circles indicate clock positions (i.e., 3, 6, 9, and 12 o'clock) where mini CPT was done.

maximum velocity of the actuator is tested to 500 mm/s, with no load applied. As the load increases, the maximum speed of the actuator decreases. During testing the controlled parameter can be switched between force- and displacement-controlled modes. Tests are regulated by a PID (Proportional, Integral, Derivative) controller, the principals of which are described next.

In the diagram of the control loop (Figure B.10(a)), the gray box (left) represents the system of a PC connected to an electronic unit, which, in turn, is connected to various transducers. This system sends out a user-defined control signal, which may be a force or displacement. The actuator receives the signal from the PC and begins moving the piston in the actuator. Two external transducers (Figure B.10(b)) measure the actual movement and force provided by the piston. The measured signal acts as a feedback signal to the PC, which compares the incoming input signal to the output signal. The piston will move until the control and feedback signals are matching. The feedback signal is recorded, with a default sample rate of 1000 Hz. The ability to apply force- and displacement-controlled tests enables the investigation of both monotonic and cyclic behavior.

For example, a small rotation, reflecting the tilt after installation of an offshore foundation, could be applied in the displacement-controlled mode.

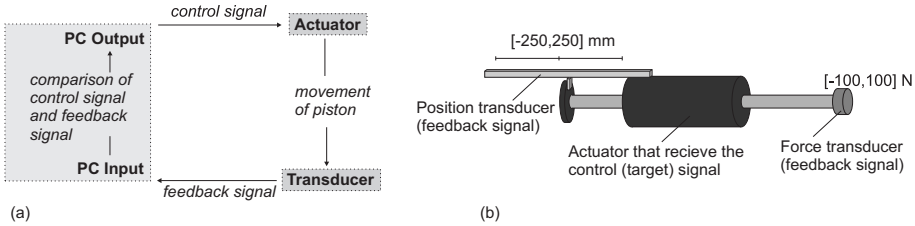

Fig. B.10: (a) Control loop for the actuator. A PC output to the actuator causes the actuator to move. The response of the movement is measured by a transducer, which sends a feedback signal to the computer, which then adjust the output signal to the actuator. (b) Positions of transducers providing the feedback signal.

Next force-controlled cyclic loading could be applied, followed by displacement-controlled displacement until failure.

Given an actuator stroke length of 500 mm, the maximum amplitude that can be applied in a displacement-controlled cyclic test is 250 mm. Performance of the PID-controlled system depends on the load amplitude and the loading rate. Hence, the loading frequency depends on piston movement and the foundation-soil stiffness. A bucket foundation with a diameter and skirt length of 0.5 m was tested for possible loading frequencies. The PID-regulated system delivered acceptable results for frequencies up to 1 Hz for load amplitudes equal the drained bearing capacity. Frequencies up to 4 Hz have been tested, but the control system was unable to produce acceptable load cycles.

Test Scenarios

The presented test setup can relatively easy be modified enabling multiple testing scenarios. Tests in this report were performed with only one actuator, although the control system is able to handle up to three actuators. This setup makes it possible to simulate various different scenarios shown in Figure B.11.

In the setup described in Figure B.11(a), the ratio of the moment to the horizontal load (M/H) is M/H equal to 0.5 m. Vertical load is changed by adding mass (i.e. permanent load) to the system. The combined weight of the bucket with transducers (654 N) and the tower (473 N) create a constant vertical load. This setup is able to simulate, for example, wave loading on a foundation for an offshore wind turbine. To investigate the ultimate limit state when the structure is loaded by the design wave, monotonic tests can be carried out by applying a prescribed displacement, simulating a static or transient load. Cyclic loading can be applied to investigate the cyclic behavior of a foundation, simulating long-term behavior or the behavior during a

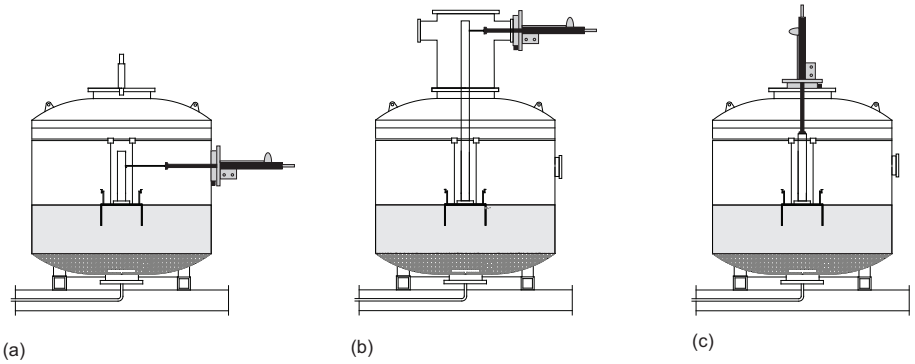

Fig. B.11: Positions for the piston. (a) position 1, (b) position 2 and (c) position 3.

single storm. The setup shown in Figure B.11(b) where M/H = 2.38 m can be used to investigate the effects of wind loading on an offshore wind turbine, or the emergency stop of a wind turbine. The weight of the tower and bucket creates a constant vertical load. It is also possible to mount the actuator on the top hatch (Figure B.11(c), in which case the foundation is loaded only vertically, simulating the situation of a foundation on a jacket structure.

Trial Tests

Two trial tests on two different bucket foundations were performed. This section describes the present test set-up and results from the two trial tests, with the purpose of demonstrating some possibilities of the test setup.

Tested Foundations

The two buckets used for the trial tests each had a diameter (D) of 500 mm and a wall thickness of 4 mm. The skirt lengths (d) were 500 and 250 mm.

The setup was prepared as described above with the sand inside the pressure tank being vibrated to a mean relative density of 90 % ± 3 %. Buckets were pressed into the soil by a vertical hydraulic actuator. A tower was mounted on the top of each tested bucket foundation (Figures B.12 and B.13), with the horizontal actuator and displacement transducers being connected to the tower.

The distance from the bucket lid to the attack point of the actuator (H_{Force}) was 0.5 m in both tests. Displacement transducers were attached to a frame connected to the inside walls of the pressure tank, which was sealed by mounting the two hatches. Pressure inside the tank was increased to maximum of 200 kPa by an air compressor. Under these conditions, the test was ready to be conducted, with the bucket exposed to a given load/displacement.

Fig. B.12: Bucket foundation installed in sand inside the pressure tank. Tower is mounted on top.

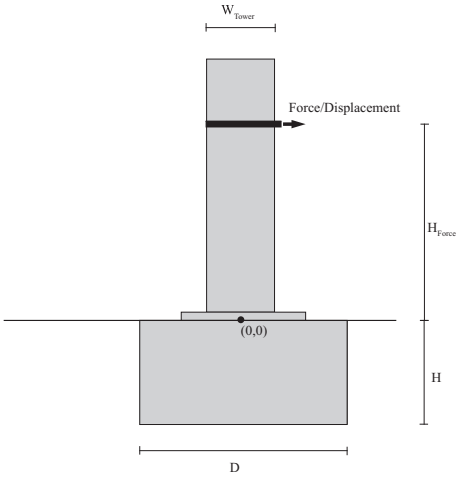

Fig. B.13: Foundation with tower on top. (Pore pressure transducers are not shown).

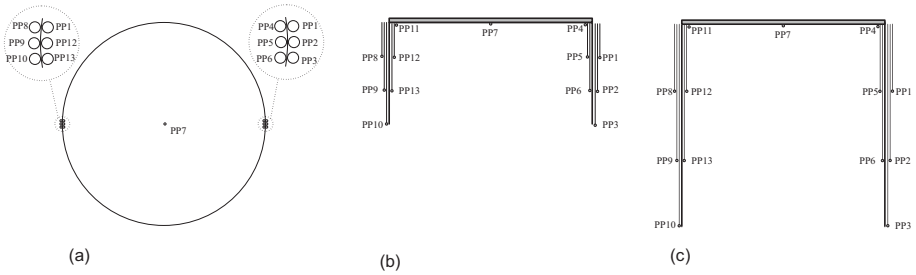

Fig. B.14: Locations of pore pressure measurements. (a) Top view of the bucket foundation, showing positions where pore pressure is measured. Bucket foundations with (b) diameter of 500 mm and skirt length of 250 mm and (c) diameter and skirt length of 500 mm.

Small tubes mounted on the skirts of the bucket enabled up to 13 pore pressure measurements to be made (Figure B.14). The tubes were connected to pressure transducers, which were saturated with water before testing to ensure correct measurements.

Transient Loading of a Bucket Foundation

This section presents the results from one dynamic test, with the actuator mounted in the position shown in Figure 11(a) The sand was vibrated with poker vibrators, shown in Figure B.6, to D_r = 90 %, as calculated from measurements by the mini CPT after vibration. A bucket with D = 500 mm and d = 250 mm was installed, and pressure inside the pressure tank was increased by 200 kPa. The bucket was loaded by a prescribed displacement to failure

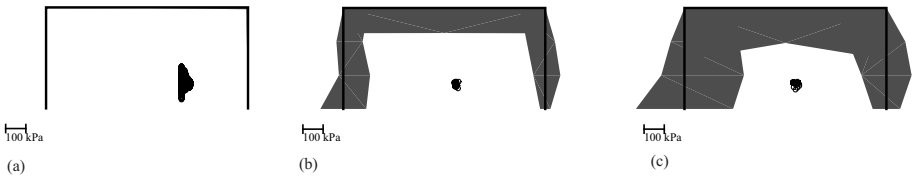

Fig. B.15: Maximum suction developed during testing, with an actuator speed of (a) 0.1 mm/s, (b) is 50 mm/s, and (c) is 100 mm/s.

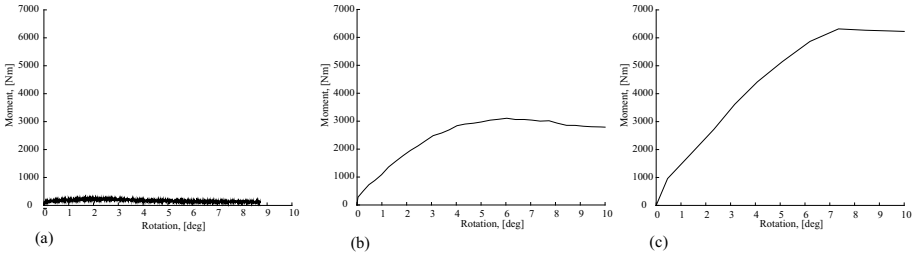

Fig. B.16: Force and pore pressure development as a function of applied rotation, with an actuator speed of (a) 0.1 mm/s, (b) 50 mm/s, and (c) 100 mm/s.

with velocities of 0.1, 50, and 100 mm/s.

The maximum measured suction (negative excess pore pressure) for each transducer is shown in Figure B.15. Suction around the skirts increased with increasing loading rate. The maximum created suction shown in Figure B.16(c) is -300 kPa, which is the cavitation pressure. Only negative excess pore pressure had developed when failure was reached. Each black circle in Figures B.16(a), B.16(b) and B.16(c) represents the rotation point of the foundation for each sample. The rotation point was calculated from the rotation and horizontal and vertical translations of the bucket, using the measurements from the displacement transducers.

As demonstrated by the plot of force as a function of rotation (Figure B.16), a relatively large rotation of 5 to 6 degrees was necessary to develop maximum resistance (i.e. to mobilize the earth pressure). Maximum suction (Figure B.15) was measured when maximum resistance was measured (Figure B.16).

These trial tests confirm that the setup can be used to measure the pore pressure development along a geotechnical structure, and that large loads and displacements can be applied in a relatively short time, which are important factors for offshore structures.

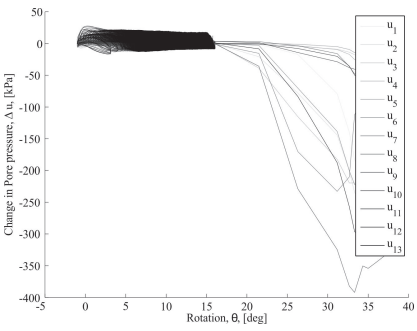

Fig. B.17: Change in pore pressure as a function of rotation. Mean load is 85 Nm and amplitude is 873 Nm.

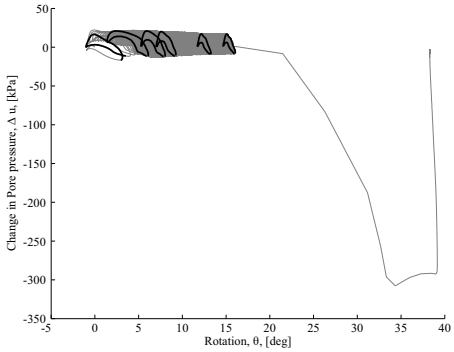

Fig. B.18: Change in pore pressure no. 13 as a function of rotation. Mean load is 85 Nm and amplitude is 873 Nm.

Cyclic Loading of a Bucket Foundation

This section, presents the results from one cyclic test, with the actuator positioned described above. Sand was vibrated to a level of relative density D_r = 90 %. A bucket, with D = 500 mm and d = 500 mm was installed, and the pressure inside the tank was increased by 200 kPa. The bucket was loaded by 1000 load cycles, with a mean load of 85 Nm and amplitude of 873 Nm. Finally, the bucket was loaded by a prescribed displacement of 150 mm to a state beyond failure with a velocity of 100 mm/s.

As in the dynamic tests, 13 pore pressure measurements were made, (Figure B.17). Pore pressure changed during a load cycle, but there was no significant pore pressure build-up as the rotation increased. After 1000 cycles, the bucket was rotated until failure was reached, and a large drop in pore pressure was observed. It was difficult to identify the individual paths of the changes in pore pressure during each load cycle from the figure containing all 13 pore pressure measurements.

Therefore, in Figure B.18, only measurements from pore pressure transducer 13 (see Figure B.14), are shown with the black stress paths corresponding to changes in pore pressure for cycle numbers 1, 10, 50, 100, 500, and 1000. This figure shows clearly that the pore pressure did not change significantly as the bucket was rotated, even though the pore pressure changes during a single cycle. The maximum and minimum values during one cycle were constant, but the rotation during one cycle decreased with an increasing number of applied cycles.

Figure B.19 depicts the moment as a function of rotation. As the cyclic part of the test was force-controlled, the maximum and minimum values of the moment were kept constant during cyclic loading. As with the pore pressure plot, the actual stress path during cyclic loading can be hard to

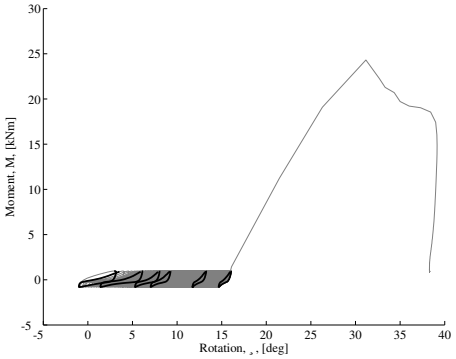

Fig. B.19: Moment as a function of rotation. Mean load is 85 Nm and amplitude is 873 Nm.

follow. Therefore, the stress paths during cycle numbers 1, 10, 50, 100, 500, and 1000 were highlighted in black. Similar to the change in pore pressure, the rotation during each cycle decreased with the number of applied load cycles.

Evaluation of the Boundary Conditions and Model Size

In addition to establishing realistic conditions, it is important to ensure that the setup boundaries do not influence the result. Effects of the boundary conditions must be tested whenever a new type of foundation is used in the test facility. In one of the trial tests, a bucket foundation with a diameter and a skirt length of 500 mm was installed in 600 mm of Aalborg University Sand No. 1. Judgement alone was thought to be insufficient to ascertain whether the boundaries were too close and would affect the results.

The boundaries of the steel tank are defined by the steel frame. Because the stiffness of the steel tank is relatively high compared to the sand inside, no radial deformation of the soil is allowed at the boundary. The steel tank is impermeable, meaning that no water flow is allowed through the tank.

To evaluate the effects of the boundary conditions on the trial tests, a PLAXIS 3D model was made estimate the size of the failure mechanism. The problem is symmetric; therefore only half of the foundation was modeled. The overall model size was 2 m (x) × 1 m (y) × 0.6 m (z). Similarly to the boundary conditions for the real steel tank, the assumptions for the model were: no horizontal straining and no flow at the boundary.

The soil consists of one layer with the properties given in Table B.2. As only the state of failure is of interest, the bilinear elasto-plastic Mohr-Coulomb material model was chosen. However, a friction angle determined

Table B.2: Parameters used in the Mohr-Coulomb model.

Parameter	Symbol	Value
Material model	-	Mohr-Coulomb
Drainage type	-	Drained
Unit weight above phreatic level	γ_{unsat}	20 kN/m^3
Unit weight below phreatic level	γ_{sat}	20 kN/m^3
Young's modulus	E′	30,000 kPa
Poisson's ratio	ν'	0.2
Cohesion	c'_{ref}	1 kPa
Friction angle	ϕ'	50°
Dilation angle	ψ	20°

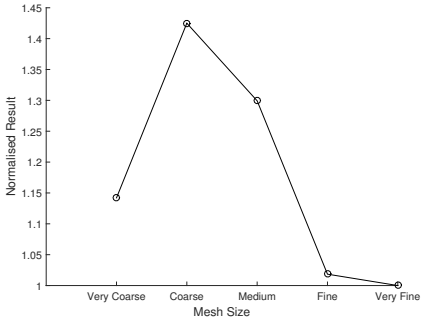

Fig. B.20: Mesh convergence. Normalized results are the bearing capacity calculated for each mesh size compared to the bearing capacity calculated with the fine mesh. Convergence was reached with the fine mesh size.

at a high stress level does not represent the soil strength at a low stress level (Figure B.2). Therefore, the friction angle and dilation angle must be determined from the mini CPT conducted during the preparation phase. A Poisson's ratio of 0.2, and Young's modulus of 30 MPa were used as representative values for the drained response. Exact values of the elastic parameters are of minor importance when investigating failure. Saturated and unsaturated unit weights of the soil were chosen to be 20 kN/m^3 because no soil is above the phreatic level of 20 m. Given these values, the total stress at the soil surface was 200 kPa, corresponding to the pressure applied in the pressure tank. The bucket was modeled as plates with a stiffness of 210 MPa. The soil-structure interaction was modelled with interface elements. The interface was modelled with an interface friction angle of 35°, such that R_{inter} = 0.59 in PLAXIS. The calculation consisted of three phases: Initial phase (calculation of initial stresses in the soil), installation phase (the bucket were wished in place) and a loading phase where the prescribed displacement (arrow in

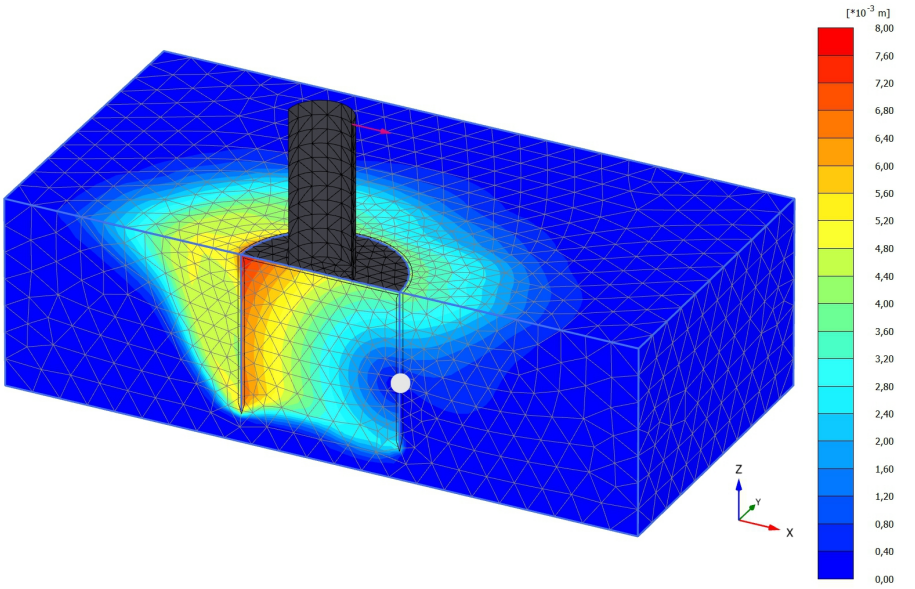

Fig. B.21: Total displacement (| u |) for the bucket foundation at failure modeled in PLAXIS 3D.

Figures B.21, B.22, B.24 and B.25) were applied.

Mesh convergence was reached with the "fine" mesh option. Thus, further refining the mesh will not affect the result (i.e. the bearing capacity). Figure B.20 reports the mesh convergence. The normalized result is the calculated bearing capacity for each mesh size, divided by the bearing capacity for the converged mesh size ("very fine").

Figure B.21 shows the incremental displacement, which is a measure of the deformation during the last step and, therefore, an indication of the failure mechanism. The figure shows a clear rotation point (light dot) inside the bucket.

In the failure line of a failure mechanism, the shear strain becomes very large as failure is approached. Thus, the plot of the total shear strain (Figure B.22) could reflect the failure mechanism.

Figures B.21 and B.22 show similar results, strongly indicating that the failure mechanism either reaches or is very close to the physical boundaries of the test setup. Therefore, the degree to which the boundaries affect the bearing capacity of the model was investigated. A larger model was created, in which the only change was the size of the model (horizontal plane is 4 m × 4 m, depth = 1.5 m). Taking advantage of the symmetry of the problem, the model dimensions were 4 m × 2 m × 1.5 m. The interface had the same properties as the soil given in Table B.2. By refining the mesh convergence

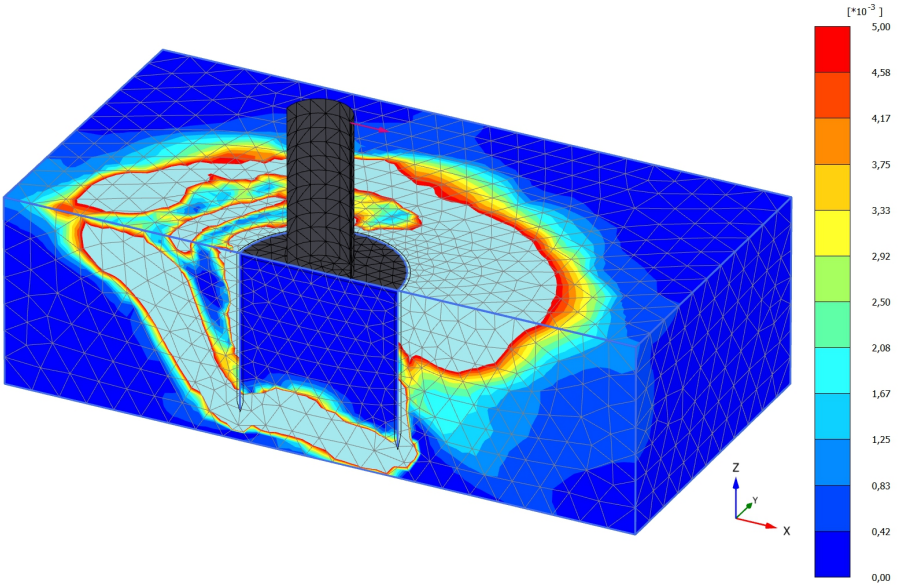

Fig. B.22: Total shear strain (γ_s) for the bucket foundation at failure modelled in PLAXIS 3D.

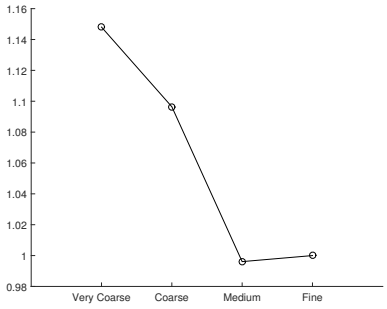

Fig. B.23: Mesh size convergence for the 4 m × 2 m × 1.5 m model. Convergence was reached with the medium mesh option, with additional refinement near the foundation. All mesh sizes were calculated with the same relative refinement near the foundation.

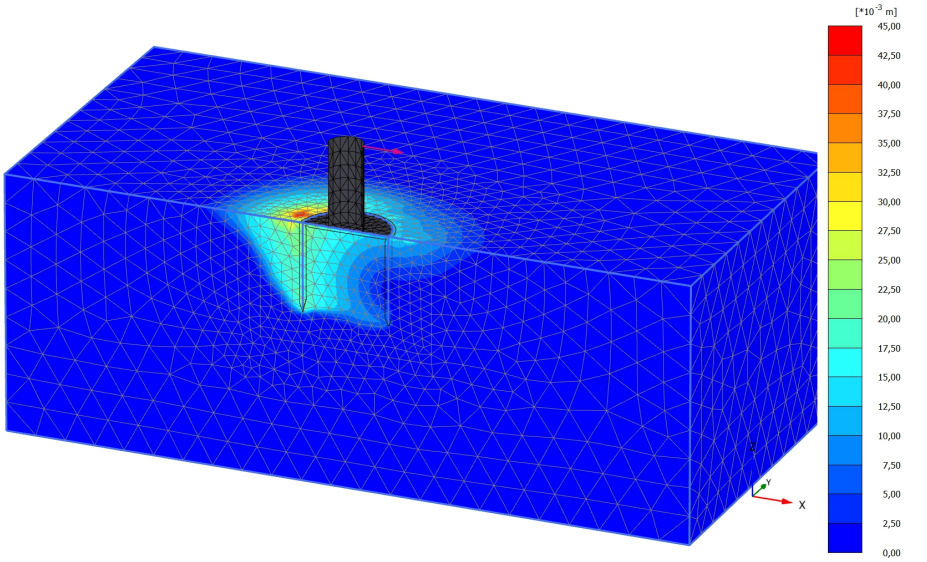

Fig. B.24: Total displacement ($|u|$) for the bucket foundation at failure modeled in PLAXIS 3D. Model size is 4 m × 2 m × 1.5 m.

was reached with the "medium" mesh option and an additional refinement close to the foundation, see Figure B.23.

The incremental displacement ($|\Delta u|$) and the total shear strain (γ_s) for the model with increased model size are shown in Figures B.24 and B.25, respectively. These figures show the same movement patterns as in Figures B.21 and B.22, except that the boundaries clearly do not affect the behavior of the foundation. To evaluate the effect of the boundaries inside the pressure tank the calculated maximum resistances for the two finite element calculations were compared.

Errors induced by the boundaries in the $1g$ tests were estimated by comparing the load displacement behavior of the two simulations. Figure 26 shows the moment (M) as a function of the rotation coursed by the applied horizontal displacement (arrows in Figures B.21, B.22, B.24 and B.25). The prescribed displacement was applied 0.5 m above the sea bed, as in the physical tests. Comparing the two curves in Figure 26 reveals a difference in the force needed to apply a given prescribed displacement. This difference is assumed to represent the error that is induced by conducting physical small-scale tests inside the pressure tank compared to a situation where the boundaries do not affect the results. Figure B.27 shows the percentage difference in the two simulations compared to the resistance calculated by the model with a size of 4 m × 2 m × 1.5 m. A power law function was fitted to estimate the error when the load-displacement curve reached a horizontal

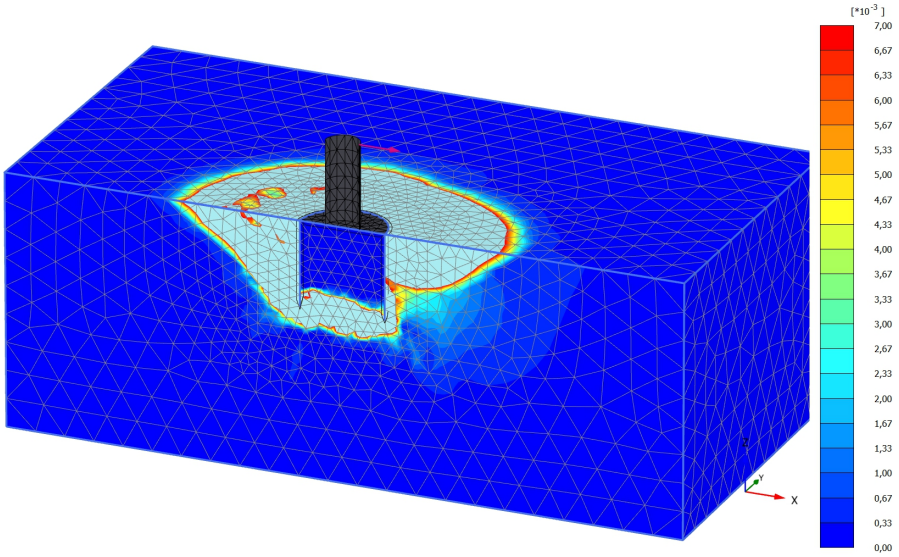

Fig. B.25: Total shear strain (γ_s) for the bucket foundation at failure modelled in PLAXIS 3D. Model size is 4 m × 2 m × 1.5 m.

asymptote. Errors induced by the boundaries in the pressure tank gave rise to an underestimation of the bearing capacity of 20 %.

Discussion

The presented 1g small-scale testing set-up was designed to investigate the behavior of offshore foundations. Compared to many other 1g small-scale testing set-ups, the presented setup has the advantages of being able to apply a total overburden pressure up to 200 kPa impact loads on a foundation. These two factors are highly relevant when investigating the effects of extreme environmental loads on an offshore foundation, where a partly drained or undrained response is expected.

However, as the tests were performed at low stress levels, the dilation was more pronounced than would be expected for a real-size structure. A life size structure may need larger deformations to generate the same amount of pore pressure as in the model. Nevertheless, pattern of the pore pressure development and the effect of generated suction should be the same in both the model and in nature.

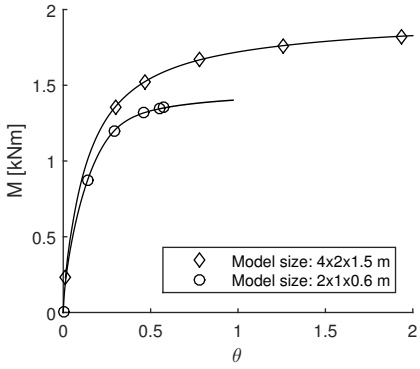

Fig. B.26: Horisontal force as a function of horizontal displacement for the two simulations with model sizes of 2 m × 1 m × 0.6 m and 4 m × 2 m × 1.5 m.

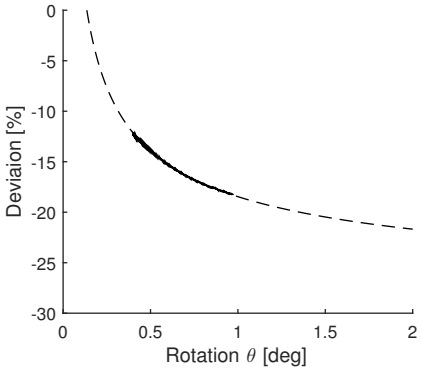

Fig. B.27: Error measured as the deviation between the presented simulations and the simulation with a model size 4 m × 2 m × 1.5 m. Solid line shows calculated data. Dashed line is a fitted power law (f(x) = axb+c, where a = 11.26, b = -0.4857 and c = -29.72913) with a horizontal asymptote equal to c. Error is estimated to be 20 % (26 % at 10° of rotation).

Conclusions

Results of the two trial tests demonstrate that the described setup is very well suited for testing offshore foundations. The actuator can be mounted in three different positions, enabling various types of testing, including mono foundations (e.g. bucket foundations), loaded by wind and waves, and multi foundations (e.g. jacket structures). The setup allows combinations of force- and displacement-controlled tests to be made, which is ideal for testing both cyclic behavior and failure. Results of the trial tests on a transiently loaded bucket foundation showed that the loading rate affects the bearing capacity of the model. Negative or no excess pore pressures were measured in all three model tests of transient behavior of a mono bucket foundation. A sufficient loading rate caused cavitation of the pore water in some areas. As the cavitation pressure is dependent on the initial pore-water pressure, increasing the initial pore-water pressure will increase the cavitation pressure, and affect the bearing capacity. For offshore structures, an increase of the pore-water pressure corresponds to an increase of water depth. Therefore, when investigating the undrained behavior of offshore structures, the scenario of an increased pore-water pressure is important. The test setup is capable of loading structures with loading rates that trigger the undrained response.

Trial tests with cyclic loading of a mono bucket foundation were per-

formed. The testing setup is able to apply cyclic loading for investigating the permanent rotation of a foundation. The cyclic loading test was performed with a load frequency of 0.1 Hz. It was not possible to predetermine a maximum loading frequency because, the performance of the PID-regulated control system is dependent on the loading amplitude, frequency, and movement of the actuator (and, therefore, the stiffness of the foundation). For the presented bucket foundation, cyclic tests were successfully performed with a loading amplitude equal to the drained bearing capacity and a frequency of 1 Hz (although data not shown). Finally, finite-element simulations of the test setup revealed that for a bucket foundation with a diameter and skirt length of 500 mm the boundaries of the pressure tank effect on the bearing capacity and underestimated the bearing capacity with 20 %. This finding emphasizes the importance of estimating the boundary effects for each tested foundation.

Acknowledgements

This project was founded by The Danish National Advanced Technology Foundation project, entitled "Cost-effective deep water foundations for offshore wind turbines".

References

Borup, M. and Hedegaard, J. (1995). *Baskarp Sand No. 15: data report 9403*. Geotechnical Engineering Group. PDF for print: 37 pp.

Bransby, M. and Yun, G. (2009). The undrained capacity of skirted strip foundations under combined loading. *Géotechnique*, 59(2):115–125.

Byrne, B. and Houlsby, G. (2004). Experimental investigations of the response of suction caissons to transient combined loading. *Journal of Geotechnical and Geoenvironmental Engineering ©ASCE*, 130(3):240–253.

DGF's Laboratoriekomité (2001). *Laboratoriehåndbogen*. Danish Geotechnical Society. ISBN 87-89833-12-0.

Gourvenec, S. (2008). Effect of embedment on the undrained capacity of shallow foundations under general loading. *Géotechnique*, 58(3):177–185.

Holtz, R.D., K. W. S. T. (2001). *An Introduction to Geotechnical Engineering*. PEARSON, 2nd edition. ISBN-13 978-0-13-701132-2,.

Ibsen, L. (2008). *Implementation of a new Foundations Concept for Offshore Wind Farms*, pages 19–33. Norsk Geoteknisk Forening. Keynote: NGM 2008.

Ibsen, L., Hanson, M., Hjort, T., and Thaarup, M. (2009). Mc-parameter calibration of baskarp sand no. 15. *DCE Technical Report*, (62).

Ibsen, L. B., Barari, A., and Larsen, K. A. (2014). Calibration of failure criteria for bucket foundations on drained sand under general loading. *Journal of Geotechnical and Geoenvironmental Engineering ©ASCE*, 140(7):1–16.

Kelly, R., Houlsby, G., and Byrne, B. (2006a). A comparison of field and laboratory tests of caisson foundations in sand and clay. *Géotechnique*, 56(9):617–626.

Kelly, R., Houlsby, G., and Byrne, B. (2006b). Transient vertical loading of model suction caissons in a pressure chamber. *Géotechnique*, 56(10):665–675.

Larsen, K. (2008). *Static Behaviour of Bucket Foundations: Thesis submitted for the degree of Doctor of Philosophy*. PhD thesis, Aalborg University, Denmark. Vol. 1: Static Behaviour of Bucket Foundations Vol 2: Static Behaviour of Bucket Foundations : test results from laboratory tests.

Nielsen, S. K., Ibsen, L. B., Sørensen, K. W., and Shajarati, A. (2013). Undrained cyclic behaviour of dense frederikshavn sand. *The Proceedings of the Twenty-third (2013) International Offshore and Polar Engineering Conference*, 2:518–525.

Zhu, B., Byrne, B., and Houlsby, G. (2013). Long-term lateral cyclic response of suction caisson foundations in sand. *Journal of Geotechnical and Geoenvironmental Engineering ©ASCE*, 139(1):73–83.

Paper C

Dynamic behaviour of mono bucket foundations subjected to combined transient loading

Søren Dam Nielsen
Lars Bo Ibsen
Benjaminn Nordahl Nielsen

The paper has been published in
V Meyer (red.), Frontiers in Offshore Geotechnics III proceedings of the third international symposium on frontiers in offshore geotechnics (isfog 2015), oslo, norway, 10-12 june 2015. vol. 1, C R C Press LLC, London , s. 313-318.

The layout has been revised

Abstract

This article presents the results from small scale testing, investigating the effect of transient combined loading of a bucket foundation. The tests are performed inside a pressure tank at Aalborg University, Denmark. The bucket foundation was installed in dense water saturated sand and transient loads were applied. The loading rate ranges from very slow, giving a drained response, to very fast, giving an undrained response. A factor of 25 was found between the drained and undrained bearing capacity.

INTRODUCTION

Locations, for new offshore wind farms, have typically greater water depths than locations for already installed wind farms. This is due to a limited number of sufficient locations near shore with relatively shallow waters. As the water depths increase for offshore wind farm sites, the relative cost of the foundation and the total cost of the offshore wind turbine increases. Therefore, optimisation of the foundation would lower the total cost of offshore wind energy. One new foundation solution for offshore wind turbines is the mono bucket foundation, see Figure C.1, which is feasible for water depths between 0 to 55 meters.

During the design of the foundation, the ultimate bearing capacity has to be determined, based on estimated extreme loads. Offshore, extreme load conditions could arise during a storm, where the tower of the wind turbine is exposed to large waves, which might be breaking. These waves induce large loads acting over a relatively small time interval. Therefore, an impact from such a wave may lead to partly drained or even a fully undrained response of the mono bucket foundation, which in dense sand will lead to an increase in the bearing capacity.

Typically, sand at offshore locations in the North Sea is dense and has a dilative behaviour. When saturated dense sand is sheared under undrained conditions, the soil attempts to dilate which creates a negative pore pressure and thereby increases the strength of the soil. The limit for how much the pore pressure can decrease is governed by the cavitation pressure of the pore water in the soil Mcmanus and Davis (1997) and Nielsen et al. (2013). The cavitation pressure is the sum of the atmospheric pressure and the hydrostatic pressure from the water. The parameters affecting whether the response of the soil is drained, partly undrained or fully undrained, are the loading rate, permeability of the soil and the seepage.

Previous research on mono bucket foundations has primarily been focusing on the drained static behaviour, e.g Ibsen et al. (2014), Byrne and Houlsby (2004). For the drained long term behaviour of mono bucket foun-

dations in sand, a cigar shaped yield surface is formulated, in the horisontal, vertical and moment load space by Ibsen et al. (2014). When it comes to the undrained behaviour of a bucket foundation in sand, no such formulation exists, and the experimental research is also limited. Bransby and Yun (2009) have made numerical simulations combined with analytical solutions to investigating failure mechanisms for the bucket foundation. Foglia et al. (2013) has previously investigated transient loading of the bucket foundation, where drained and partly drained behaviour was obtained. However, a fully undrained response of the bucket was never achieved.

This article investigates the dynamic behaviour of a bucket foundation.

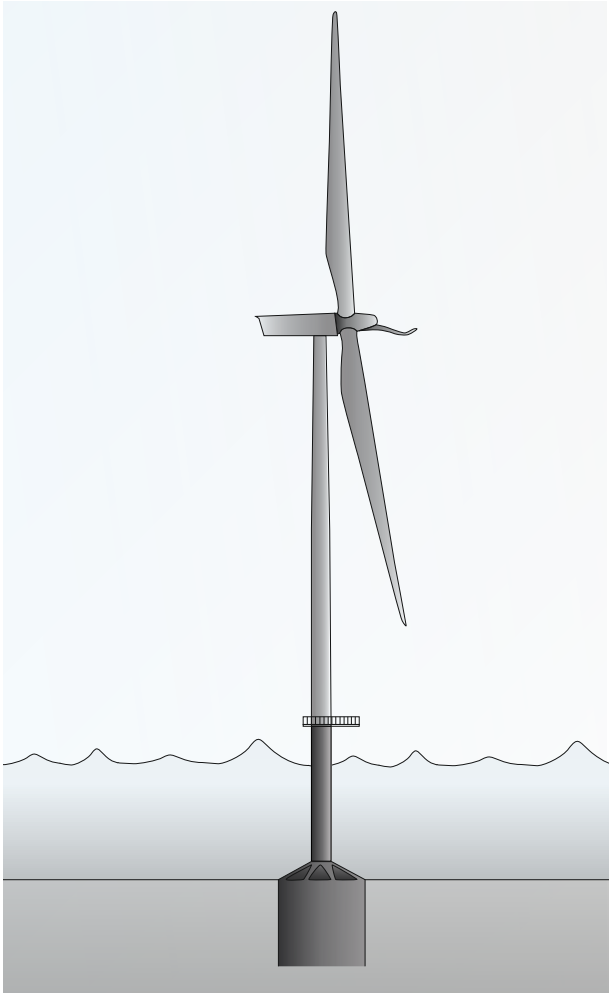

Fig. C.1: Offshore wind turbine installed on a bucket foundation.

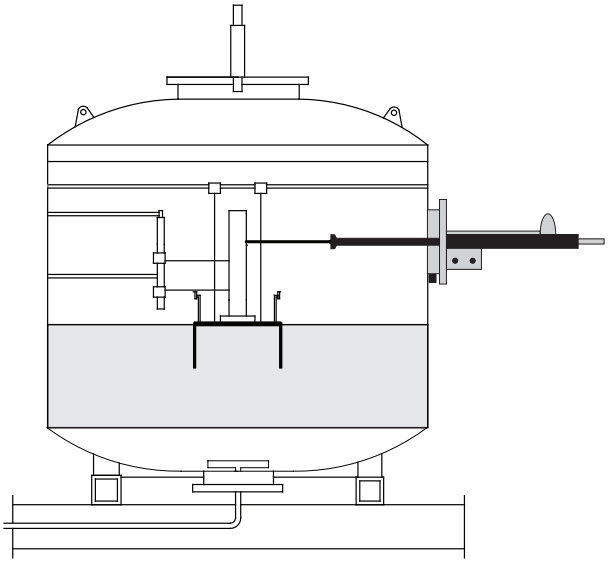

Fig. C.2: Pressuretank, in which the test is conducted. On the right side of the pressure tank the hydraulic actuator is mounted. Inside the pressure tank a layer of 0.6 m of sand is placed (grayhatched area) in which the bucket foundation is installed.

The research takes its basis in small scale laboratory tests, performed in the geotechnical laboratory at Aalborg University, Denmark. Each test was performed with different loading rates in the range between drained and undrained behaviour. During testing pore pressures along the in- and outside of the skirt were measured. For low loading rates, no pore pressure was built up, and thereby the drained behaviour was found. Increasing the loading rate induced a larger and larger generation of negative pore pressure. At a given rate the pore pressure reached a limit and at this limit, the undrained bearing capacity was found.

TEST SETUP

The test set up used for the presented research is a pressure tank which also has been used by Foglia et al. (2013), but as explained earlier fully undrained conditions were never met. Consequently, the testing facility has been improved by the installation of a new actuator with a longer length of stroke. All experiments in this research were conducted inside a steel pressure tank, see Figure C.2 with inner dimensions of: diameter of 2.1 meter and a maximum height of 2 meters. The test medium consists of 0.6 m of water saturated Aalborg University Sand No. 1, which has a maximum and minimum void ratio of 0.86 and 0.55, respectively, determined according to Danish Standard

DGF's Laboratoriekomité (2001). The water level is 6-7 cm above the sand, to insure fully saturated conditions. The sand is vibrated to a relative density, R_d, at 90 %. The instrumentation is also shown in Figure C.2. On the right side of the pressure tank, the hydraulic actuator is mounted which is connected to a tower on top of the bucket via a steel wire. Inside the pressure tank, a steel frame is placed on which displacements transducers are mounted: two for horisontal and two for vertical displacements.

All tests are performed with a small scale bucket foundation with a diameter, D, of 0.50 m and a skirt length, d, of 0.25 m. In Figure C.3, the bucket is sketched and positions of the displacements transducers are shown. As noted, both vertical and horisontal displacements are measured in two positions.

Pore pressures are measured in 13 positions, see Figure C.4: One position in the center below the lid, six on the skirts inside and six on the skirts outside. Outside the positions in the skirts are $1/3d$, $2/3d$ and d, whereas inside the positions are right under the lid, $1/3d$ and $2/3d$. Hereof, one half is positioned on the front and the other half is positioned at the back. The

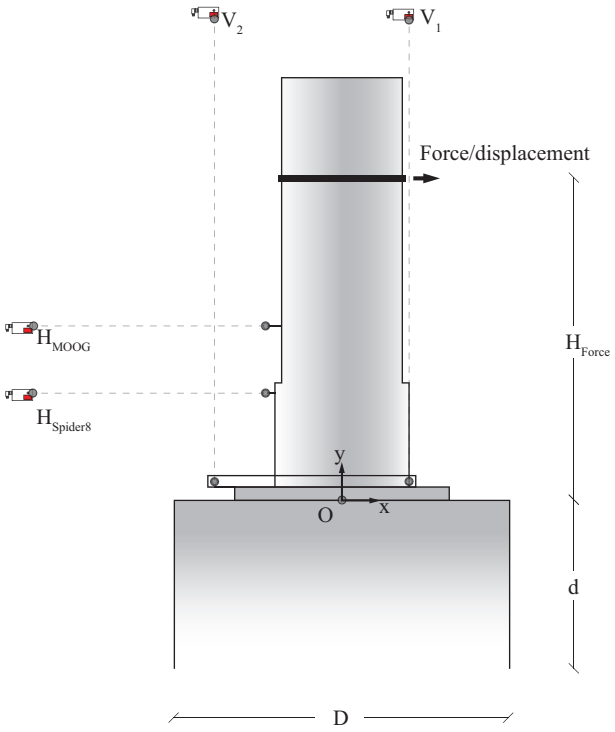

Fig. C.3: Test setup including small scale bucket foundation, attack point for force/displacement and displacement measuring system.

Table C.1: Dynamic test programme for bucket foundations. ** Control value for the actuator velocity. ** Actual rotational speed based on measurements.*

Test No.	d/D	Loading rate* [mm/s]	Rotational speed** [°/s]
Prj1304-H01	0.5	0.1	0.1
Prj1304-H02	0.5	1.0	0.9
Prj1304-H03	0.5	10	8.8
Prj1304-H04	0.5	50	32.1
Prj1304-H05	0.5	100	81.8
Prj1304-H06	0.5	200	122.6

front refers to the positions closest to the actuator and the back the positions furthest away. A drawing of the positions is given in Figure C.4. All tests were conducted with a total overburden pressure of 200 kPa, and taking into account the atmospheric pressure, corresponding to a total pressure of approximately 300 kPa.

Test programme

The test programme includes six tests with different loading rates and is listed in Table C.1. All tests were regulated by the speed of the actuator which is given a control signal, which in Table C.1 is named Loading rate. Increasing resistance from the foundation against rotation complicates the system control of the actuator and the target speed might not be possible to reach. Therefore, the actual rotational speed is calculated based on the measured displacements.

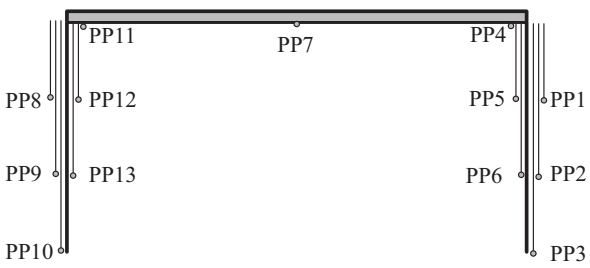

Fig. C.4: Positions of pore pressure measurements on the small scale bucket foundation.

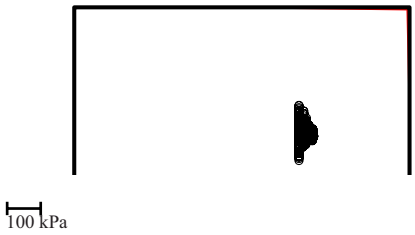

Fig. C.5: Maximum pore pressure build up during test Prj1304-testH01, with an actuator speed of 0.1 mm/s listed in Table C.1. The Figure shows, that no pore pressure developed during the test. Hence, a drained response.

DYNAMIC EFFECTS OF BUCKET FOUNDATION

In this section, the test results will be presented. Pore pressure will be given a positive sign and suction will refer to negative pore pressures. The main results from the tests are given in Table C.2

As all tests were performed with an overburden pressure of 200 kPa, the absolute pore water pressure is 300 kPa (ignoring the tiny hydraulic pressure). Therefore, when the pore water pressure is reduced by 300 kPa, cavitation occurs. When this phenomenon occurs, the water changes from a liquid phase into a gas phase, i.e. boiling. At 100 kPa, the water starts boiling at 100 °C and for 20 °C the water starts boiling at a pressure of a few kPa. When cavitation is present, the pore pressure has reached a minimum level, and ultimate strength of the soil is reached. Table C.2 provides an overview of the displacements and resistance of the foundation. It is seen that a positive vertical translation is found, indicating an upward movement of the bucket foundation during testing. This upward translation along with the dilative behaviour of the soil will generate suction during undrained loading conditions.

Pore Pressure Development

During testing, the pore pressures were measured in order to indicate the drainage conditions, i.e. whether the soil response is drained, partly drained or fully undrained. Three tests are chosen for showing examples of the observed behaviour of the foundation. The examples are shown in Figures C.5, C.6 and C.7. In the Figures, the bucket foundation is depicted and the filled area shows the maximum measured suction during a test. In the Figures, a scale of 100 kPa is provided. It should be repeated that suction is negative pore pressure, and the Figures therefore show that only negative pore pressure is generated during testing. In Figure C.5, the test with an actuator

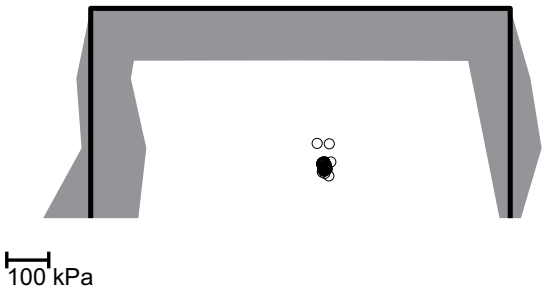

Fig. C.6: Maximum pore pressure build up during test Prj1304-testH04, with an actuator speed of 50 mm/s listed in Table C.1. The Figure shows, that some pore pressure developed during the test, but cavitation was not reached. Hence, a partly drained response.

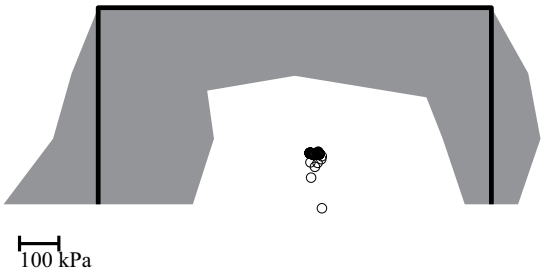

Fig. C.7: Maximum pore pressure build up during test Prj1304-testH05, with an actuator speed of 100 mm/s listed in Table C.1. The Figure shows, that pore pressure developed during the test and reached the cavitation pressure. Hence, a completely undrained response.

speed of 0.1 mm/s is depicted. The bucket cross section is sketched, and pore pressure development is shown as gray hatched areas. Right to the center of the bucket cross section a black area is shown. The area consists of circles which all indicate the calculated rotation point for every measurement.

The slowest test at 0.1 mm/s, Figure C.5, developed almost no pore pressure, indicating a drained situation. By increasing the loading rate to 1 mm/s, some negative pore pressure, or suction, were developed and increasing the loading rate to 10 mm/s the developed suction were increased even more.

In Figure C.6, the loading rate is increased to 50 mm/s and the created suction has increased significantly. Along the skirts, only suction is created, both on the outside and inside of the foundation and under the lid. These measurements are illustrated by the filled area indicating the magnitude of the maximum suction and the scale shows the absolute value. From Figure C.6, it is seen that the maximum suction is created inside on the left part

of the skirt $2/3d$ from the lid, corresponding to PP13 in Figure C.4. This response is from the back moving upwards in contrast to the front, which moves downwards. The upward movement has an expansive effect, and the downward movement has a contractive effect on the soil. At the back of the foundation, the dilative effect will therefore be enhanced by rotation whereas the front will have a reduction in dilative effect. As the pore pressure development is dependent on the dilative behaviour, it could also be expected that the maximum suction were created in the back part of the skirt where the movement enhances the dilative behaviour and the upward translation of the bucket.

By further increase in loading rate, the maximum measured suction reaches 300 kPa, indicating cavitation and therefore also indicating that the ultimate undrained bearing capacity is reached for this test setup. This postulate is proved by conducting another test with an even faster loading rate at 200 mm/s showing the exact same result, where the foundation fail due to cavitation of the pore water. The induced suction is shown in Figure C.7, and by comparing with Figure C.6, the patterns of the suction are the same. Therefore, PP13 in Figure C.4 is where the maximum suction of 300 kPa is reached. Based on these observations, the ultimate bearing capacity, for this setup, is reached when cavitation occur in just one position. If the total overburden is increased an increase in bearing capacity is also increased.

Drained and Undrained Bearing Capacity

As mentioned previously, indications of when the ultimate bearing capacity is reached are measured. Looking at Figures C.8, C.9 and C.10 which show the applied force and pore pressures as functions of rotation of the bucket, the needed force for a given rotation is highly dependent on the created suction. The larger created suction, the larger force is needed to rotate the bucket a certain amount of rotations. The drained response is shown in Figure C.8 and a maximum resistance of 250 Nm is measured. As mentioned earlier, no suction is developed when drained response is obtained. At a loading rate of 50 mm/s, the suction increases, and thereby also the resistance against rotation to 3105 Nm, see Figure C.9. The ultimate undrained bearing capacity is reached at a loading rate of 100 mm/s, and as the suction did not increase further by increased loading rate, it means that a maximum resistance against rotation is measured to 6320 Nm, see Figure C.10.

The force-rotation curve for all tests is shown in Figure C.11 illustrating how the resistance increases with increasing loading rate and rotation. It is observed that maximum resistance is reached after a rotation of 5-8 degrees.

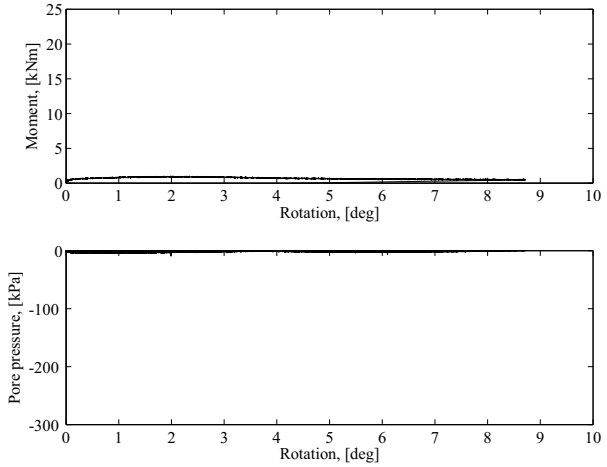

Fig. C.8: Pore pressure build up and moment as a function of applied rotation, from the test with an actuator speed of 0.1 mm/s listed in Table C.1. No pore pressure build up is measured. Hence, a drained response.

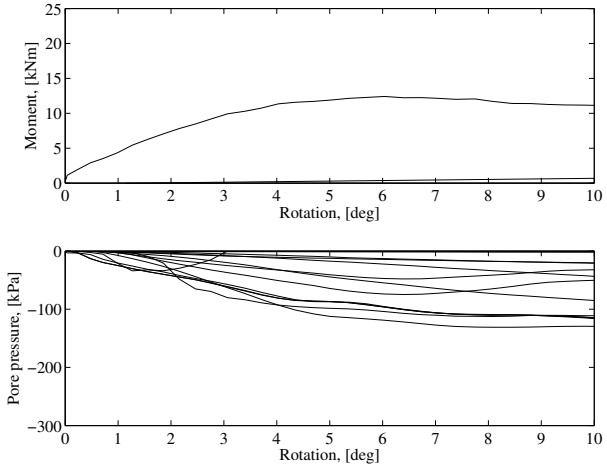

Fig. C.9: Pore pressure build up and moment as a function of applied rotation, from the test with an actuator speed of 50 mm/s listed in Table C.1. Some pore pressure build up is measured, in the range between zero and the cavitation level. hence, a partly drained response.

Rotation and translation

From the measurements of displacement, the point of rotation is calculated. The rotation points are shown as circles in Figures C.5, C.6 and C.7. As mentioned, right to the centre of the bucket cross section a black area is shown. The area consists of circles, which all indicate the calculated rotation

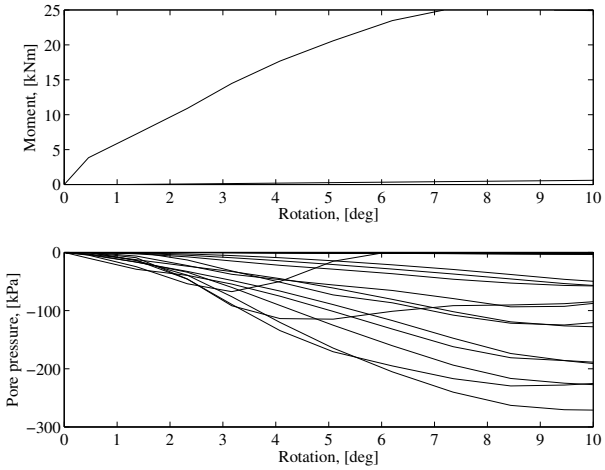

Fig. C.10: Pore pressure build up and moment as a function of applied rotation, from the test with an actuator speed of 100 mm/s listed in Table C.1. The measured pore pressure build up reaches the limit for cavitation. Hence, an undrained response.

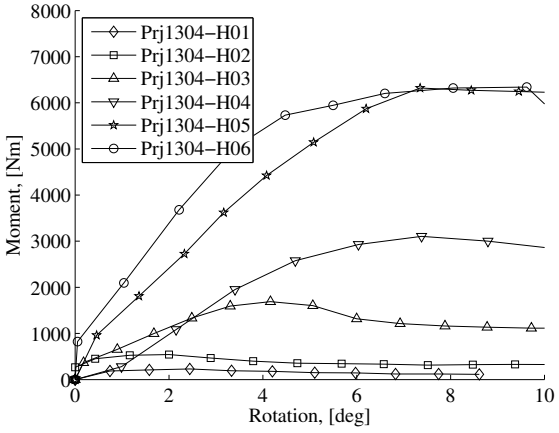

Fig. C.11: Force-rotation curve for all tests.

point for every measurement. The deviation is largest in the beginning of the test and as the rotation increases, the rotational movement of the bucket becomes more consistent and the change in rotational points are decreased.

Another thing to notice is the rotation points, which are marked with black circles in Figures C.5, C.6 and C.7 are moving towards the vertical centreline of the bucket foundation, as the behaviour changes from a drained to a more and more undrained behaviour. One possible explanation could be that the failure mechanism for drained conditions is governed by a logarith-

Table C.2: *Vertical and horisontal translation and rotation of the bucket foundation along with the ultimate bearing capacity. * Control value for the actuator velocity. ** Actual rotational speed based on measurements*

Test No.	Loading rate* V [mm/s]	Rotational speed** $\dot{\theta}$ [°/s]	Vertical translation v [mm]	Horisontal translation h [mm]	Rotation θ [°]	Capacity M_{ult} [Nm]
Prj1304-testH01	0.1	0.1	-	-	-	250
Prj1304-testH02	1.0	0.9	1.9	41.9	12.9	560
Prj1304-testH03	10	8.8	2.4	41.6	12.6	1700
Prj1304-testH04	50	32.1	2.1	38.5	11.5	3105
Prj1304-testH05	100	81.8	2.6	40.3	12.3	6333
Prj1304-testH06	200	122.6	2.8	41.3	11.2	6342

mic spirit, whereas for undrained conditions a circular shape of the slip plane is governed. Hence, the point of rotation for undrained conditions is closer to the vertical symmetry line of the bucket foundation than the rotation points in the drained situation.

Looking at the calculated rotation points, a trend indicates that as the response goes from drained to undrained behaviour, the rotation points move horisontally towards the centreline of the bucket. This also indicates a change in failure mechanism when the response gets closer to undrained.

Normalisation

Figure C.12 shows the resistance against rotation normalised with respect to the drained capacity as a function of rotation. The Figure indicate a factor of 25 between the drained and undrained bearing capacity. The increase in rotational resistance is already explained by the induced suction, which increase the effective stresses in the soil, and thereby the strength of the soil, resulting in an increased bearing capacity of the foundation.

In Figure C.13, the normalised bearing capacity is shown as a function of normalised impact time, $t_{i,norm}$. The bearing capacity is normlised with the drained bearing capacity. The impact time is the time interval from zero to maximum resistance, and is normalised with the ratio between seepage in

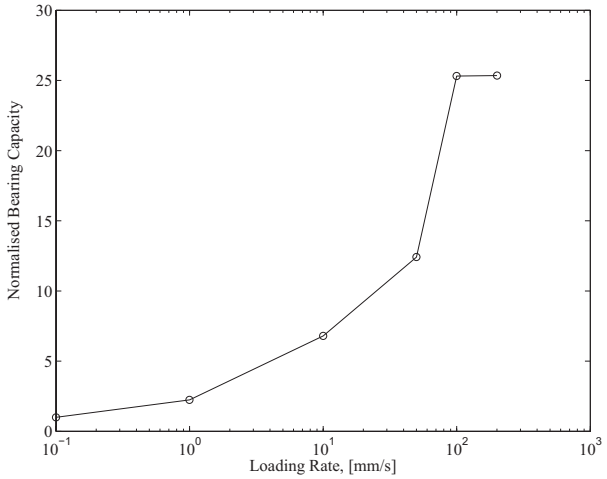

Fig. C.12: Normalised bearing capacity as a function of loading rate.

prototype, L_p, which is assumed to be 30 m, and seepage in model, measured to 1 m. From the Figure it is seen that an impact time less than 54 seconds will lead to undrained response of the upscaled foundation. Furthermore, an impact time of approximately 7620 seconds, i.e. 127 min, is needed in order to obtain the drained bearing capacity. In between 1 minute and 127 minutes, partly drained response is measured.

RESPONSE OF REAL SCENARIOS

Direct scaling of the obtained results to real size structures is not possible, as a range of parameters does not scale equally. The most important parameters are: pressure distribution and stress level.

At low stresses, the friction and dilation angles are higher compared to higher stress levels. A higher dilation angle will introduce more dilation, which will result in larger changes in pore pressure and along with the friction angle, a relatively higher bearing capacity might be measured, compared to an upscaled foundation. Hence, experiments at high stress level could be suggested for future work.

Other scale effects might also influence the results. Parameters which are unscaled are the size of the sand grains and the water itself, resulting in an unscaled hydraulic conductivity.

In Figure C.13 the impact time is normalised with the ratio between seepage length in prototype and model, L_p/L_m = 30, the impact time to produce completely undrained response of a prototype foundation is 54 s. For off-

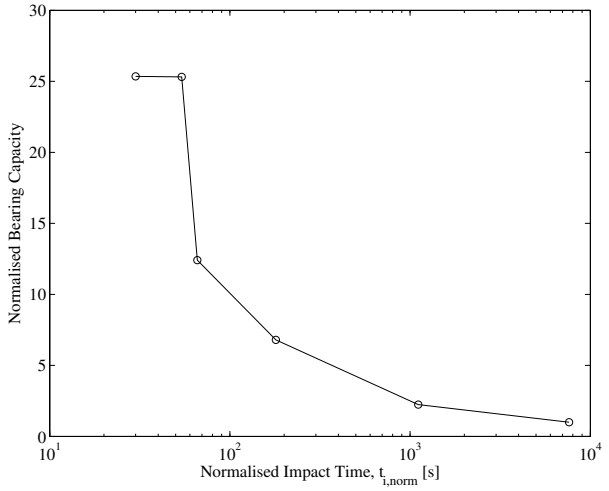

Fig. C.13: Normalised bearing capacity as a function of impact time. The bearing capacity is defined as the maximum force and is normalised with the drained bearing capacity. The impact time is the time it takes to go from 0 to maximum resistance. The abscissa is calculated as: $t_{i,norm} = t_{impact} L_p / L_m$.

shore conditions where wave periods typically are in the range 10-14 s, the impact time for a non-breaking wave can conservatively be estimated to half the period, i.e. 5-7 s. For a real size bucket foundation with a skirt length of 15 m, the seepage length is estimated to 30 m and undrained behaviour is to be expected for a prototype of this size.

Although it is not believed that it is possible to scale the results directly into real size structures, the tendency will still apply for real size bucket foundations installed in dense sand.

CONCLUSION

The rate effect of combined loading of small-scale bucket foundations has been investigated. The results show that suction is created both on the inside and outside of the skirt. This behaviour is caused by the dilative behaviour of the dense sand, and it is shown that the undrained bearing capacity is limited by cavitation, and thereby the initial water pressure. For real structures, the water pressure will be dependent on the water depth, meaning that the greater water depths, the larger undrained bearing capacity.

From Figure C.11 it is seen that the bearing capacity increases with the loading rate, and from Figures C.5, C.6 and C.7 it is shown that the measured suction is also increased, meaning that the response becomes closer to undrained behaviour, as the loading rate increases. It is measured that

the undrained bearing capacity is 25 times the drained bearing capacity, see Figure C.12. It is also found, that rather large deformations are needed in order to reach the undrained bearing capacity. Finally, in Figure C.13 a graph indicating when a real size bucket would have undrained, partly drained and completely drained response is provided.

References

Bransby, M. and Yun, G. (2009). The undrained capacity of skirted strip foundations under combined loading. *Géotechnique*, 59(2):115–125.

Byrne, B. and Houlsby, G. (2004). Experimental investigations of the response of suction caissons to transient combined loading. *Journal of Geotechnical and Geoenvironmental Engineering ©ASCE*, 130(3):240–253.

DGF's Laboratoriekomité (2001). *Laboratoriahåndbogen*. Dansk Geoteknisk Forening.

Foglia, A., Ibsen, L., Nielsen, S., and Mikalauskas, L. (2013). A preliminary study on bucket foundations under transient lateral loading. *The Proceedings of the Twenty-third (2013) International Offshore and Polar Engineering Conference*, 2:465–471.

Ibsen, L. B., Barari, A., and Larsen, K. A. (2014). Calibration of failure criteria for bucket foundations on drained sand under general loading. *Journal of Geotechnical and Geoenvironmental Engineering ©ASCE*, 140(7):1–16.

Mcmanus, K. J. and Davis, R. O. (1997). Dilation-induced pore fluid cavitation in sands. *Géotechnique*, 47(1):pp. 173–177.

Nielsen, S. K., Ibsen, L. B., Sørensen, K. W., and Shajarati, A. (2013). Undrained cyclic behaviour of dense frederikshavn sand. *The Proceedings of the Twenty-third (2013) International Offshore and Polar Engineering Conference*, 2:518–525.

Paper D

Transient Loaded Bucket Foundations in Saturated Dense Sand - a Demonstration of The Boot Effect

Søren Dam Nielsen
Lars Bo Ibsen
Benjaminn Nordahl Nielsen

The paper has been submitted for publication in
Journal of Geotechnical and Geoenvironmental Engineering

The layout has been revised

Abstract

The mono bucket foundation is a cost-effective foundation for offshore wind turbines. During a storm these foundations are exposed to large wave loads with a short duration. This paper investigates the effect of increasing loading rate on the bearing capacity for two mono bucket foundations installed in dense sand inside a pressure tank. One foundation has an aspect ratio, skirt length (L) relative to the diameter (D), L/D of 0.5 and the other a ratio of 1.0. The foundations are brought to failure with varying loading rates, resulting in drained, partly drained up to undrained behaviour of the foundation. Increases in bearing capacity are observed as the loading rate increases. This is caused by a combination of dilative soil behaviour and the suction created by the upward movement. This has been defined as *the boot effect*. For the mono bucket foundations, the boot effect resulted in an increased bearing capacity that was measured 18 to 25 times higher than the drained capacity. Furthermore, the stiffness also increases with increasing loading rate and thereby the boot effect. The stiffness of the partly drained response is measured up to four times higher compared to drained behaviour.

Key Words: Mono bucket foundation, undrained behaviour, transient loading, the boot effect.

Introduction

Locations for new offshore wind farms, have typically greater water depths than locations for already installed wind farms. This is seen in the chosen positions for the development of offshore wind in the United Kingdom, which include for example Dogger Bank and Horn Sea, Renewable UK (2015). As the water depths increases for offshore wind farm sites, the relative cost of the foundation and the total cost of the offshore wind turbine increases. A cost-effective foundation is the mono bucket foundation, Houlsby et al. (2005) and Ibsen (2008) and is illustrated in Figure D.1. During the design of the foundation, the ultimate bearing capacity has to be determined, based on estimated extreme loads. Offshore, extreme load conditions often arise during a storm, where the shaft of the mono bucket foundation is exposed to large waves, which might be breaking. These breaking waves induce large loads with a short duration. Therefore, an impact from such a wave may lead to partly undrained or even a fully undrained response of the mono bucket foundation, which in dense sand will lead to an increase in bearing capacity.

Typically, sand on offshore locations in the North Sea is dense, Byrne and

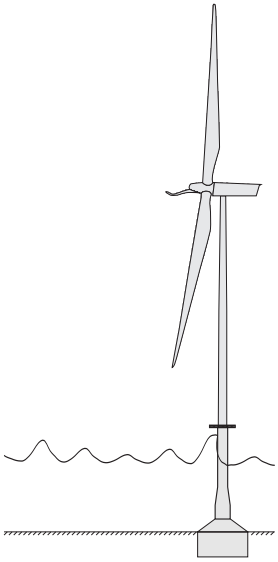

Fig. D.1: Mono bucket foundation supporting an offshore wind turbine foundation.

Houlsby (1999) and Houlsby et al. (2005). When saturated dense sand is sheared under undrained conditions, the soil attempts to dilate, which creates a negative excess pore pressure and thereby increases the strength of the soil. The cavitation pressure of the pore water in the soil governs the limit for how much the excess pore pressure can decrease Nielsen et al. (2013). The cavitation pressure is the sum of the atmospheric pressure and the hydrostatic pressure, and will therefore increase with water depth. The parameters affecting whether the response of the soil is drained, partly undrained or fully undrained, are the loading rate, permeability of the soil and the seepage length.

Previous research on mono bucket foundations, has primarily focused on the drained static behaviour, e.g. Byrne and Houlsby (2004), Larsen (2008), Ibsen et al. (2014) and Foglia et al. (2015). For the drained long-term behaviour of mono bucket foundations in sand, a cigar-shaped yield surface is formulated in the space formed by the horizontal, the vertical and the moment load. When it comes to the undrained behaviour of a bucket foundation in sand, no such formulation exists and the experimental research is also limited. Gourvenec (2008) and Bransby and Yun (2009) made numerical simulations combined with analytical solutions in investigating failure mechanisms for the bucket foundation.

Foglia et al. (2013) previously investigated transient loading of the bucket foundation where drained and partly undrained behaviour were obtained. But, a fully undrained response of the bucket was never achieved.

This paper presents results from a series of small-scale tests on two different buckets, installed in dense sand. The foundations had a diameter (D) of 500 mm and skirt lengths (L) of 250 mm and 500 mm. Hence aspect ratios L/D of 0.5 and 1.0. The behaviour during transient loading is investigated, and the response is measured from drained and partly drained to fully undrained conditions. A significant increase in bearing capacity is observed with increasing loading rate which is caused by dilative soil behaviour and the boot effect.

Theory

The suction measured in the experiments are created by a combination of the dilative behaviour of the sand and the movement pattern of the bucket foundation. The suction created by the movement of the mono bucket foundation is called *The Boot Effect*. The excess pore pressure (Δu) is then a sum of the two contributions

$$\Delta u = \Delta u_{boot} + \Delta u_{dilation} \tag{D.1}$$

Δu_{boot} is the excess pore pressure (negative) from the boot effect and $\Delta u_{dilation}$ is the excess pore pressure from the soil response (negative for dilative soils).

"The Boot Effect"

"*The Boot Effect*" is the suction, and thereby additional strength, created by the movement of the bucket. The name is metaphorical and draws the picture of a boot stuck in mud. Pulling out the boot slowly, will release the boot from the mud. Trying to pull the boot out with a rapid movement, the boot will barely move and will still be stocked in the mud.

The same behaviour is seen when testing the mono bucket foundation in the lab. A more scientific explanation of the movement is based on the yield surfaces developed by e.g. Byrne and Houlsby (1999), Ibsen et al. (2014) and Ibsen et al. (2015). An illustration of a yield surface in the $M/D - H$ plane is given in Figure D.2 for constant vertical load. The yield surface is only for illustrative purpose and the relative sizes between them are not comparable to real foundations. The figure shows a yield surface for a footing with aspect ratio $L/D = 0$ (no skirts). By increasing the skirt length, and thereby the aspect ratio, the yield surface rotates, Ibsen et al. (2014). This involves a change in the movement pattern. In the presented test setup the loading goes in the direction $(M/D)/H = 1$, as illustrated in Figure D.2. Following this loading path until the yield surface is reached, it is seen that the normal vector to the yield surfaces have different directions. As the bucket movement

is described by the normal to the yield surface an increasing skirt length will lead to less rotation of the foundation compared to horisontal movement.

Looking at the yield surface in $H - V$ space illustrated in figure D.3, it is seen that for low and constant vertical loads the normal to the yield surface is pointing left. Hence, even though the vertical load is downwards the movement will be upwards.

Therefore, when the loads on a mono bucket structure is dominated by horisontal and moment loading, the center of the lid, see Figure D.4, will move horisontal in the direction of the horisontal load and rotate in the direction of the moment. In any case, the bucket foundation will be exposed to a vertical load from the self weight. However, even though the vertical force is downwards, the vertical movement for light structures are upwards.

The uplift will create a tiny space between the bucket lid and the soil surface, as illustrated in Figure D.4. In drained conditions no excess pore pressure is generated and water will flow into the bucket and fill out the gap (square hatched area in Figure D.4). Therefore, no suction will be created, and no boot effect will be present. When the load duration becomes so short that the surrounding water will be unable to dissipate, undrained conditions are created. In this situation, a negative excess pore pressure will be generated. The negative excess pore pressure will create a downward force, counteracting the upward movement. A rapid load, will therefore lead to an upwards movement, resulting in suction in the pore water. Hence the effective stresses and thereby the bearing capacity increases. The shorter load duration the more suction is generated.

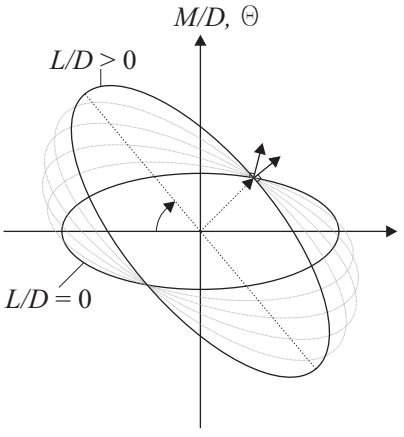

Fig. D.2: Illustrative yield surfaces in $M/D - H$. For increasing skirt length the yield surface is rotated and expands.

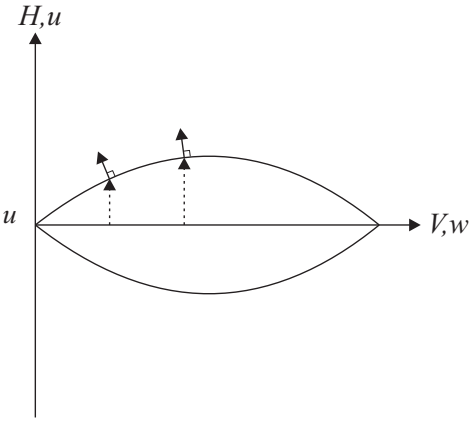

Fig. D.3: Illustrative yield surface in $H - V$ space.

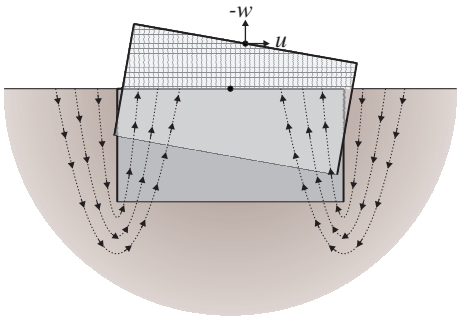

Fig. D.4: Illustration of the boot effect.

Table D.1: Initial stress conditions for the dynamic triaxial tests on Aalborg University Sand No. 1.

Test	p'_0	q_0	u_0	p_0
Test A	100 kPa	0 kPa	200 kPa	300 kPa
Test B	200 kPa	0 kPa	100 kPa	300 kPa

Dilative soil behaviour

Firstly, the undrained soil behaviour has been investigated in order to get a better understanding of the behaviour. The study includes undrained triaxial tests (Test A and Test B) on Aalborg University Sand No. 1, with a relative density of 90 %, Nielsen et al. (2013). Table D.1 provides the initial stress conditions for Test A and Test B. Both tests are isotropic consolidated to a level of total mean stress at 300 kPa, but with different combinations of pore pressure and effective mean stresses, see Table D.1.

Figure D.5 shows the stress strain curve for the two tests and that they have the same strength. Hence, the shear strength in undrained conditions of the soil and, thereby, the undrained bearing capacity of a foundation depend on the initial total stresses, i.e. the combination of effective stresses and pore pressure.

Figure D.6 shows the deviator stress, q, as a function of mean effective stresses, p'. The figure depicts both the effective (ESP) and total stress paths (TSP): the initial effective stress paths deviate from each other whereas the total stress paths are identical. Thereby another indication of the fact that the shear strength of a dense soil in undrained conditions is dependent on the total stress level. The point at which the total and effective stress paths intersect the failure envelope is different, see Figure D.6. The difference on the x-axis is the cavitation pressure, which is accounted for in the effective stress path and not in the total stress path. Hence, adding the cavitation

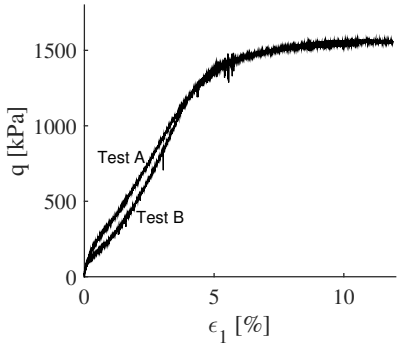

Fig. D.5: $\epsilon_1 - q$ diagram for undrained loaded Aalborg University Sand No. 1. ESP is the effective stress path, and TSP is the total stress path.

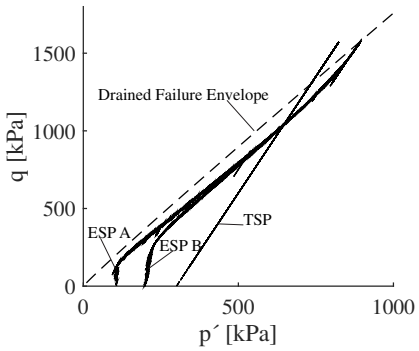

Fig. D.6: $p' - q$ diagram for undrained loaded Aalborg University Sand No. 1.

pressure, which is equal the atmospheric pressure ($\approx$ 100 kPa), the same strength can be found both from the effective and the total stress paths.

These tests show that the shear strength in undrained conditions is dependent on the combination of effective stress level and the initial pore pressure. Offshore, the initial pore pressure is dependent on the water depth. The higher the water depth, the higher initial pore pressure, and thereby also the higher shear strength in undrained conditions for dilative soils.

Experimental Setup

Nielsen et al. (2016) describes the test setup and procedure in detail. The laboratory tests were conducted on two different bucket foundations with skirt lengths (L) of 250 mm and 500 mm, and both with a diameter (D) of 500 mm, see figure D.7. The bucket foundations will be referred to as the bucket with L/D = 0.5 and L/D = 1.0, respectively. Along the skirts in specifically chosen positions, metal tubes were attached and connected to pressure transducers. In this way, it was possible to measure the pore pressure along the skirts during testing. Figure D.7 illustrates the positions of the measuring points for both buckets. Before installation, the pore pressure measuring system is water saturated in order to prevent plugging of the system.

The test setup consists of a large sealable pressure tank, The Pressure Tank, and is depicted in Figure D.8. It is almost spherical with an internal diameter of 2 meters. Inside the pressure tank, is a layer of water saturated Aalborg University Sand No. 1 where the bucket foundation is installed. The sand is a fine graded sand. The sand is prepared by using a poker vibrator

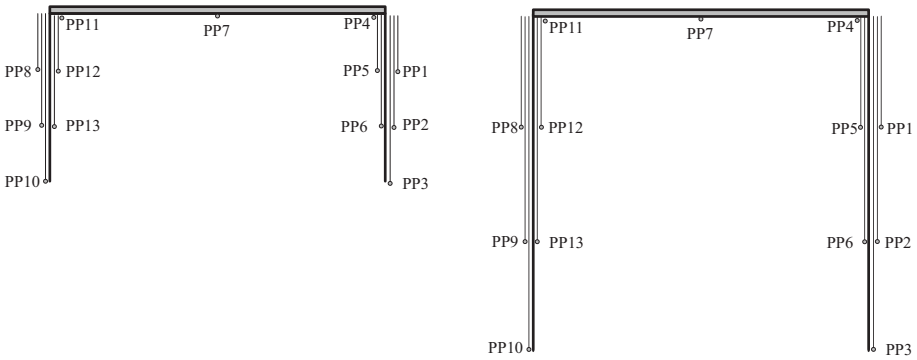

Fig. D.7: Position for pore pressure measurement points on the bucket foundations with $L/D = 0.5$ (left) and $L/D = 1.0$ (right).

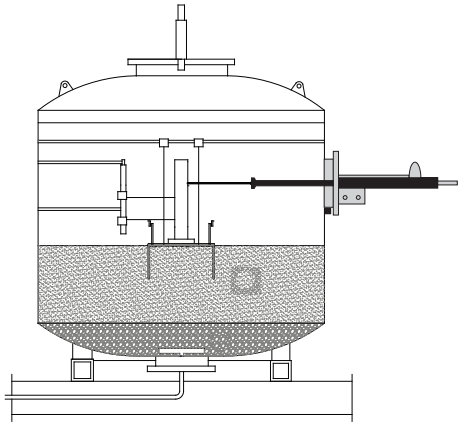

Fig. D.8: The pressure tank

and is vibrated in a specific pattern. After vibration the initial soil conditions are documented, by conducting CPT tests with a laboratory CPT probe described in Larsen (2008). After the foundation is installed, a correct ratio between horizontal force and moment is ensured by mounting a tower on top of the foundation. The tower is then connected to a powerful hydraulic actuator, which can either be force or displacement controlled. The actuator can deliver up to 100 kN and move 0.5 meter in one second. This makes it ideal for testing the transient behaviour of foundations. Two vertical displacement transducers and one horizontal are used to determine the rotation, vertical and horizontal translation.

Before testing, the pressure tank is sealed and the internal pressure is increased. The increased pressure simulates the water depth and thereby the pressure at seabed from the water above it, and also have the effect as

back pressure in a triaxial apparatus. All data is recorded and stored with a sample rate of 1000 Hz.

Detection of Drained and Undrained Behaviour

Drained behaviour is, in general, defined as a situation where all changes in loads are transferred as effective stresses, meaning that no excess pore pressure can develop. Undrained behaviour is defined as the situation where the volumetric strains are zero, $\epsilon_V = 0$. Hence, no water flow is allowed and all changes in loads will be transferred as a change in excess pore pressure. For soils with a contractive behaviour the generated excess pore pressure will be positive, and for dilative soils the excess pore pressure will be negative.

In the experiments, drained behaviour will be detected when no excess pore pressure is building up. An undrained condition is detected when an increase in loading rate does not lead to further changes in the excess pore pressure. This is the conditions which for dilative soils will lead to cavitation.

Test Programme

The test programme includes 12 small-scale tests with two aspect ratios L/D. The two test series on the half ($L/D = 0.5$) and full ($L/D = 1.0$) bucket are listed in Table D.2. The test name consists of either an H or F, referring to either the half ($L/D = 0.5$) or the full ($L/D = 1.0$) bucket, respectively. This is followed by a number counting from one to the final number of tests in a given series.

Table D.2 gives the ratio between the skirt length (L) and the diameter (D). The loading rate is the control signal which the actuator aims after, where the load cell measures whether or not the control signal has been reached. The rotational speed is the actual rotational speed determined by the measurements.

Results

Initial Conditions for Experiments

All tests were conducted with the same initial conditions. The initial condition was investigated by laboratory CPT tests, calibrated against triaxial tests in order to estimate correct parameters for the soil Ibsen et al. (2009). For each experiment, five laboratory CPT tests were performed. Table D.3 lists the relative density and the friction angle from these tests stating the mean values,

Table D.2: Dynamic test programme for bucket foundations. * Control value for the actuator velocity. ** Actual rotational speed based on measurements.

Test No.	L/D	Loading rate* [mm/s]	Rotational speed** [°/s]
H01	0.5	0.1	0.1
H02	0.5	1.0	0.9
H03	0.5	10	8.8
H04	0.5	50	32.1
H05	0.5	100	81.8
H06	0.5	200	122.6
F01	1.0	0.1	0.1
F02	1.0	1.0	0.7
F03	1.0	10	6.8
F04	1.0	50	29.3
F05	1.0	100	46.1
F06	1.0	200	90.9

$\bar{R_D}$ and $\bar{\phi}$, and the standard deviations, σ_{R_D} and σ_ϕ, of both parameters. Due to the low stress levels, the measured friction angles are high.

Bearing Capacity

The measured moments are normalised with the diameter (2R) where R is the radius of the foundation, as suggested by Butterfield et al. (1997). Figures D.9 plots the normalised moment as a function of rotation for all tests on the $L/D = 0.5$ bucket. The figure show, that the resistance against rotation increases with an increasing loading rate. When the loading rate increases, less pore water is able to dissipate. Hence, an increased loading rate will trigger a more undrained response. The undrained response generates negative excess pore pressure, which increases the bearing capacity. Therefore, the resistance against rotation increases with an increasing loading rate, as observed in Figures D.9 and D.10.

In order to give a more general picture of the response, the measured bearing capacities need to be normalised. In Figures D.11 and D.12 the maximum moment from each test in Figures D.9 and D.10 are normalised with the drained bearing capacitynd plotted against the rotational speed. The drained bearing capacity is where no excess pore pressure is generated and is measured to 250 Nm and is the lowest bearing capacity of the tests. The test with the lowest rotational speed then has a normalised bearing capacity of 1.0, and at fully undrained response the bucket has a normalised bearing capacity of 25. This means that the undrained bearing capacity for the experimental set up is measured 25 times larger than the drained bearing capacity.

By increasing the rotational speed beyond 81.8°/s (2^{nd} highest rotational

Table D.3: Average and standard deviation of relative density and friction angle. $\bar{R_D}$ and $\bar{\phi}$ is the mean value of the relative density and the friction angle and σ_{R_D} and σ_ϕ are the associated standard deviations.

Test	$\bar{R_D}$	σ_{R_D}	$\bar{\phi}$	σ_ϕ
H01	87.6	0.9	54.0	0.1
H02	88.6	3.6	54.1	0.5
H03	86.8	5.7	53.8	0.9
H04	90.2	3.2	54.4	0.5
H05	85.4	2.7	53.6	0.4
H06	86.0	2.5	53.7	0.4
F01	89.2	2.1	53.7	0.3
F02	89.6	1.4	54.3	0.2
F03	89.2	2.2	54.2	0.3
F04	89.7	3.3	54.3	0.5
F05	86.4	1.2	53.8	0.8
F06	89.0	4.3	54.2	0.6

speed in Figure D.11), no extra resistance is measured. This indicates that completely undrained response is measured at rotational speeds of 81.8 $^\circ$/s and higher. If undrained response is observed the pore water pressure should reach the cavitation pressure of approximately -300 kPa, which is the sum of the atmospheric pressure ($\approx$ 100 kPa) and the pressure applied inside the pressure tank (200 kPa).

The moment as a function of rotation for the $L/D = 1.0$ bucket, is presented in Figure D.12. The graph shows the same trend, where the bearing capacity of the foundation increases with the loading rate.

In the same manner, the bearing capacities are normalised with the measures drained bearing capacity for the $L/D = 1.0$ bucket. Figure D.12 depicts the normalised bearing capacities as a function of rotational speeds. Compared to Figure D.11, there is no distinct plateau, but undrained response is assumed when the measured excess pore pressure reaches the same level as the undrained tests on the $L/D = 0.5$ bucket. Figure D.12 shows a factor of 18 between the undrained and drained bearing capacity.

Excess Pore Pressure Build-Up

The increase in bearing capacity can be explained by the dilative soil behaviour and the boot effect. In drained conditions, the loading rate is low compared to the seepage and hydraulic conductivity, that no excess pore pressure will be generated during loading. As the loading rate increases, more excess pore pressure is unable to dissipate during loading, and because of the dilative behaviour of the soil and the upward movement of the bucket

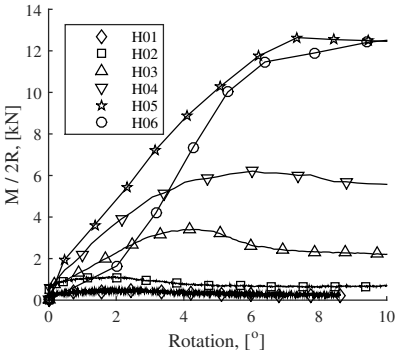

Fig. D.9: Moment normalised with the diameter (2R) as a function of applied rotation for all six tests performed on the $L/D = 0.5$ bucket.

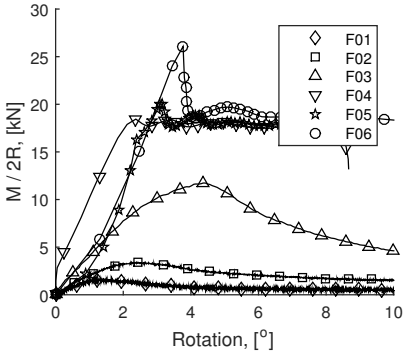

Fig. D.10: Moment normalised with the diameter (2R) as a function of applied rotation for all six tests performed on the bucket with $L/D = 1.0$.

the excess pore pressure is negative. This causes an increase in effective stresses, and thereby a higher bearing capacity. During all tests, only negative excess pore pressure (suction) developed. Hence, maximum suction will be referred to as maximum excess pore pressure, despite the negative sign. Rotational speeds (ω_p) is the average rotational speed until peak resistance of the bucket is reached, which is symbolised by the index p on ω_p.

Figures D.13 to D.24 shows the development of excess pore pressure along the skirts, where linear interpolation has been used between the measuring points (see Figure D.7). The Figures D.13 to D.24 also show the calculated rotation points, which is marked with black circles. Furthermore, the dashed line indicate the cavitation pressure of the pore water. The Figures D.13, D.15, D.17, D.19, D.21 and D.23 show the pore pressure distribution along the skirts on the $L/D = 0.5$ bucket. Figure D.13 shows completely drained behaviour reached at 0.1 °/s, as no excess pore pressure is measured along the skirts. In figure D.15 a very litle excess pore pressure is developed at 0.9 °/s (though it is not visible in the figure). Hence, almost drained behaviour. The Figures D.17, D.19 show some generation of excess pore pressure with speeds of 8.8 °/s and 32.1 °/s. Finally, reaching a maximum in Figures D.21 and D.23 with rotational speeds of more than 81.8 °/s.

Similar results have been obtained by testing the $L/D = 1.0$ bucket. Figures D.14 and D.16 show drained behaviour and almost drained behaviour, with rotational speeds of 0.1 °/s and 0.7 °/s, respectively. Figures D.18, D.20 and D.22 show partly drained response measured at ω_p of 6.8 °/s, 29.3 °/s and 46.1 °/s. Finally, Figures D.24 show undrained response reached at ω_p of 90.7 °/s.

Looking at the pore pressure distribution pattern for the two buckets, a

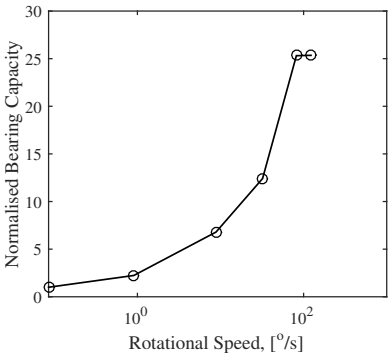

Fig. D.11: $L/D = 0.5$. Normalised bearing capacity as a function of rotation. The maximum moments measured during each test in Figure D.9 are plotted as a single point, normalised with the maximum moment in the drained test, i.e. the test where the minimum moment was measured.

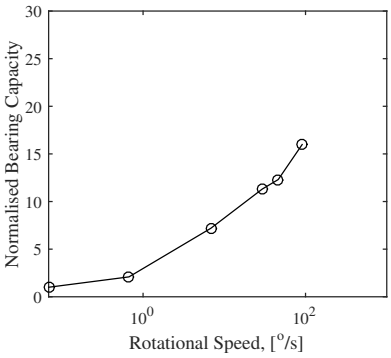

Fig. D.12: $L/D = 1.0$. Normalised bearing capacity as a function of rotation. The maximum moments measured during each test in Figure D.10 are plotted as a single point, normalised with the maximum moment in the drained test, i.e. the test where the minimum moment was measured.

different pattern is seen on the $L/D = 0.5$ bucket and the $L/D = 1.0$ bucket. On the left side (back) of the bucket, the upward movement and the effect of rotation enhance the suction effect. On the right side (front), the uplift and the effect of rotation counteract each other. Therefore, it is expected that the highest suction is created on the back side. This is also the case for both buckets. On the $L/D = 0.5$ bucket maximum suction is measured at position PP13 (see figure D.7) which can be seen in Figures D.13 to D.24. The $L/D = 1.0$ bucket on the other hand, creates the largest suction at PP10.

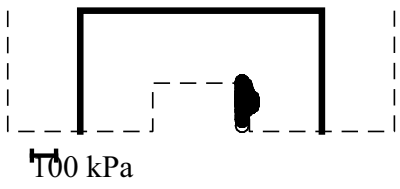

Fig. D.13: $L/D = 0.5$, 0.1 °/s. Drained behaviour is observed.

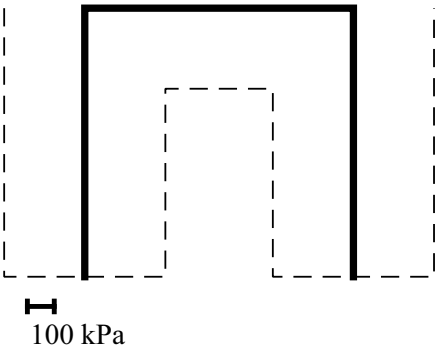

Fig. D.14: $L/D = 1.0$, 0.1 °/s. Drained behaviour is observed.

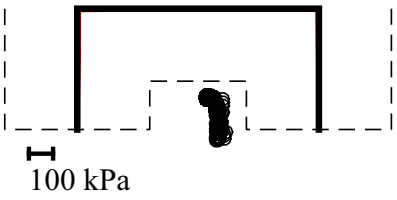

Fig. D.15: $L/D = 0.5$, 0.9 °/s. Almost drained behaviour is observed.

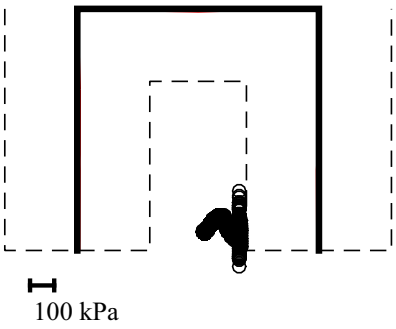

Fig. D.16: $L/D = 1.0$, 0.7 °/s. Almost drained behaviour is observed.

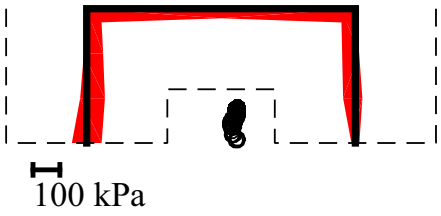

Fig. D.17: $L/D = 0.5$, 8.8 °/s. Partly drained behaviour is observed.

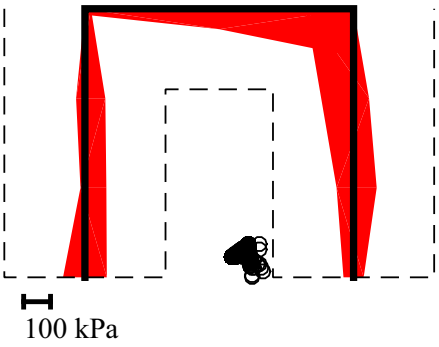

Fig. D.18: $L/D = 1.0$, 6.8 °/s. Partly drained behaviour is observed.

Rotation and Translation

From the displacement measurements on the bucket foundation, the rotation, θ [°], the horizontal, u [mm], and vertical, w [mm], translation are calculated. From the rotation and translations, the rotation point is calculated with the coordinates (x_{rot}, y_{rot}) in Equation (D.2).

$$\begin{bmatrix} x_{rot} \\ y_{rot} \end{bmatrix} = \begin{bmatrix} 1-\cos\theta & -\sin\theta \\ -\sin\theta & 1-\cos\theta \end{bmatrix}^{-1} \times \begin{bmatrix} u \\ -w \end{bmatrix} \tag{D.2}$$

Figure D.25 illustrates the used signconvention and follow the description given in Butterfield et al. (1997). Figures D.13 to D.24 depicts the calculated rotation points as black circles. The figures all show how the maximum suction generated during testing is distributed along the skirt and lid. The dashed line indicates the cavitation pressure. It is calculated as the applied pressure inside the pressure tank added the atmospheric pressure. Hence,

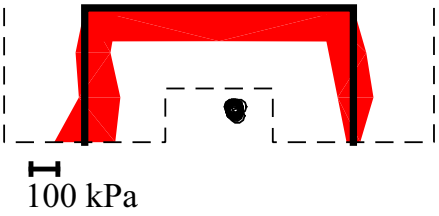

Fig. D.19: $L/D = 0.5$, 32.1 °/s. Partly drained behaviour is observed.

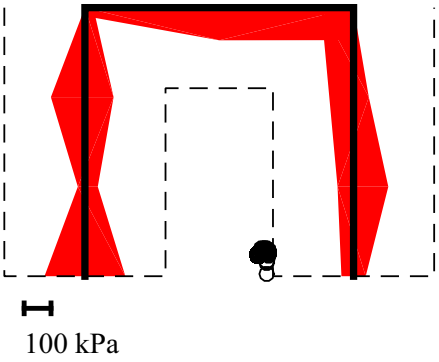

Fig. D.20: $L/D = 1.0$, 29.3 °/s. Partly drained behaviour is observed.

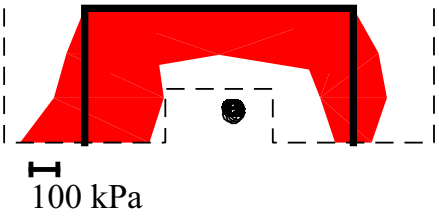

Fig. D.21: $L/D = 0.5$, 81.8 °/s. Undrained behaviour is observed.

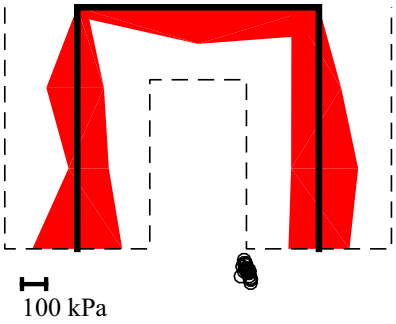

Fig. D.22: $L/D = 1.0$, 46.1 °/s. Partly drained behaviour is observed.

it is assumed equal to 300 kPa. Table D.4 gives the rotation and translation when peak resistance is measured for the $L/D = 0.5$ bucket and in Table D.5 for the $L/D = 1.0$ bucket.

Figures D.13 to D.24 show the rotation point moves towards the center when the behaviour changes from drained to undrained behaviour.

Figures D.26 and D.27 illustrates the direction of the movements at failure presented in Table D.4 and D.5. In Figure D.26 it is seen, as expected, that an increasing aspect ratio (L/D) reduces the rotation compared to the horisontal translation. However, no clear trend is seen for changing loading rates, and therefore no indications of that the boot effect has any effect on the relation between rotation and horisontal movement. Figure D.27 shows that an increasing loading rate leads to less uplift relative to the horisontal movement. Comparing the directions of the arrows in Figure D.27 with the illustration in Figures D.10 and D.11, show an increase in vertical load for light structures will lead to less uplift. The boot effect is enhanced with increasing loading

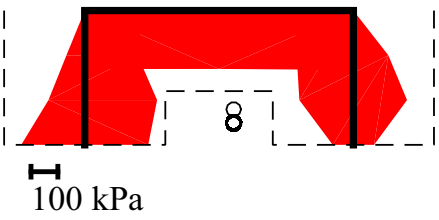

Fig. D.23: $L/D = 0.5$, 122.6 °/s. Undrained behaviour is observed.

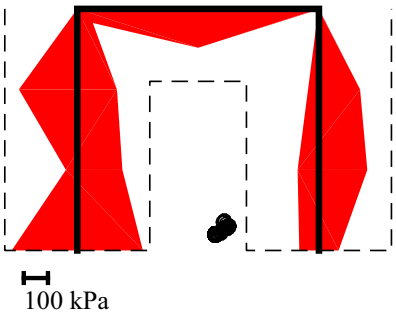

Fig. D.24: $L/D = 1.0$, 90.0 °/s. Undrained behaviour is observed.

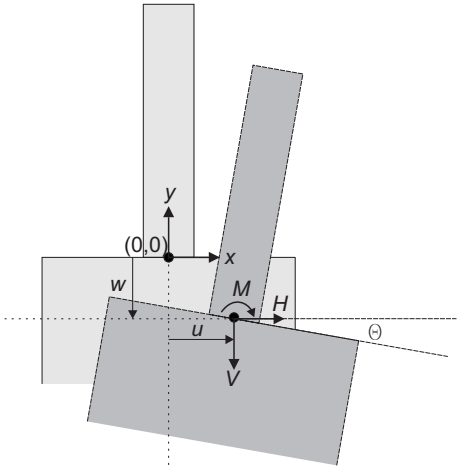

Fig. D.25: Sign convention for interpretating test resulsts.

rated, creating more suction. The suction acts as an additional vertical load and thereby increases the total vertical load on the foundation. Hence, as seen in Figure D.27, an increased loading rate reduces the upward movement of the foundation. These observations also explains why the rotation point moves towards the bucket center, which corresponds to a less eccentric loaded foundation.

Initial Stiffness

The design driver for offshore structures with a high sensitivity to inclination is often related to deformation. An example of such a structure could be an offshore wind turbine, for which design codes as the DNV, recommends a maximum rotation of 0.50 degrees, DNV-OS-J101 (2013). Therefore, the

Table D.4: Rotation, translation and coordinates for the rotation point at peak strength for the bucket with $L/D = 0.5$.

ω_p °/s	θ_p °	w_p mm	u_p mm	x_{rot} mm	y_{rot} mm
0.1	2.0	-3.6	6.6	106	-192
0.9	1.8	-1.1	6.6	39	-209
8.8	4.2	-1.8	14.6	31	-195
32.1	6.0	-2.0	19.5	29	-184
81.8	8.4	-2.1	23.6	30	-184
122.6	10.9	-2.0	35.9	27	-184

Table D.5: Rotation, translation and coordinates for the rotation point at peak strength for the bucket with $L/D = 1.0$.

ω_p °/s	θ_p °	w_p mm	u_p mm	x_{rot} mm	y_{rot} mm
0.1	1.2	-2.0	-	-	-
0.7	2.4	-1.8	18.5	53	-442
6.8	4.4	-3.0	33.5	56	-439
29.3	2.4	-3.4	18.7	92	-450
46.1	3.1	-4.6	29.3	99	-542
90.9	3.8	-2.7	29.0	56	-439

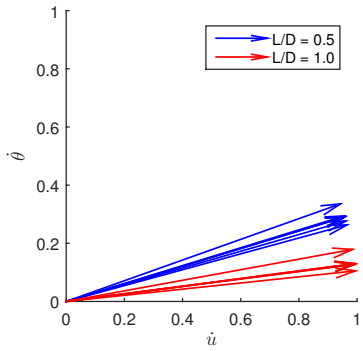

Fig. D.26: Movement pattern in $\theta - u$ space at failure. $\dot{\theta}$ and $\dot{u}$ are the incremental rotation and horisontal displacement, respectively.

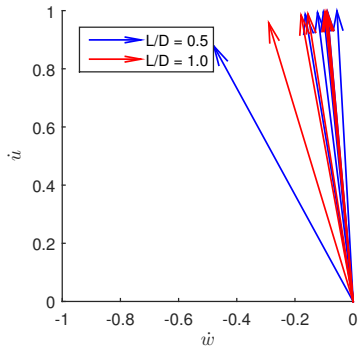

Fig. D.27: Movement pattern in $u - w$ space at failure. $\dot{u}$ and $\dot{w}$ are the incremental horisontal and vertical displacement, respectively.

initial stiffness of the foundation is interesting with respect to large forces with a short duration. In Figure D.27, the initial parts of the moment rotation curves, for the $L/D = 0.5$ bucket, are shown for tests with a rotational speed of: 0.1, 0.9, 8.8 and 32.1 °/s. Curves for faster loading rates are excluded due to a low number of measurements in this range. Looking at the secant stiffness from 0 to 0.5 degrees of rotation, there is a significant increase as the loading rate increases. Table D.7 lists these measured secant stiffness for the $L/D = 0.5$ bucket. Table D.7 shows a significant increase in the initial stiffness. Comparing the drained case with a rotational speed of 0.1 °/s and a partly drained situation with a rotational speed of 32.1 °/s, there is a significant increase by a factor of 4 in rotational stiffness of the bucket.

Looking at the $L/D = 1.0$ bucket, there is an even higher increase in rotational stiffness. Figure D.28 shows the initial part of the moment rotation curve, and Table D.7 provides the results. Once again, the tests conducted with high loading rate are disregarded due to too few data points within the

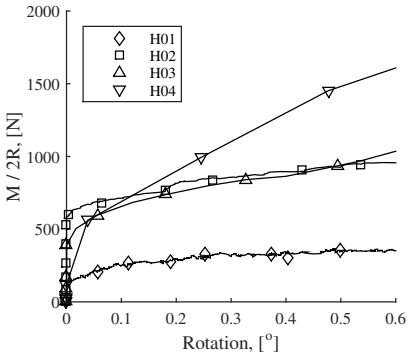

Fig. D.28: Initial part of the moment rotation curve for $L/D = 0.5$ bucket.

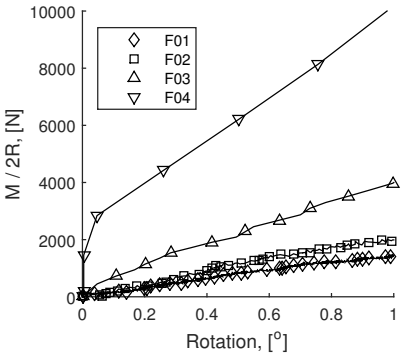

Fig. D.29: Initial part of the moment rotation curve for $L/D = 0.5$ bucket.

Table D.6: Normalised secant stiffness, $E_{sec}/E_{sec,static}$, for the $L/D = 0.5$ bucket. θ_{sec} is the rotation at the point where the secant stiffness is measured and $R_{\theta,sec}$ is the foundation resistance for the given rotation.

ω	θ_{sec}	$R_{\theta,sec}$	$E_{sec}/E_{sec,static}$
0.1	0.50	174.5	1
0.9	0.50	466.7	2.7
8.8	0.49	467.9	2.7
32.1	0.48	725.7	4.3
81.8	*Too few data points*		
122.6	*Too few data points*		

Table D.7: Normalised secant stiffness, $E_{sec}/E_{sec,static}$, for the $L/D = 1.0$ bucket. θ_{sec} is the rotation at the point where the secant stiffness is measured and $R_{\theta,sec}$ is the foundation resistance for the given rotation.

ω	θ_{sec}	$R_{\theta,sec}$	$E_{sec}/E_{sec,static}$
0.1	0.50	416	1
0.7	0.50	592	1.4
6.8	0.49	1045	2.6
29.3	0.50	3105	7.5
46.1	*Too few data points*		
90.9	*Too few data points*		

range. In this case, an increase in secant stiffness is enhanced up to a factor of 7.5, and an even higher factor is expected for undrained conditions.

Discussion

The small scale tests on both buckets, showed that the bearing capacity increases with increasing loading rate and that the increase was a combination of dilative soil behaviour and the boot effect. Furthermore, the rotation at which the maximum resistance is measured increases with loading rate. In other terms, the pore pressure build-up increases with the loading rate, because the difference between generated pore pressure and dissipated pore pressure increases. Combining these effects explains why a larger and larger amount of rotation is needed in order to reach maximum bearing capacity, as the increased bearing capacity comes from the generated suction. Looking

at the location of the rotation points given in Tables 4 and 5, there is a relatively large change from drained to partly drained behaviour, whereas partly drained and undrained response end in the same location. This indicates that just a little excess pore pressure will change the failure mechanism.

Intuitively, the hydraulic conductivity, the seepage and the impact time/ loading rate influence whether the response is drained, partly drained or undrained. These parameters are related to the movement of the bucket.

Furthermore, there is an increase in stiffness. As soil stiffness is dependent on the effective stress level, a stiffness increase can only be expected when negative excess pore pressure is present. If a situation of possitive excess pore pressure is present, a decrease in stiffness is to be expected.

Practical relevans and potential applications

The increase in bearing capacity has only been investigated for a foundation in dilative soils. The effective stress level govern the drained bearing capacity, whereas the total stress level govern the undrained bearing capacity. In this particular test setup, the effective stresses are very low (in the range 5-10 kPa), and the total stresses are relatively high (200 kPa). For a real foundation with a diameter of 15 meter installed at a water depth of 20 meters, the range of the average effective stresses would be (75-150 kPa) and the total stress level would be in the range (275-350 kPa). The ratio between the effective and total stress levels will determine how much extra strength could be expected. For practical cases on approximately 20 meters of water the expectation is an increase in bearing capacity with a factor of 2-4, by including the boot effect. A potential application is to account for the boot effect in the design of the bearing capacity of structures exposed to loads with a short duration. However, it is always important to consider the loading duration compared to the seepage. Otherwise, by designing a foundation only for drained situation, a hidden safety against slamming forces is made. Lastly, it should be mentioned that a greater water depth, will increase the necessary negative excess pore pressure to trigger cavitation. Hence, the effects limited by cavitation will be even larger at increasing water depth.

Large rotations are not allowed for an offshore wind turbine. Still, at rotations less than 0.5° the resistance against rotation is increased significant by including the effect of transient loading. Figures D.27 and D.28 show factors of approximately four and six, respectively. Besides, the response is only partly drained, and a fully undrained response is expected to have a higher ratio between drained and undrained resistance.

Conclusions

This article presents results on small-scale bucket foundations installed in dense sand and exposed to monotonic loading of varying duration until complete failure of the soil. These tests showed a significant increase in bearing capacity when the load triggered an undrained response of the soil, compared to a drained response. Factors between the drained and undrained response were measured to 18 and 25.

The boot effect showed to have a positive enhancing effect on the performance of the foundation. The excess pore pressure developed along the skirt and lid for both buckets were all negative, due to the upward movement of the foundation combined with the dilative soil behaviour. Though, the distribution of the excess pore pressure is different for the two ratios.

Not only does the bearing capacity increase with increasing suction (negative excess pore pressure), the stiffness increases as well. The increase in rotational stiffness is higher for the $L/D = 1.0$ bucket compared to the $L/D = 0.5$ bucket. The measurements showed factors of four and six, respectively.

Acknowledgements

The authors would like to acknowledge The Danish National Advanced Technology Foundation project "Cost-effective deep water foundations for offshore wind turbines" which funded this project.

References

Bransby, M. and Yun, G. (2009). The undrained capacity of skirted strip foundations under combined loading. *Géotechnique*, 59(2):115–125.

Butterfield, R., Houlsby, G. T., and Gottardi, G. (1997). Standardized sign conventions and notation for generally loaded foundations. *Géotechnique*, 47(5):1051–1054.

Byrne, B. and Houlsby, G. (1999). Drained behaviour of suction caisson foundations on very dense sand. *Offshore Technology Conference*.

Byrne, B. and Houlsby, G. (2004). Experimental investigations of the response of suction caissons to transient combined loading. *Journal of Geotechnical and Geoenvironmental Engineering ©ASCE*, 130(3):240–253.

DNV-OS-J101 (January 2013). *DNV-OS-J101, Design of Offshore Wind Turbine Structures*. DNV.

Foglia, A., Gottardi, G., Govoni, L., and Ibsen, L. B. (2015). Modelling the drained response of bucket foundations for offshore wind turbines under general monotonic and cyclic loading. *Applied Ocean Research*, 52:80–91.

Foglia, A., Ibsen, L. B., Nielsen, S. K., and Mikalauskas, L. (2013). A preliminary study on bucket foundations under transient lateral loading. *The Proceedings of the Twenty-third (2013) International Offshore and Polar Engineering Conference*, pages 465–471.

Gourvenec, S. (2008). Effect of embedment on the undrained capacity of shallow foundations under general loading. *Géotechnique*, 58(3):177–185.

Houlsby, G. T., Ibsen, L. B., and Byrne, B. W. (2005). Suction caissons for wind turbines. *Frontiers in Offshore Geotechnics: ISFOG, Perth, WA, Australia*, 130:75–93.

Ibsen, L. (2008). *Implementation of a new Foundations Concept for Offshore Wind Farms*, pages 19–33. Norsk Geoteknisk Forening. Keynote: NGM 2008.

Ibsen, L., Hanson, M., Hjort, T., and Thaarup, M. (2009). Mc-parameter calibration of baskarp sand no. 15. *DCE Technical Report*, (62).

Ibsen, L. B., Barari, A., and Larsen, K. A. (2014). Calibration of failure criteria for bucket foundations on drained sand under general loading. *Journal of Geotechnical and Geoenvironmental Engineering ©ASCE*, 140(7):1–16.

Ibsen, L. B., Barari, A., and Larsen, K. A. (2015). Effect of embedment on the plastic behaviour of bucket foundations. *Journal of Waterway, Port, Coastal, Ocean Engineering*, 141(6):1–9.

Larsen, K. (2008). *Static Behaviour of Bucket Foundations: Thesis submitted for the degree of Doctor of Philosophy*. PhD thesis, Aalborg University, Denmark. Vol. 1: Static Behaviour of Bucket Foundations Vol 2: Static Behaviour of Bucket Foundations : test results from laboratory tests.

Nielsen, S. D., Ibsen, L. B., and Nielsen, B. N. (2016). Advanced laboratory setup for testing offshore foundations. *Geotechnical Testing Journal*, 39(4). July 2016, DOI: 10.1520/GTJ20150135.

Nielsen, S. K., Ibsen, L. B., Sørensen, K. W., and Shajarati, A. (2013). Undrained cyclic behaviour of dense frederikshavn sand. *The Proceedings of the Twenty-third (2013) International Offshore and Polar Engineering Conference*, 2:518–525.

Renewable UK (2015). Offshore wind. http://www.renewableuk.com/en/renewable-energy/wind-energy/offshore-wind/.

Paper E

Response of Cyclic Loaded Bucket Foundations in Saturated Dense Sand

Søren Dam Nielsen
Lars Bo Ibsen
Benjaminn Nordahl Nielsen

The paper has been submitted for publication in
Journal of Geotechnical and Geoenvironmental Engineering

The layout has been revised

Abstract

One of the major concerns of designing offshore wind turbine foundations are to address the effects of cyclic loading. This paper described the results from a test series on a small scale mono bucket foundation installed in water-saturated dense sand exposed to cyclic loading with 1.0 Hz. The model by LeBlanc et al. (2010) has been calibrated to fit the test results. Compared to previous tests the presented test program has been conducted under partly drained conditions due to a higher load frequency and in addition the foundations have been pre loaded by cyclic loads simulating small wave impacts prior to major storm events. An example of calculating the accumulated rotation for a full size structure is presented, and it is compared to the results by Zhu et al. (2013). The paper also presents a cyclic load response diagram, which is a tool to be used in a pre design of a mono bucket foundation. The diagram gives the designer a quick overview of the cyclic load response, and the effect of increasing of decreasing the foundation size.

Key Words: Mono bucket foundation, 1g model testing, cyclic loading, accumulated rotation.

Introduction

The mono bucket foundations (described by Ibsen (2008)) is a cost-effective competitor to mono pile foundations to support offshore wind turbines. These are exposed to severe environmental loads from wind and waves, and in some areas also ice, currents and seismic loads. Especially the wave loads are cyclic of nature and during a storm, wave loading may be the dominating load. Design codes as Det Norske Veritas (2010) require that the effect of cyclic loading on the soil properties, and thereby the foundation behaviour is assessed during the design phase. However, no standardised way of taking cyclic loading into account has been presented.

Authors have formulated different procedures to take the cyclic load effects into account. One example is described by Achmus et al. (2009), which presents numerical simulations on mono pile foundations. Here a method to describe the secant stiffness degredation has been used, which is calibrated against triaxial tests. Other methods using triaxial data are presented by Andersen and Berre (1999), Andersen (2009) and Andersen (2015) where cyclic contour diagrams are used.

Zhu et al. (2013) investigated the effect of cyclic loading on a small scale bucket foundation in dry loose sand with a loading frequency of 0.1 Hz, and calibrated the expression to a model describing the accumulated rotation.

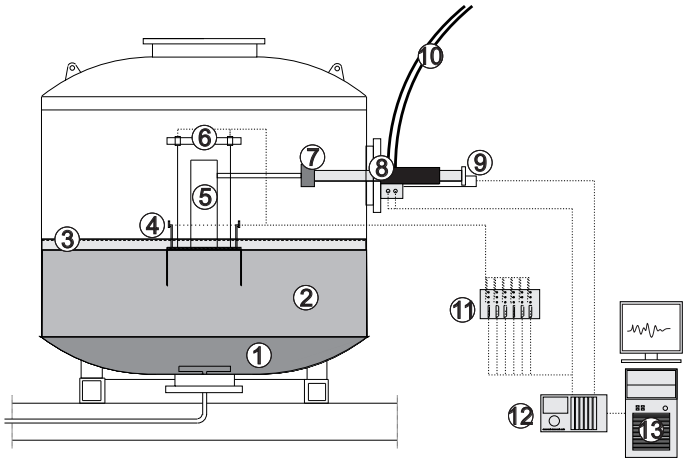

Fig. E.1: Experimental setup used for testing. 1 is gravel, 2 is Aalborg University Sand No. 1, 3 is water table, 4 is pressure transducers, 5 is tower 6 is vertical displacement transducers, 7 is load cell, 8 is hydraulic actuator, 9 is horisontal displacement transducer, 10 is hydraulic hoses, 11 is a distribution box, 12 is MOOG PTC and 13 is a PC with MOOG software.

The expression took into account the nature of the cyclic load, defined in two parameters: ζ_b and ζ_c and was originally developed by LeBlanc et al. (2010) for mono piles. Foglia (2015) performed tests on cyclic loaded bucket foundations in water saturated dense sand, and calibrated the same model. Foglia (2015) found some deviations compared to Zhu et al. (2013). Some of the deviations were addressed the different relative densities of the soil used for the two test programmes.

This paper described the results from a test series on a small scale mono bucket foundation installed in water-saturated dense sand exposed to cyclic loading with 1.0 Hz. The model by LeBlanc et al. (2010) has been calibrated to fit the test results.

Experimental Setup

This section presents a brief description of the used laboratory set-up, shown in Figure E.1, which are described in details by Nielsen et al. (2016). The set-up consists of a steel tank as shown in Figure E.1. Lowest is a layer of gravel (1), overlayered by 0.6 m of water saturated Aalborg University Sand No. 1 (2) with the characteristic in Table E.1. The water table (3) is 6-10 com above the sand layer. On the side of the tank is mounted a hydraulic actuator (8), which is able to be either force or displacement controlled. A load cell (6) is mounted on the inner side of the tank in the end of the piston. All data is collected and stored on the computer (13). The PC is also, via the MOOG

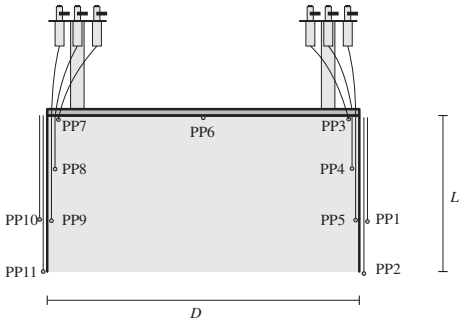

Fig. E.2: Small scale bucket foundations with pore pressure measurement system. D is the diameter and L is the skirt length.

Table E.1: Characteristics for Aalborg University Sand No. 1.

Parameter	Symbol	Value
Grain size, 50 %	d_{50}	0.14 mm
Uniformity coefficient	d_{10}/d_{50}	1.78
Specific gravity	G_s	2.64
Maximum void ratio	e_{max}	0.854
Minimum void ratio	e_{min}	0.549

Portable Test Controller (12), used to run the tests.

The tests are performed on a small scale bucket foundation with a diameter (D) of 0.5 m and a skirt length (L) of 0.25 m and a skirt thickness (t) of 4 mm. Figure E.2 show the pore pressure measuring system (pressure transducers) on top of the foundation. From the pressure transducers small metal tubes are connected to the skirts, and thereby measures the pore pressure in selected positions as shown in Figure E.2.

The foundation was installed in a dense water saturated sand (Aalborg University Sand No. 1) with the parameters given in Table E.1. Rod vibrators were used to prepare the sand, to a level of relative density of approximately 90 %. The sand was inside a pressure tank, which is a steel tank that can be hermetic sealed and an increase in internal pressure is possible. This could for example simulate the mud line of an offshore structure, where the hydrostatic pressure from the ocean will lead to a high pore water pressure at sea bed. The skirts of the foundation were pushed into the sand until contact between the lid and soil surface was observed. After installation, a tower was mounted on top of the foundation (the total weight of foundation and tower is 1.1 kN). A horisontal moving actuator was then connected to the tower, which during testing exposed the foundation to horisontal and moment loading. The actuator was PID controlled, and for high frequencies (>1Hz) and large displacements (several mm) the regulation became unsta-

ble. Displacement transducers were connected to the foundation, measuring vertical displacement in two positions and horisontal movement in one position. From these measurements the rotation and vertical and horisontal translation of the bucket center is calculated. Before the tests were initiated, the pressure tank was sealed and the pressure inside the tank was increased by 200 kPa, corresponding the a water depth of 20 m. Additionally, the increased water pressure ensured a better measure of the excess pore pressure (corresponding to back pressure in a triaxial test). After increasing the internal pressure, the tests were initiated.

Test Programme

The test programme consisted of 15 tests listed in Table E.2. Tests 01-05 and 08 were used for investigating the effect of load frequency and the effect of precycling. Tests 06-15 were used for calibration of a model describing accumulated rotation for a mono bucket foundation. Table E.2 presents values of ζ_b (relative maximum load during a cycle) and ζ_c (minimum compared to maximum load during a cycle), which are defined in Equations (E.15) and (E.16) where M_{min} and M_{max} are taken as mean values for all 1000 cycles. The target value of M_{min} and M_{max} for tests 01-04 are identical. However, they are not giving the same value for ζ_c. This is because the PID controlled actuator was unable to apply the correct force within the given load period for the first cycles at high frequencies.

During the life time of an offshore wind turbine the numbers of waves hitting the structure may exceed hundreds of thousands. However, Foglia (2015) presented results showing that most deformation occured within the first 300 cycles and that after 1000 cycles the additional rotation became insignificant. Therefore, 1000 load cycles are applied in every cyclic test in the presented test program.

Frequency dependency

In order to investigate the effect of the load frequency on the accumulated rotation, four tests were conducted with a load amplitude of 500 N and a mean value of 0 N. All tests were applied 1000 cycles with a frequency varying from test to test. The applied frequencies were: 4 Hz, 2 Hz, 1 Hz, 0.5 Hz and 0.1 Hz. The normalised rotation as a function of number of cycles for the tests are shown in Figure E.3. Here, $\Delta\theta$ is the accumulated rotation and θ_s is the rotation measured in a monotonic test at the load level corresponding to the maximum load during cyclic loading. This is illustrated in Figure E.7.

Figure E.3 shows that an increasing load frequency will lead to an increase in accumulated rotation. All tests reaches a plateau, at which no further

Table E.2: Test program for cyclic tests, where ζ_b and ζ_c are calculated from the measured force. *Precycling are 1000 cycles with a load amplitude of 25 N around zero.

Test	Precycling*	ζ_b	ζ_c	f	N
01	No	1.0	-0.8	4.0	1000
02	No	0.9	-0.9	2.0	1000
03	No	0.9	-1.1	1.0	1000
04	No	0.9	-1.0	0.5	1000
05	Yes	0.8	-1.0	4.0	1000
06	Yes	0.3	-0.5	1.0	1000
07	Yes	0.4	-1.0	1.0	1000
08	Yes	0.8	-1.0	1.0	1000
09	Yes	0.9	0.0	1.0	1000
10	Yes	0.6	0.0	1.0	1000
11	Yes	0.4	0.0	1.0	1000
12	Yes	0.4	-0.4	1.0	1000
13	Yes	0.2	0.0	1.0	1000
14	Yes	0.6	-0.6	1.0	1000
15	Yes	0.8	0.5	1.0	1000

rotation is accumulated. The plateau is reached after approximately 50 cycles for frequencies of 0.5 Hz and 1.0 Hz, after approx. 100 cycles for 2.0 Hz, and after 400 cycles for 4.0 Hz. For the tests on 0.1 Hz, the accumulated rotations were very small. Hence the plateau was reached during the first cycle.

Figure E.4 shows that the excess pore pressure is highest for the tests with the highest frequency and lowest for the test with the lowest frequency. The excess pore pressure increases until it reaches a peak after 10 to 15 cycles. After the peak the excess pore pressure drops to a permanent value significantly lower than the peaks. As higher frequencies leads to a higher positive excess pore pressure, this can explain the larger accumulated rotations, as the stiffness decreases with decreasing effective stresses.

It has been shown that the accumulated rotation is dependent on the loading frequency. Therefore, it is important to chose a frequency that reflect the effects occurring for a full size structure exposed to wave loading. Hence, in order to avoid scale effects related to the load frequency, a proper scaling law must be applied.

Scaling of load period

When performing small-scale laboratory tests a proper scaling law is important. In this paper the focus is on investigating the transient behaviour, and thereby the effect of exces pore pressure. Therefore, the degree of consolidation (U) is used as a scaling parameter for the load frequency and is given

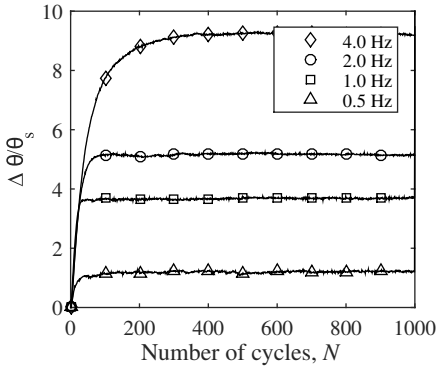

Fig. E.3: Rotation as a function of number of cycles ($\theta(N)$) for four tests with amplitude and mean value of 500 N and 0 N, respectively. Frequency were changed from tests to tests from 4 Hz to 0.5 Hz.

as

$$\frac{1}{U^6} = 1 + \frac{1}{2\,T^3} \tag{E.1}$$

where the dimensionless time factor (T) is given as

$$T = \frac{c_v}{H^2} t = \frac{k\,M}{\gamma_w\,H^2} t \tag{E.2}$$

where c_v is the coefficient of consolidation, H is the seepage length and t is the time. k is the hydraulic conductivity, M is the constrained modulus of the soil and γ_w is the unit weight of water. In order to have the same degree of consolidation in nature (index N) and model (index M), the dimensionless time factor must be the same. Hence,

$$T_N = T_M$$

and thereby,

$$\frac{k_N\,M_N}{\gamma_{w,N}\,H_N^2} t_N = \frac{k_M\,M_M}{\gamma_{w,M}\,H_M^2} t_M \tag{E.3}$$

A scaling factor (λ) for each parameter is presented as

$$\lambda_X = \frac{X_N}{X_M}$$

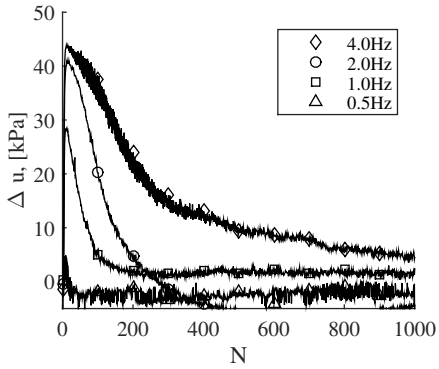

Fig. E.4: Excess pore pressure as a function of number of cycles ($\Delta u(N)$) for four tests with amplitude and mean value of 500 N and 0 N, respectively. Frequency were changed from tests to tests from 4 Hz to 0.1 Hz.

Thereof,

$$\lambda_t = \frac{\lambda_{\gamma_w}\ \lambda_H^2}{\lambda_k\ \lambda_M} \tag{E.4}$$

Using Janbu's tangent modulus concept, the constrained modulus (M) for sand (assumed elasto-plastic) can be estimated as:

$$M = m\sqrt{\sigma'\ \sigma_a} \tag{E.5}$$

The scaling factor for the constrained modulus, λ_M, can be found as:

$$\lambda_M = \frac{M_N}{M_M} = \frac{m_N\sqrt{\sigma'_N\ \sigma_{a,N}}}{m_M\sqrt{\sigma'_M\ \sigma_{a,M}}} = \lambda_m\ \sqrt{\lambda_{\sigma'}\ \lambda_{\sigma_a}} = \sqrt{\lambda_{\sigma'}} \tag{E.6}$$

Here it is assumed that $m_N = m_M$ and $\sigma_{a,N} = \sigma_{a,M}$. Equation (E.4) is the rewritten to:

$$\lambda_t = \frac{\lambda_H^2}{\sqrt{\lambda_{\sigma'}}} \tag{E.7}$$

The scaling factors for seepage and effective stress level can then be determined as:

$$\lambda_H^2 = \frac{H_N^2}{H_M^2} = \frac{L_N^2}{L_M^2} = \frac{6^2\text{m}}{0.25^2\text{m}} = 24^2 \tag{E.8}$$

$$\sqrt{\lambda_{\sigma'}} = \sqrt{\frac{30}{1.25}} = \sqrt{24} \tag{E.9}$$

Here prototype dimensions are $D = 12$m and $L = 6$m. Finally, the scaling factor for time can be calculated.

$$\lambda_t = \frac{\lambda_H^2}{\sqrt{\lambda_{\sigma'}}} = \frac{30^2}{\sqrt{30}} = 117.6 \tag{E.10}$$

The time in nature is assumed to be a wave period of 10 seconds. The period used in the laboratory is the estimated to:

$$t_M = \frac{t_M}{\lambda_t} = \frac{10s}{164} = 0.0851\text{s} \tag{E.11}$$

This will result in a load frequency in the laboratory of 11.8 Hz.

Calculating c_v from monotonic bucket test

The hydraulic conductivity for the laboratory conditions has been found to 5e-5 m/s by Sjelmo (2012). Assuming $m_M = 400$ for dense sand and $\sigma'_M = 0.5 \cdot 0.25\text{m} \cdot 10\text{kN/m}^3 = 1.25\text{kPa}$, the coefficient of consolidation ($c_{v,M,cal}$) is calculated to

$$c_{v,M,cal} = \frac{k\ M}{\gamma_w} = \frac{5 \cdot 10^{-5}\text{m/s}\ 4470\text{kPa}}{10\text{kN/m}^3} = 0.0224\text{m}^2/\text{s} \tag{E.12}$$

The calculated coefficient of consolidation is given in Equation (E.12). This expression is general, for all stress levels. However, conducting laboratory element tests at low confining pressure are related to uncertainties, and thereby the validity of the expression for very low confining pressures are questioned. Therefore, the coefficient of consolidation is estimated from a monotonic test on the same small scale model as used for cyclic loading in this paper. The foundation is loaded transient, with a loading rate resulting in undrained conditions. After being rotated until failure, where negative excess pore pressure has been generated, the dissipation of the excess pore pressure is monitored. Figure E.5 shows how the excess pore pressure dissipates over time. The 13 symbols shows the maximum (negative) excess pore pressure where the rotation of the foundation has stopped for each of the positions

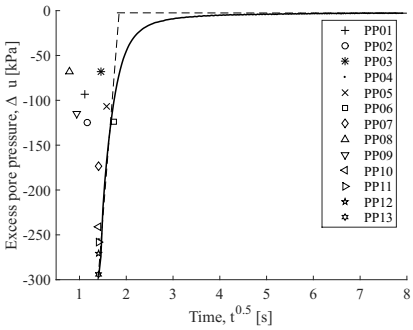

Fig. E.5: Dissipation of excess pore pressure.

where pore pressure were measured. The figure plot excess pore pressure Δu against the square root of time $\sqrt{t}$. A straight line is fitted to the first part and another to the part giving a horisontal asymptote. The intersection of these lines are assumed to be the dissipation time.

A similar method is described for 1D dissipation tests to determine c_v, where a plot of deformation with time is made, and two straight lines are fitted to the beginning and final part of the curve. This method assumes that the settlements of a soil sample will be linear with $\sqrt{t}$. The intersection of the two lines are the consolidation time, Randolph and Gourvenec (2011). The intersection of the two lines gives the time, which is used to calculate c_v in

$$c_{v,M,lab} = T(U = 50\%)\frac{h^2}{t} = 0.2\frac{\left(\frac{2}{3}\cdot 0.25\text{m}\right)^2}{1.8^2\text{s}} = 0.0017\text{m}^2/\text{s} \tag{E.13}$$

By changing the coefficient of consolidation for the laboratory tests and keep all other parameters unchanged, the model frequency resulting in equal degree of consolidation is 1.28 Hz. However, as described by Nielsen et al. (2016), the maximum load frequencies, that produces reliable results on a bucket foundation of the used size is 1.0 Hz. Therefore this frequency has been used for testing the cyclic behaviour of the foundation.

Accumulated Rotation Model

The method to calculate the accumulated rotation (Equation E.14) for a mono pile, developed by LeBlanc et al. (2010), has been used for mono bucket foundations in dry sand with loading frequencies of 0.1 Hz by Zhu et al. (2013) and in dense water saturated sand by Foglia (2015).

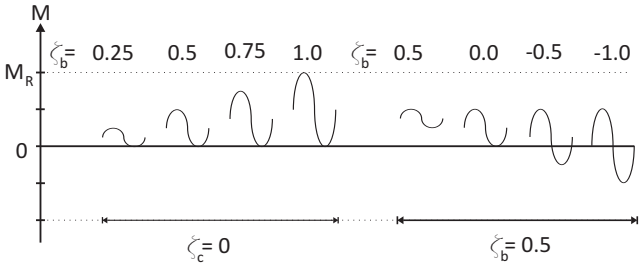

Fig. E.6: Examples of ζ_b and ζ_c.

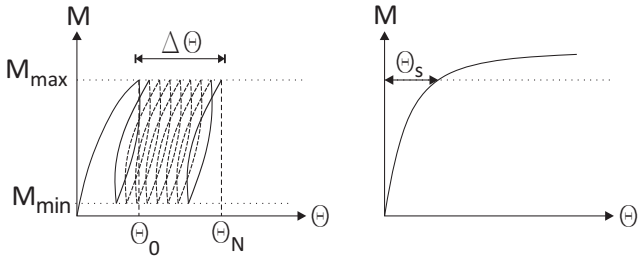

Fig. E.7: Definition of M_{max} , M_{min}, $\Delta\theta$ and θ_s.

$$\frac{\Delta\theta(N)}{\theta_s} = T_b(\zeta_b)\ T_c(\zeta_c)\ N^{\alpha} \tag{E.14}$$

Here α is found by fitting the test results to a power law function. $T_b(\zeta_b)$ and $T_c(\zeta_c)$ are functions determined from laboratory results. ζ_b and ζ_c are shown in Figure E.6 and are defined as

$$\zeta_b = \frac{M_{max}}{M_R} \tag{E.15}$$

$$\zeta_c = \frac{M_{min}}{M_{max}} \tag{E.16}$$

where M_R, M_{max} and M_{min} are illustrated in Figures E.7 and E.8. Figure E.8 depicts the monotonic moment rotation curve for the bucket foundation which has been precycled. Zhu et al. (2013) defined, as suggested by Villalobos (2006), M_R as the intersection of two lines, where one was fitted to the initial part of the moment rotation curve and a second line fitted to the last part, which is dominated by plastic deformations. The normalised curve is given in Figure E.13.

For mono piles LeBlanc et al. (2010) found $\alpha = 0.31$. For mono bucket foundations Zhu et al. (2013) found $\alpha = 0.39$ and Foglia (2015) found $\alpha =$

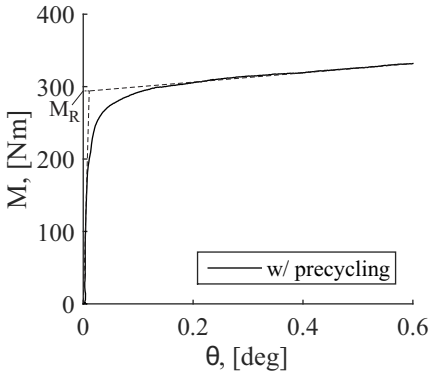

Fig. E.8: Moment rotaion curve for precycled bucket and definition of M_R. The full behaviour is seen in Figure E.13.

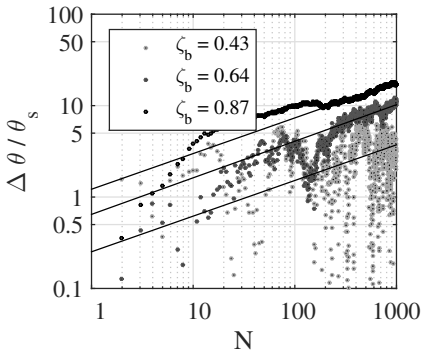

Fig. E.9: $\zeta_c = 0$.

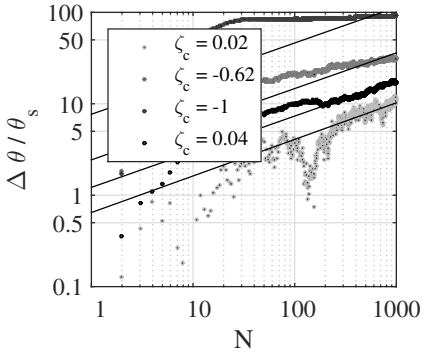

Fig. E.10: $\zeta_b = [0.5; 0.7]$.

0.19. Equation (E.14) is a power law function which, in a log log plot, is depicted linear. Figure E.9 shows the normalised accumulated rotation as a function of applied load cycles for tests with $\zeta_c = 0$. Data points are illustrated with dots, whereas the fitted lines are shown as solid lines. The figure show a large scatter on the tests with $\zeta_b = 0.33$, which is due to very small rotations of the bucket in this test. Hence, noise is dominating the signal. Therefore, that the accumulated rotation in this test is assumed zero. A power law is fitted with the least square method, and $\alpha = 0.39$ is found. This corresponds very well to the findings by Zhu et al. (2013).

Figure E.10 is similar to Figure E.9, but shows the fit for tests with $\zeta_b \in [0.6; 0.9]$. Authors presents different functions for T_b and T_c which are reported in Table E.3. LeBlanc et al. (2010) describes that $T_b(\zeta_b, R_d)$ is dependent on the ratio defined by ζ_b and the relative density (R_d) of the soil. Figure

Table E.3: Expressions for T_b and T_c used by other authors.

Author	Expression
Zhu et al. (2013)	$T_b = \begin{cases} 0, & \text{for } \zeta_b < 0.23 \\ 0.67\zeta_b - 0.16, & \text{for } \zeta_c \geq< 0.23 \end{cases}$
	$T_b = 0.7\zeta_b^2$
	$T_c = \begin{cases} 5.7 + 5.7\zeta_c, & \text{for } \zeta_b < -0.7 \\ 1 - \zeta_c, & \text{for } \zeta_c \geq< -0.7 \end{cases}$
Foglia (2015)	$T_b = 2.41\zeta_b^{1.64}$

E.11 shows $T_b(\zeta_b)$ for tests with $T_c(\zeta_c = 0) = 1$.

Figure E.11 shows the fits by Zhu et al. (2013), Foglia (2015) and the one presented in Equation (E.17) which has been fitted to the obtained data. The data shows to be inbetween the expression for T_b found by Foglia (2015) and Zhu et al. (2013). A quadratic function is fitted to the presented data to make comparrison to the quadratic function found by Zhu et al. (2013).

$$T_b = 1.59\zeta_b^2 \tag{E.17}$$

Foglia (2015) explains the deviation between the results obtained by Foglia (2015) and Zhu et al. (2013) by the different levels of relative density. The presented data in this paper are conducted on relative densities very similar to the ones by Foglia (2015) and as the presented function in Equation (E.17) give higher estimations of T_b, it is believed that some of the deviation can be explained by the relative density. The deviation between the presented data and Foglia (2015) may be addressed the load frequencies, which is the only major difference between the two test series. Here the increased water pressure ensured a better saturation of the sand, which is important for the measured excess pore pressure response.

Figure E.12 shows $T_c(\zeta_c)$ and it is seen that the data deviate significant from the expression for T_b used by Zhu et al. (2013) and Foglia (2015). However, for the test series, shown in Table E.2, a clear indication of accumulated rotation for two-way loading were observed. A linear function is fitted to the data shown in Figure E.11. The expression is given as

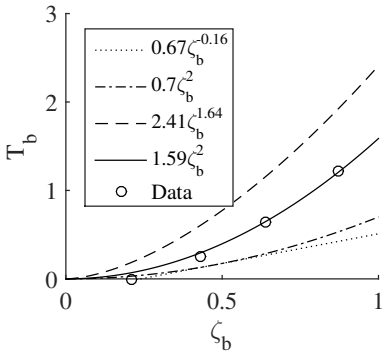

Fig. E.11: T_b for $\zeta_c = 0$.

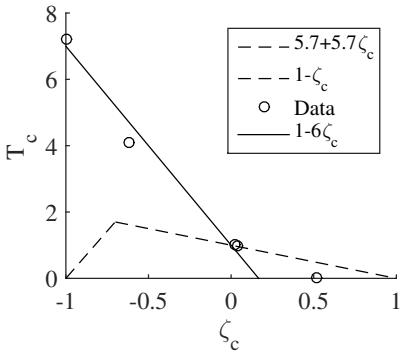

Fig. E.12: T_c for $\zeta_b \in [0.5; 0.7]$.

$$T_c = \begin{cases} 1 - 6\zeta_b, & \text{for } -1 < \zeta_c < 0.17 \\ 0, & \text{for } 0.17 < \zeta_c < 0.0 \end{cases} \tag{E.18}$$

The expression assumes no accumulated rotation for $\zeta_c > 0.17$, and as seen in Figure E.12 no accumulated rotation is measured for $\zeta_c = 0.5$. The expression is significant different from the ones found by Zhu et al. (2013). Based on the investigations on frequency dependency it is believed that this change is due to the loading frequency, and thereby the generated excess pore pressure. This is also what is found in triaxial testing, where two-way loading is found to produce higher excess pore pressure than one-way loaded samples. This finding show the importance of modeling correct drainage conditions.

Precycling vs. no precycling

When performing triaxial tests for offshore design, the samples are often pre-shared, simulating the effect of loads from small waves hitting the structure before any significant storm arises, Andersen (2009). Therefore, the effect of precycling (preloading with cyclic loads) is investigated. The precycling has been chosen to 1000 cycles with a cyclic load with amplitude of 0.05 M_{ult}, measured in a drained monotonic test without precycling. For the presented bucket foundation, M_{ult} has been measured to 250 Nm. Measurements during precycling showed no accumulated rotation. However, by testing the monotonic and cyclic response of the foundation the stiffness and strength of the soil showed to increase.

Firstly, a second monotonic tests were performed, to measure the influence of precycling on the bearing capacity. Figure E.13 shows that after pre-

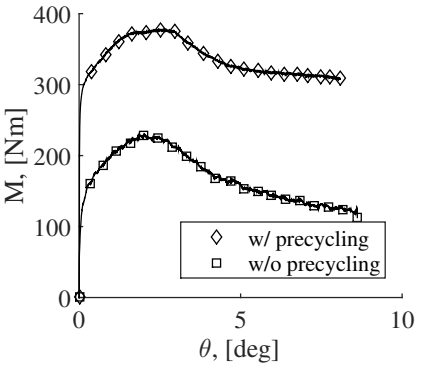

Fig. E.13: Effects of precycling on the ultimate drained capacity.

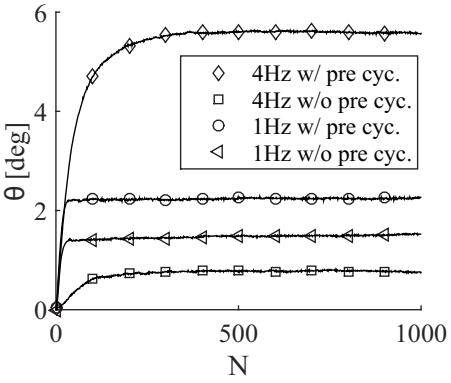

Fig. E.14: Effects of precycling the accumulated rotation.

cycling the bearing capacity (M_{ult}) increased from 225 Nm to 370 Nm.

Secondly, four cyclic tests were performed to envestigate the influence of precycling. The four tests were the combination of tests with 1 Hz and 4 Hz and with and without preshearing, all with an amplitude of 250 Nm and a mean value of 0 Nm. Figure E.14, show that precycling have a huge influence on the accumulated rotation. The two tests performed with 1Hz showed a reduction in maximum accumulated rotation of 36 % and the tests with 4 Hz showed a reduction in maximum accumulated rotation of 86 %. The tests show an indication of that the effect of precycling increases with increasing loading frequency for the precycling.

Two-way loading

The expression for T_c proposed by Kelly et al. (2006) and later used by Foglia (2015) assumes that symmetric two way loading do not lead to any accumulated rotation. As shown in Figure E.15 this is not, what has been observed during the test programme in Table E.2. Figure E.15 shows a significant accumulated rotation for two-way loaded ($\zeta_c = -1.0$) tests with $\zeta_b = 0.69$ and 0.66. For $\zeta_b = 0.35$ a minor accumulated rotation is observed.

However, the tests conducted by Kelly et al. (2006) and Foglia (2015) were conducted with a load frequency of 0.1 Hz and on a bucket foundation which were not precycled. Looking at Figure E.3 it is seen that for cyclic tests on a bucket foundation with no precycling and a load frequency of 0.1 Hz, no accumulation of rotation is seen even for a test with a load amplitude equal the drained bearing capacity.

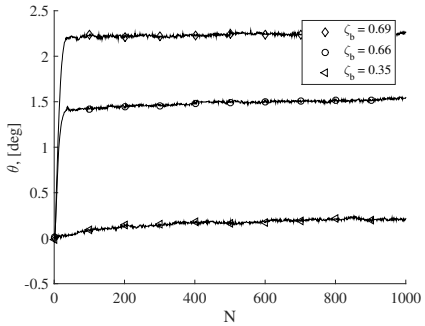

Fig. E.15: Tests where $\zeta_c = -1.0$ and $f = 1.0$ Hz.

Threshold for no deformation

Tests no. 11 and 13 in Table E.2, resulted in so small accumulated rotation, that they were unmeasurable. The two tests had values of ζ_c of 0.0. This was combined with values of ζ_b of 0.4 and 0.2. Common for the tests are that they are one-way loaded with a small load amplitude. For test no. 07 where $\zeta_b = 0.4$ and $\zeta_c = -1$, the accumulated rotation is also small (less than 0.05°). Hence it is believed that there exists cyclic load conditions, that do not lead to any rotation.

Therefore, T_b could also be fitted as a straight line resulting in a threshold for T_b where no rotation will accumulate.

Post Cyclic Undrained Capacity

Each test ended with an investigation of the post cyclic undrained capacity. This was investigated after the cyclic load program was applied. Here the bucket was brought to failure with a loading rate triggering undrained response of the foundation. A representative example of the post cyclic bearing capacity together with the monotonic undrained behaviour are shown in Figure E.16. Beside having an increased bearing capacity, the tangent stiffness has also increased for the post cyclic behaviour. The ratio between the post cyclic capacity and the monotonic capacity are in average 1.46 with a standard deviation of 0.08. This means that the post cyclic capacity is 40-50 % higher than pre cyclic capacty.

Discussion

The presented tests showed that two-way loading lead to the largest rotations. This effect is strongly believed to be caused by the drainage conditions, which

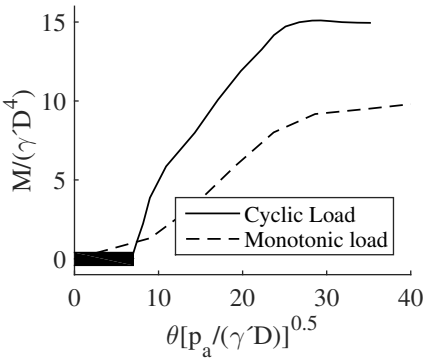

Fig. E.16: A representative example of the post cyclic bearing capacity.

in the presented tests showed generation of excess pore pressure. This is in good agreement with the general knowledge that undrained two-way loading leads to higher excess pore pressure compared to one-way loading, and thereby lower effective stresses. As shown in Figure E.3 load frequencies of 0.1Hz will produce insignificant rotation for the presented test setup, and the higher load frequency the more excess pore pressure is generated (see Figure E.4), and therefore larger rotations are observed.

This is in contradiction to the observations in previous findings by Zhu et al. (2013) and Foglia (2015), where symmetric two-way loading did not lead to any accumulation of rotation. The major difference in the experiments is the load frequencies. Looking at Figures E.11 and E.12 the largest deviations is found for T_c. For T_c Zhu et al. (2013) and Foglia (2015) found no accumulation of rotation due to symmetric two-way loading. It is therefore important to have equivalent drainage conditions between full scale and laboratory tests.

Prediction of Full Scale Cyclic Response

Zhu et al. (2013) presented an estimation of accumulated rotation based on laboratory tests. For comparison these loading conditions are applied in the example given below. The scaling relations given by Kelly et al. (2006) is used, and as stated by Zhu et al. (2013) the parameters in Table E.4 must be identical.

For the presented data $\tilde{V} = 0.88$, compared to $\tilde{V} = 0.19$ and $\tilde{V} = 0.57$ in Zhu et al. (2013). The load eccentricity in the presented tests are $\tilde{e} = 1.0$ compared to $\tilde{e} = 1.875$ and $\tilde{e} = 2.069$ in Zhu et al. (2013). Despite these differences, the same loading conditions are used: $N = 10^7$, $\zeta_b = 0.3$ and

Table E.4: Normalised parameters for mono bucket foundation.

Parameter	Symbol	Normalised symbol	Expression	Value
Aspect ratio	η		$\eta = L/D$	0.5
Load eccentricity	e	$\tilde{e}$	$\tilde{e} = M/(HD)$	1.0
Moment load	M	$\tilde{M}$	$\tilde{M} = M/(\gamma' D^4)$	Test specific
Horisontal load	H	$\tilde{H}$	$\tilde{H} = H/(\gamma' D^3)$	Test specific
Vertical load	V	$\tilde{V}$	$\tilde{V} = V/(\gamma' D^3)$	0.88
Rotation	θ	$\tilde{\theta}$	$\tilde{\theta} = \theta[p_a/(\gamma' D)]^{0.5}$	Test Specific

$\zeta_c = -0.2$. For the presented tests $\tilde{M} = 0.21$ corresponding to $\tilde{\theta} = 0.021^\circ$. Assuming $\gamma' = 8.5\text{kN/m}^3$, $p_a = 101\text{kPa}$ and $D = 21\text{m}$, the static rotation $\theta_s = 0.0279^\circ$. This results in an accumulated rotation of $\Delta\theta = 4.71^\circ$. This has to be compared to 0.834° calculated by Zhu et al. (2013) and a significant difference is seen.

A possible explanations for the deviation can be addressed to that the expressions for T_b and T_c are different, common for both is that the fitted functions for the presented tests gives higher values compared to Zhu et al. (2013), which will lead to higher calculated rotations. These deviations is the total effect of precycling and higher load frequency.

As mentioned by Zhu et al. (2013) one way to reduce the calculated accumulated rotation is by increasing the diameter. Thereby the ultimate capacity (M_R) increases and with the same loads, ζ_b will decrease.

Average and Cyclic Load Response

When investigating cyclic loading by triaxial testing, the response is often shown in a diagram with the normalised average load vs the normalised load amplitude. This concept is used to present the data from the presented test programme. The average load ratio (ALR) ans cyclic load ratio (CLR) are defined as

$$ALR = \frac{M_a}{M_{ult}} \tag{E.19}$$

$$CLR = \frac{M_{cyc}}{M_{ult}} \tag{E.20}$$

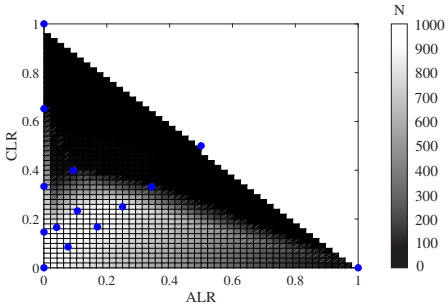

Fig. E.17: Linear interpolation between data points. The points (0,0), (0.5,0.5), (0,1) and (1,0) are artificial points.

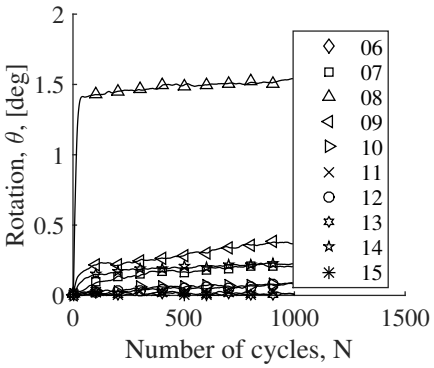

Fig. E.18: Accumulated rotation as a function of applied load cycles.

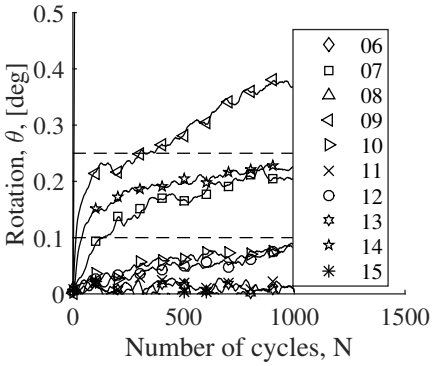

Fig. E.19: Accumulated rotation as a function of applied load cycles, with indications on limits used in Figure E.17

Where M_a and M_{cyc} are the mean and amplitude of the cyclic load, respectively. M_{ult} is the drained bearing capacity. Each test is represented by a dot in Figures E.17 and E.20. Figure E.17 shows linear interpolation of the data points and Figure E.20 shows the rotation after 1000 cycles. The diagram is divided into three sections: no cyclic load effects, cyclic load effects and severe cyclic load effects. The exact definitions of the area will be dependent on the criteria for the foundation. However, for this test series $\theta \leq 0.1^\circ$ is defined as no cyclic load effects, $0.1^\circ \leq \theta \leq 0.25^\circ$ is defined as cyclic load effects, and $\theta \geq 0.25$ is defined as severe load effects.

The rotation as a function of applied number of load cycles are shown in Figures E.18 and E.19. Figure E.18 presents all tests. The limits of 0.1° and 0.25° is shown in Figure E.19. For tests which does not reach 0.1° of rotation, 1000 cycles are presented in Figure E.17. For tests which crosses the two limits, the numbers of cycles can be read off the ordinate.

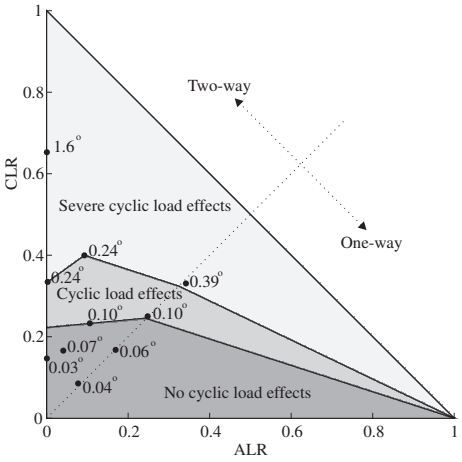

Fig. E.20: Cyclic load response diagram.

For load combinations in the no cyclic load effects zone loads are insignificant. For load combinations in the cyclic load effects zone, the effect of cyclic loading should be considered and load combinations in the severe load effects zone should be avoided. The cyclic load diagram (Figure E.20) can be used in a pre design giving a quick idea of the cyclic load effect.

Conclusions

This paper presents a calibration of a model describing the accumulated rotation of a mono bucket foundation. Laboratory tests have shown that the response of the foundation is highly dependent on the loading frequency. For the presented test set-up load frequencies below 0.1 Hz, showed to develop no excess pore pressure, whereas tests with load frequencies above 0.5 Hz develops significant excess pore pressure during the first cycles. The excess pore pressure dissipates over time and minor significant permanent pore pressure is observed. The higher loading frequency, and thereby higher excess pore pressure, leads to higher accumulated rotation.

The presented calibration of the model described in Equation (E.14) gives larger rotations compared to the calibration made under drained conditions by Zhu et al. (2013). The major difference between the two models are the formulation for T_c. The significant deviation between the two formulations is explained by the loading frequency which for the presented tests is relatively high triggering partly drained response, whereas previous tests has been under drained conditions. Therefore two-way loading becomes more severe for the model calibrated in this paper. Hence, it is concluded that obtaining

the correct drainage conditions between full scale and model tests are very important, when investigating the accumulated rotation of a mono bucket foundation. From the experiments, it is therefore concluded that when the drainage conditions becomes partly drained, two-way loading will lead to accumulation of permanent rotation.

The paper also presents a cyclic load response diagram, which is a tool for pre design of a mono bucket foundation. It can give an overview of the cyclic load response, and the effect of increasing or decreasing the size (bearing capacity) of the foundation.

Acknowledgements

The authors would like to acknowledge The Danish National Advanced Technology Foundation project "Cost-effective deep water foundations for offshore wind turbines" which funded this project.

References

Achmus, M., Kuo, Y.-S., and Abdel-Rahman, K. (2009). Behavior of monopile foundations under cyclic lateral load. *Computers and Geotechnics*, 36(5):725–735.

Andersen, K. H. (2009). Bearing capacity under cyclic loading - offshore, along the coast, and on land. the 21st bjerrum lecture presented in oslo, 23 november 2007. *Canadian Geotechnical Journal*, 46(5):513–535.

Andersen, K. H. (2015). Cyclic soil parameters for offshore foundation design. *Frontiers in Offshore Geotechnics III*, pages 5–82.

Andersen, K. H. and Berre, T. (1999). Behaviour of a dense sand under monotonic and cyclic loading. *ECSMGE XII Geotechnical Engineering for Transportation Infrastructure. Proc.*,, 2:pages 667–676.

Det Norske Veritas (2010). Design of offshore wind turbine structures. *OFFSHORE STANDARD DNV-OS-J101*.

Foglia, A. (2015). *Bucket foundations under lateral cyclic loading: Submitted for the degree of doctor of philosophy*. PhD thesis, Aalborg University, Department of Civil Engineering, Aalborg University.

Ibsen, L. (2008). *Implementation of a new Foundations Concept for Offshore Wind Farms*, pages 19–33. Norsk Geoteknisk Forening. Keynote: NGM 2008.

Kelly, R., Houlsby, G., and Byrne, B. (2006). A comparison of field and laboratory tests of caisson foundations in sand and clay. *Géotechnique*, 56(9):617–626.

LeBlanc, C., Houlsby, G., and Byrne, B. (2010). Response of stiff piles in sand to long-term cyclic lateral loading. *Géotechnique*, 60(2):79–90.

Nielsen, S. D., Ibsen, L. B., and Nielsen, B. N. (2016). Advanced laboratory setup for testing offshore foundations. *Geotechnical Testing Journal*, 39(4). July 2016, DOI: 10.1520/GTJ20150135.

Randolph, M. and Gourvenec, S. (2011). *Offshore Geotechnical Engineering*. Sangeet Patra, 1st edition. ISBN: 978-0-415-47744-4.

Sjelmo, Å. (2012). Soil - structure interaction in cohesionless soils due to monotonic loading. Masters thesis, Department of civil engineering, Aalborg University.

Villalobos, F. A. (2006). *Bucket foundations under lateral cyclic loading*. PhD thesis, University of Oxford, United Kingdom.

Zhu, B., Byrne, B., and Houlsby, G. (2013). Long-term lateral cyclic response of suction caisson foundations in sand. *Journal of Geotechnical and Geoenvironmental Engineering ©ASCE*, 139(1):73–83.

Paper F

Performance of a Mono Bucket Foundation - a Case Study at Dogger Bank

Søren Dam Nielsen
Lars Bo Ibsen
Søren A. Nielsen

The paper has been submitted for publication in
Journal of Journal of Ocean and Wind Energy

The layout has been revised

Abstract

This paper presents results from measurements on a mono bucket foundation supporting a met mast at Dogger Bank, which is a location of a future wind farm. The foundation is installed at a water depth of 23 meters and in soil conditions with layers of dense sand and stiff clay. The mono bucket foundation has a diameter of 15 meters and a skirt length of 7.5 meters. The presented work is: the water surface elevation, the inclination of the bucket lid and the generation of excess pore pressure inside the bucket, which contain data from a half year of measurements. The measurements show that the structure has been exposed to more than one severe storm. The paper describes the behaviour of the mono bucket foundation, in terms of rotation and excess pore pressure generation. The measurements are used to identify the general behaviour of the full size mono bucket foundation and show evidence on the presence of the boot effect during impact loads.

Key Words: Mono Bucket Foundation, Rotation, Pore Pressure, Monitoring, Dogger Bank

Introduction

In September 2013 a mono bucket foundation was installed at Dogger Bank, see Figure F.1, supporting a meteorological measuring mast, which in the industry is referred to as a met mast. The purpose of the erection was to collect data concerning the environmental conditions at the location, which is used in the design of a wind farm.

A mono bucket foundation consists of 3 parts: The shaft, the lid and the skirt, as shown in Figure F.2: The mono bucket foundation consists of three parts: Lowest the skirts, middle the lid and on top the shaft. On top of the shaft was mounted a platform, on which the met mast was fixed. In order to document the behaviour of the foundation, various transducers were installed on the mono bucket foundation and platform. Only the transducers from which measurements are used in this paper will be presented here: Wave radar, pressure transducers, inclinometers, and accelerometers.

The wave radar is mounted on a platform at the top of the shaft and measures the distance to the water surface. The pressure transducers, inclinometers and accelerometers, from which data are presented, are all mounted on the lid of the foundation. Pressure transducers are mounted below the lid, in order to measure the pore pressure in the soil inside the mono bucket foundation. The inclinometers and the accelerometers are all installed on the top side of the lid. Accelerometers are mounted both on the lid and on the

Fig. F.1: Location of Dogger Bank. West to Dogger Bank is Great Britain and east is Denmark.

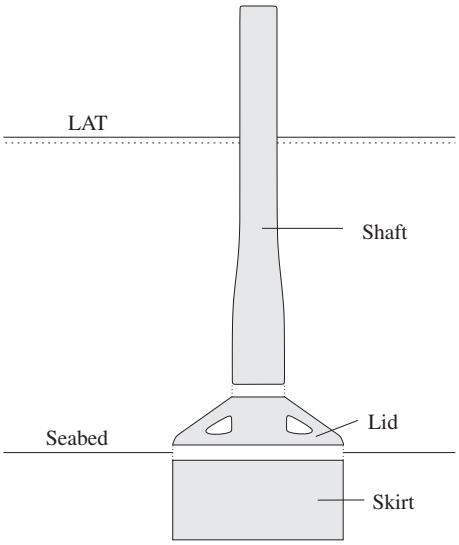

Fig. F.2: The mono bucket foundation consists of three parts: Lowest the skirts, middle the lid and on top the shaft.

platform.

On the 23^{rd} of September 2013 data collection of measurements of all transducers started, and the results shown in this paper are from the first half year after installation.

The Project Area

Dogger Bank is a sand bank in between Great Britain to the west and Denmark to the east, see Figure F.1. The water depth (LAT) at the location is measured to 23 meters. The soil conditions at the position of the mono bucket foundation are layers of very dense sand and stiff clay, see Table F.1.

Table F.1: Soil profile for the location at the met mast at Dogger Bank.

Depth	Soil
0.0 - 2.0 meters	Very dense sand
2.0 - 5.0 meters	Stiff Clay
5.0 - 5.5 meters	Very dense sand
5.5 - 13.6 meters	Stiff Clay
13.6 - 26.0 meters	Stiff Clay

The installed mono bucket foundation has a diameter of 15 meters and a

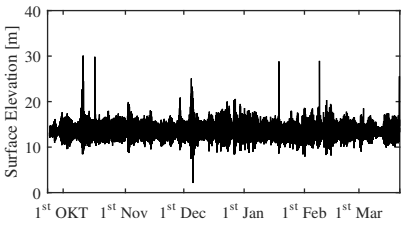

Fig. F.3: Measured surface elevation with no modifications.

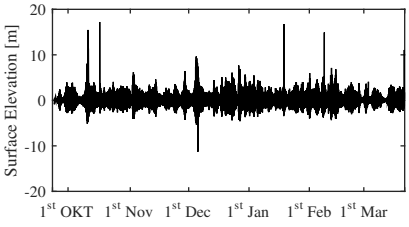

Fig. F.4: Measurements of surface elevation. The tidal effect has been removed using FFT analysis.

skirt length of 7.5 meters. Thereby, the skirt tip is located in stiff clay.

The water surface elevation is measured by the wave radar. The measured surface elevation is depicted in Figure F.3. The data shows a 12 hour tidal variation in the water surface elevation. By removing the tidal effects a clearer picture of the wave conditions is obtained, and the surface elevation without tidal variation is given in Figure F.4.

From these figures it is possible to detect storm events, and such events occurred in October and December 2013. From the October storm the surface elevation ranges from approximately -5 meters below mean water level to + 15 meters above mean water level, indicating wave heights of up to almost 20 meters.

It should though be mentioned, that peaks in the surface elevation not only can be due to high waves, but also splashes from breaking waves. Looking at the three narrow peaks in the middle of October, the middle of January and the middle of February may be due to splashed from waves hitting the structure. Prior the peaks, there is no indication of a larger storm event, and neither after. Therefore, it is not believed that these measurements are indicating a large wave, but rather splashes from waves. The peak in early October though indicates a huge wave.

Performance The First Half Year

In this section, the focus will be on rotation and pore pressure build up. Two inclinometers were installed on the lid: one in the N-S direction and one in the E-W direction. Unfortunately, the inclinometer measuring the rotation in the N-S direction was broken, and no measurements are available in this direction. Pore pressure was measured in one of three clay chambers by a pressure transducer.

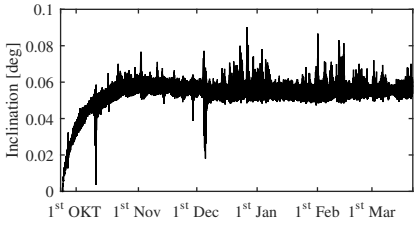

Fig. F.5: Measured inclination of the Mono Bucket Foundation in the East-West direction. First day of monitoring was 23^{rd} of September 2013.

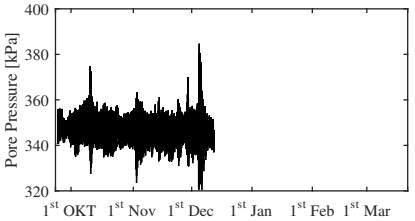

Fig. F.6: Measured pore pressure inside the mono bucket foundation.

Rotation

When designing an offshore wind turbine foundation several aspects must be considered in the design phase. One design criteria is a calculation of the permanent deformations during the life time of the structure. For offshore foundations supporting a wind turbine the rotation must not exceed the wind turbine manufacturer's specification (often 0.5°), which by the park owner often is split into 0.25° from installation and 0.25° during operation. Therefore, an estimate of the permanent deformation is very important in offshore wind turbine foundation design. Nevertheless, how the cyclic loads experienced offshore influence the soil behaviour and thereby the foundation behaviour is complex.

In Figure F.5 the measured East-West inclination of the Mono Bucket Foundation after installation is shown as a function of time. From the figure it is seen that in the middle of November 2013 the rotation stabilises, i.e. after approximately one and a half month. Not even later storm events lead to an increase in permanent rotation.

During the storms in October and December 2013, elastic responses of the foundation are measured. This is seen in Figure F.5, where a temporary rotation is measured during impacts of large waves. However, when the large wave has passed the structure, the rotation is reversed, i.e. no permanent deformation, and therefore elastic response.

Later and less severe storms as the ones in the beginning of January and February 2014 also lead to elastic response of the foundation, but no plastic deformation occur, meaning no increase in permanent rotation. The accumulated permanent rotation during operation is measured to 0.06° in the East-West direction. It should though be mentioned that the main wave direction is closer to North-South, but the inclinometer, measuring the rotation is this direction was unfortunately defect.

Pore Pressure

Another phenomenon that, according to the literature as (Ibsen, 1998), (Andersen, 2009), and Nielsen et al. (2013), can occur is pore pressure build up. This effect can be shown both theoretical and experimental. Both the theoretical explanations and triaxial testing has shown that cyclic loading can lead to both positive and negative pore pressure build up in undrained loading conditions. Whether positive or negative pore pressure build up is expected is dependent on the initial stress state, the initial density of the soil and the loading conditions. Sufficiently small cyclic loads or sufficiently high seepage will lead to dissipation of the excess pore pressure, and no pore pressure build up will be observed.

The pore pressure measured under the lid of the bucket foundation is shown in Figure F.6, and indicates that no permanent excess pore pressure is building up. After an incident in December 2013, the signals became corrupted and are therefore not shown. Even though, the pore pressure is generated in a dense sand layer, dissipation of excess pore pressure is not allowed since the skirt is penetrated into clay.

Comparisons of Buoyancy and change in water elevation

Figure F.6 indicates a tidal variation in the measured excess pore pressure. To verify if this variation is due to the tidal variation in the surface elevation, the estimated effect on the excess pore pressure from the tidal variation in the surface elevation is estimated.

The periods of the tidal waves are relatively long compared to the diameter of the bucket. This is not the case for wind generated waves during a storm, where the measured surface elevation will not be representative over the diameter of the bucket. Therefore the change in pressure, for wind generated waves, will be unevenly distributed over the lid, as illustrated in Figure F.7b. The pressure from tidal waves will be evenly distributed, as illustrated in Figure F.7a.

In order to clarify the effect of change in buoyancy and water level on the pressure, the effects are calculated by Equation (F.1) and the principles are shown in Figure F.8. A change in water surface elevation will change the hydrostatic pressure over the lid and the buoyancy of the shaft will change. Hence, during high tides the total pressure on the lid will increase, and so will the buoyancy of the shaft due to the additional displaced water. In situations of low tides, the situation will be vice versa. Additionally, the clay, which has a low permeability, will prevent water flow under the lid. The resulting force from the added pressure on the lid and the buoyancy will then lead to a change in pore pressure, measured by the pressure transducer. This change in pressure is calculated by Equation (F.1).

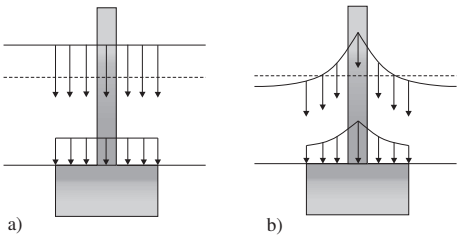

Fig. F.7: a) Pressure distribution on the lid from tidal waves. b) Pressure distribution on the lid from wind generated waves. Dashed line indicate mean water level.

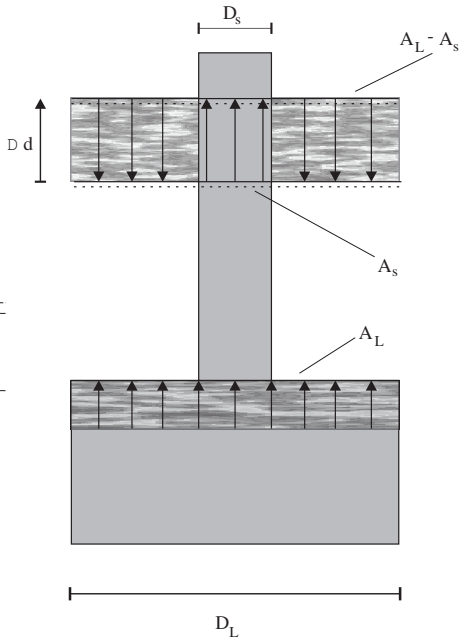

Fig. F.8: A change in surface elevation leads to a change in buoyancy and thereby induce pore water pressure. DS and DL are the diameter of the shaft and lid, respectively. The area under the lid is AL and AS is the cross sectional area of the shaft.

$$\Delta u = \Delta d \gamma_w \frac{A_L - A_S - A_S}{A_L} = \Delta d \gamma_w \frac{D_L^2 - 2D_S^2}{D_L^2} \tag{F.1}$$

where γ is the unit weight of water, DS is the shaft diameter and DL is the diameter of the lid. These are 4 and 15 meters, respectively resulting in $\Delta u \approx 8.6 \Delta d$ [kPa]. As mentioned, it is assumed that no water flow will occur, due to the low permeability of the clay and that all change in buoyancy will be counteracted by suction inside the bucket.

In Figure F.9 the measured pore pressure from tidal variations is shown as the gray line. As the pressure transducer got corrupted after the December storm, measurements are only shown until then. The pore pressure calculated by Equation (F.1) is in Figure F.9 shown as the black line. From the figure a decent match is seen. Hence, it is concluded that the tidal effect is caused by the tidal variation in the water surface elevation. The tidal effects are hereafter removed, as the tidal effect will not be a part of this investigation. The measured excess pore pressure, where tidal effects are removed, is

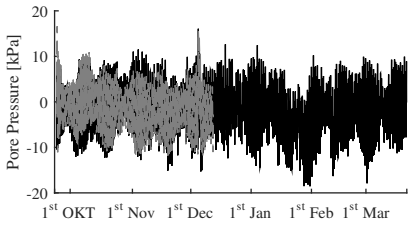

Fig. F.9: Calculated (black) and measured (gray) pore pressure due to tidal variations.

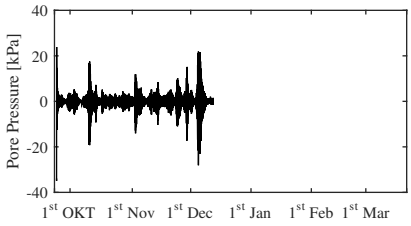

Fig. F.10: Measured excess pore pressure inside the mono bucket foundation, where the measured pore pressure due do tidal variation has been removed.

shown in Figure F.10.

Fluctuations in Excess Pore Pressure During a Storm

The concern related to what cause the fluctuations in excess pore pressure is thought to be related to either buoyancy, cyclic load effects in the soil or a combination hereof.

There is no doubt that the change in buoyancy due to tidal variation in water level is measured. Therefore, changes in buoyancy due to wind generated waves are also believed to influence the measurements. If the change in measured excess pore pressure should only be created from the change in surface elevation, the fluctuations should follow the same trend as the surface elevation. Looking at the surface elevation during storm events in Figure F.3 the positive peaks are higher than the negative peaks, which also is illustrated in Figure F.7b where the principals of the nature of surface elevation during a storm is depicted. This is not the case for the measured pressure in Figure F.10, where the sizes of positive and negative pressures are approximately the same.

October Storm 2013

As mentioned, the storm in October did lead to an impact of a huge wave. The surface elevation measured 60 s prior and after the wave impact is shown in Figure F.11. From the figure no indication of the large wave is seen prior to the time 0 s, where a wave height of almost 20 meters is seen.

The measured rotation of the foundation during this instance is shown in Figure F.12. The data show that the small rotations measured during impact loads are reversed during unloading. Hence the foundation response can be considered elastic. This means that no significant accumulated rotation is observed during the impact of the huge wave.

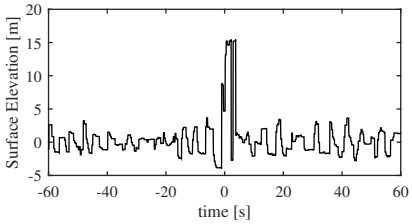

Fig. F.11: Surface elevation in the time of impact by monster wave.

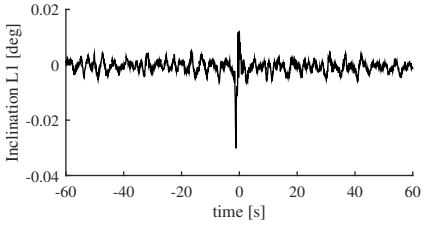

Fig. F.12: Calculated (black) and measured (gray) pore pressure due to tidal variations.

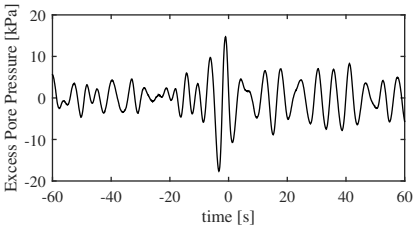

Fig. F.13: Measured excess pore pressure inside the mono bucket foundation, where the measured pore pressure due do tidal variation has been removed.

Comparing Figure F.11 and Figure F.12 to the measured excess pore pressure in Figure F.13 it is seen that the wave impact triggered a larger response in the excess pore pressure, than the smaller waves. The largest response in the excess pore pressure is measured as a suction of 17 kPa, corresponding to an additional downward stabilising force of 3 MN (300 tons).

The observations from the measurements of surface elevation, rotation of the foundation and the excess pore pressure, indicates the presence of the boot effect, which enhances the foundation performance to loads with a short duration.

Figure F.14 and Figure F.15 depict the measured acceleration of the lid and platform, respectively. The maximum acceleration of the foundation lid under the large wave impact is measured to 0.03 m/s^2. This indicates that the foundation hardly did move during the impact. However, the acceleration of the platform was measured to 0.85 m/s^2.

These are very much like the measurements, collected on the Drauptner E oil rig during the impact of a 26 m high monster wave, presented in Hansteen et al. (2003). The foundation of the platform is a four legged jacket structure, supported by skirted foundations (bucket foundations). During the impact an acceleration of 0.03 m/s^2 was measured on the foundation, and at the platform an acceleration of 0.4 m/s^2 was measured. The low acceleration level of the foundation was explained by the excess pore pressure response, which

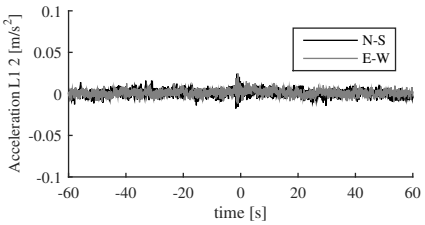

Fig. F.14: Calculated (black) and measured (gray) pore pressure due to tidal variations.

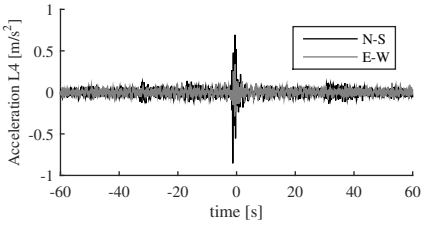

Fig. F.15: Measured excess pore pressure inside the mono bucket foundation, where the measured pore pressure due do tidal variation has been removed.

counteracted the wave impact, by suction on the impact side and positive pressure on the other side.

Comparing the results from the Drauptner E platform with the measurements on the mono bucket foundation at Dogger Bank, similarities of the measurements is seen, even though the loads are very different.

The dominating load on the bucket on the Drauptner E platform is axial tension and compression, whereas the mono bucket at Dogger Bank is dominated by moment loading. The measurements presented here also indicate that during the event of an impact from a large wave, the excess pore pressure counteract the huge loads, which is seen in the low acceleration levels and inclinations of the foundation. Comparing the relative acceleration of the platform at the Drauptner E with the relative acceleration at the Dogger Bank met mast, the acceleration level of the Dogger Bank met mast is the highest, which is expected as the structure is more flexible than the oilrig.

Comparison with Laboratory Tests

Nielsen et al. (2016c) and Nielsen et al. (2016b) presents results from model tests on a mono bucket foundation with a diameter of 0.5 m and a skirt length of 0.25 m. Hence an aspect ratio of 0.5, as the one installed at Dogger Bank. The test set-up is presented by Nielsen et al. (2016a). This section presents comparison of the behaviour measured in lab and at Dogger Bank.

Accumulated Rotation

The laboratory test set-up consists of a pressure tank, as illustrated in Figure F.16. Inside is a layer of water saturated Baskarp Sand (2). Below is a layer of gravel (1), with the purpose of ensuring a better saturation of the sand. The water level (3) is kept 5-10 cm above the sand layer. The model bucket foundation with a tower on top (4) is installed in the sand. On the bucket

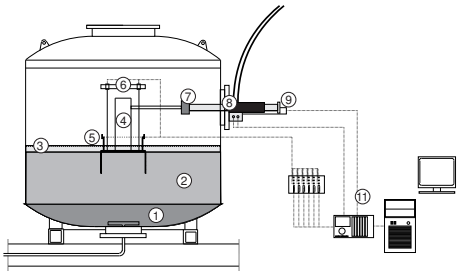

Fig. F.16: The pressure tank. A laboratory test facility at Aalborg University.

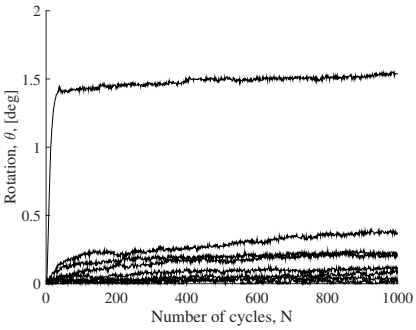

Fig. F.17: Accumulated rotation as a function of applied cycles for 8 tests.

foundation is mounted pressure transducers (5), which are able to measure the excess pore pressure along the skirts. The loads are applied by a powerful hydraulic actuator (8). The Force is measured by a load cell (7) and the movement is captured by tree displacement transducers (6) and (9). All data are collected and stored on a computer via a MOOG PTC (11). Before testing, the pressure tank is sealed and the internal pressure is increased by 200 kPa. This corresponds to the pressure experienced at seabed for a water depth of 20 m. beside simulating water depth, the pressure has the same affects as a backpressure in a triaxial apparatus, which improve the saturation.

Several methods assume that each load cycle contributes to the permanent rotation of a foundation exposed to cyclic loading. However, this is not observed during the monitoring of the mono bucket foundation at Dogger Bank. This is in good agreement with the laboratory results seen in Nielsen et al. (2016b). Figure F.17 show the accumulated rotation as a function of applied load cycles. The general trend in the laboratory tests was that the accumulation rotation almost stagnates after a few hundreds of cycles, even for loads with a very large amplitude (close to the drained bearing capacity). This effect was also observed by (Foglia, 2015).

Accumulated Excess Pore Pressure

Nielsen et al. (2016b) showed that excess pore pressure only developed in the first cycles, where significant deformation occurred. Figure F.18 shows the measured excess pore pressure for the tests presented in Figure F.17. It is seen that all tests reach a stable state after the first hundreds of load cycles, whereafter no change in the excess pore pressure is seen. Hence, over time no significant change in permanent excess pore pressure were observed. The same thing is observed from the measurements on the mono bucket foundation at Dogger Bank. As mentioned, Figure F.6 show that no permanent pore

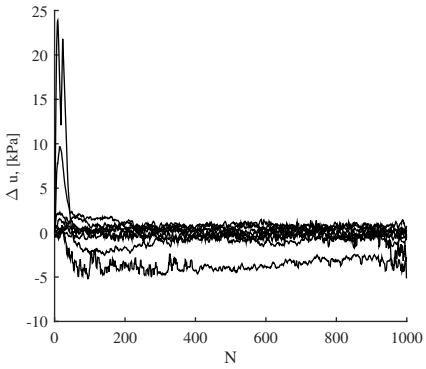

Fig. F.18: Excess pore pressure as a function of applies numbers of load cycles for 8 tests.

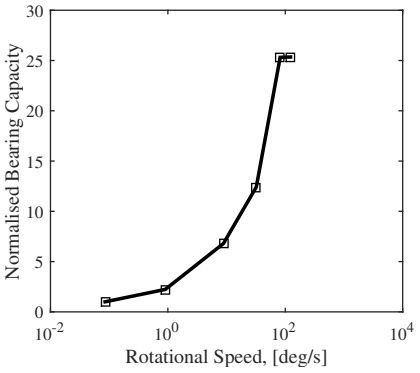

Fig. F.19: Normalised bearing capacity as a function of rotational speed. Squares indicate a test.

pressure build up is measured. However, a pore pressure response is seen on impacts from the individual waves.

Response on Impact Loads

Nielsen et al. (2016c) presents transient monotonic loaded small scale bucket foundations. The main findings were that loads with short duration triggers a response in the excess pore pressure. Thereby the soil behaviour is partly drained.

For short duration loads, negative excess pore pressure were generated, mainly due to the boot effect. The boot effect is described as the suction (negative pore pressure) generated by an uplift of the foundation. The more boot effect, the higher bearing capacity of the foundation. This means that an increasing loading rate will lead to a higher bearing capacity. This is illustrated in Figure F.19 where the rotational speed is plotted on the ordinate. The corresponding bearing capacity normalised with the drained bearing capacity is plotted at the abscissa. This behaviour is also seen at Dogger Bank, where Figure F.13 show the measured excess pore pressure response. It is here seen that the impact of the large waves induce a pore pressure response. This response in excess pore pressure seems to reduce the load effect on the foundation, as seen in Figure F.14 where small accelerations are measured.

Conclusions

After installation of a mono bucket foundation, supporting a met mast, at Dogger Bank in 2013, measurements of various parameters have been made.

Some of these measurements are shown in this paper.

The paper focuses on the long term behaviour in terms of permanent rotation and the pore pressure build up and the short term behaviour in terms of analyzing the impact of a large wave. The long term behaviour showed an accumulated rotation in the E-W direction from operation of 0.06°, which were reached after one to two months of operation, after which it stabilizes, and no further permanent rotation is measured. Additionally, the monitoring of the structure showed no indications of a general pore pressure build up over time.

Looking at the storm event, an elastic response of the foundation is observed, as the wave impact from the huge waves did not led to any permanent rotation of the foundation. Also the acceleration of the foundation is measured very low. The absence of deformations is explained by the pore pressure response, which counteract the loads from the wave impact.

The behaviour measured at Dogger Bank and the measurements performed in the geotechnical laboratory at Aalborg University mutually confirm the behaviour of the mono bucket foundation. The observed response with drained long term behaviour (no excess pore pressure) and an undrained behaviour or partly drained behaviour during impact loads, is also what previously has been observed at the Drauptner E platform, despite the different loading conditions.

Acknowledgments

This project was founded by The Danish National Advanced Technology Foundation project, entitled “Cost-effective deep water foundations for offshore wind turbines”. Data has kindly been provided by Universal Foundation A/S.

References

Andersen, K. H. (2009). Bearing capacity under cyclic loading - offshore, along the coast, and on land. the 21st bjerrum lecture presented in oslo, 23 november 2007. *Canadian Geotechnical Journal*, 46(5):513–535.

Foglia, A. (2015). *Bucket foundations under lateral cyclic loading: Submitted for the degree of doctor of philosophy*. PhD thesis, Aalborg University, Department of Civil Engineering, Aalborg University.

Hansteen, O. E., Jostad, H. P., and Tjelta, T. I. (2003). Observed platform response to a monster wave. In Myrvoll, F., editor, *Field Measurements in Geomechanics*, pages 73–86. A.A. Balkema Publishers.

Ibsen, L. B. (1998). The mechanism controlling static liquefaction and cyclic strength of sand. *Proc. Int. Workshop on Physics and Mechanics of Soil Liquefaction*, pages 29–39.

Nielsen, S. D., Ibsen, L. B., and Nielsen, B. N. (2016a). Advanced laboratory setup for testing offshore foundations. *Geotechnical Testing Journal*, 39(4). July 2016, DOI: 10.1520/GTJ20150135.

Nielsen, S. D., Ibsen, L. B., and Nielsen, B. N. (2016b). Response of cyclic loaded bucket foundations in saturated dense sand. *Submitted to Journal of Geotechnical and Geoenvironmental Engineering*.

Nielsen, S. D., Ibsen, L. B., and Nielsen, B. N. (2016c). Transient loaded bucket foundations in saturated dense sand - a demonstration of the boot effect. *Submitted to Journal of Geotechnical and Geoenvironmental Engineering*.

Nielsen, S. K., Ibsen, L. B., Sørensen, K. W., and Shajarati, A. (2013). Undrained cyclic behaviour of dense frederikshavn sand. *The Proceedings of the Twenty-third (2013) International Offshore and Polar Engineering Conference*, 2:518–525.

Appendix G

Manual for Pressure Tank

This manual describes the overall procedure for preparing a test inside the pressure tank. Furthermore, it describes the hydraulic actuator which are used to apply load/displacement and the custom made electrical components. It is not a detailed step by step description of how to perform a specific test, as this may change from one tests to another. Therefore, this manual is aiming at assisting researchers, that are familiar with experimental work.

G.1 Safety Instructions

These safety instructions are written 25^{th} November 2013. The latest version of safety instructions is to be found at *www.aau.dk* and anyone working in the laboratory is obliged to read and follow the latest version of the safety instructions.

G.1.1 Safety Shoes

Anyone working in the Laboratory must wear safety shoes.

G.1.2 Using the Crane

When you or anyone else is using the crane everybody near the crane must wear safety helmet.

G.1.3 Specific Safety Instructions

This section will describe the current rules of safety specific connected to performing experiment described by this manual.

Anyone being on top of the pressure tank must wear safety helmet (also when the crane is not in use.). Also the gate on the balcony must be closed all the time. Only when someone or something is entering or leaving the top, the gate is allowed to be opened.

When hydraulic actuator is switched on nobody is allowed to be inside the tank, unless a special agreement is made.

G.2 Test Set-Up

The pressure tank is shown in Figures G.1 and G.2.

Fig. G.1: Pressure Tank.

Fig. G.2: Pressure Tank.

The white steel container shown in the pictures are the pressure tank, which possible to seal hermetical. The tank has two openings: one in the top and one in the side. An illustration of the pressure tank is presented in Figure G.3. The figure show how the individual parts in the test set-up is connected. As shown in Figure G.3, a gravel layer is placed lowest inside the pressure tank. On top on the gravel (2), a 60 cm thick sand layer (3) is placed. The sand is Aalborg University Sand no. 1, also called Baskarp sand, which is graded sand from Sweden. The larger grain are rounded while the smaller grains are angular. To avoid mixture of the sand and gravel a geotex canvas i placed between the layers, allowing free water flow, but prevent the sand to fill out the voids in the gravel. The sand is saturated by a water inlet (1) in the bottom of the tank. To ensure fully saturation the water table (4) is adjusted to 5-10 cm above the sand surface.

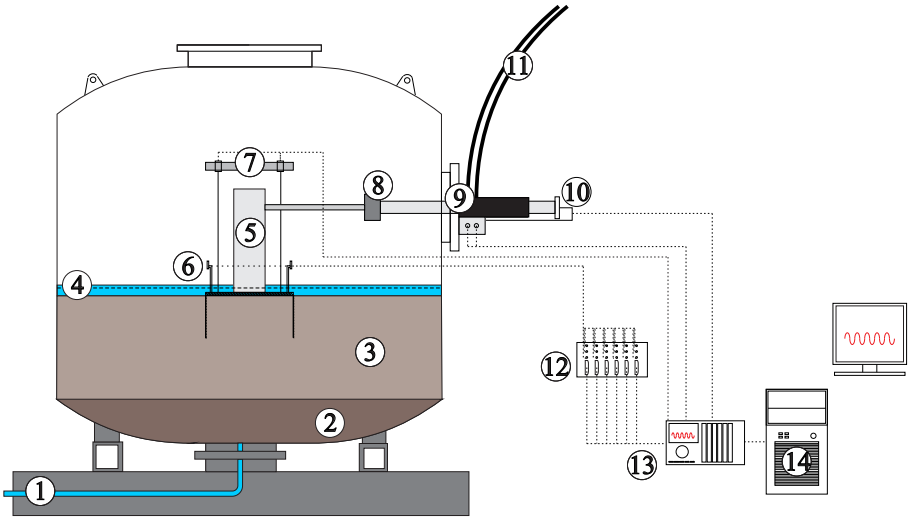

Fig. G.3: Test setup: 1 Water inlet, 2 Gravel, 3 Sand, 4 Water level, 5 Tower, 6 Pore pressure transducer, 7 Vertical displacement transducers, 8 Load cell, 9 MOOG hydraulic actuator, 10 Horisontal displacement transducer, 11 Hydraulic cables, 12 distribution box, 13 MOOG PTC, 14 PC with MOOG ITS.

On the side of the pressure tank a hydraulic actuator (9) is mounted. On the one end, inside the pressure tank, of the piston a load cell (8) is mounted. The load cell measures the force which the actuator applies the foundation, whereas the horisontal displacement transducer (10) measures the position of the actuator. The actuator is controlled via a MOOG portable test controller unit (13) by a PC (14) with MOOG Integrates Test Software.

Any foundation can be tested, but the foundation presented in Figure G.3 is a small scale bucket foundation. The bucket foundation is installed by pushing it into the soil, and on top of the foundation a tower (5) is mounted to transfer the loads from the actuator to the foundation. On the bucket foundation, pressure transducers are mounted to measure the pore pressure along the skirts. The vertical movement is measured by two ASM wire transducers (7). The pressure transducers are via the distribution box (12) connected to the MOOG PTC, whereas the displacement transducers are connected directly to the MOOG PTC. All data are collected and stored on the PC.

G.3 Special Equipment

This manual will only describe equipment that need extra attention. It is the hydraulic MOOG actuator and the electrical wiring between transducers and MOOG PTC, which are not described in the associated manuals.

G.3.1 Hydraulic Actuator

The set up has two hydraulic actuators: one which is used for CPT-testing and installation of the bucket, and one which is used during testing. The one used for installation is named *installation actuator*, and the other is named *MOOG actuator*, since MOOG is the company who delivered the control system for that actuator.

The installation actuator is controlled by an up/down button. Hence, only one speed of the piston is available.

The MOOG actuator is controlled via MOOG Integrated Test Suite, *MITS*, which is able to control the actuator very precisely. The actuator can be controlled either by force or by prescribed displacement. Therefore, the transducers used to control the actuator must be calibrated and tuned to the specific task.

Calibration

All transducers, which are used, must be calibrated in order to convert the electrical signal to an engineering unit, i.e. N, Pa, m. The calibration only convert the electrical signal into an engineering value. Therefore, the calibration is independent of type of test. Each transducer needs to be calibrated and will have a unique calibration factor. This calibration factor is input for the MITS for each channel. Hence, it is important to connect the transducers accordingly the calibration factors specified in the software.

Tuning

The actuator is controlled by a PID regulation (Proportional, Integral and Derivative). The system works as depicted in Figure G.5. The user of the system choose a control signal, that the actuator should respond on. This signal is compared to the signal measured by the relevant transducer (feedback signal). If a mismatch between the two signals are observed, the software will adjust the signal to the servo vale telling it to move either forth or back. This loop continues until a satisfying match between the control signal and the feedback signal is measured. For the present set-up the load cell and the horisontal displacement transducer (see Figure G.3) are used as feedback signals, when the load or displacement controlled option is chosen, respectively. One example is: load controlled sequence is chosen and therefore the signal from the load cell is used as a feedback signal. The user choose a load sequence that the actuator should produce. The control signal then describe the force as a function of time that the actuator should deliver. The actuator adjust the force by moving the piston forth and back to match the control signal. How aggressively the actuator should react to the control signal is defined by tuning the system the feedback transducer. Figure G.5 sows three

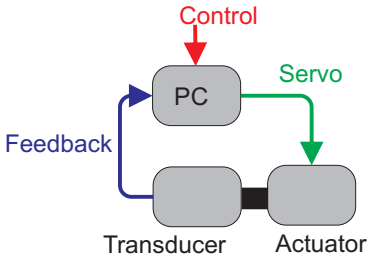

Fig. G.4: PID control system.

examples: One where the system is tuned to aggressively, one which is well tuned, and one which is to passive. The red line indicate the control signal. As mentioned above, if the control signal and feedback signal do not match,

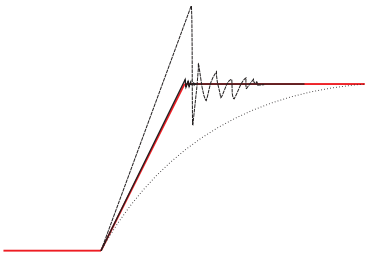

Fig. G.5: Example of why tuning is important. The red line indicate the control signal. Dashed line indicate a too aggressive response, the dotted line show a too passive response and the full line show a well tuned response.

the computer will send a signal to the servo valve to either increase or decrease the oil flow in order to get the actuator to move. The value of the P-gain will tell how aggressive the system is, i.e. how fast the actuator will get the feedback signal to match the control signal. If the P-gain is too high it will overshoot the control signal. On the other hand, if the P-gain is too low it will take relatively long time to reach the control signal. The value of the P-gain not only depends on the loading sequence, but also on the stiffness of test object. The stiffer the material is, the more sensitive is the control system oscillation, which cause large vibrations. Therefore, is the P-gain not only depending on the loading sequence, but also on the material.

Recommendations for tuning:

When tuning it is highly recommended to start with P-gain equal to 0.1 and increase it little by little, and be ready to push the emergency stop button. It is advised to tune the system on a load sequence as close as possible to the test to be conducted. A simple thing as change in the amplitude or frequency

amp [N]	frequency [Hz]	P-gain	I-gain	D-gain	Damping
50	4.0	1.1	0.3	0.9	0.0
100	4.0	0.8	0.3	0.9	0.0
500	4.0	0.8	0.3	0.9	0.0
500	0.5	0.7	0.3	0.9	0.0

Table G.1: Tuning of Force Controlled - 20.08.2015

could demand a new tuning.

For tuning it is advised to start the tuning with square waves, and when tuning is thought to be done, also to check sinusoidal waves.

Tuning for Force Controlled Cyclic Tests - 20.08.2015: Before starting preparing a test it is always a good idea to test whether the system is able to apply the wanted load conditions. i.e. combination of frequency, load type, size of load. Testing on the small bucket in unprepared soil gave the best tuning with the parameters given in Table G.1.

G.3.2 Wiring of Transducers

Documentation for the MOOG hard ware can be found in the associated manuals, along with descriptions of the wiring of: load cell, magnetostrictive position sensor and the Portable Test Controller (PTC). However, some of the connections were custom made, and is the documentation hereof is given below.

Pressure Transducers

In order to make is possible to connect up to 18 pressure transducers (full bridge transducers), a distribution box were made. Figure G.6 show the connection between the MOOG PTC and the distribution box, which the pressure transducers were attached to. The box consists of 6 DB37 sockets and 18 7 pin LEMO sockets.

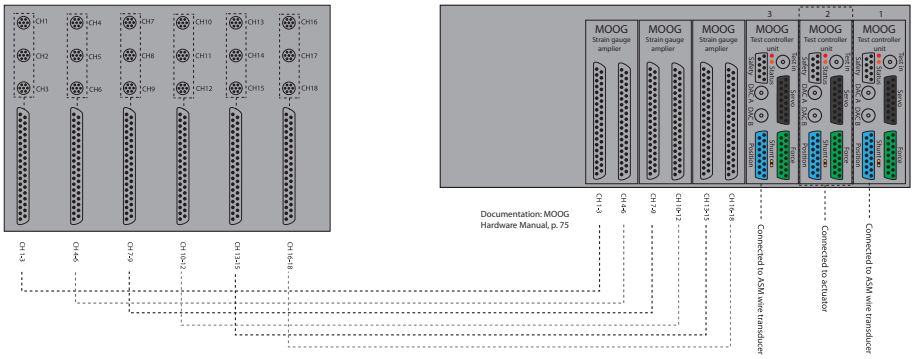

Fig. G.6: MOOG PTC.

The internal wiring of the box is illustrated from the inside in Figure G.7.

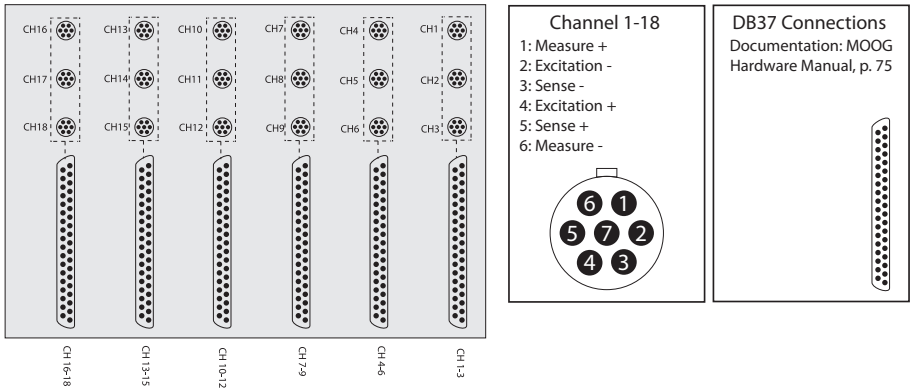

Fig. G.7: Distribution box seen from inside.

The wiring between each pressure transducer (HBM P3MBA, 5bar and 10 bar) and the distribution box is illustrated in Figure G.8. Additional information of the pressure transducer can be found in the corresponding manual.

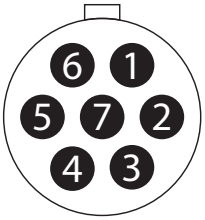

Type: HBM P3MBA
5bar/10bar
1: Measure - (red)
2: Sense + (green)
3: Excitation + (blue)
4: Sense - (gray)
5: Excitation - (black)
6: Measure + (white)

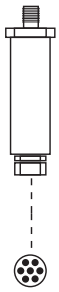

Fig. G.8: Wire connection of pressure transducer.

Internal Displacement Transducers

The displacement transducers mounted inside the pressure tank, were wire transducers of the type: ASM WS1000-R1k, which is a potentiometer. The potentiometers were connected directly to Position socket on the MOOG PTC, as illustrated in Figure G.9.

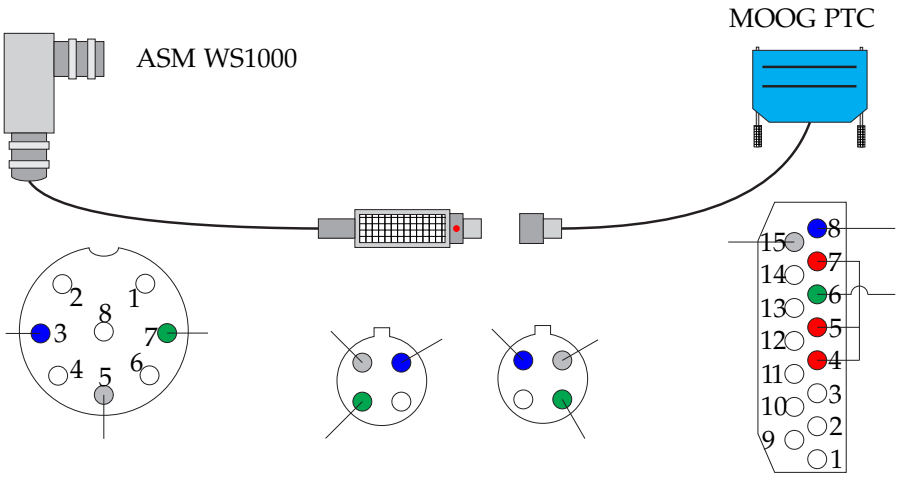

Fig. G.9: Wire connection of AMS wire transducers.

G.4 Preparation of laboratory tests

Conducting a test inside the pressure tank can be divided into 3 sub tasks: preparing the soil, installation of the foundation and other equipment and conducting the test. This procedure will also be divided into these three categories. Each category is listed below with additional subitems. Each of the items below will be described and can also be used as a check list.

1. Preparation of Sand
   - Leveling
   - Loosening
   - Vibration
   - CPT-Testing
2. Installation of Foundation
   - Saturating pore pressure measuring system
   - Installation of Bucket
   - Close the valve on the Bucket
   - Connecting cables
   - Mounting Tower
   - Mounting internal frame
   - Mounting and connecting displacement transducers
   - Connecting actuator to test object
   - Sealing the Pressure Tank
3. Conducting a Test

G.4.1 Preparation of the soil

Leveling

Firstly, a leveled surface is ensured. After leveling the soil surface, the sand is loosened by an upward gradient.

Loosening of the sand

The sand is loosened to get the sand back to the same initial state prior to vibration, so the same vibration procedure will lead to approximately the same soil conditions. This is done by applying an upward gradient on 0.91. The gradient is applied by letting water flow from a tank situated above the water surface in the tank. The water must enter the soil under a suitable velocity, to avoid a development of flow channels which could reduce the soil strength.

The upward gradient on 0.91 is based on experiments performed earlier at AAU. The hydraulic gradient, i, describes the reduction in energy, or head loss, per unit length. $i = \Delta h/l$ where Δh is loss of energy between two arbitrary heights/sections [m] and l is the length of a sample [m]. With the sample length of 60 cm and a gradient on 0.91, this equals to a pressure

height of 55 cm. The gradient is applied for 5 minutes and the nozzle is then closed.

After loosening the sand, the water level in the tank should be approximately 6 cm above the sand surface. The water level can be adjusted by either letting water flow out with the bottom valves or letting water through the side of the tank above the sand surface. If water have to be let in above the sand surface a metal plate is placed on top of the sand to avoid washing away sand at the inlet.

Vibration

The goal of the vibration is to create a sand volume that is densely packed, i.e. a relative density at around 0.82 - 0.92. The sand should be completely covered by water, else the rod of the vibrator will pull air into the sand. A suitable water level is approximately 6 cm above the sand surface. For vibration of the sand inside the pressure tank, a circular deck with holes in a grid with 20 cm between each hole is inserted.

Every second hole is marked with a dot, so it is easier to keep track of the vibration pattern. A vibration pattern, where firstly, the 12 holes closest to the center is vibrated, followed by every second hole. Then the 12 middle holes again followed by vibration of the remaining holes. This patters has shown acceptable results in most cases.

CPT-testing

In order to determine the established soil conditions, mini CPT-testing is performed. The equipment to perform the CPT's are: a CPT probe, a beam, a transition peace and an actuator. If the soil conditions are satisfied, the foundation installation phase can begin. If not, further vibration is needed.

G.4.2 Installation of foundation and arranging measuring devices

Saturating pore pressure measuring system

Firstly all pore pressure transducers are saturated with water, to ensure a more stable and correct measure of the pore pressure. The foundation is lowered into a barrel filled with water. A syringe is then used to saturate the transducers, by filling the system with water and then close the valves mounted on the pore pressure measuring system.

Installation of Bucket

The foundation is brought into the pressure tank from the top hatch. It is placed on a metal plate on the sand surface. An actuator is then mounted on the top opening and is used to install the foundation.

Close the valve on the Bucket

After installation the valve on the bucket is closed.

Connecting cables

Next, the cables from all transducers are led though a flange in the tank with matching holes.

Mounting Tower

The tower is lowered down through the top hatch, and is then mounted on top of the bucket.

Mounting internal frame

Inside the pressure tank it is possible to mount internal frames, on which e.g. displacement transducers can be mounted.

Mounting and connecting displacement transducers

The displacement transducers are mounted on the internal frame, connected to the foundation and electrical wires are led through a hatch and connected.

Connecting actuator to test object

In this step extra attention is needed!, as it is necessary to operate inside the tank while high pressure is on the large hydraulic actuator. Firstly the actuator is turned on and the piston is moved to the correct position (displacement controlled). After finding the correct position a steel rod is fixed on the piston and on the tower. As the actuator is very power full, it is important that the safe and unsafe areas inside the tank is fully understood. Figure G.10 show the principle of the safe area (not red). However, all users are advised to inspect the worst case scenario by them self (Actuator at maximum stroke with the tower in front).

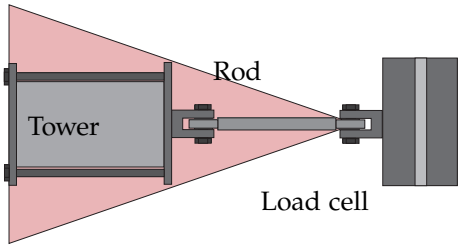

Fig. G.10: Illustration of the actuators working area.

Sealing the Pressure Tank

When the piston is connected to the tower, a last check is made to ensure that every thing is set up correctly, and all signals are working. When everything is ready, the two openings in the tank are sealed hermetically.

G.4.3 Conducting a test

The last step is to conduct the test. The test sequence is specified by the user in the MOOG Integrated Test Software which also records the specified data.

Appendix H

Laboratory Results

Test Overview of Monotonic Tests

Test No.	Aspect Ratio L/D	Loading Rate $[mm/s]$	Angular Velocity $[^\circ/s]$
Mon01	0.5	0.1	0.1
Mon02	0.5	1.0	0.9
Mon03	0.5	10	8.8
Mon04	0.5	50	32.1
Mon05	0.5	100	81.8
Mon06	0.5	200	122.6
Mon07	1.0	0.1	0.1
Mon08	1.0	1.0	0.7
Mon09	1.0	10	6.8
Mon10	1.0	50	29.3
Mon11	1.0	100	46.1
Mon12	1.0	200	90.9

Table H.1: List of Monotonic tests

Test No. Mon01

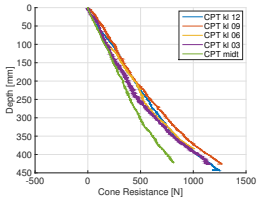

(a) Tip resistance with depth.

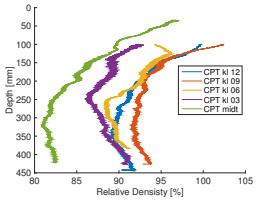

(b) Relative density with depth

Fig. H.1: CPT data for prepararion for Test No. 01

Load type	Test information
Monotonic	Loading rate = 0.1 mm/s

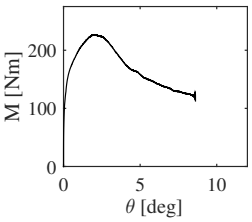

(a) M(θ).

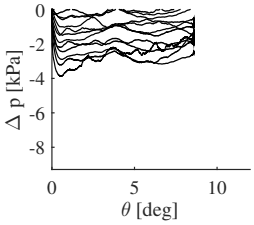

(b) Δu(θ).

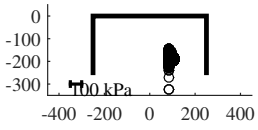

(c) Maximum pore pressure.

Test No. Mon02

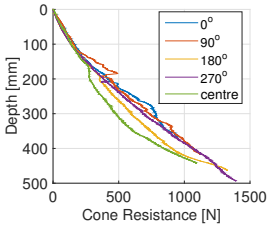

(d) Tip resistance with depth.

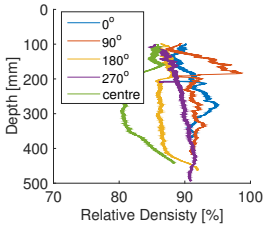

(e) Relative density with depth

Fig. H.2: CPT data for prepararion for Test No. 01

Load type	Test information
Monotonic	Loading rate = 1.0 mm/s

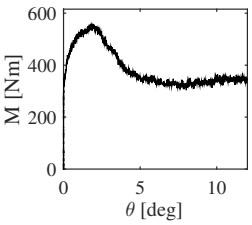

(a) M(θ).

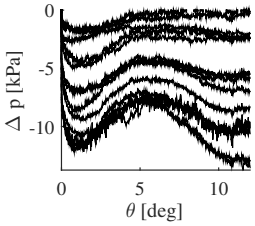

(b) Δu(θ).

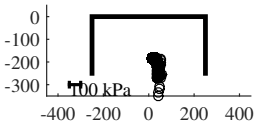

(c) Maximum pore pressure.

Test No. Mon03

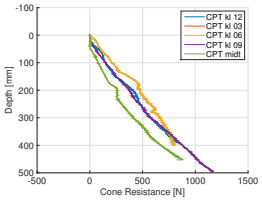

(d) Tip resistance with depth.

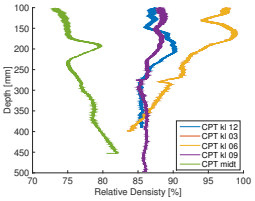

(e) Relative density with depth

Fig. H.3: CPT data for prepararion for Test No. 01

Load type	Test information
Monotonic	Loading rate = 10 mm/s

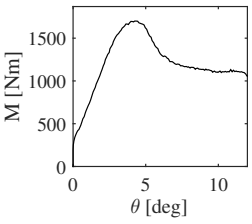

(a) M(θ).

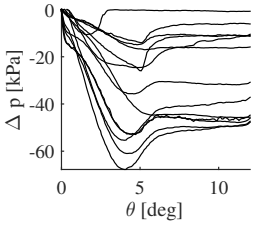

(b) Δu(θ).

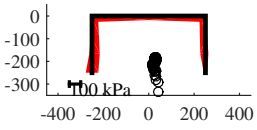

(c) Maximum pore pressure.

Test No. Mon04

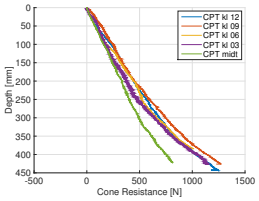

(d) Tip resistance with depth.

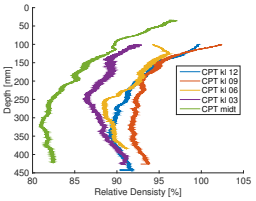

(e) Relative density with depth

Fig. H.4: CPT data for prepararion for Test No. 01

Load type	Test information
Monotonic	Loading rate = 50 mm/s

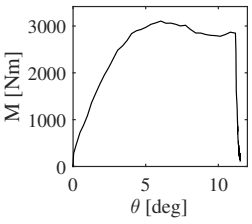

(a) M(θ).

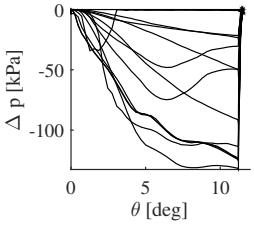

(b) Δu(θ).

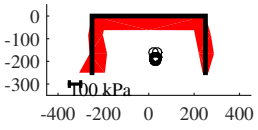

(c) Maximum pore pressure.

Test No. Mon05

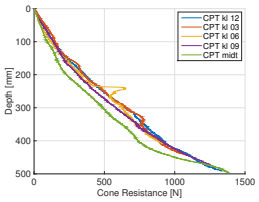

(d) Tip resistance with depth.

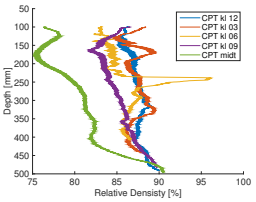

(e) Relative density with depth

Fig. H.5: CPT data for prepararion for Test No. 01

Load type	Test information
Monotonic	Loading rate = 100 mm/s

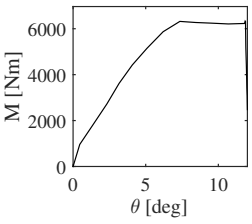

(a) M(θ).

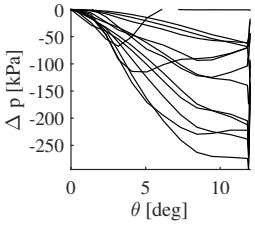

(b) Δu(θ).

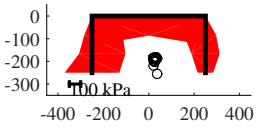

(c) Maximum pore pressure.

Test No. Mon06

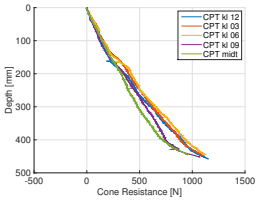

(d) Tip resistance with depth.

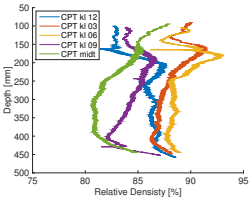

(e) Relative density with depth

Fig. H.6: CPT data for prepararion for Test No. 01

Load type	Test information
Monotonic	Loading rate = 200 mm/s

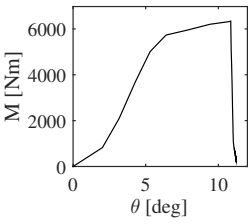

(a) M(θ).

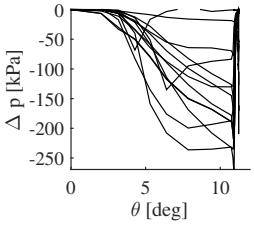

(b) Δu(θ).

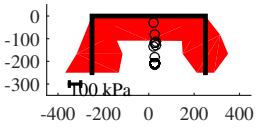

(c) Maximum pore pressure.

Test No. Mon07

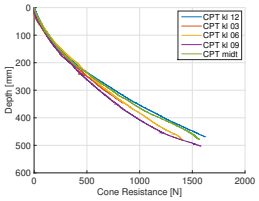

(d) Tip resistance with depth.

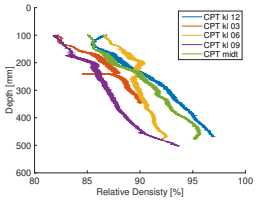

(e) Relative density with depth

Fig. H.7: CPT data for prepararion for Test No. 01

Load type	Test information
Monotonic	Loading rate = 0.1 mm/s

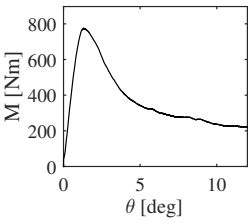

(a) M(θ).

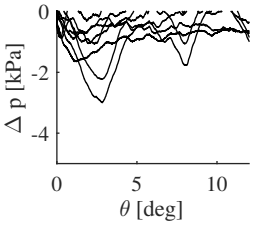

(b) Δu(θ).

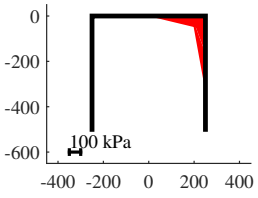

(c) Maximum pore pressure.

Test No. Mon08

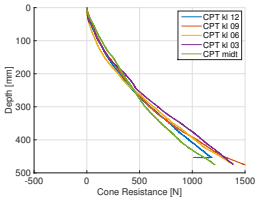

(d) Tip resistance with depth.

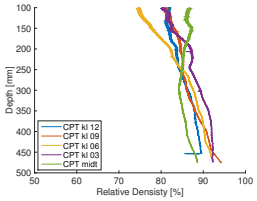

(e) Relative density with depth

Fig. H.8: CPT data for prepararion for Test No. 01

Load type	Test information
Monotonic	Loading rate = 1.0 mm/s

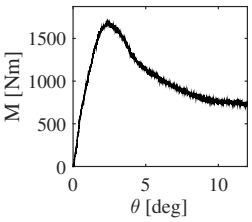

(a) M(θ).

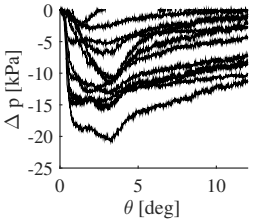

(b) Δu(θ).

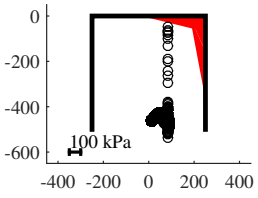

(c) Maximum pore pressure.

Test No. Mon09

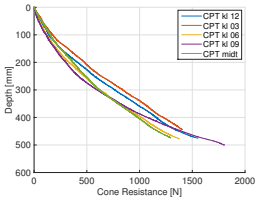

(d) Tip resistance with depth.

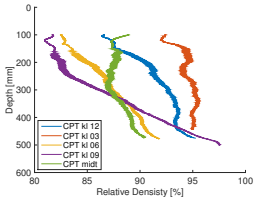

(e) Relative density with depth

Fig. H.9: CPT data for prepararion for Test No. 01

Load type	Test information
Monotonic	Loading rate = 10 mm/s

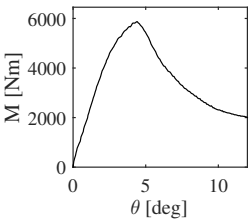

(a) M(θ).

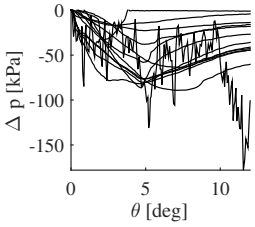

(b) Δu(θ).

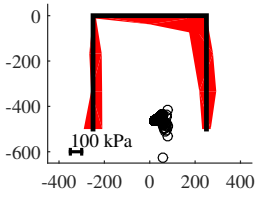

(c) Maximum pore pressure.

Test No. Mon10

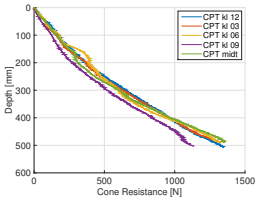

(d) Tip resistance with depth.

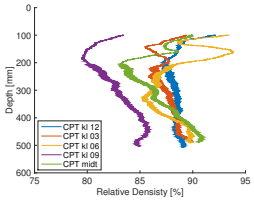

(e) Relative density with depth

Fig. H.10: CPT data for prepararion for Test No. 01

Load type	Test information
Monotonic	Loading rate = 50 mm/s

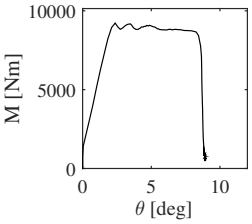

(a) M(θ).

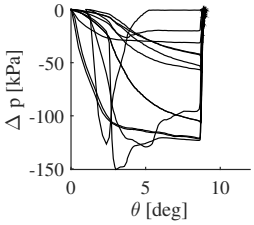

(b) Δu(θ).

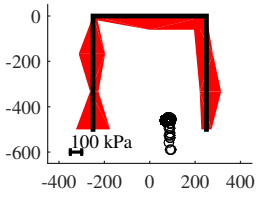

(c) Maximum pore pressure.

Test No. Mon11

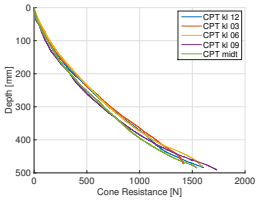

(d) Tip resistance with depth.

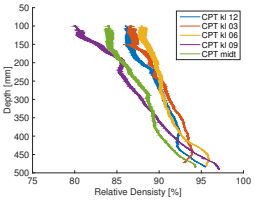

(e) Relative density with depth

Fig. H.11: CPT data for prepararion for Test No. 01

Load type	Test information
Monotonic	Loading rate = 100 mm/s

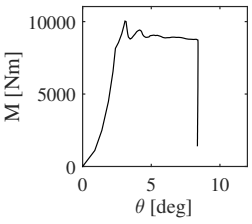

(a) M(θ).

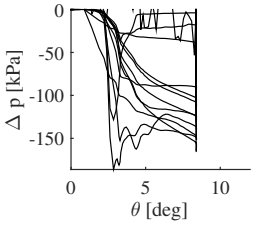

(b) Δu(θ).

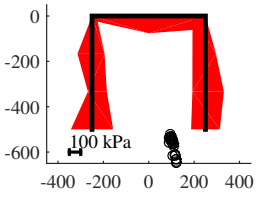

(c) Maximum pore pressure.

Test No. Mon12

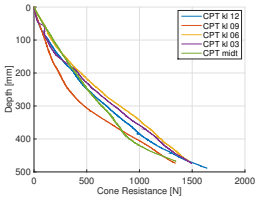

(d) Tip resistance with depth.

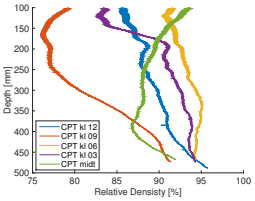

(e) Relative density with depth

Fig. H.12: CPT data for prepararion for Test No. 01

Load type	Test information
Monotonic	Loading rate = 200 mm/s

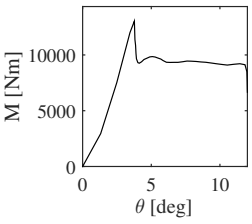

(a) M(θ).

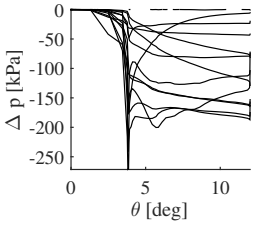

(b) Δu(θ).

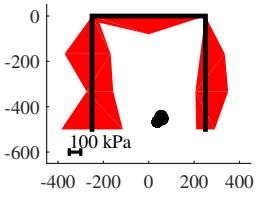

(c) Maximum pore pressure.

Test Overview of Cyclic Tests

Test No.	Frequency [Hz]	Amp. [M]	Mean [M]	Number of Cycles	Pre-cycling	ζ_b	ζ_c
Cyc01	4.0	252	28	1000	No	1.00	-0.80
Cyc02	2.0	240	13	1000	No	0.90	-0.90
Cyc03	1.0	265	-13	1000	No	0.90	-1.10
Cyc04	0.5	252	0	1000	No	0.90	-1.00
Cyc05	4.0	225	0	1000	Yes	0.80	-1.00
Cyc06	1.0	63	21	1000	Yes	0.30	-0.50
Cyc07	1.0	112	0	1000	Yes	0.40	-1.00
Cyc08	1.0	224	0	1000	Yes	0.80	-1.00
Cyc09	1.0	126	126	1000	Yes	0.90	0.00
Cyc10	1.0	84	84	1000	Yes	0.60	0.00
Cyc11	1.0	56	56	1000	Yes	0.40	0.00
Cyc12	1.0	79	34	1000	Yes	0.40	-0.40
Cyc13	1.0	28	28	1000	Yes	0.20	0.00
Cyc14	1.0	135	34	1000	Yes	0.60	-0.60
Cyc15	1.0	56	168	1000	Yes	0.80	0.50

Table H.2: List of cyclic tests. $M_R = 280N$. All tests performed on bucket with $L/D = 0.25$

Test No. Cyc01

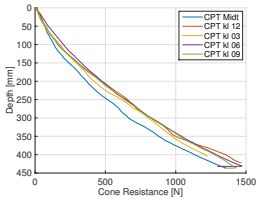

(d) Tip resistance with depth.

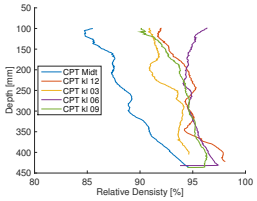

(e) Relative density with depth

Fig. H.13: CPT data for prepararion for Test No. 01

Load type	Test information
Cyclic	f = 4.0 Hz, N_{pre} = 0, N = 1000 M_{cy} = 252 kN, M_a = 28 kN

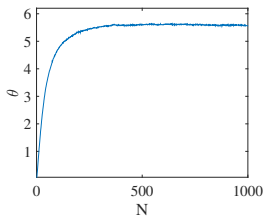

(a) Rotation as a function of number of cycles.

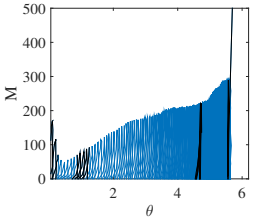

(b) Moment as a function of rotation.

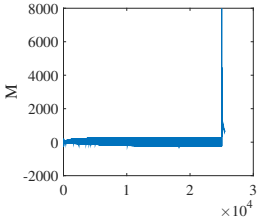

(c) Moment as a function of sample number.

Fig. H.14: Results from test Cyc01

Test No. Cyc02

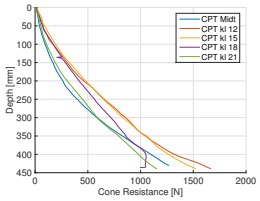

(a) Tip resistance with depth.

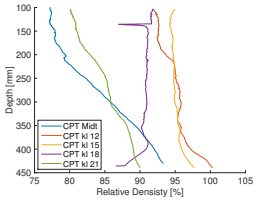

(b) Relative density with depth

Fig. H.15: CPT data for prepararion for Test No. 02

Load type	Test information
Cyclic	f = 2.0 Hz, N_{pre} = 0, N = 1000
	M_{cy} = 240 kN, M_a = 13 kN

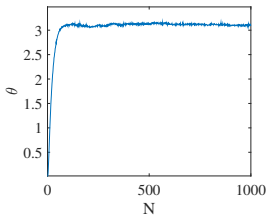

(a) Rotation as a function of number of cycles.

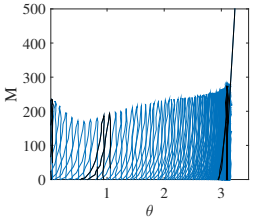

(b) Moment as a function of rotation.

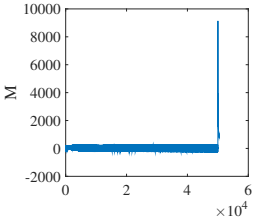

(c) Moment as a function of sample number.

Fig. H.16: Results from test Cyc02

Test No. Cyc03

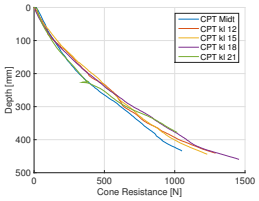

(a) Tip resistance with depth.

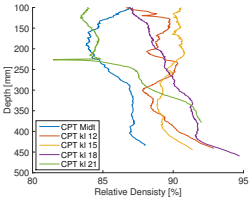

(b) Relative density with depth

Fig. H.17: CPT data for prepararion for Test No. 03

Load type	Test information
Cyclic	f = 1.0 Hz, N_{pre} = 0, N = 1000
	M_{cy} = 265 kN, M_a = -13 kN

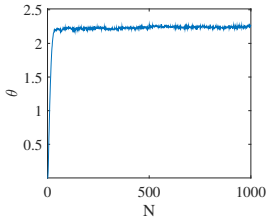

(a) Rotation as a function of number of cycles.

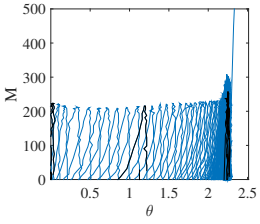

(b) Moment as a function of rotation.

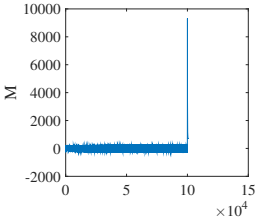

(c) Moment as a function of sample number.

Fig. H.18: Results from test Cyc03

Test No. Cyc04

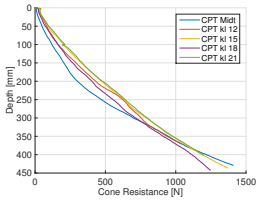

(a) Tip resistance with depth.

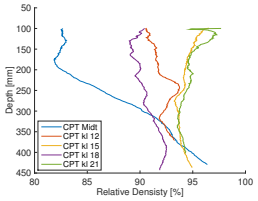

(b) Relative density with depth

Fig. H.19: CPT data for prepararion for Test No. 04

Load type	Test information
Cyclic	f = 0.5 Hz, N_{pre} = 0, N = 1000 M_{cy} = 252 kN, M_a = 0 kN

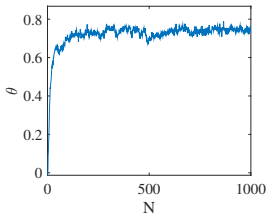

(a) Rotation as a function of number of cycles.

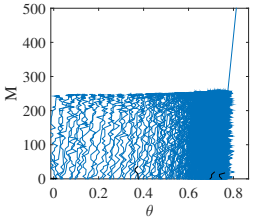

(b) Moment as a function of rotation.

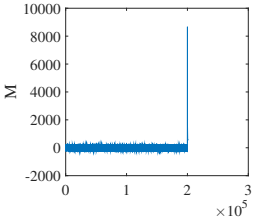

(c) Moment as a function of sample number.

Fig. H.20: Results from test Cyc04

Test No. Cyc05

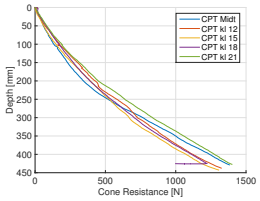

(a) Tip resistance with depth.

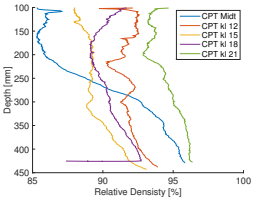

(b) Relative density with depth

Fig. H.21: CPT data for prepararion for Test No. 05

Load type	Test information
Cyclic	f = 4.0 Hz, N_{pre} = 1000, N = 1000
	M_{cy} = 225 kN, M_a = 0 kN

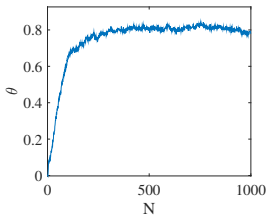

(a) Rotation as a function of number of cycles.

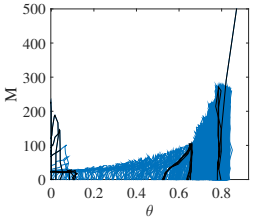

(b) Moment as a function of rotation.

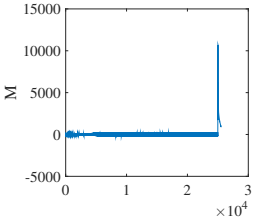

(c) Moment as a function of sample number.

Fig. H.22: Results from test Cyc05

Test No. Cyc06

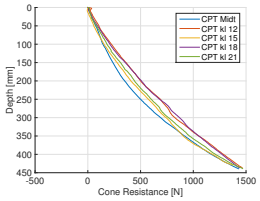

(a) Tip resistance with depth.

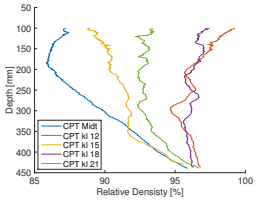

(b) Relative density with depth

Fig. H.23: CPT data for prepararion for Test No. 06

Load type	Test information
Cyclic	f = 1.0 Hz, N_{pre} = 1000, N = 1000
	M_{cy} = 63 kN, M_a = 21 kN

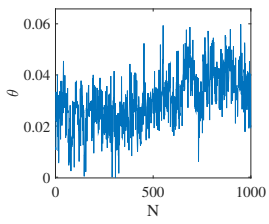

(a) Rotation as a function of number of cycles.

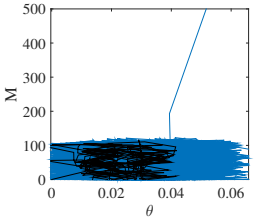

(b) Moment as a function of rotation.

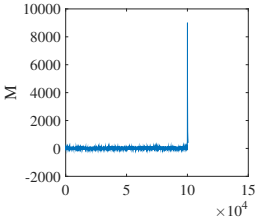

(c) Moment as a function of sample number.

Fig. H.24: Results from test Cyc06

Test No. Cyc07

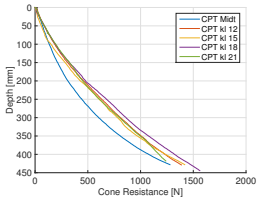

(a) Tip resistance with depth.

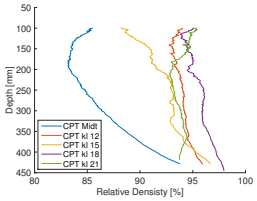

(b) Relative density with depth

Fig. H.25: CPT data for prepararion for Test No. 07

Load type	Test information
Cyclic	f = 1.0 Hz, N_{pre} = 1000, N = 1000
	M_{cy} = 112 kN, M_a = 0 kN

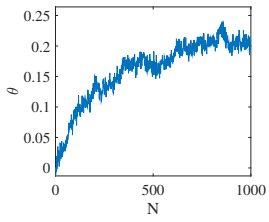

(a) Rotation as a function of number of cycles.

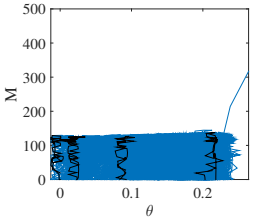

(b) Moment as a function of rotation.

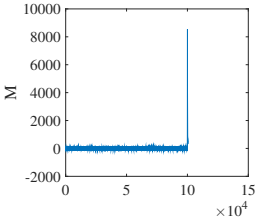

(c) Moment as a function of sample number.

Fig. H.26: Results from test Cyc07

Test No. Cyc08

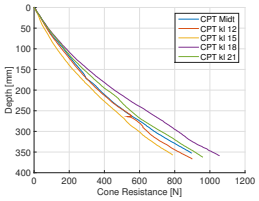

(a) Tip resistance with depth.

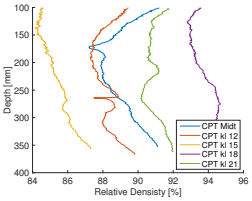

(b) Relative density with depth

Fig. H.27: CPT data for prepararion for Test No. 08

Load type	Test information
Cyclic	f = 1.0 Hz, N_{pre} = 1000, N = 1000
	M_{cy} = 224 kN, M_a = 0 kN

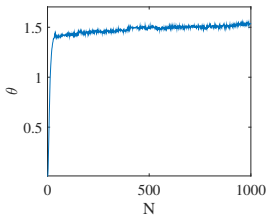

(a) Rotation as a function of number of cycles.

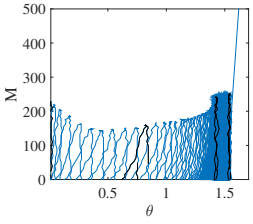

(b) Moment as a function of rotation.

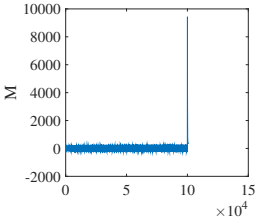

(c) Moment as a function of sample number.

Fig. H.28: Results from test Cyc08

Test No. Cyc09

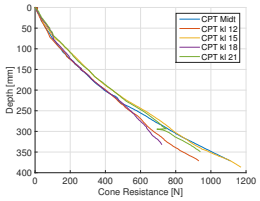

(a) Tip resistance with depth.

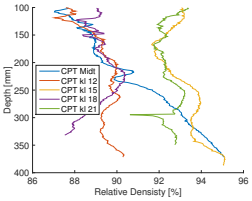

(b) Relative density with depth

Fig. H.29: CPT data for prepararion for Test No. 09

Load type	Test information
Cyclic	f = 1.0 Hz, N_{pre} = 1000, N = 1000
	M_{cy} = 126 kN, M_a = 126 kN

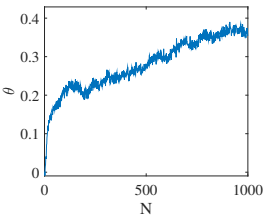

(a) Rotation as a function of number of cycles.

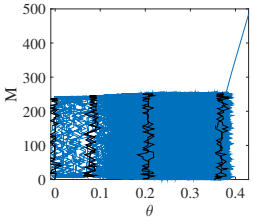

(b) Moment as a function of rotation.

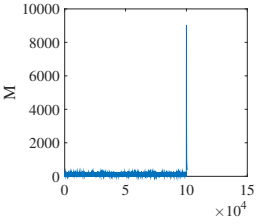

(c) Moment as a function of sample number.

Fig. H.30: Results from test Cyc09

Test No. Cyc10

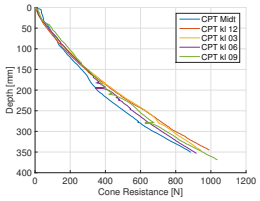

(a) Tip resistance with depth.

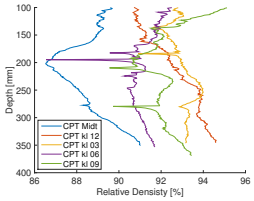

(b) Relative density with depth

Fig. H.31: CPT data for prepararion for Test No. 10

Load type	Test information
Cyclic	f = 1.0 Hz, N_{pre} = 1000, N = 1000
	M_{cy} = 84 kN, M_a = 84 kN

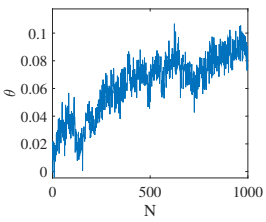

(a) Rotation as a function of number of cycles.

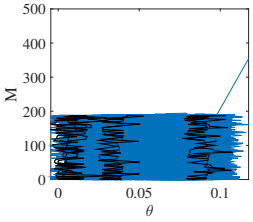

(b) Moment as a function of rotation.

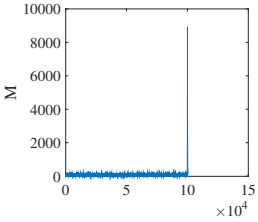

(c) Moment as a function of sample number.

Fig. H.32: Results from test Cyc10

Test No. Cyc11

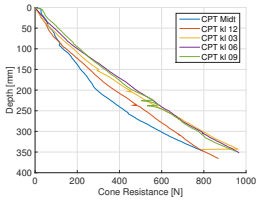

(a) Tip resistance with depth.

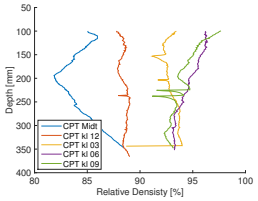

(b) Relative density with depth

Fig. H.33: CPT data for prepararion for Test No. 11

Load type	Test information
Cyclic	f = 1.0 Hz, N_{pre} = 1000, N = 1000
	M_{cy} = 56 kN, M_a = 56 kN

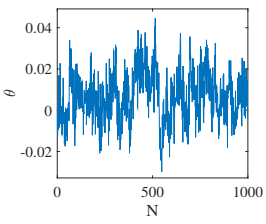

(a) Rotation as a function of number of cycles.

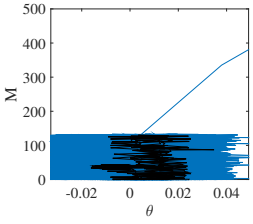

(b) Moment as a function of rotation.

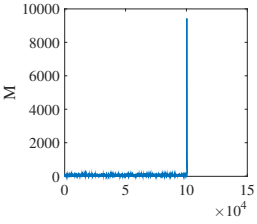

(c) Moment as a function of sample number.

Fig. H.34: Results from test Cyc11

Test No. Cyc12

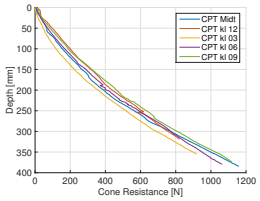

(a) Tip resistance with depth.

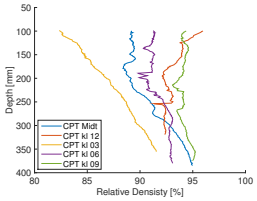

(b) Relative density with depth

Fig. H.35: CPT data for prepararion for Test No. 12

Load type	Test information
Cyclic	f = 1.0 Hz, N_{pre} = 1000, N = 1000
	M_{cy} = 79 kN, M_a = 34 kN

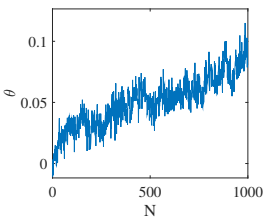

(a) Rotation as a function of number of cycles.

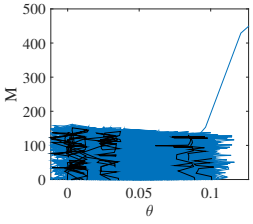

(b) Moment as a function of rotation.

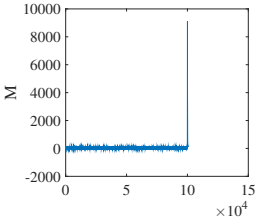

(c) Moment as a function of sample number.

Fig. H.36: Results from test Cyc12

Test No. Cyc13

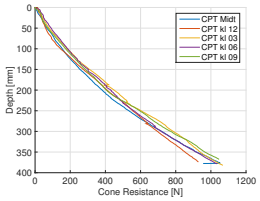

(a) Tip resistance with depth.

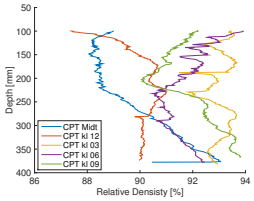

(b) Relative density with depth

Fig. H.37: CPT data for prepararion for Test No. 13

Load type	Test information
Cyclic	f = 1.0 Hz, N_{pre} = 1000, N = 1000
	M_{cy} = 28 kN, M_a = 28 kN

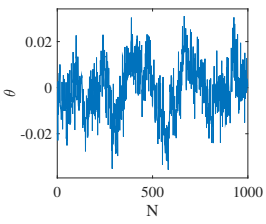

(a) Rotation as a function of number of cycles.

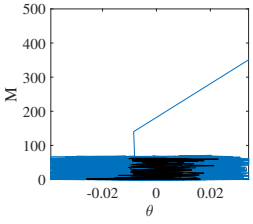

(b) Moment as a function of rotation.

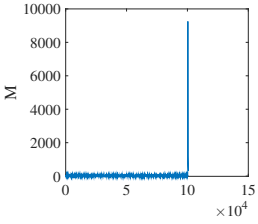

(c) Moment as a function of sample number.

Fig. H.38: Results from test Cyc13

Test No. Cyc14

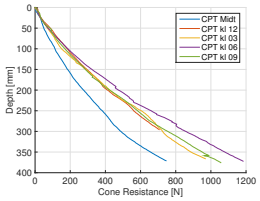

(a) Tip resistance with depth.

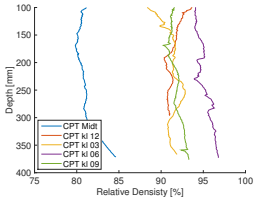

(b) Relative density with depth

Fig. H.39: CPT data for prepararion for Test No. 14

Load type	Test information
Cyclic	f = 1.0 Hz, N_{pre} = 1000, N = 1000
	M_{cy} = 135 kN, M_a = 34 kN

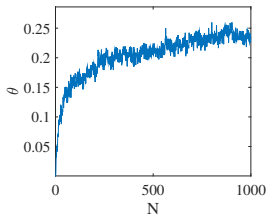

(a) Rotation as a function of number of cycles.

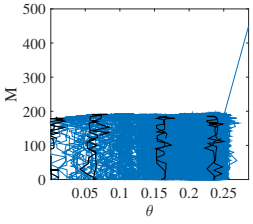

(b) Moment as a function of rotation.

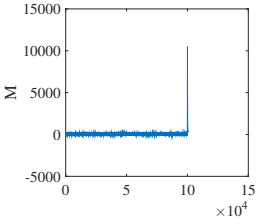

(c) Moment as a function of sample number.

Fig. H.40: Results from test Cyc14

Test No. Cyc15

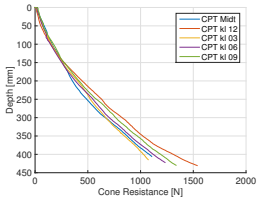

(a) Tip resistance with depth.

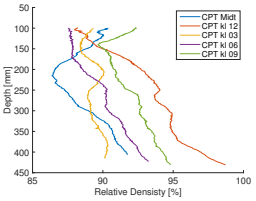

(b) Relative density with depth

Fig. H.41: CPT data for prepararion for Test No. 15

Load type	Test information
Cyclic	f = 1.0 Hz, N_{pre} = 1000, N = 1000
	M_{cy} = 56 kN, M_a = 168 kN

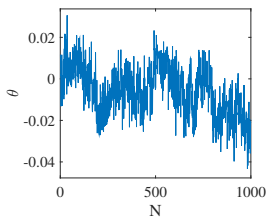

(a) Rotation as a function of number of cycles.

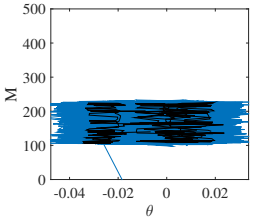

(b) Moment as a function of rotation.

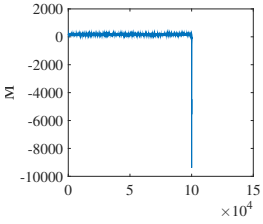

(c) Moment as a function of sample number.

Fig. H.42: Results from test Cyc15

SUMMARY

Today, 80 % of all European offshore wind turbines are installed on monopiles. A cost-effective alternative to the monopile is the mono bucket foundation. For an offshore wind turbine foundation in open seas, the dominant load is often coming from waves..

During storms, large waves are formed and when hitting the foundation they induce high impact loads with a short duration. It is important that the foundation is able to resists these huge loads. Fortunately, the conducted research showed that the capacity of the mono bucket foundation is high to impact loads. When exposed to a huge wave load the foundation is sucked to the seabed, creating extra capacity during the impact.

Over the life-time of an offshore wind turbine foundation will be hit by millions of waves. Each wave might lead to a permanent rotation of the foundation. Therefore, it is important to be able to estimate the total deformation accumulating for each wave impact. The presented research has shown indications that only the first waves contribute to the permanent rotation. These indications are seen in small-scale laboratory tests and on a full-scale mono bucket foundation.

ISSN (online): 2246-1248
ISBN (online): 978-87-7112-552-8

AALBORG **UNIVERSITY PRESS**